# 11ème Conférence Internationale des Energies Renouvelables

Editor : Dr. Ahmed Rhif (Tunisia)

# ICID

International Centre for Innovation & Development

## 11$^{ème}$ Conférence Internationale des Energies Renouvelables

Proceedings of Engineering & Technology

-PET-

Editor : Dr. Ahmed Rhif (Tunisia)

# Committees

## Honorary General Chairs

Bendifallah Leila (ALG)

El Mati Khoumri (MAR)

Georges Descombes (FRA)

## General Chairs

Ahmed Rhif (TUN)

Fatima Zohra Boufadi (ALG)

Jeru Achyl Hounogbe (SEN)

Tayane Souad (MAR)

## Steering Committee

Abdoulaye Bouya Diop (SEN)

Akrouch  Soukaina (MAR)

Allé Dioum (SEN)

Belatel Mimi (ALG)

Birane Mouhoub (ALG)

Djeghlal M.Lamine (ALG)

Ines Ben Sassi (TUN)

Kasbadji Merzouk Nachida  (ALG)

Meriem Hayani Mechkouri (MAR)

Nada Chtioui (TUN)

Nawel Seddiki (ALG)

Rekioua Djamila (ALG)

Sahbeni Kawther (TUN)

Salma El Aimani (MAR)

Sara Zatir (ALG)

Taher Bahi (ALG)

Yosra Lahdheri (TUN)

Youssef Soufi (ALG)

## Technical Committee

Abdelkrim Khireddine (ALG)

Abdellah Mechaqrane (MAR)

Barara Mohamed (FRA)

Bedoud Khouloud (ALG)

Berbaoui Brahim (ALG)

Cherkaoui Abdeljabbar (MAR)

Djalila Boudemagh (ALG)

El Fadar Abdellah (MAR)

Fateh Mebarek-Oudina (ALG)

Gherbi Mohamed (ALG)

Hadja Fatima Mehnane (ALG)

Haitham Saad Mohamed Ramadan (FRA)

Kamal Reklaoui (MAR)

Kheiri Abdelhamid (FRA)

Kouzou Abdallah (ALG)

Madiha Yessari (MAR)

Manal Marzouq (MAR)

Mhamed Hammoudi (ALG)

Mounir Gaidi (UAE)

Mustapha Hatti (ALG)

Rabhi Selma  (ALG)

Rachid Benchrifa (MAR)

Rafika Boudries (ALG)

Rahmouni Soumia (ALG)

Sellam Mebrouk (ALG)

Slimane Semghouli (MAR)

Sofiane Amara (ALG)

Youssef Errami (MAR)

Zohra Ameur (ALG)

# Summary

# Bi- objective optimization of two R744 Booster refrigeration systems using Genetic Algorithm

Yosra Ben Salem[#1], AhmedBellagi[#2]

[#]*L.R.Thermique et Thermodynamique des Procédés Industriels*
*Ecole Nationale d'Ingénieurs de Monastir, E.N.I.M, University of Monastir, Tunisia*

`[1]yosraisetkelibia@gmail.com, [1]ahmedbellagi@gmail.com`

*Abstract*— **The objective of this study is the optimization and the comparison of two transcritical CO2 Booster refrigeration systems for simultaneous heating and cooling applications .A CO2–booster two-stage chiller combining transcritical cycle in cascade with a subcritical (conventional) and flash gas by-pass is compared with a system with parallel compression. The examined units produce refrigeration at two temperatures levels and hot water at 75°C. For this purpose, a computer model has been developed using Engineering Equation Solver first to simulate the two systems at steady state for different operating parameters and then to evaluate the two configurations performances based on coefficient of performance (COP) as well as exergetic efficiency ($\eta_{ex}$) , including component wise irreversibility and subsequently optimizes the main operating variables to reach the maximum performance. A multi-objective optimization model using genetic algorithm and weight approach is established. For optimal factors and same cooling duty of two refrigerators, the second unit exhibits significant performance improvement.**

*Keywords*— **CO2 Booster refrigeration; Exergy analysis; Comparaison; multi-objective optimization; Genetic Algorithm .**

## I. INTRODUCTION

In commercial supermarket refrigeration systems and others applications, the most used refrigerants are R22, R404A (a blend of R125 / R143a / R134a) and R134a, which have a high global warming potential (GWP) [1–3]. The use of harmful working fluids causes abnormal climate changes and accelerates the global warming effect [4–7]. Especially, after the legislative actions, such as the EU F-Gas Regulations [8] and the Montreal Protocol Kigali Amendment [9], the usual working fluids are substituted with the natural fluids such as carbon dioxide (R744), ammonia (or R717) and propane(R290) [10]. However, the carbon dioxide seems to be the best attractive refrigerant due to the high toxicity of R717 and to the high flammability of the refrigerant R290.R744 is ecofriendly with $GWP = 1$ and $ODP = 0$. Further advantages of carbon dioxide are high latent heat of evaporation, non-flammability and non-toxicity. The research on carbon dioxide refrigeration systems is quite dynamic, with researcher paying attention to the post protocol era of green cooling technologies. Nowadays, CO2 based refrigeration, system in heating, air conditioning and ventilation is quiet common in the industrialized countries [11-14]. CO2 has been used as a refrigerant in the low-temperature circuit of cascade units and in transcritical systems [15]. CO2 refrigeration units are now successively used in commercial supermarkets all around the world. However, transcritical CO2 refrigeration systems tend to be more popular in moderate climates such as Northern Europe where the refrigeration system operates a majority of the time in the more efficient subcritical region[16] .CO2– booster two-stage chiller combining transcritical cycle in cascade with a subcritical (conventional) has been recognized as one of the most promising configuration. Active research is being carried out to enhance the performance of the booster unit. In an effort to increase the efficiency of the transcritical CO2 system and to make it applicable to warmer climates, several researchers have investigated the energy performance of the transcritical refrigeration system in various regions across Europe [17-18].Tsamos et al.[19] investigated various configuration of the R744 refrigeration systems used in retail food applications in warm and moderate climates. The have compared four systems in terms of cooling capacities, power consumption and environmental effect. They found that the CO2 booster chiller with flash gas bypass has the highest efficiency with energy saving 5.0% and 3.65% for warms and moderate climate operating conditions. Extensive works have shown that the carbon dioxide booster chiller has a higher coefficient of performance (COP) than harmful working fluids based systems [20]. Many

researchers have considered the use of parallel compression with the flash gas [21-22]. Chesi et al [23] presented an experimental analysis of commercial R744 parallel compression and estimated the key factors that influence the global performance of the cycle. Sarkar [25] calculated a COP enhancement of 47.3% compared to the system with only intermediate receiver and they concluded that the refrigeration system with auxiliary compressor is mainly affected by the pressure of the receiver. Carbon dioxide Booster refrigeration systems are generally analyzed for cooling applications. As of now, no available literature discusses the implementation of R744 booster chiller for simultaneous heating and cooling application. However, this system can simultaneously produce heating and cooling energies. The difference of proposed work from other studies is that the system with and without parallel compressor is analyzed and optimized for simultaneous heating and cooling application. For this purpose, a multi-objective optimization model using response surface method and genetic algorithm is established.

## II. EXAMINED REFRIGERATION SYSTEMS

In this study, two different refrigeration units are investigated. These units are depicted in Figs 1(a-b).

The first examined unit includes two compressors with an intermediate receiver as Fig1.a exhibits. For this refrigeration system, the high pressure $P_{LL}$, the pressure of the intermediate receiver, $P_{int}$ and the ratio of cooling capacity of evaporators, $p = \frac{Q_{LT}}{Q_{MT}}$ have to be optimized in order to achieve maximum performance. The second system is shown in Fig1.b and it is a CO2 booster unit with flash gas and parallel compression. This unit has similarities with the first system but it is different. They are three compressors, one booster, one at the MT stage and one at parallel stage.
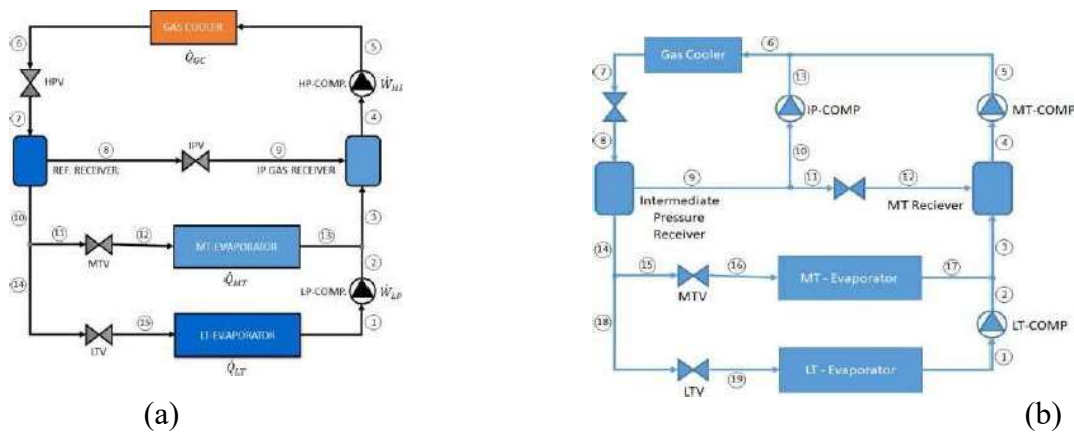


Fig.1 Schematic diagram of the CO2 booster refrigeration systems (a): With flash gas by-pass, (b): With parallel compression and flash gas by-pass.

## III. MATHEMATICAL FORMULATION

In this work, the two refrigeration systems are examined separately for different operating parameters.

The formulation of the first examined refrigeration system is given with all the proper details, while for second system only the extra equations are given. Some assumptions for thermodynamic calculations are presented as below:

- Analysis under steady state conditions.
- Isenthalpic throttling.
- Adiabatic but non-isentropic compressions.
- Isobaric evaporation and gas cooling.
- Saturated vapor at inlet of compressors LT and MT.
- Saturated vapor exiting intermediate pressure receiver.
- the kinetic and potential energies are not taken into account
- The mass flow rate of refrigerant circulating in the first cycle is 1 kg/s.

- The reference temperature and pressure are 25°C and 1 bar
- Water temperature entering gas cooler: 25°C.
- Water temperature leaving gas cooler: 75°C.
- the heat loss to the environment from the cycle component are ignored

In this section, the first and the second laws of thermodynamics are combined to derive useful equation for computing the total lost work of the refrigeration systems. A computer model has been developed first to simulate the system at steady state for different operating conditions and then to evaluate the system performance based on COP as well as exergetic efficiency, including component wise irreversibility.

Energy balance

$$0 = \sum (\dot{m}H)_{in} - \sum (\dot{m}H)_{out} + \sum (W)_{in} - \sum (W)_{out} + \sum (Q)_{in} - \sum (Q)_{out}$$

Entropy balance

$$\Delta(\dot{m}S)_{flowing\ streams} - \frac{\dot{Q}_0}{T_0} - \sum_i \frac{\dot{Q}_i}{T_i} = \Delta \dot{S}_{irr}$$

*CO2 refrigerators model equations*

Energy and exergy of each component of the CO2 booster are calculated in the following model equations:

| | | |
|---|---|---|
| Valve (HPV, BPV, MTV and LTV) equations (index i for input and o, for output) | $n_i = n_o$ <br> $\dot{I}_V = \dot{m}_i \big( (h_i - h_o) - T_0(s_i - s_o) \big) = \dot{m}_i T_0 (s_o - s_i)$ | (5) |
| MT-evaporator | $\dot{Q}_{MT} = \dot{m}_{11}(h_{13} - h_{10})$ <br> $\dot{I}_{MTEV} = \dot{m}_{11}\big( (h_{12} - T_0 s_{12}) - (h_{13} - T_0 s_{13}) \big) + \dot{Q}_{MT}\left[ 1 - \left( \frac{T_0}{T_{13}} \right) \right]$ | (6) |
| LT-evaporator | $\dot{Q}_{LT} = \dot{m}_L(h_1 - h_{10})$ <br> $\dot{Q}_{LT} = \beta \dot{Q}_{MT}$ <br> $\dot{I}_{LTEV} = \dot{m}_1\big( (h_{13} - T_0 s_{13}) - (h_1 - T_0 s_1) \big) + \dot{Q}_{LT}\left[ 1 - \left( \frac{T_0}{T_1} \right) \right]$ | (7) |
| LP-compressor | $W_{LP} = \dot{m}_L(h_2 - h_1)$ <br> $\dot{I}_{LPC} = \dot{m}_L\big( (h_1 - T_0 s_1) - (h_2 - T_0 s_2) \big) + \dot{W}_{LP}$ | (8) |
| HP-Compressor | $W_{HC} = \dot{m}_3(h_5 - h_4)$ <br> $\dot{I}_{HPC} = \dot{m}_3\big( (h_4 - T_0 s_4) - (h_5 - T_0 s_5) \big) + \dot{W}_{HP}$ | (9) |
| P-Compressor | $W_{PC} = \dot{m}_{17}(h_{18} - h_8) = \alpha\, \dot{m}_8(h_{18} - h_8)$ <br> $\dot{I}_{PC} = \dot{m}_8\big( (h_8 - T_0 s_8) - (h_{18} - T_0 s_{18}) \big) + \dot{W}_{PC}$ | (10) |
| Gas mixer 1 | $\dot{m}_{10} h_3 = \dot{m}_1 h_2 + \dot{m}_{11} h_{13}$ <br> $\dot{I}_{MIX1} = \dot{m}_{11}(h_{13} - T_0 s_{13}) + \dot{m}_1(h_2 - T_0 s_2) - \dot{m}_{10}(h_3 - T_0 s_3)$ | (11) |
| Gas mixer 2 | $\dot{m}_3 h_3 = \dot{m}_8 h_8 + \dot{m}_{10} h_3$ <br> $\dot{I}_{MIX2} = -\dot{m}_3(h_4 - T_0 s_4) + \dot{m}_8(h_8 - T_0 s_8) + \dot{m}_{10}(h_3 - T_0 s_3)$ | (12) |
| Gas mixer 3 | $\dot{m}_{19} h_{19} = \dot{m}_{17} h_{18} + \dot{m}_8 h_8$ | (13) |

$$\dot{I}_{MIX3} = \dot{m}_{17}(h_{18} - T_0 s_{18}) + \dot{m}_5(h_5 - T_0 s_5) - \dot{m}_6(h_{19} - T_0 s_{19})$$

| Gas cooler (Configuration1) | $-Q_{GC_1} = \dot{m}_5(h_5 - h_6) = \dot{m}_{w1}(h_{wo} - h_{wi})$ <br> $\dot{I}_{GC_1} = \dot{m}_5\big((h_5 - T_0 s_5) - (h_6 - T_0 s_6)\big) + \dot{m}_{w1}\big((h_{wi} - T_0 s_{wi}) - (h_{wn} - T_0 s_{wn})\big)$ | (14) |
|---|---|---|
| Gas cooler (Configuration2) | $-Q_{GC_2} = \dot{m}_6(h_{19} - h_6) = \dot{m}_{w1}(h_{wn} - h_{wi})$ <br> $\dot{I}_{GC2} = \dot{m}_6\big((h_{19} - T_0 s_{19}) - (h_6 - T_0 s_6)\big) + \dot{m}_{w2}\big((h_{wi} - T_0 s_{wi}) - (h_{wo} - T_0 s_{wo})\big)$ | (15) |

As mentioned earlier, the performance criteria used are the coefficient of performance, $COP$, defined for both units as follows:

| Config1 | $COP_1 = \dfrac{Q_{MT_1} + Q_{LT_1} - Q_{GC_1}}{W_{LP_1} + W_{HP_1}}$ | (18) |
|---|---|---|
| Configur2 | $COP_2 = \dfrac{Q_{MT} + Q_{LT} - Q_{GC_2}}{W_{LP_n} + W_{HP_n} + W_{PC}}$ | (19) |

and the exergetic efficiency, $\eta_{ex}$

| Config1 | $\eta_{ex1} - 1 \quad \dfrac{I_1}{W_{LP} + W_{HP}}$ <br> $= \dfrac{\left(\frac{T_0}{T_{LT}} - 1\right)Q_{LT} + \left(\frac{T_0}{T_{MT}} - 1\right)Q_{MT} - \left(1 - \frac{T_0}{T_{win}}\right)Q_{GC_1}}{W_{LP} + W_{HP}}$ | (20) |
|---|---|---|
| Config2 | $\eta_{ex1} - 1 \quad \dfrac{I_2}{W_{LP} + W_{HP} + W_{PC}}$ <br> $= \dfrac{\left(\frac{T_0}{T_{LT}} - 1\right)Q_{LT} + \left(\frac{T_0}{T_{MT}} - 1\right)Q_{MT} - \left(1 - \frac{T_0}{T_{win}}\right)Q_{GC_2}}{W_{LP} + W_{HP} + W_{PC}}$ | (21) |

For the first cycle, optimization of this cycle using the factors $P_{GC}$, the pressure of the intermediate receiver, $P_{int}$ and the parameter $\beta$ which is defined as the ratio of cooling capacity of evaporators, $\beta - \frac{Q_{LT}}{Q_{MT}}$.

The optimization factors for the second refrigeration system are the high pressure $P_{GC}$, the pressure of the intermediate receiver, $P_{int}$ and the split ratio of flash gas, $x - \frac{m_{11}}{m_9}$.

As can be seen from fig2, COP1 is varying between 2.878 and 4.561, while ηex1 is changing in the interval 0.311 to 0.458. For second system, COP2 is always larger than 4, fluctuating between 4.113 and 4.7. The exergetic efficiency on the other side is varying between 0.429 and 0.493. As can be noted from these 3D-surfaces, $COP_1$ and firstly rise with increasing gas cooler pressure, reach a maximum at roughly 105–110 bars and then begin to slowly decrease for larger pressures.

In analogy to Figs 3, Figs 4 illustrate in 3D–representation the effect on $COP_2$ and of their corresponding parameters, , and the bypass vapor split factor, As can be observed, increasing $P_{gc}$ affects negatively both performance criteria while enlarged values of split factor improve these performances. $COP_2$ and firstly increase with increasing refrigerant receiver pressure $P_{int}$, attain a maximum at about 50 bars and then slowly decline.

(a)


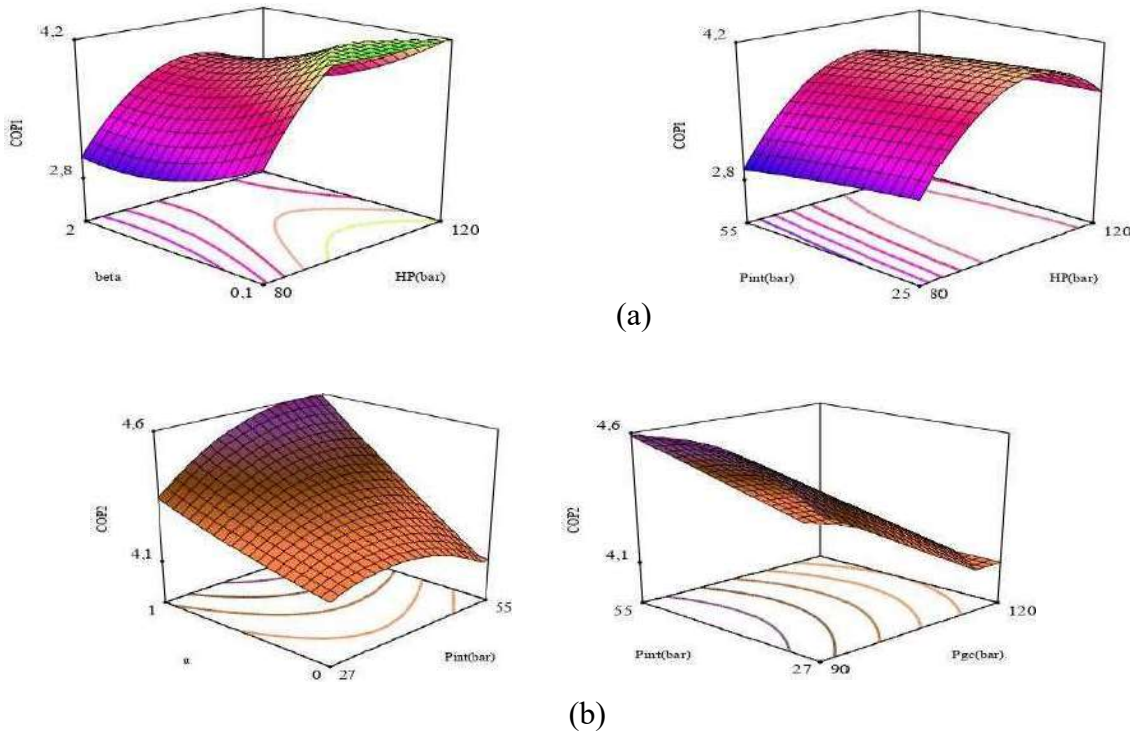
(b)

**Fig. 2** 3D plot of COP of refrigerators (a): First system; (b): Second system.
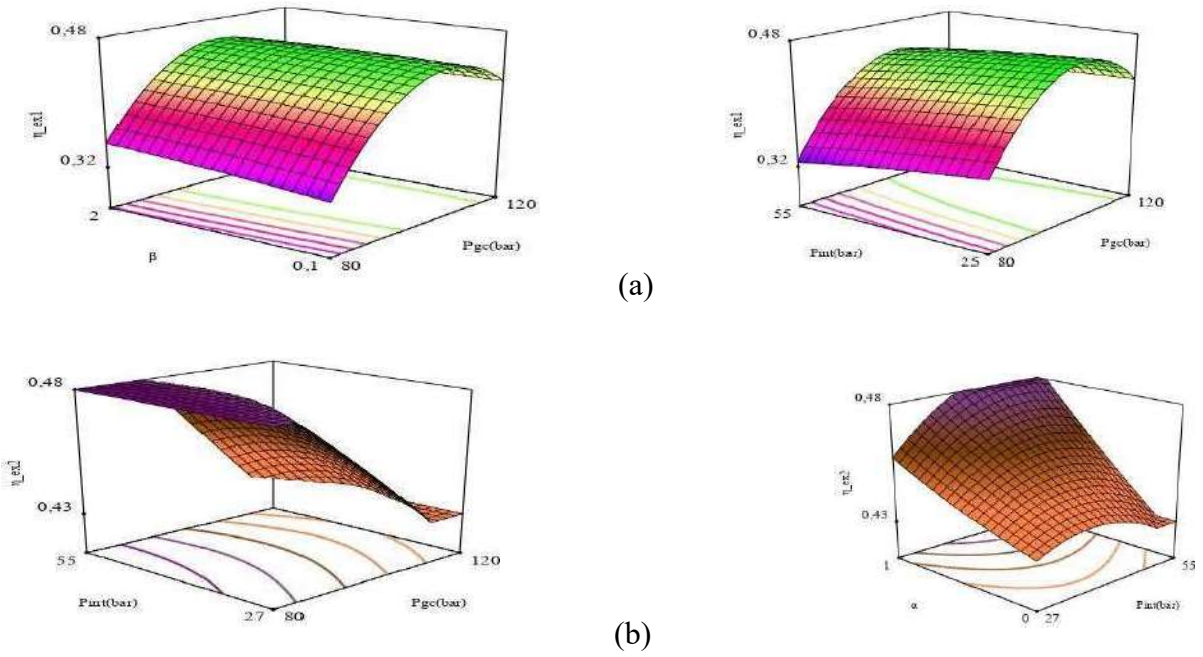


(a)



(b)

**Fig. 3** 3D plot of $\eta_{ex}$ of refrigerators (a): First system; (b):Second system.

## IV. BI-OBJECTIVE OPTIMIZATION USING GENETIC ALGORITHM

In an R744 vapor compression refrigeration system, it is desired to maximize the coefficient of performance and the thermodynamic efficiency, Consequently, the combination of these factors would lead to an improvement in performance of CO2 booster refrigeration unit and reduction in total lost work. The comparison of these objective functions at different values of input operating conditions becomes more complicated when optimize them simultaneously. Accordingly, in this work, a multi-objective optimization is carried out to achieve the optimal conditions taking into account more than one target at the same time.

| Refrigeration system | Optimization factors | Factor limits | Objective functions |
|---|---|---|---|
| With flash gas by-pass | HP,Pint,β | HP:[80 to 120] Pint:[27 to 55] β: [0 to 2] | Max COP Max $\eta_{ex}$ |
| With parallel compression and flash gas by-pass | HP,Pint,α | HP:[90 to 120] Pint:[27 to 55] α: [0 to 1] | Max COP Max $\eta_{ex}$ |

In the optimization simulations, the COP1 and $\eta_{ex}$ simultaneously are used as the objective functions .The goal of this part is to find a good set of factors that will meet all the objective functions.

The three parameters in the genetic method that are responsible for determine the optimum solutions are:
- The number of individuals in a population= 35
- The number of generations to explore=62
- The maximum mutation rate=0.26

For the carbon dioxide booster cycles considered in this work, the combined objective function can be obtained using the Weight approach. For this purpose, we need to assign weights to each response. The bi-objective function (MOF) is calculated by summing the all responses with some relative weights, as follows:

$$\text{Maximum } (MOF = w_1 \times COP_2 + w_2 \times \eta_{EX2})$$

$0 \le w_1, w_2 \le 1$
$w_1 + w_2 = 1$
w1 and w2 are the weighting coefficients for the COP1, $\eta_{EX1}$, COP2, $\eta_{EX1}$ and Qgc, respectively.

TABLE I: OPTIMAL PARAMETER SETTINGS (SINGLE OBJECTIVE OPTIMIZATION)

| | Coefficient of performance, $COP$ | | | | Exergy efficiency, $\eta_{ex}$ | | | |
|---|---|---|---|---|---|---|---|---|
| | $P_5$ (bar) | $P_7$ (bar) | $\beta / \alpha$ (-) | Max. $COP$ | $P_5$ (bar) | $P_7$ (bar) | $\beta / \alpha$ (-) | Max. $\eta_{ex}$ |
| Configuration 1 | 106.65 | 27 | 0.01 | 4.58 | 103.381 | 27 | 2 | 0.466 |
| Configuration 2 | 90,20 | 52,3 | 1 | 4.902 | 90,45 | 51,12 | 1 | 0.517 |

The maximum coefficient of performance for the booster system with bypass gas is achieved at the lowest value of the parameter $\beta$ and the lower range value of the pressure of the refrigerant receiver $P_7$. This maximum of is located at an intermediate value of the gas cooler pressure, $P_5 = 106.65$ bar.

For booster system with bypass gas and parallel compression, the coordinates of the maxima of $COP$ (4.90) and $\eta_{ex}$ (0.517) are very close: lowest feasible gas cooler pressure, largest value of split ratio ($\alpha = 1$) and an intermediate value of the refrigerant receiver pressure ($P_7 = \ldots$ bar and 51.12 bar).

The incorporation of a parallel compressor into a transcritical CO2-booster with bypass gas enhances its performances, the coefficient of performance is 6.5% higher and the exergy efficiency is more than 11% larger.

The MOF are now used to find out the optimal parameter setting maximizing the performance criteria of both systems. Fig represents the results of bi-objective optimization for the CO2 booster cycle with parallel compression for some values of weighing coefficients.

Fig 4 indicates a comparison between the single and multi-objective optimization for the CO2 booster cycle with parallel compression for some values of weighing coefficients.
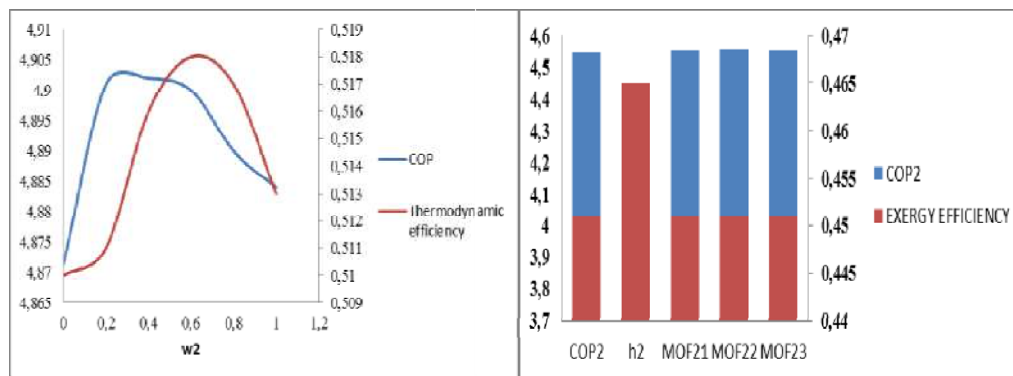


**Fig. 4** A comparison between single and multi-objective optimization using weight approach for two refrigerators.

In the first case of multi-objective function (MOF23), the two objective COP2 and $\eta_{ex}$ are assumed to be of the same weights (the same importance). However, in MOF22 case COP2 is preferred to exergetic efficiency $\eta_{ex}$ while in MOF23 case this trend is reversed. The results reveal that MOF23 case seems to be the best choice among those studies.

## V. CONCLUSIONS

In this study, the comparative thermodynamic performance evaluation of the refrigeration systems is performed. They two systems produce cooling energies at two levels of temperature and heating using energy available in the working fluid simultaneously. In this context, the effect of some operating factors on the coefficient of performance and the exergetic efficiency are investigated. The main results that have been achieved in this work can be summarized as follows:

- Both energy and exergy analysis reveals that R744 Booster with parallel compression and flash gas bypass improve the performance in comparison with that of CO2–booster two-stage chiller combining transcritical cycle in cascade with a subcritical and flash gas by-pass.
- Under same operating conditions, the optimized design of Booster unit with parallel compression achieves the lowest exergy destruction rate, representing a significant reduction of 31% in comparaison with the optimizes design of system zith only flash gas by-pass.

REFERENCES

[1] Eyerer S, Dawo F, Kaindl J, Wieland C, Spliethoff H. Experimental investigation of modern ORC working fluids R1224yd(Z) and R1233zd(E) as replacements forR245fa. Appl Energy 2019;240:946–63.

[2] Ge YT, Tassou SA. Thermodynamic analysis of transcritical $CO_2$booster refrigeration systems in supermarket. Energy Convers Manage 2011;52:1868–75.

[3] Nawaz K, Ally MR. Options for low-global-warming-potential and natural refrigerants Part 2: performance of refrigerants and systemic irreversibilities. Int JRefrig 2019;106:213–24.

[4] Saad Dilshal, Ali RazaKalair,Nasrullah Khan. Review of carbon dioxide ($CO_2$) based heating and cooling technologies: Past, present, and future outlook.Int J Energy Res.2020;44 1408-1463. https://doi.org//10.1016/er.5024.

[5] Yu B, Yang J, Wang D, Shi J, Chen J. An updated review of recent advances on modified technologies in transcritical$CO_2$refrigeration cycle. Energy. 2019;189:116147https://doi.org/10.1016/j.energy.2019.116147.

[6] Pearson A. Carbon dioxide—new uses for an old refrigerant.Int J Refrig. 2005;28(8):1140-1148. https://doi.org/10.1016/j.ijrefrig.2005.09.005.

[7] European Commission. Regulation (EU) No 517/2014 of the European Parliament and of the Council of 16th April 2014 on fluorinated greenhouse gases and repealing Regulation (EC) No 842/2006, 2014.

[8] UNFCCC. Doha Amendment to the Kyoto Protocol. Doha,Qatar: UNFCCC; 2012.

[9] Dubey AMK, Suresh, Agrawal Das Ghanshyam. Thermodynamic analysis of a transcritical $CO_2$/propylene (R744–R1270) cascade system for cooling and heating applications. Energy Convers Manage 2014;86:774–83.

[10] Saad Dilshad, Ali Raza Kalair, Nasrullah Khan (2019) :*Review of carbon dioxide (CO2) based heating and cooling technologies: Past, present, and future outlook*.International Journal of Energy Research

[11] Annual energetic evaluation of multi-stage dedicated mechanical subcooling carbon dioxide supermarket refrigeration system in different climate regions of China using genetic algorithm
Yilmaz Fatih, Ozturk Murat, Selbas Resat,(2019) *Comparative thermodynamic performance assessment of two-stage cycle for various refrigerants* International Journal of Exergy

[12] S.M. Hojjat Mohammadi, –*Theoretical investigation on performance improvement of a low-temperature trans-critical carbon dioxide compression refrigeration system by means of an absorption chiller after-cooler‖*. Appl. Therm. Eng. 138, pp. 264–279, 2018.

[13] R. Llopis, L. Nebot-Andrés, D. Sánchez, J. Catalán-Gil, R. Cabello, –*Subcooling methods for CO2 refrigeration cycles: a review”*. Int. J. Refrig‖. 93, pp. 85–107, 2018.

[14] R. Llopis, L. Nebot-Andrés, R. Cabello, D. Sánchez, J. Catalán-Gil,‖ *Experimental evaluation of a CO 2 transcritical refrigeration plant with dedicated mechanical subcooling‖*. Int. J. Refrig. 69, pp. 361–368, 2016.

[15] K.M. Tsamos, Y.T Ge, I. Santosa, S.A. Tassou, G. Bianchi, Z. Mylona, –*Energy analysis of alternative CO 2 refrigeration system configurations for retail food applications in moderate and warm climates‖*. Energy Convers. Manag. 150, pp. 822–829, 2017.

[16] Tsamos,K.M, Ge,Y.T, Santosa,IDewa, Tassou,S.A,Bianchi,G,Mylona,Z:*Energy analysis of alternative CO 2 refrigeration system configurations for retail food applications in moderate and warm climates*,Energy Conversion and Management 822-829.

[17] Liu,Shengchun, Lu,Fenping,Dai,Baomin,Nian,Victor,Li,Hailong,Li,Jiayu,Li,Hailong *Performance analysis oft wo stage compression transcritical CO2 refrigeration system with R290 mechanical subcooling unit*, Energy.

[28] Esposito,Fabio,Chesi,Andrea,Ferrara,Giovanni,Ferari,Giovanni *Experimental analysis of R744 parallel compression cycle Applied* Energy.

[19] SARKAR, J. (2012). *TRANSCRITICAL CO2 REFRIGERATION SYSTEMS: COMPARISON WITH CONVENTIONAL SOLUTIONS AND APPLICATIONS*. International Journal of Air-Conditioning and Refrigeration, 20(04), 1250017. doi:10.1142/s2010132512500174.

[20] Gullo, P., Hafner, A., & Banasiak, K. (2018). *Transcritical R744 refrigeration systems for supermarket applications: Current status and future perspectives*. International Journal of Refrigeration, 93, 26310. doi:10.1016/j.ijrefrig.2018.07.001 10.1016/j.ijrefrig.2018.07.001.

[21] Wang, S., Tuo, H., Cao, F. and Xing, Z. (2013) ‗*Experimental investigation on air-source transcritical CO2 heat pump water heater system at a fixed water inlet temperature*‗, International journal of refrigeration, Vol.36 No.3, pp 701-706, DOI: 10.1016/j.ijrefrig.2012.10.011.

[22] Yu, B., Yang, J., Wang, D., Shi, J. and Chen, J. (2019) ‗*An updated review of recent advances on modified technologies in transcritical CO2 refrigeration cycle*', Energy, Vol. 189,10.1016/j.energy.2019.116147.

[23] D'Agaro, P., Cortella, G. and Polzot, A. (2018) ‗*R744 Booster integrated system for full heating supply to supermarkets*', International Journal of Refrigeration, Vol. 96, pp 191-200.DOI: 10.1016/j.ijrefrig.2018.09.028.

[24] Dai, B., Cao, Y ., Liu, S., Ji, Y., Sun, Z., Xu, T., Zhang, P and Nian, V. (2022) ‗*Annual energetic evaluation of multi-stage dedicated mechanical subcooling carbon dioxide supermarket refrigeration system in different climate regions of China using genetic algorithm*‗, Journal of Cleaner Production, Vol.333, 130119, DOI: 10.1016/j.jclepro.2021.130119.

# Numerical Calibration of Single Junction Perovskite Solar Cells: Performance Modeling and Optimization

A. Khaoura[#1], H. Zeboudj[#2], S. M. Mekhrouf[#3] W. Nasri[#4], B. Hadri[#5]

[#1]*Laboratoire ERSE,Département de Génie Electrique, Université Abdelhamid Ibn Badis Mostaganem,
Route de Belhacel 27000, Faculté des Sciences et de la Technologie, MOSTAGANEM,*

[#1]`amirakharoua@gmail.com`
[#2]`zeboudj47@gmail.com`
[#3]`makrelouf2020@gmail.com`
[#4]`n.wissem@yahoo.com`
[#5]`hadriba@yahoo.fr`

*Abstract* - **The work described in the paper highlights: the potential of single junction Perovskite solar cells due to their novel crystalline structure and advantages in efficiency and cost reduction. We undertook numerical calibration of a specific cell ($CS_{0.05}(MA_{0.10}FA_{0.90})_{0.95}Pb(I_{0.90}Br_{0.10})_3$) to match simulated performance with experimental measurements. Details were specified including the electron transport layer (ETL), active Perovskite layer, and hole transport layer (HTL) characteristics. Initial simulations showed significant discrepancies between the simulated and experimentally measured metrics, including short-circuit current density (Jsc), open-circuit voltage (Voc), fill factor (FF) and power conversion efficiency (η or Eff). However, through an iterative adjustment process of tuning parameters such as layer thicknesses, defect densities, and interface properties, we achieved satisfactory agreement between simulation and experiment, providing a calibrated model (Jsc=24.18 mA/cm2, Voc=1105.67 mV, FF=74.34% and Eff=19.88%). We have studied the impact of several factors such as layer thickness and doping concentration in the multilayer solar cell on cell parameters such as (FF), ($V_{OC}$), ($J_{SC}$), and (η or Eff). The optimization and the simulation results revealed that the single junction perovskite solar had the highest power conversion efficiency of 23.78%**

*Keywords*— **Solar cell- Perovskite- Halides- Modeling- Simulation Tcad Silvaco.**

## I. INTRODUCTION

Improving the performance and reducing the costs of current solar cell technology are dynamic areas of research in sustainable energy. This research is actively focused on enhancing the performance and lowering the costs of existing solar cells. The key to achieving these goals is to optimize the design of solar cells so that the light-absorbing material generates charge carriers with large diffusion lengths and small effective masses. Such charge carriers exhibit high mobility, which is favorable for increasing the performance of solar cells. Since the first realization of Perovskite solar cells (PSCs) showing an efficiency (Eff) of around 3.8% in 2009 , the performance of these devices has been boosted to reach a certified Eff of around 25.2% in just a few years [1], [2], [3], [4]. Most PSCs use a lead halide Perovskite with an organic-inorganic hybrid network, which has recently shown exceptional performance thanks to modifications in device configurations and the addition of different interfacial layers.

In this study, we are interested in a single junction solar cell using a Perovskite with the formula $CS_{0.05}(MA_{0.10}FA_{0.90})_{0.95}Pb(I_{0.90}Br_{0.10})_3$ as the absorber material. This is a hybrid Perovskite based on cesium, formamidinium (FA) and methylammonium (MA), with lead as the metal cation.

The incorporation of cesium and the partial substitution of MA by FA helps improve the thermal and structural stability of the Perovskite [5]. The addition of bromine mixed with iodine increases the band gap, enhancing the open-circuit voltage.

This Perovskite composition thus offers an excellent compromise between optical absorption, charge carrier mobility, durability and stability [6].

Some authors have studied the $CS_{0.05}(MA_{0.10}FA_{0.90})_{0.95}Pb(I_{0.90}Br_{0.10})_3$ perovskite solar cell. We can cite the work of Saliba et al. (2016) published in Science, where they studied the effect of incorporating rubidium cations (Rb+)

into this perovskite composition. They fabricated solar cells with a TiO2/perovskite/spiro-OMeTAD structure, varying the Rb+ concentration from 0% to 5% molar. Structural analyses show that inserting the large Rb+ cations into the perovskite crystal lattice helps reduce defects and improve crystalline quality. This results in a significant increase in photovoltaic performance. The conversion efficiency reaches 21.1% with 5% Rb+, compared to 18.4% without rubidium [7].

The authors attribute this improvement to better charge carrier mobility thanks to the reduction in defects, which is notably manifested by an increase in short-circuit current.

The work of Lee and al. (2020) published in Joule, studied the influence of the bromide ratio in this perovskite composition. They fabricated a series of colloidal nanocrystals with formula Cs0.05(MA0.15FA0.85)0.95Pb(I1-xBrx)3 with x varying from 0 to 0.15.

Structural analysis shows that increasing incorporation of Br- causes a band gap increase from 1.6 eV (x=0) to 2.3 eV (x=0.15), while maintaining the perovskite structure. These nanocrystals were integrated as the top cell in a stacked perovskite tandem solar cell. Adjusting the band gap by the Br- ratio in the top layer helped optimize sunlight absorption [8].

A record tandem efficiency of 18.1% was measured using composition x=0.10 (Eg = 2.15 eV) for the top cell The work of Yi et al. (2016) published in Energy & Environmental Science studied the effect of mixing methylammonium (MA) and formamidinium (FA) cations in this composition. They prepared a series of absorbers with formula $(MA)_{1-x}(FA)_x PbI_3$ and analyzed the structural evolution as a function of x. The results highlight that mixing the small MA+ cations with the larger FA+ cations causes distortion of the perovskite lattice which increases disorder (entropy). This entropic effect helps stabilize the black perovskite phase at room temperature over a wide range of compositions. Incorporating FA also improves the electronic properties and durability of the perovskite. Solar cells made with composition x=0.9 showed an efficiency of 18.9%, confirming the benefit of the entropic stabilization approach by cation mixing [9].

In this study, we are interested in numerically calibrating the single junction $CS_{0.05}(MA_{0.10}FA_{0.90})_{0.95}Pb(I_{0.90}Br_{0.10})_3$ perovskite solar cell, with the goal of obtaining simulation performance matching experimental measurements, performing numerical simulations using Tcad Atlas software with these initial parameters, thus generating current-voltage (J-V) curves and other electrical characteristics of the perovskite solar cell [10], and adjusting key parameters such as electronic state densities (Nc, Nv), dielectric permittivities, and electron and hole mobilities, progressively minimizing the gap between the simulated and experimental data. Once the calibrated parameters are validated, we leverage the adjusted model to simulate the performance of the perovskite solar cell under various layer thickness and doping concentration in the multilayer solar cell

## II. STRUCTURE OF THE PEROVSKITE SOLAR CELL

We precisely defined the structure of the solar cell, including the composition of layers such as the SnO2 ETL layer [11], which possesses specific parameters such as the bandgap (Eg) of 3.72 eV, an acceptor concentration (Na) of 1e19 cm-3, and a thickness (d) of 40 nm.

The active perovskite layer, Cs(Mafa)Pb(Ibr), is also thoroughly detailed [12], featuring a bandgap (Eg) of 1.6 eV, an acceptor concentration (Na) of 1e15 cm-3, and a thickness (d) of 500 nm. The Spiro-OMeTAd HTL layer is characterized by a bandgap (Eg) of 2.72 eV [13], a donor concentration (Nd) of 1e19 cm-3, and a thickness (d) of 220 nm.
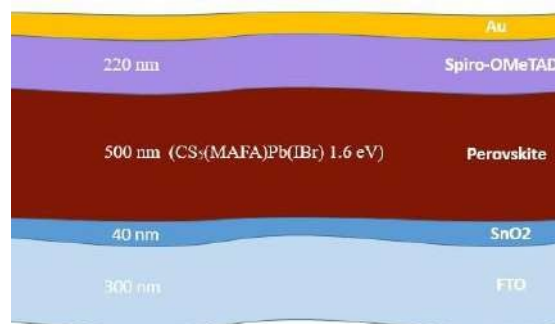


Fig. 1  Schematic of the standard Perovskite solar cell.

Fig. 1 shows a visual representation of a Perovskite solar cell (PSC), with a cross-sectional diagram illustrating the typical p-i–n structure..
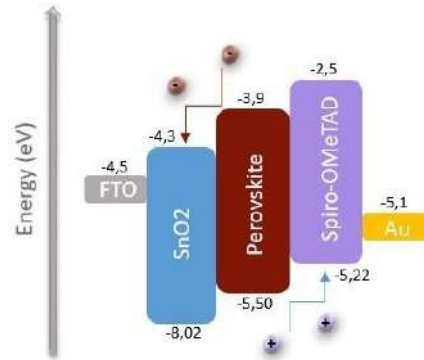


Fig. 1  The energy band diagram of the standard Perovskite solar cell

Fig. 2 explains the flow of carriers across the different layers of a typical PSC (Perovskite solar cell) by drawing a schematic diagram of the energy levels.

### III. RESULTATSOF CALIBRATION AND DISCUSSION
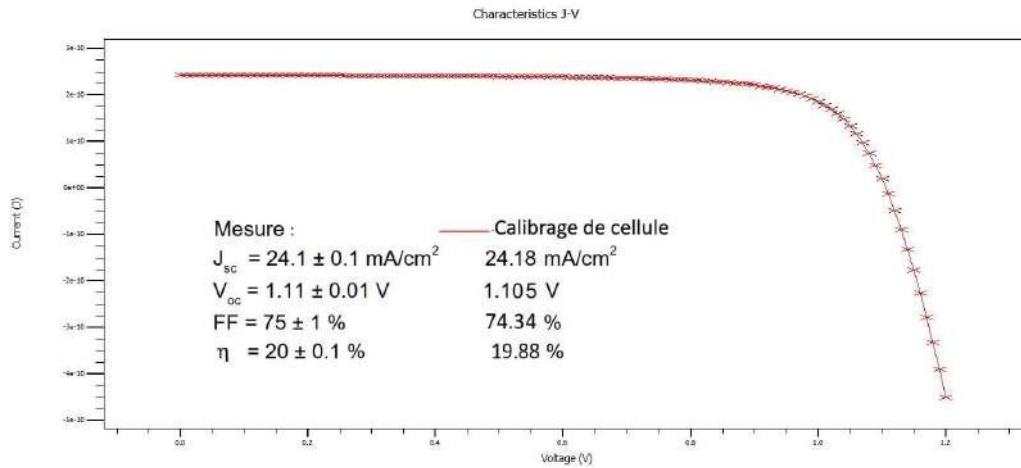


Fig. 3 Simulation and experimental J–V curves of standard Perovskite solar cell

The J-V curves were acquired using the AM 1.5G standard solar spectrum. The current density–voltage (J–V) curves of calibrated perovskite solar cells are shown in Fig. 3 under standard illumination. When compared to measured individual cell properties [14], the Jsc, Voc, FF, and Eff match well. These proved to be accurate in simulating and optimizing perovskite cells using numerical models. Consequently, trust in further exploring the tandem cells.

Seckin Akin created a single junction-based Perovskite solar cell model ($CS_{0.05}(MA_{0.10}FA_{0.90})_{0.95}Pb(I_{0.90}Br_{0.10})_3$, 1.6 eV) with an initial efficiency of 20% (Jsc = 24.1 mA.cm$^{-2}$, Voc = 1.11 V, FF = 75 %) [15].

Until the two sets of data satisfactorily matched, we tweaked the important parameters. Jsc=24.1825 mA/cm2, Voc=1105.67 mV, FF=74.3384%, and Eff=19.8765% are among the values that were acquired. We used the modified model to estimate how the Perovskite solar cell would function in different layer thickness and doping concentration scenarios. This made it possible for us to forecast the Perovskite cell's performance with accuracy and opened the door to investigating optimization options to raise the cell's efficiency in converting solar energy.

### IV.                                        SOLAR CELL OPTIMIZATION

In the optimization phase we will study:

A. The Effect of Thickness on the Performance of Single-Junction Perovskite Solar Cells. We attempted to vary the Thickness of the three layers ETL HTM and Perovskite, to achieve maximum efficiency, as shown in Figures 4, 5 and 6.
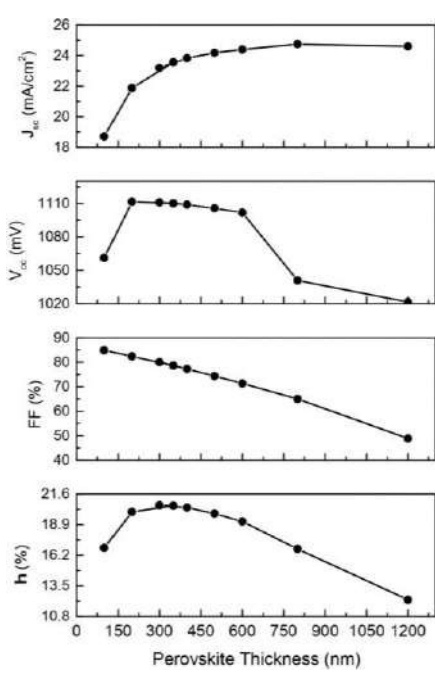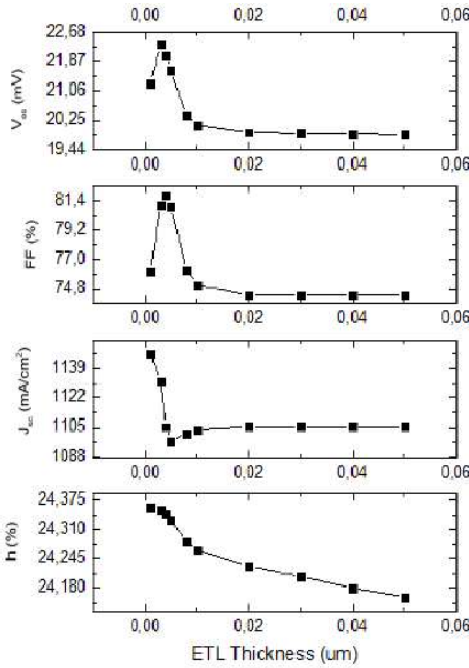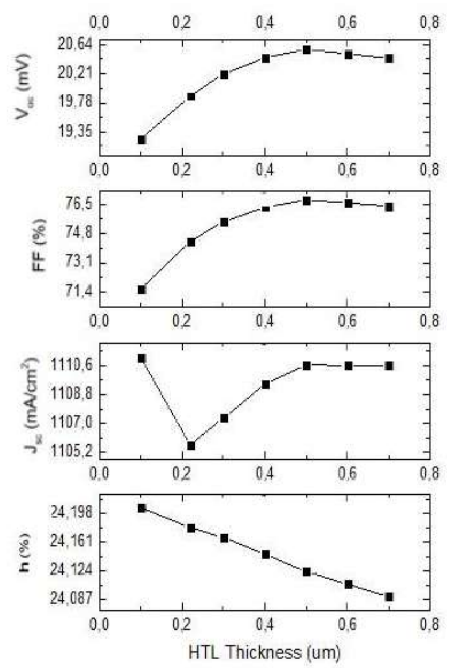
| Fig 4 | Fig 5 | Fig 6 |

Fig 4, 5 and 6: Effects of Perovskite, ETL and HTL layer thickness variation on solar cell performance, (Jsc) short circuit current density, (Voc) Open-circuit voltage, (FF) Fill factor, (h) efficiency.

The effect of Perovskite thickness on the performance parameters is shown in Fig. 4 As observed from the various performance graphs, the highest efficiency value is obtained for a thickness of 0.3 nm. As observed from Figure 4 a) and c) , both the efficiency Jsc , Voc exhibit a similar trend.

As the thickness of the Perovskite layer ranges from 0.6nm to 1.2nm, there is a rapid decline in Voc values. Simultaneously, the form factor decreases with the thickness ranging from 0.1nm to 1.2nm. Additionally, the short-circuit current density (Jsc) is impacted by the thickness increase, showing a non-linear growth.

Concerning the electron transport layer (ETL), the power conversion efficiency (PCE or Eff) presents a peak value of 22.3408% at an optimal thickness of 0.003 nm. Equivalently, the fill factor (FF), open circuit voltage (Voc), and short circuit current density (Jsc) concurrently demonstrate maximal values at a thickness of 0.003 nm. Over the thickness range spanning 0.4 nm to 0.1 nm, the Eff, FF, Jsc, and Voc exhibit only marginal variation with respect to ETL thickness.

Regarding the hole transport layer (HTL), the power conversion efficiency (PCE) reaches a peak value of 19.3153% at an optimized thickness of 0.37 nm. The open circuit voltage (Voc) displays a sharp decline as a function of increasing thickness. Meanwhile, the short circuit current density (Jsc) exhibits a linear decrease over the thickness range spanning 0.2 nm to 0.68 nm

B. The impact of changing doping concentration of Single-Junction Perovskite Solar Cells. We attempted to vary the doping concentration of the three layers ETL HTM and Perovskite, to achieve maximum efficiency, as shown in Figures 7, 8 and 9.



| a) | b) | c) | d) |
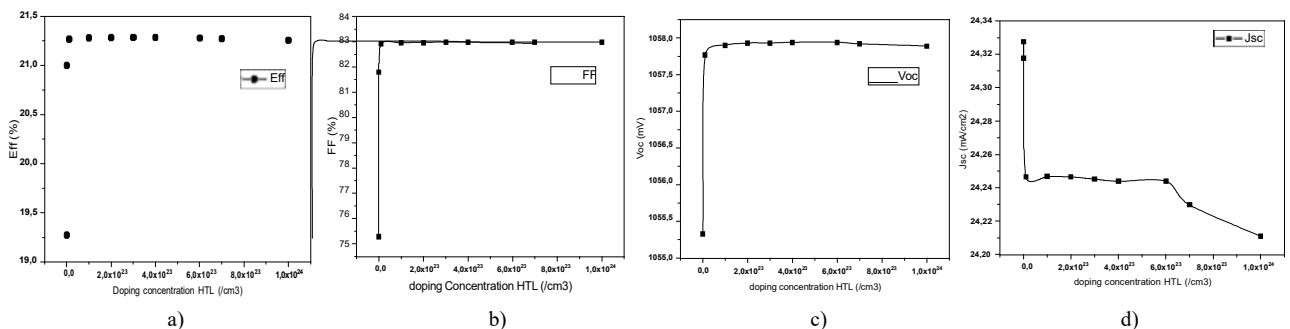
Fig 7: The HTL layer doping concentration variation effect on a) Efficiency b) Fill Factor c) Voc d) Short circuit current density



a)    b)    c)    d)
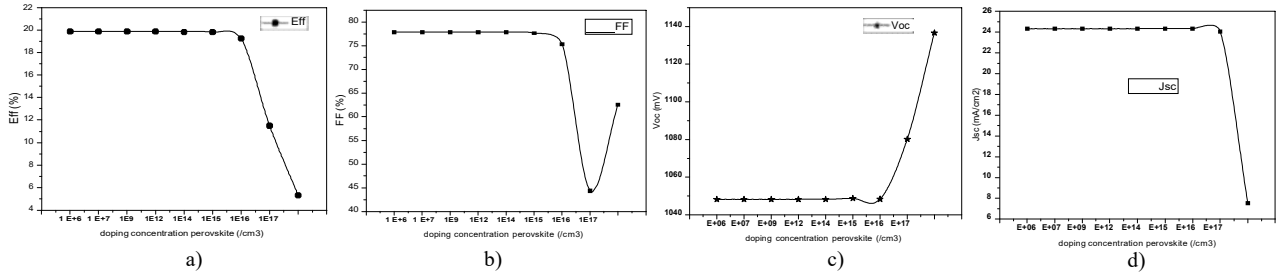
Fig 8: Perovskite layer doping concentration variation effect on a) efficiency b) Fill Factor c) Voc d) short circuit current density



a)    b)    c)    d)
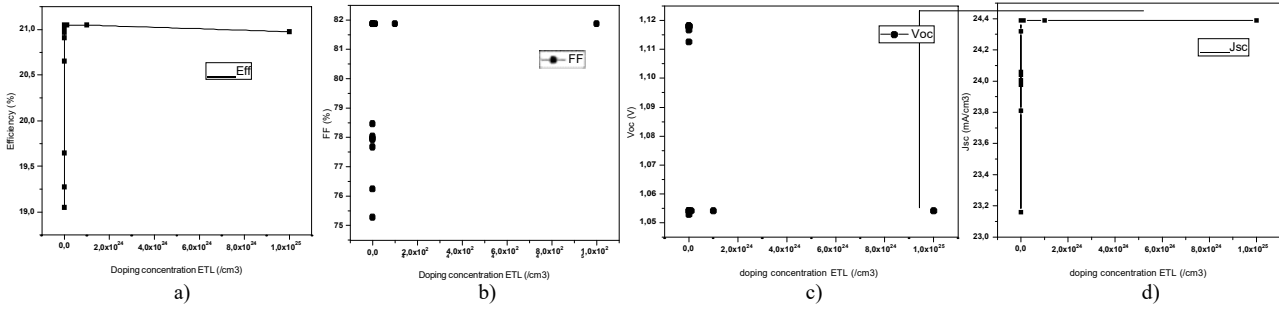
Fig 9: ETL layer doping concentration variation effect on a) efficiency b) Fill Factor c) Voc d) short circuit current density

For the electron transport layer (ETL), maximum energy conversion efficiency peaks at 21.0482% given an optimal doping density of $\sim 10^{21}$ cm$^{-3}$. Similar trends are observed for the short-circuit current density ($J_{sc}$) and fill factor (FF) as a function of doping concentration. But open circuit voltage ($V_{oc}$) proves insensitive across doping densities, maintaining a value of $\approx 1.12$V over $10^{20}$-$7 \cdot 10^{20}$ cm$^{-3}$, before settling around 1.05V for higher doping in the $10^{22}$-$10^{25}$ cm$^{-3}$ range.
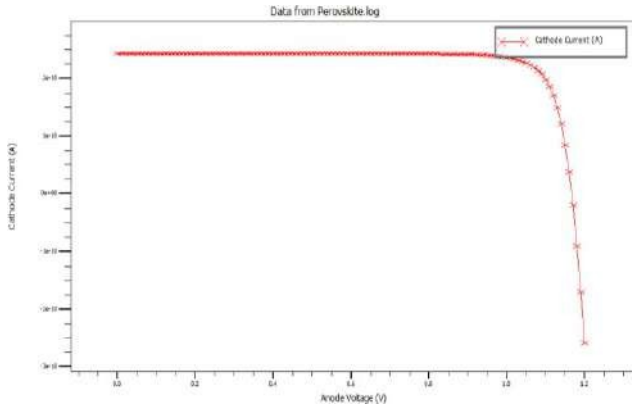


Fig. 10: I-V characteristic of the optimized structure
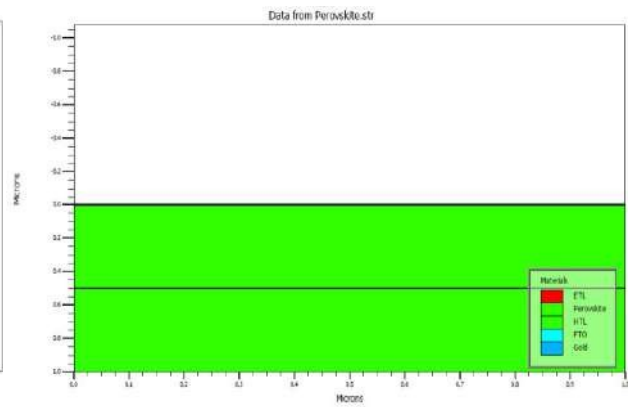


Fig. 11: Structure of the photovoltaic solar cell

Figures 10 and 11 represent the I-V characteristic of the optimized structure and the structure of the photovoltaic solar cell. The optimized results are Voc=1.17V, FF=83.87%, Jsc=24.31 mA/cm2, FF=83.87%, Eff=23.78%, Furthermore, the quantum efficiency (QE) is reported at a notable 0.92, further emphasizing the enhanced performance achieved through optimization. These results collectively underscore the success of the design improvements in achieving superior photovoltaic performance.

## V. CONCLUSIONS

In this work, we first calibrated the structure of the $Cs_{0.05}(MA_{0.10}FA_{0.90})_{0.95}Pb(I_{0.90}Br_{0.10})_3$ perovskite solar cell by tuning various physical parameters. Our modeling achieved electrical outputs comparable to experimental measurements. With this baseline established, we proceeded to optimize the cell by systematically varying the thickness and doping density of each layer, specifically the electron transport layer (ETL), perovskite absorber, and hole transport layer (HTL). Optimization yielded appreciable performance gains relative to the base configuration. The champion cell reached a short circuit current density (Jsc) of 24.31 mA/cm$^2$, an open circuit voltage (Voc) of 1.17 V, a fill factor (FF) of 83.87 %, and a maximum power conversion efficiency (PCE or η) of 23.78 %. Moving forward, we will assess whether these substantial simulated boosts in efficiency can be experimentally realized through careful manipulation of layer thicknesses and doping levels. If fabricable, such tuned architectures could meaningfully advance the deployability and competitiveness of perovskite photovoltaics. We will also model more complex cell stacks and interfaces to further close the gap between simulated and achievable efficiencies.

## REFERENCES

[1] M. Grätzel, M. K. Nazeeruddin, P. Gao, R. Humphry-Baker, S. J. Moon, N. Pellet, J. Burschka, Sequential deposition as a route to high-performance perovskite-sensitized solar cells. Nature, 499(7458), 316-319, (2013).

[2] The NREL Best Research-Cell Efficiencies website. Available: https://www.nrel.gov/pv/assets/pdfs/

[3] M. Saliba et al. "How to make over 20% efficient perovskite solar cells in regular (n–i–p) and inverted (p–i–n) architectures." Chem. Mater. 30, 4193–4201 (2018).

[4] C. Huang, P. Lin, N. Fu, C. Liu, B. Xu, K. Sun, D. Wang, X. Zeng. "Facile Fabrication of Highly Efficient ETL-free Perovskite Solar Cells with 20% Efficiency by Defect Passivation and Interface Engineering." Chem. Commun. 55, 2777−2780 (2019).

[5] B. Yang, M. Wang, M. Hu, X. Zhou, Z. Zang. "Highly Efficient Semitransparent CsPbIBr2 Perovskite Solar Cells via low-Temperature Processed In2S3 as Electron-Transport-Layer." Nano Energy. 57, 718−727 (2019).

[6] N.-G. Park & K. Zhu. "Scalable fabrication and coating methods for perovskite solar cells and solar modules." Nat. Rev. Mater. 5, 333–350 (2020).

[7] M. Saliba, T. Matsui, K. Domanski, J.-Y. Seo, A. Ummadisingu, S. M. Zakeeruddin, J.-P. Correa-Baena, W. R. Tress, A. Abate, A. Hagfeldt, M. Grätzel. "Incorporation of rubidium cations into perovskite solar cells improves photovoltaic performance." Science, 354, 206–209 (2016).

[8] W. Yensheng, G. Yi, B. Deski, S. Dottermush, C. Haining, J. Zhong, B.S. Richrads. "Experimental Determination of Complex Optical Constants of Air-Stable Inorganic CsPbI3 Perovskite Thin Films." Physica Status Solidi, 14, Wiley Online Library (2020).

[9] Y. Chenyi, L. Jingshan, M. Simone, B. Ariadni, A. Negar, G. Carole, M. Z. Shaik, R. Ursula, G. Michael. "Entropic stabilization of mixed A-cation ABX3 metal halide perovskites for high-performance perovskite solar cells." Energy Environ. Sci, 9, 656-662 (2016).

[10] J.-F. Guillemoles, T. Kirchartz, D. Cahen, U. Rau. "Guide for the perplexed to the Shockley–Queisser model for solar cells." Nat. Photonics. 13, 501–505 (2019).

[11] Y. Zhao, H. Zhang, X. G. Ren, H. L. Zhu, Z. Huang, F. Ye, D. Ouyang, K. W. Cheah, A. K. Y. Jen, W. C. Choy. "Thick TiO2-Based Top Electron Transport Layer on Perovskite for Highly Efficient and Stable Solar Cells." ACS Energy Lett. 3, 2891−2898. (2018).

[12] H. Zhou, Q. Chen, G. Li, S. Luo, T. B. Song, H. S. Duan, Z. Hong, J. You, Y. Liu, Y. Yang. "Interface Engineering of Highly Efficient Perovskite Solar Cells." Science, 345, 541−545. (2014).

[13] Y. Xu, Q. Niu, L. Zhang, C. Yuan, Y. Ma, W. Hua, W. Zeng, Y. Min, J. Huang, R. Xia. "Highly Efficient Perovskite Solar Cell Based on PVK Hole Transport Layer." Polymers (Basel). 31, 14-49. (2022).

[14] Y. Wang, X. Liu, Z. Zhou, P. Ru, H. Chen, X. Yang, L. Han. "Reliable Measurement of Perovskite Solar Cells." Adv Mater. 31-47, (2019).

[15] S. Akin. "Hysteresis-Free Planar Perovskite Solar Cells with a Breakthrough Efficiency of 22% and Superior Operational Stability over 2000 h." ACS Applied Materials & Interfaces. 11(45), 39998-40005 (2019).

# Influence of Temperature and Composition on Thermophysical Properties of Binary Mixtures of 2-Amino-2-methyl-1-propanol with Solvents

**Amal Ayad [1*], Aouicha Belabbaci [1], Amina Negadi [1], Ariel Hernández [2], Bakusele Kabane [3], Indra Bahadur [4], Latifa Negadi [1,5]**

[1] LATA2M, Laboratoire de Thermodynamique Appliquée et Modélisation Moléculaire, University of Tlemcen, Post Office Box 119, Tlemcen 13000, Algeria

[2] Departamento de Ingeniería Industrial, Facultad de Ingeniería, Universidad Católica de la Santísima Concepción, Alonso de Ribera 2850, Concepción, Chile

[3] Department of Physical Chemistry laboratories, Faculty of Applied Sciences, Durban University of Technology, Durban-4001, South Africa

[4] Department of Chemistry and Materials Science Innovation & Modelling Research Focus Area, School of Physical and Chemical Sciences, Faculty of Natural and Agricultural Sciences, North-West University (Mafikeng Campus), Private Bag X2046, Mmabatho 2735, South Africa

[5] Thermodynamics Research Unit, School of Engineering, University of KwaZulu-Natal, Howard College Campus, King George V Avenue, 4041 Durban, South Africa

* amel.ayad@univ-tlemcen.dz

## ABSTRACT

The densities, $\rho$, speeds of sound, $u$, and refractive indices, $n_D$, have been measured for the binary mixtures of 2-Amino-2-methyl-1-propanol (AMP) with acetonitrile, toluene, 1-hexanol and 1-pentanol over the whole composition range at three temperatures (T = 303.15, 313.15 and 323.15 K) and at atmospheric pressure. Experimental data have been used to calculate the isentropic compressibility, $\kappa_S$, excess molar volumes, $V_m^E$, deviation in isentropic compressibilities, $\Delta \kappa_S$, and deviation in refractive indices, $\Delta n_D$, for all systems and correlated as function of temperature using Redlich-Kister polynomial equation. The excess properties of binary mixtures were found to be positive, negative or exhibit S-shape curves as a function of the composition. The results were interpreted in terms of molecular interactions and molecular structures occurring in the binary mixtures.

**Keywords:** density; speed of sound; refractive index; AMP; excess properties; Redlich-Kister equation.

## 1. Introduction

Carbon dioxide ($CO_2$) is one of the primary greenhouse gases produced by human activities that contributes to climate change. Carbon dioxide has been captured using a number of separation procedures, including membrane separation, adsorption, and absorption. The use of non-aqueous solutions of alkanolamines results in increases in the rate of absorption of $CO_2$.[1-3]

The literature has revealed that acetonitrile can form stable complexes with the carbon dioxide.[4] Acid gases are eliminated from gas mixtures or liquid hydrocarbons using alkanolamines. Understanding the molecular interactions between the components of the mixtures requires knowledge of the thermodynamics and acoustics of binary mixtures comprising alkanolamines with various types of solvents, including acetonitrile, alkanol, and hydrocarbons.

In this work, the experimental data of density, speed of sound and refractive index for binary mixture are presented at different temperatures. Excess properties such as excess molar volumes, $V^E$, deviation in isentropic compressibilities, $\Delta ks$, and deviation in refractive indices, $\Delta n_D$ were calculated from the experimental values and fitted using Redlich-Kister equation.[5]

## 2. Methods

Density and speeds of sound measurements for the pure liquids 2-Amino-2-methyl-1-propanol (AMP), acetonitrile, toluene, pentanol, and 1-hexanol and their binary mixtures were measured by using an Anton Paar (DSA 5000 M) digital vibrating tube densimeter and a sound velocity analyser operated at different temperature between the range of T = (303.15 to 323.15) K and at 0.1 MPa.

A digital refractometer (Anton Paar Abbemat 300) was utilized to conduct the refractive index measurements involving pure solvents and their corresponding binary mixtures at 303.15 K to 323.15 K with an uncertainty of 0.0004 in refractive index.

## 3. Results

The plots of $V^E$ and $\Delta ks$ versus $x_{AMP}$ have been presented in Figs. 1 and 2, respectively. For the binary mixtures of AMP (1) + 1-pentanol (2), the excess molar volumes are negative over the entire composition range of the mole fraction of AMP and for all the investigated temperatures, but an S-shaped variations of $V^E$ was observed for the (AMP + 1-hexanol) binary system.

The deviation in isentropic compressibilities in AMP + acetonitrile are negative and decrease with increasing temperature. The negative values arise from a decrease in free-space, and this impact contributes toward the negative values of the isentropic and deviation.
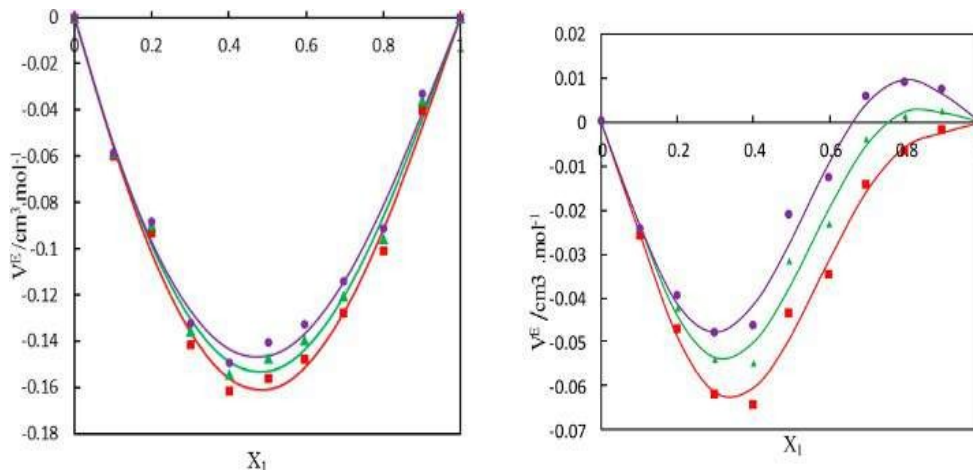
**Fig. 1.** Excess molar volume for the binary mixtures: (a) {AMP (1) + 1-pentanol (2)}, (d) {AMP (1) + 1-hexanol (2)} as function of the composition expressed in the mole fraction of AMP at 303.15 K (red ■), 313.15 K (green▲), and 323.15 K (purple ●). Solid lines: Redlich−Kister correlation.
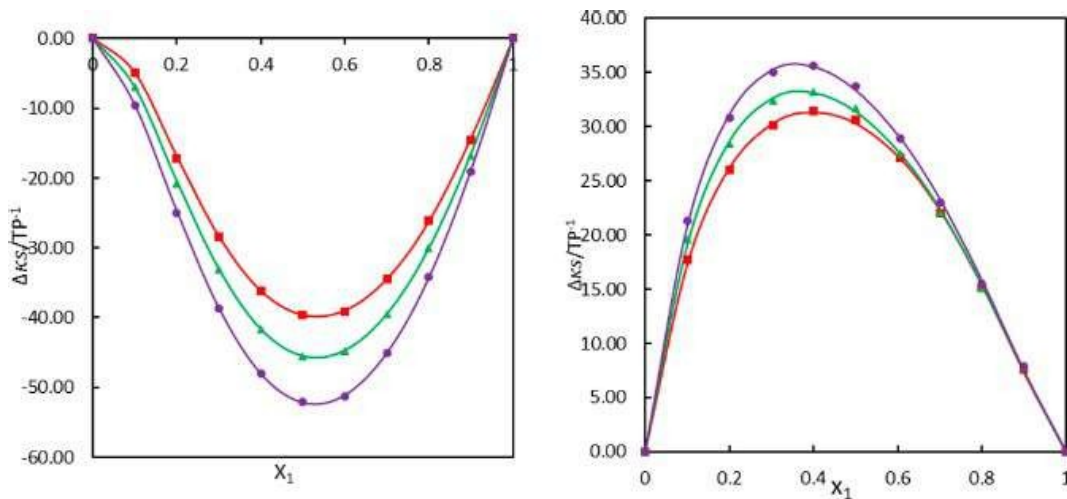


**Fig. 2.** Deviation in isentropic compressibility for the binary mixtures: (a) {AMP (1) + acetonitrile (2)}, (b) {AMP (1) + toluene (2)}, as function of the composition expressed in the mole fraction of AMP at 303.15 K (red ■), 313.15 K (green▲), and 323.15 K (purple ●). Solid lines: Redlich−Kister correlation.

## 4. Conclusions

At atmospheric pressure and temperatures ranging from 303.15 K to 323.15 K with 10 K variations throughout the whole composition range, the experimental properties of density ($\rho$), speed of sound (u) and refractive index ($n_D$) were obtained. The excess and deviation properties of $V^E$, $\Delta ks$, $\Delta n_D$ were calculated and fitted to the Redlich-Kister equation.

The excess properties of the prepared binary mixtures were found to be positive, negative, or S-shape curves as a function of the composition of $x_{AMP}$. The results have been interpreted in terms of molecular interactions and molecular structures occurring between the binary systems. At higher temperatures, more intermolecular interactions were seen, indicating that there is good packing in the AMP's voids and that all of the compounds' interaction sites are easily available.

## References

[1] Bhagat, et al., S. Volumetric and optical properties of binary mixtures of 2-amino-2-methylpropan-1-ol with alkanol (C1-C3) at T = (298.15−318.15) K. J. Mol. Liq. 2021, 323, 114640.

[2] Zhanget al., Thermodynamics of aqueous amines: excess molar heat capacities,

volumes, and expansibilities of {water+ methyldiethanolamine (MDEA)} and {water + 2-amino-2-methyl-1-propanol (AMP). J.

Chem. Thermodyn. 2002, 34, 679−710.

[3]  Balchandaniet al., Bandyopadhyay, S. Thermally induced characterization and modeling

of physicochemical, acoustic, rheological, and thermodynamic properties of novel blends of (HEF + AEP) and (HEF + AMP) for $CO_2/H_2S$ absorption. Environ. Sci. Pollut. Res. 2019, 26, 32209−32223.

[4] Williams, H. L.; Rice, B. M.; Chabalowski, C. F. Investigation of the CH3CN−CO2 Potential Energy Surface Using

Symmetry Adapted Perturbation Theory. J. Phys. Chem. A. 1998, 102, 6981−6992.]

[5] Redlich, O.; Kister, A. T. Algebraic Representation of Thermodynamic Properties and the Classification of Solutions. Ind. Eng. Chem. 1948, 40, 345−348.

# Fuzzy Logic Direct Torque Control of SEIG Driven by a Variable-Speed Wind Turbine

Kahina BERABEZ[1], Kassa IDJDARENE[1], Farid HAMOUDI[2], Abdelmounaim TOUNZI[3], Ismail HACINI[1]

[1]*Laboratoire de Technologie Industrielle et de l'Information, Faculté de Technologie, Université de Bejaia, Algeria.*
[2]*Laboratoire de Maîtrise des Energies Renouvelables, Faculté de Technologie, Université de Bejaia, Algeria.*
[3] *Univ. Lille, Arts et Metiers Institute of Technology, Centrale Lille, Junia, ULR 2697 - L2EP, F-59000 Lille, France.*

```
Email 1 - kahina.berabez@univ-bejaia.dz
Email 2 - kassa.idjdarene@univ-bejaia.dz
Email 3 - farid.hamoudi@univ-bejaia.dz
Email 4 - abdelmounaim.tounzi@univ-lille.fr
Email 5 - ismail.hacini@univ-bejaia.dz
```

*Abstract*— **This study deals with direct torque control based on fuzzy logic strategy. The purpose is to control the terminal voltage of a Self-excitation induction generator (SEIG) that supplies autonomous load and is driven by a variable speed wind turbine. The main objective of this control strategy is to ensure constant DC bus voltage, regardless of the variations the load and wind speed. Besides, to minimization of the torque and flux ripples is taken as another focus in paper. The present study includes the saturation effect of the magnetic material and the dynamic model, which is carried out in (α-β) frames by the Concordia transform. The proposed system, is validated through simulation tests under MATLAB/Simulink.**

*Keywords*— **Self-Excitation, Saturation, Autonomous, DTC Control, Fuzzy Logic.**

## I. INTRODUCTION

The evolution of wind energy and the use of SEIGs for remote area electrical generation are indeed notable developments [1]. The cost-effectiveness and robustness of SEIGs make them a promising choice for providing electricity in areas that are not connected to the main grid. While SEIGs offer several advantages, they are not without challenges [1][2]; in fact, wind speed and load variations have a negative impact on the output voltage and frequency, and the need for power electronics, with an appropriate control technique, to convert the variable output into stable electricity can be issued to address this challenge. For this purpose, several control techniques have been proposed in the literature, and numerous of them use direct or indirect field-oriented control (FOC) methods [2][3]. Nonetheless, these methods are susceptible to the impact of both internal parameter variations and external disturbances. To address these limitations, Direct Torque Control (DTC) has arisen as an alternative approach to FOC and has received notable attention and recognition in recent years [4][5]. DTC is characterized by its robustness and high dynamic performance. It doesn't require a PWM (Pulse Width Modulation) modulation block or an inner current control loop like classical FOC methods, which simplifies the control system and improves dynamic performance [2][5]. However, it's important to note that DTC is afflicted by challenges, such as high torque and flux ripples due to hysteresis comparators, resulting in mechanical vibrations and undesirable acoustic noise, compromising the overall performance of the electrical machine [5][6][7].

To address these drawbacks, researchers proposed several solutions; in [8] a Space Vector Modulation (DTC_SVM) control is proposed, where the traditional switching table has been replaced by an SVM algorithm, and hysteresis comparators have been substituted with PI controllers. Furthermore, there have been innovations such as Predictive DTC (P_DTC) control [9]. Fuzzy logic regulators have been employed as alternative to hysteresis regulators in numerous contributions [5][6][10]. Additionally, in [10][11] the authors proposed the use of 12 sectors instead of six to mitigate flux fluctuations. Moreover, certain authors have suggested reducing ripple by incorporating multilevel inverters into the system [7].

Our study focuses on the implementation of the Fuzzy DTC control technique, which is based on fuzzy logic, aimed to enhance conventional DTC. The fundamental concept behind this approach involves the substitution of

the Takahashi switching table and hysteresis controllers with a fuzzy logic inference system, in order to generate an optimized voltage vector, thereby maintaining a constant DC bus voltage. Furthermore, it helps steer the flux and torque towards their respective reference values. The simulation results clearly demonstrate that the proposed approach yields substantial improvements. A comparison between the two controllers reveals a significant reduction in torque and flux ripple, as well as a decrease in the total harmonic distortion (THD) of the stator current. This rest of the paper is structured as follows: the modelling of the SEIG is briefly summarized in Section (2). The stator flux and torque estimation with the strategy principle fuzzy FDTC are developed in section (3). The simulation results and discussions are presented in section (4). Section (5) comes to a conclusion of the paper.

## II. PROPOSED SYSTEM DESCRIPTION AND MODELING

The system investigated in this article encompasses the following key components: a wind turbine, a three-phase squirrel cage asynchronous generator, a converter (rectifier/inverter), an autonomous load, along with a DC-side capacitor and a battery employed for generator excitation. figure 1 illustrates a schematic overview of the global studied system.
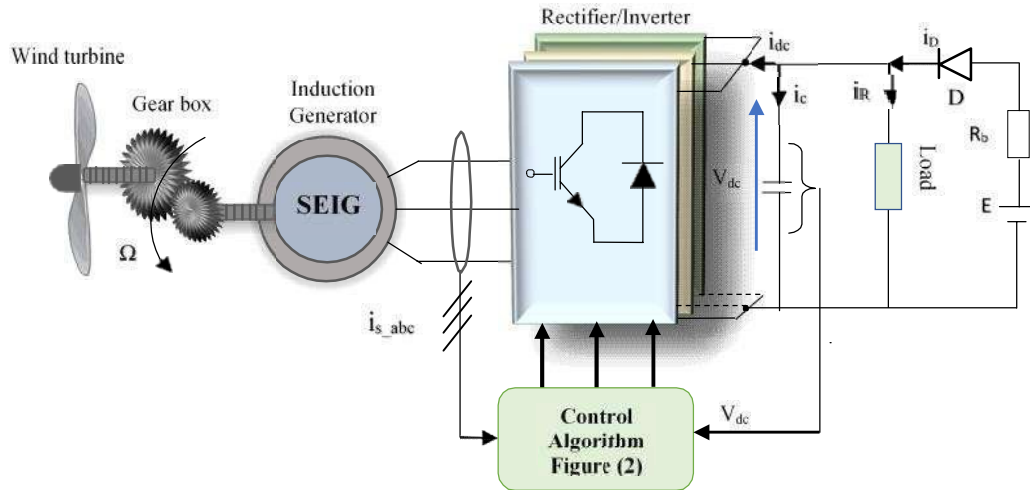


Fig. 1 The studied system

### A. Induction machine model

The SEIG dynamic model in the two phase (α-β) references is given by equation (1). It is worth mentioning that the phenomenon saturation is taking into account via a magnetization inductance $L_m$ [2].

$$
\begin{bmatrix} V_{s\alpha} \\ V_{s\beta} \\ 0 \\ 0 \end{bmatrix} = \begin{bmatrix} R_s & 0 & 0 & 0 \\ 0 & R_s & 0 & 0 \\ 0 & \omega_r.l_r & R_r & \omega_r.(l_r+L_m) \\ \omega_r.l_r & R_r & \omega_r.(l_r+L_m) & R_r \end{bmatrix} \begin{bmatrix} i_{s\alpha} \\ i_{s\beta} \\ i_{m\alpha} \\ i_{m\beta} \end{bmatrix} + \begin{bmatrix} l_s & 0 & L_m+L_m'.\frac{i_{m\alpha}^2}{|i_m|} & L_m'.\frac{i_{m\alpha}.i_{m\beta}}{|i_m|} \\ 0 & l_s & L_m'.\frac{i_{m\alpha}.i_{m\beta}}{|i_m|} & L_m+L_m'.\frac{i_{m\beta}^2}{|i_m|} \\ l_r & 0 & l_r+L_m+L_m'.\frac{i_{m\alpha}^2}{|i_m|} & L_m'.\frac{i_{m\alpha}.i_{m\beta}}{|i_m|} \\ 0 & l_r & L_m'.\frac{i_{m\alpha}.i_{m\beta}}{|i_m|} & l_r+L_m+L_m'.\frac{i_{m\beta}^2}{|i_m|} \end{bmatrix} \begin{bmatrix} \frac{di_{s\alpha}}{dt} \\ \frac{di_{s\alpha}}{dt} \\ \frac{di_{m\alpha}}{dt} \\ \frac{di_{m\beta}}{dt} \end{bmatrix} \quad (1)
$$

Where: $R_s$, $R_r$, are the stator and rotor phase resistances, $l_s$ and $l_r$ are the self-inductances. $v_{s\alpha}$, $v_{s\beta}$, $i_{s\alpha}$ and $i_{s\beta}$: are the (α-β) axis components of the stator voltages and currents respectively. $i_{m\alpha}$ and $i_{m\beta}$ are the magnetizing currents, along the α and β axis, given by:

$$i_{m\alpha} = i_{s\alpha} + i_{r\alpha}$$
$$i_{m\beta} = i_{s\beta} + i_{r\beta}$$

$\quad$ (2)

$i_{r\alpha}$ and $i_{r\beta}$: represent the α-β rotor currents.

The magnetizing current $i_m$ is defined as:

$$i_m = \sqrt{i_{m\alpha}^2 + i_{m\beta}^2}$$

$\quad$ (3)

$\omega_r$: is the rotor angular speed.
With: $\omega_r = p\Omega$

$\quad$ The saturation effect is taken into account by the expression of the magnetizing inductance $L_m$ with respects to $i_m$ with using a polynomial approximation, of degree 12 [2]. The $L_m$ with respects to $i_m$, is given by the following equation:

$$L_m = f\left(|i_m|\right) = \sum_{j=0}^{n} a_j \cdot |i_m|^j$$
$$L_m' = \frac{dL_m}{d|i_m|} = \frac{d}{d|i_m|}\left(f\left(|i_m|\right)\right) = \sum_{j=0}^{n} j \cdot a_j \cdot |i_m|^{j-1}$$

$\quad$ (4)

$\quad$ The different parameters of the studied squirrel induction machine are given in appendix

### III. CONTROL STRATEGY'S PRINCIPLE (CDTC)

Direct Torque Control (DTC) is a control strategy that focuses on the direct regulation of a machine's torque. Unlike classical vector control, it doesn't require a PWM modulation block or an inner current control loop. Instead, it selects optimal inverter voltage vector based on a switching table [2][5][11]. The controlled variables are the stator flux and the electromagnetic torque, regulated using a two and three-level hysteresis controllers and is then used as input, along with a flux angle, for a switching table I. The evolution of the flux is partitioned into six sectors (1...6), each spanning 60 degrees.

TABLE I
THE SWITCHING TABLE OF CDTC [3]

| Δφ | ΔTem | Sectors Si | | | | | |
|---|---|---|---|---|---|---|---|
| | | S1 | S2 | S3 | S4 | S5 | S6 |
| 1 | 1 | V₂ | V₃ | V₄ | V₅ | V₆ | V₁ |
| | 0 | V₇ | V₀ | V₇ | V₀ | V₇ | V₀ |
| | -1 | V₆ | V₁ | V₂ | V₃ | V₄ | V₅ |
| 0 | 1 | V₃ | V₄ | V₅ | V₆ | V₁ | V₂ |
| | 0 | V₀ | V₇ | V₀ | V₇ | V₀ | V₇ |
| | -1 | V₅ | V₆ | V₁ | V₂ | V₄ | V₅ |

The primary objective is to maintain these two instantaneous values within a specified range around their desired set points. The estimation of the stator-flux vector relies one component of voltage and current in the α and β axes of the SEIG [2][3]. The stator currents in the stationary reference frame (α, β) are given as follows:

$$i_{s\alpha} = \sqrt{\frac{3}{2}} i_{sa}$$
$$i_{s\beta} = \sqrt{\frac{1}{2}}(i_{sb} - i_{sc})$$

$\quad$ (5)

The α and β components of the stator voltage are computed using Eq (6), taking into account the DC voltage and the inverter switching states [3].

$$\begin{cases} V_{s\alpha} = \sqrt{\frac{3}{2}}V_{dc}\left(S_a - \frac{1}{2}(S_b + S_c)\right) \\ V_{s\beta} = \sqrt{\frac{1}{2}}V_{dc}(S_b - S_c)2 \end{cases} \tag{6}$$

The magnitude of the stator flux is given by:

$$\Phi_s = \sqrt{\Phi^2_{s\alpha} + \Phi^2_{s\beta}} \tag{7}$$

Where, where the stator flux $(\Phi_{s\alpha}, \Phi_{s\beta})$ is estimated according to Eq (8) [3].

$$\begin{cases} \Phi_{s\alpha} = \int_0^t (V_{s\alpha} - R_s i_{s\alpha})dt \\ \Phi_{s\beta} = \int_0^t (V_{s\beta} - R_s i_{s\beta})dt \end{cases} \tag{8}$$

The equation of the electromagnetic torque is given from the stator flux $(\Phi_{s\alpha}, \Phi_{s\beta})$ components and the stator current $(i_{s\alpha}, i_{s\beta})$ as [3]:

$$T_{em} = p(\Phi_{s\alpha} i_{s\beta} - \Phi_{s\beta} i_{s\alpha}) \tag{9}$$

The stator-flux space is segmented into six sectors, and its angle ($\theta s$) is determined using Eq (10) [11]:

$$\theta_s = \tan^{-1}\left(\frac{\Phi_{s\beta}}{\Phi_{s\alpha}}\right) \tag{10}$$

## IV. FUZZY DTC

The FDTC system operates on the same fundamental principles as the conventional DTC [11], while a fuzzy logic inference system is introduced as a replacement for hysteresis controllers and switching tables [5][10]. This adaptation aims to enhance the system's performance, by leveraging the flexibility and adaptability offered by fuzzy logic, in lieu of the rigid structures of hysteresis controllers and switching table [10][11]. The combination of fuzzy logic and the conception DTC grant a reduction in ripples in electromagnetic torque and stator flux and to enhance studied system performance. In this novel approach, the fuzzy controller takes the electromagnetic torque error, stator flux error, and the angle of sector identification as inputs, while producing the switching vectors ($V_0$, $V_1$..., $V_6$) as outputs [5][11]. The functional diagram depicting the application of this fuzzy controller, referred to as FDTC, is outlined in figure 2.
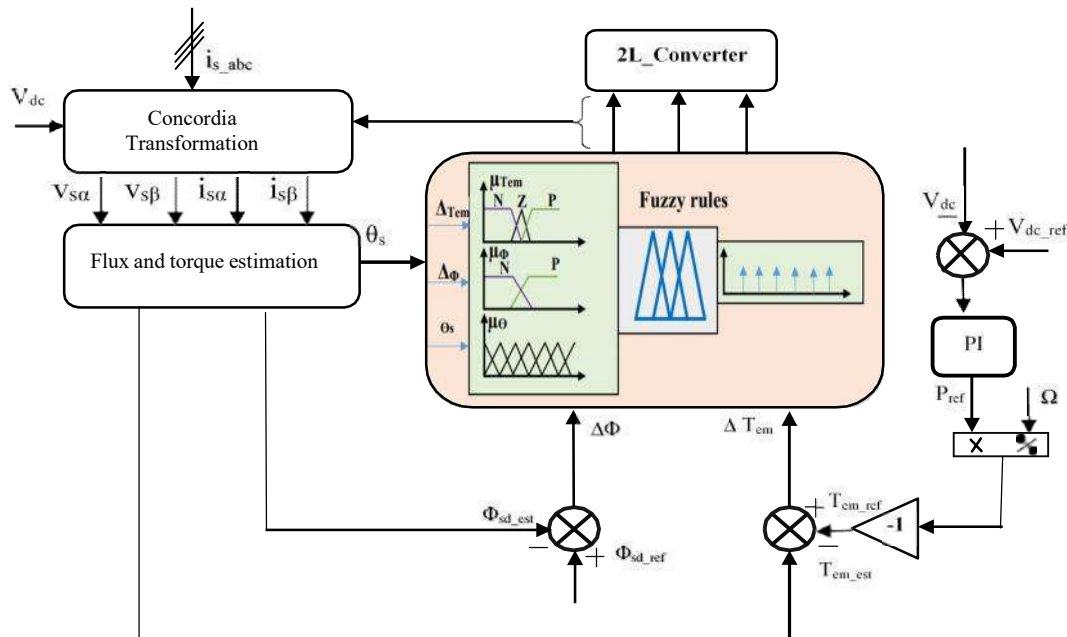


Fig. 2 Synoptic schema of the FL_DTC Algorithm applied to SEIG

The torque error fuzzy input comprises three linguistic variables (P: Positive, Z: Zero, and N: Negative), while the flux error fuzzy input consists of two linguistic variables (P: Positive and N: Negative). The third input, stator flux position $\theta_s$, is divided into six sectors, each represented by a distinct fuzzy set ($S_1$-$S_6$) [11]. These sectors are determined using Eq (13) [5].

$$(2n - 3) \frac{\pi}{6} \le S(n) \cdot (2n - 1) \frac{\pi}{6} \qquad (11)$$

Figure 2 illustrates the set of voltage vectors delivered by the two-level inverter
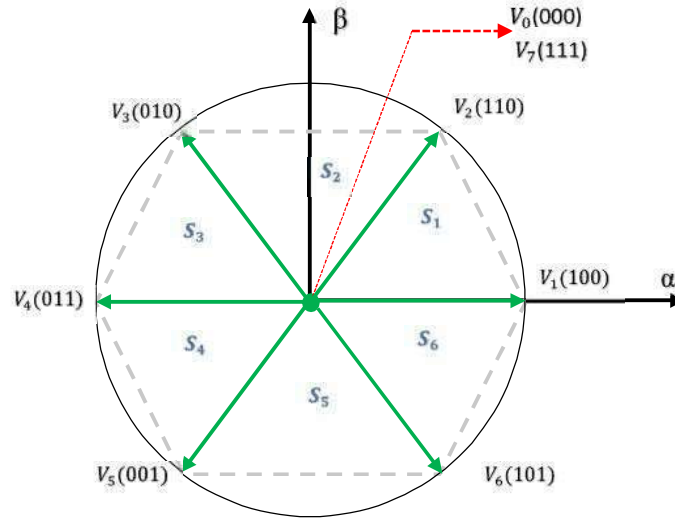


Fig. 3 Voltage vectors delivered by the two-level inverter

The fuzzy switching table is characterized by 36 fuzzy rules, as illustrated in Table II.

TABLE III
FUZZY DTC SWITCHING TABLE [5]

| Δφ | ΔTem | Sectors Si | | | | | |
|----|------|-----|-----|-----|-----|-----|-----|
| | | S1 | S2 | S3 | S4 | S5 | S6 |
| p | P | $V_2$ | $V_3$ | $V_4$ | $V_5$ | $V_6$ | $V_1$ |
| | Z | $V_7$ | $V_0$ | $V_7$ | $V_0$ | $V_7$ | $V_0$ |
| | N | $V_6$ | $V_1$ | $V_2$ | $V_3$ | $V_4$ | $V_5$ |
| Z | P | $V_3$ | $V_4$ | $V_5$ | $V_6$ | $V_1$ | $V_2$ |
| | Z | $V_0$ | $V_7$ | $V_0$ | $V_7$ | $V_0$ | $V_7$ |
| | N | $V_5$ | $V_6$ | $V_1$ | $V_2$ | $V_4$ | $V_5$ |

## V. SIMILATION RESULTS AND DISCUSSION.

In this work, the flux reference is set to 0.7Wb, while the DC voltage reference is set at 465V. During startup, the (SEIG) is driven at a synchronous speed, and then a variation is applied in the speed profile as shown in figure 4. The load represented by its resistance R, initially set to 80 Ω is increased 90 Ω at t= 2 sec, before it returns to its initial value at t= 4 sec. According to figure 5, one can observe that the DC bus voltage closely follows its reference value with a slight overshoots at 2 and 4 sec, due to abrupt load change.

Figure 6 illustrates the electromagnetic torque ($T_{em}$) evolution, showcasing that the estimated torque closely follows its reference for both control techniques (CDTC and FDTC). In Figure 7, a zoom of the $T_{em}$ reveals noticeable reductions in ripples when employing the FDTC control technique.

Figure 8 depicts the response of stator flux magnitude, illustrating its precise reference tracking for both strategies. Furthermore, Figure 9 highlights a substantial ripple diminution with the proposed (FDTC) strategy. Figure 10 shows the circular stator flux trajectory for both strategies, where it can be clearly seen that the proposed (FDTC) has a smoother circular path in comparison with the (CDTC).

Regarding the stator current depicted in Figure 11, it is observable that its component shows a sinusoidal waveform. The stator currents demonstrate a lack of harmonic components, as indicated by the spectrum illustrated

in Figure 12, characterized by a significant THD reduction in the stator current, when using (FDTC), compared to classical control (CDTC).



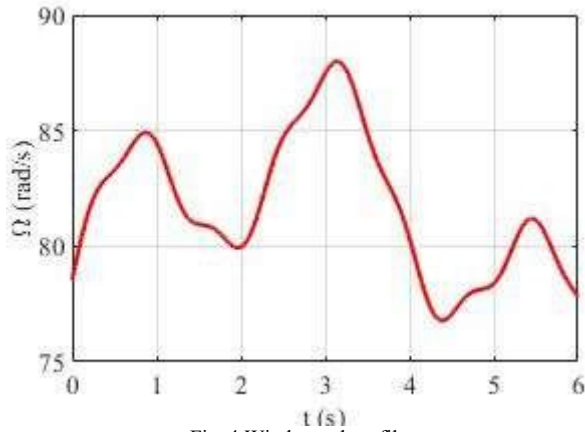Fig. 4 Wind speed profile
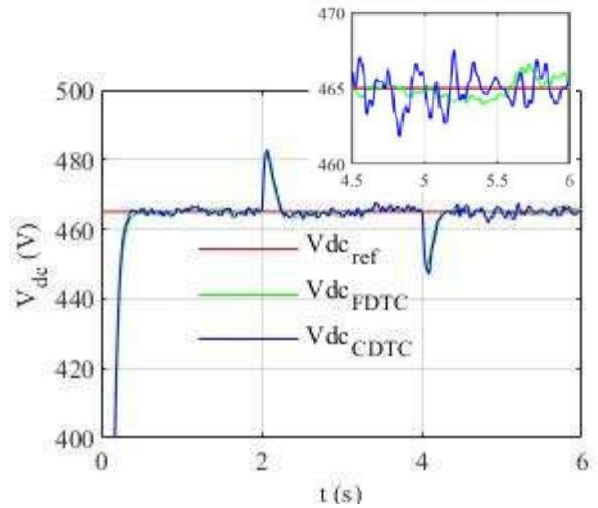


Fig. 5 $V_{dc}$ voltage with its zoom
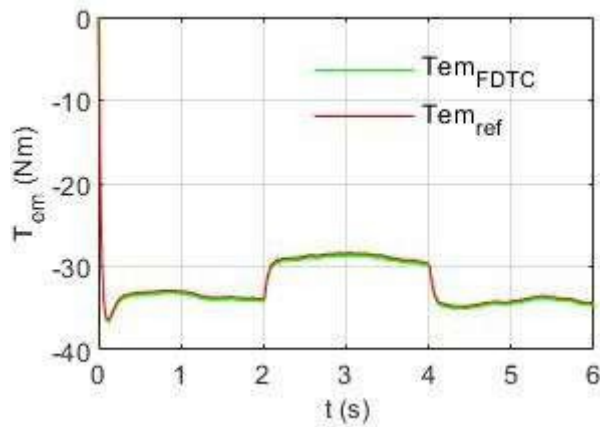


(a) FDTC
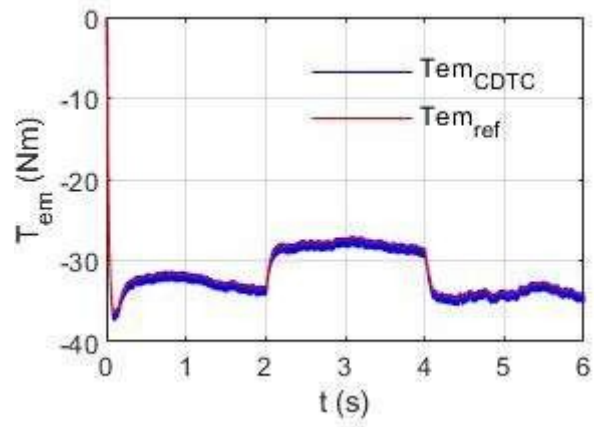
(b) CDTC

Fig. 6 Electromagnetic torque evolution
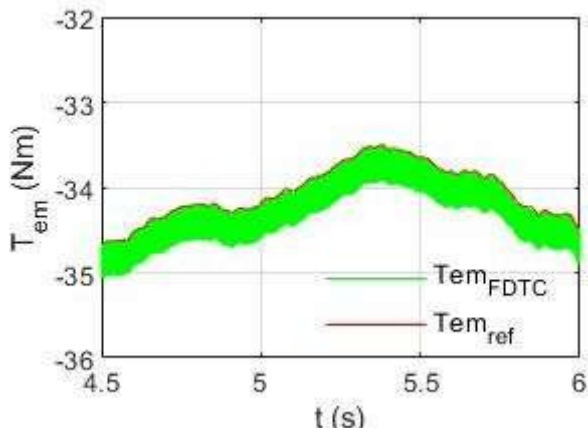


(a) FDTC
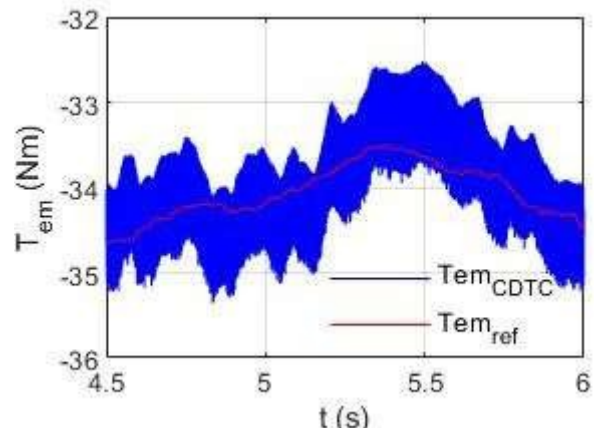
(b) CDTC

Fig. 7 Zoom on electromagnetic torque

25

(a) FDTC

(b) CDTC
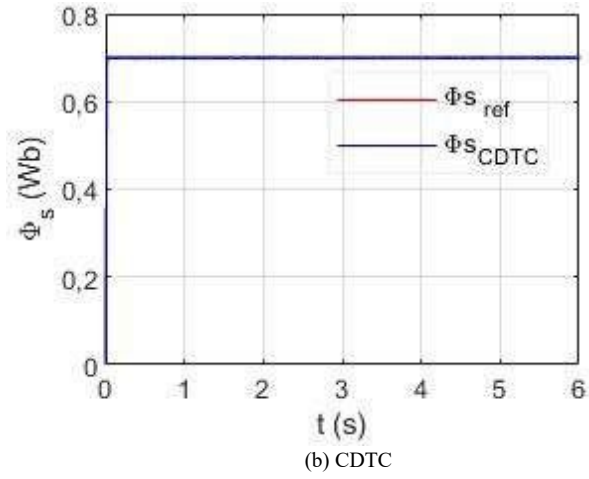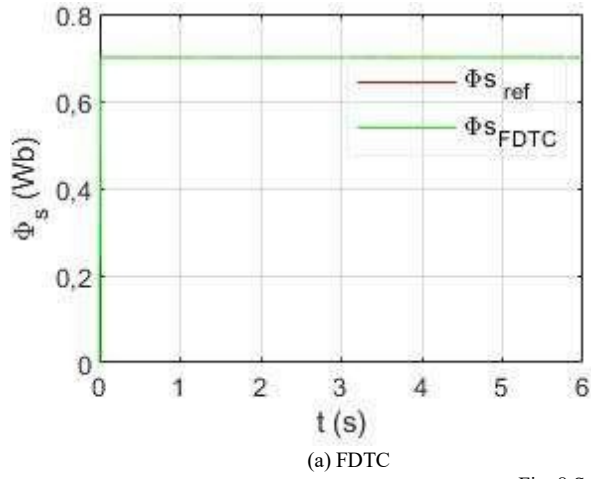
Fig. 8 Stator flux response



(a) FDTC

(b) CDTC
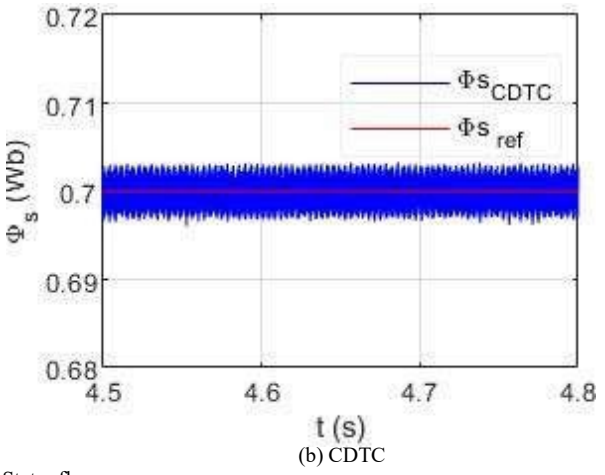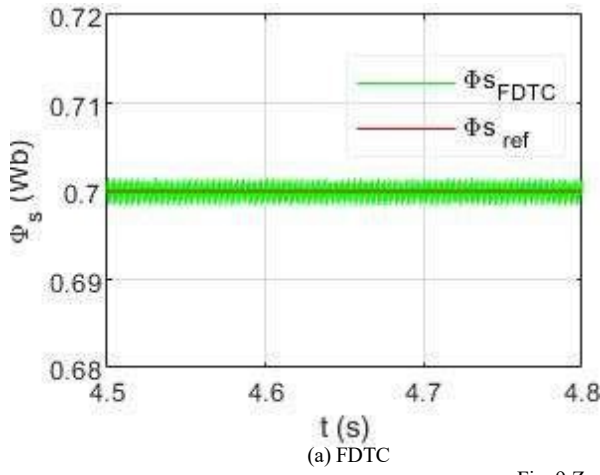
Fig. 9 Zoom on Stator flux
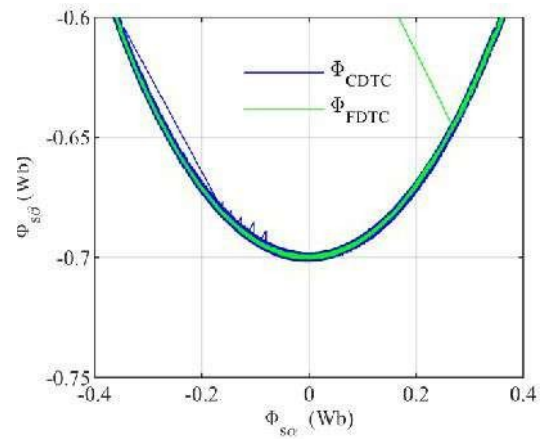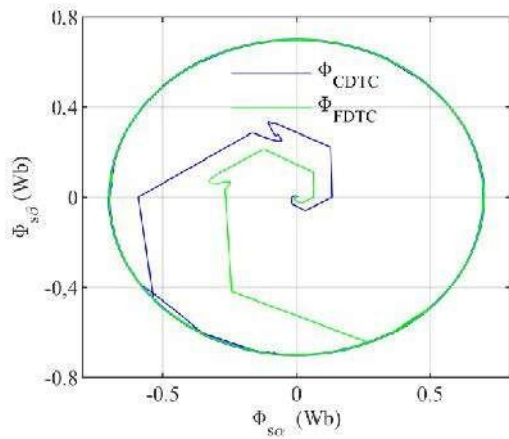


Fig. 10 Stator flux trajectory with zoom
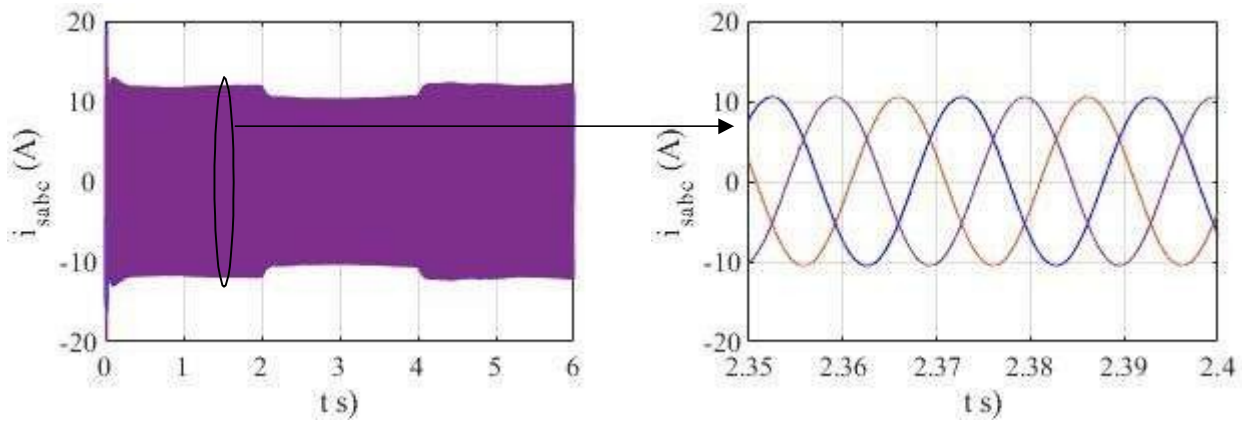
Fig. 11 The stator current with its zoom



(a) FDTC  (b) CDTC
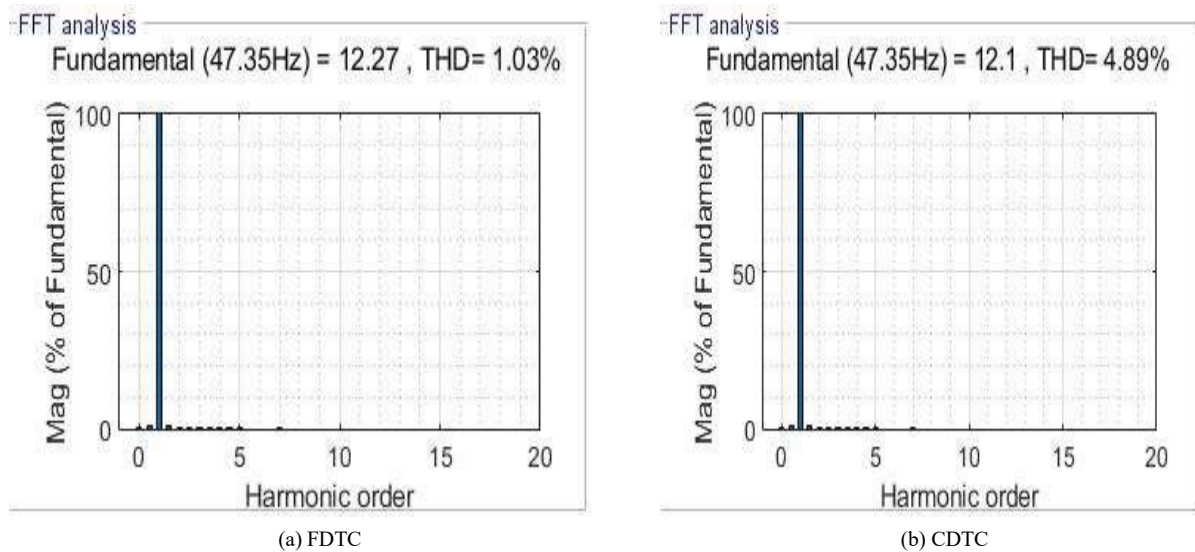
Fig. 12 Stator current harmonic spectrums

## VI. CONCLUSIONS

The objective of the present paper consists to control the voltage of the induction generator in an autonomous variable speed wind system. The proposed control combines the fuzzy logic regulation to the well known DTC, to enhance the performances of the SEIG regardless of the load and wind speed conditions. The obtained results show the effectiveness of the proposed control, characterized by a fine regulation of the DC bus voltage and the stator flux, all with minimizing the torque and flux ripples.

The proposed FDTC maintains the sturdy, uncomplicated, and highly dynamic characteristics of the CDTC while mitigating its shortcomings associated with torque/flux ripples and harmonic stator current. This leads to diminished mechanical vibrations and overall performance enhancement of the system.

## ACKNOWLEDGMENT

## REFERENCES

[1] M. Bašić, M. Bubalo, D. Vukadinović, & al. "Sensorless maximum power control of a stand-alone squirrel-cage induction generator driven by a variable-speed wind turbine". Journal of Electrical Engineering & Technology, 2021, vol. 16, p. 333-347.

[2] K. Berabez, F. Hamoudi, K. Idjdarene, & I. Hacini, "Advanced Terminal Voltage Control of Self-Excited Induction Generators in VariableSpeed Wind Turbines Using a Three-Level NPC Converter". Mathematical Modelling of Engineering Problems, Jun2023, Vol. 10, p805-814 (2023).

[3]   K. Idjdarene, D. Rekioua, T. Rekioua, A. Tounzi, A, " Direct torque control strategy for a variable speed wind energy conversion system associated to a flywheel energy storage system". In 2009 Second International Conference on Developments in Systems Engineering, Dhabi, United Arab Emirates, pp. 17-22. 10.1109/DeSE.2009.47.

[4]   K. Premalatha, & al, "Self-excitation system for control of wind turbine driven induction generator using direct torque control. Journal of Vibration and Control, 2016, vol. 22, no 3, p. 736-755.

[5]   O. Djoudi, S.L. Belaid, & S. Tamalouzt (2023). "Multilevel Converter and Fuzzy Logic Solutions for Improving Direct Control Accuracy of DFIG-based Wind Energy System". Periodica Polytechnica Electrical Engineering and Computer Science, 67(2), PP. 136-148, (2023).

[6]   W. Ayrir, A. Haddi, "Fuzzy 12 sectors improved direct torque control of a DFIG with stator power factor control strategy". International Transactions on Electrical Energy Systems, 29(10): e12092, (2019).

[7]   N. El Ouanjli, & al, (2019). "Direct torque control of doubly fed induction motor using three-level NPC inverter". Protection and Control of Modern Power Systems, 4(1), 1-9.

[8]   I. Issad, K. Idjdarene, & S. Lalouni, "Direct torque control using space vector modulation of wind pumping system with storage". Rev. Roum. Sci. Techn.–Électrotechn. et Énerg, 63(4), 397-402. (2018).

[9]   M. Mokhtari, S.A. & Davari, "Predictive torque control of DFIG with torque ripple reduction". In 2016 IEEE International Conference on Power and Energy (PECon) (pp. 763-768). IEEE. (2016, November).

[10]  C.T.S. Dagang, G. Kenne, & Muluh, F. A. (2021). "Fuzzy logic direct torque/power control for a self-excited induction generator driven by a variable wind speed turbine". International Journal of Dynamics and Control, 9, 1210-1222.

[11]  Belaid, S. L. (2021). "Improved IM DTC by using a fuzzy switching table in PV applications". Elektrotehniski Vestnik, 88(1/2), 26-32.

APPENDIX

Parameters of the SEIG:
Rated power = 5,5 kW, Frequency 50 Hz, ,Rated voltage =230/400V, current =23.8/13.7 A, Rotation speed = 690 rpm, Inertia = 0.230 kg.m$^2$,Friction =0,0025 N.m/rads$^{-1}$, Stator resistance R$_s$= 1,07131Ω
Rotor resistance R$_r$= 1,29511 Ω, Number of pair of poles =4

# Metamaterial inspired Two-Port Microstrip MIMO Antenna For 5G communication Applications

H. Benosman[1], MA.Rabah[2], F.Bousalah[3]

[1]*Department of telecommunication, Faculty of Technology*
*Abou-Bekr Belkaïd University,* Tlemcen, Algeria

[2]*Algerian Space Agency-Satellite development center*
*Bir El Djir 31130, Oran, Algeria*

[3]*Department of telecommunication, Faculty of Technology*
*Abou-Bekr Belkaïd University,* Tlemcen, Algeria

```
Email 1 – benosmanh@yahoo.fr
Email 2 – Arabah6@gmail.com

Email 3 – Bousalah.fayza@gmail.com
```

*Abstract:* **This paper introduces a circular-shaped complementary split ring resonator (CSRR) filtering structure designed to enhance isolation of the MIMO antenna system. The research focuses on developing a straightforward and compact CSRR design. To assess the filtering element's performance and enhance isolation among closely situated antenna elements, arrays of configured CSRR structures are introduced between two antenna elements. This configuration integrates an array of configured CSRR elements with the printed antenna on both the top and bottom layers. The proposed filtering elements exhibit a remarkable 25 dB improvement in isolation compared to a simple array. The entire structure has been simulated using the CST MWS simulator. The efficiency of the proposed antenna makes it well-suited for 5G communication applications.**

*Key words*: **microstrip antennas, MIMO system, mutual coupling, complementary split ring resonator, CST MWS.**

## I. INTRODUCTION

In recent years, the rapid expansion of advanced services has created a growing demand for increased data transmission capacity and higher data rates. Individual antenna elements typically have a wide radiation pattern and low directivity. While one approach to enhance antenna directivity is by enlarging the physical dimensions of the radiators, this method is often impractical. Alternatively, one can increase the electrical size of the antenna by constructing an array of similar elements, there by boosting antenna directivity [1]. A phased array antenna is composed of precisely arranged radiating elements of finite size, which are fed by a suitable feed network. Printed antennas, in particular, are well-suited for use as phased array elements due to their benefits such as being low-profile, lightweight, cost-effective, and easy to manufacture [2]. However, mutual coupling between the antenna elements has a significant impact on terminal impedance, radiation pattern, and gain in adaptive arrays [3]. To address the issue of terminal impedance mismatch, it is crucial to ensure that the mutual impedance is purely reactive at the resonant frequency [4].

Mutual coupling becomes particularly significant in array configurations due to two primary sources of coupling: free space radiation and surface wave effects [5, 6]. Several researchers have proposed a range of techniques aimed at mitigating these coupling effects. These techniques encompass the open-circuit voltage method [7–9], the element pattern method [10], the perturbation method [11], and the calibration method [12]. While these mathematical methods deliver highly precise results, their complexity tends to increase as the size of the array and the need for beam scanning grow. Additionally, implementing these methods typically necessitates the availability

of multiple preliminary experimental results to effectively compensate for coupling. An increasingly popular and straightforward method for mitigating the correlation between coupled antennas involves the utilization of metamaterial structures. This approach has gained significant traction within the realms of electromagnetics and antenna technology. Split ring resonators metamaterial (SRR) [4, 13–15] and their complementary counterparts, named complementary split ring resonators (CSRR) [16–18], have been suggested as solutions for uncoupling the array elements. The initial model of mu-negative (MNG) split ring resonator (SRR) was first introduced by Pendry [19]. The application of Babinet's principle led to the development of complementary split ring resonators (CSRR) [20]. The epsilon negative (ENG) CSRR was initially presented in [21], deriving it by applying duality to the SRR, effectively exchanging the roles of metal and dielectric. This interchange involves swapping the electrical and magnetic properties between the CSRR and the SRR. However, it is essential for both the CSRR and the SRR to have approximately the same resonant frequency [21]. As a result, the resonance frequency of the CSRR can be readily derived from the SRR in a straightforward manner.

In this work, we propose the study of a MIMO system applicable in 5G communications antenna networks. The aim is to show the role that these structures can play in minimizing the coupling between the two antenna elements. The CST MWS simulation software was used for the design of the antenna array. The different sections of this work will be organized as follows: The first section will address the design of the antenna element which will be used to define the antenna array. Then, we will proceed to the simulation of a two-element MIMO antenna inspired by MMTs. The MIMO antenna presented in this work is an excellent candidate for 5G communication. It offers several advantages, including a low ECC, high diversity gain, significant peak gain, minimal channel capacity loss, and most importantly, extremely high isolation.

## II. DESCRIPTION OF THE ANTENNA GEOMETRY

The antenna geometric configuration can be illustrated in Figure 1. The antenna under consideration is designed on a standard 0.254 mm thickness Rogers RT Duroid dielectric substrate, possessing a loss tangent of 0.002 and a relative permittivity of 2.2. The design involves two circular patches, both excited using a coaxial feed with a characteristic impedance of 50 Ω located at 0.6 mm from the center of the structure to ensure good adaptation. The radiating elements within the MIMO antenna maintain an edge-to-edge separation of 0.66 λ, equivalent to 7.9 mm. The dimensions of the antenna element have been determined to correspond to an operational frequency of 25 GHz. The total dimensions of the antenna array are $17 \times 8.6\ mm^2$. The radius $a$ of the patch antenna can be calculated from theoretical equations found in literature and equal to 0.77 mm [22] :

$$f_r = \frac{k_{nm}c}{2\Pi a_e \sqrt{\varepsilon_r \mu_r}}.$$ (1)

$$a = a_e \sqrt{1 + \frac{2h}{\Pi r \varepsilon_r \mu_r}\left[\ln\left(\frac{\Pi r}{2h}\right) + 1.7726\right]}$$ (2)

where :
$f_r$ is the resonance frequency of the patch antenna,
$a_e$ is the effective radius,
$a$ is the physical radius, $c$ is the speed of light in vacuum. $\varepsilon_r$, $\mu_r$ and $h$ are respectively the relative permittivity, the relative permeability and the thickness of the dielectric board used.
$K_{nm}$ is the $m^{th}$ non-zero root of the derivation of the Bessel function of $n^{th}$ order ($K_{11} = 1.84118$).

In MIMO systems, the isolation between the elements that compose them is of crucial importance and must be taken into account as one of the essential parameters. When two antenna elements are positioned in close proximity, the electromagnetic field emitted by one element impacts the current distribution on the other. This effect leads to a modification of the port impedance (active impedance) for all the elements within the array, resulting in a pronounced adverse impact on the overall array performance. The way to address this issue involves

reducing the mutual impedance of the antennas, both the real and imaginary components, to approach zero at the antenna's resonant frequency. This state can be attained by augmenting the isolation between the antenna elements.
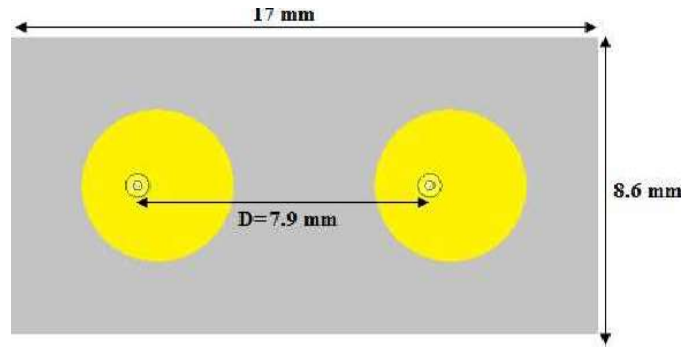


**Fig1 :** Geometry of the two-port MIMO system

To enhance antenna isolation, the CSRR filtering structure is introduced between the microstrip patches. Achieving a robust stopband response with a conventional microstrip antenna is challenging with just a single CSRR. Our objective here is to significantly enhance the band-rejection capabilities by arranging the CSRRs in a periodic array. Figure 2 illustrates the schematic diagram and the equivalent circuit model of the CSRR unit cell. The primary advantage of the CSRR lies in its high filtering capacity, which is valuable for suppressing coupling and achieving a compact size.
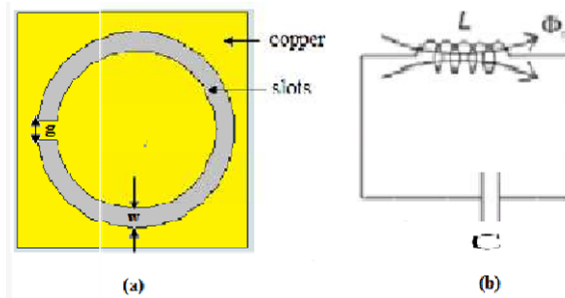


**Fig 2 :** CSRR unit cell. (a) Schematic diagram. (b) Equivalent circuit model.

The provided dimensions for the CSRR under consideration can be found in Table 1. These parameters have been optimized for operation around the 25 GHz frequency. For the substrate, a standard material, specifically Rogers RT Duroid with a thickness of h=0.254 mm has been chosen.

TABLE I

UNIT CELL DIMENSIONS

| Parametres | radius | w | g | h | t |
|---|---|---|---|---|---|
| Values (mm) | 0.77 | 0.15 | 0.15 | 0.254 | 0.035 |

To show the physical properties of the designed structure, S parameters for the unit cell are calculated with the mentioned boundaries along the wave propagation. Next, the effective material parameters can be extracted from the S parameters as it is described in [23], where :

$$z = \sqrt{\frac{(1+S_{11})^2 - S_{21}^2}{(1-S_{11})^2 - S_{21}^2}}.$$

$$n = \frac{1}{kd}\cos^{-1}\left[\frac{1}{2S_{21}}(1 - S_{11}^2 + S_{21}^2)\right]$$

$k$ and $d$ are the wave vector and the thickness of the slab. $z$ and $n$ indicate the wave impedance and refractive index, respectively. The magnetic permeability, can be calculated from these S-parameters by using MATLAB tool. Alternatively, $\varepsilon$ can be calculated mathematically from the equation of $\varepsilon = n / z$.

Figure 3 displays the computed scattering parameters, S11 and S21, for the configured CSRR. The structure is resonant and presents a strong band rejection at the 25 GHz frequency, which implies that most of the energy of the incident wave is blocked by the cell. Furthermore, Figure 4 illustrates the electric permittivity (ε) and magnetic permeability (μ) derived from the scattering parameters (S). The permittivity (eps) is negative in real part in the frequency band around the resonance, located between 24.7 and 26.15 GHz, while the permeability (mu) in real part remains positive throughout the working band as shown in Figure 4 (b).
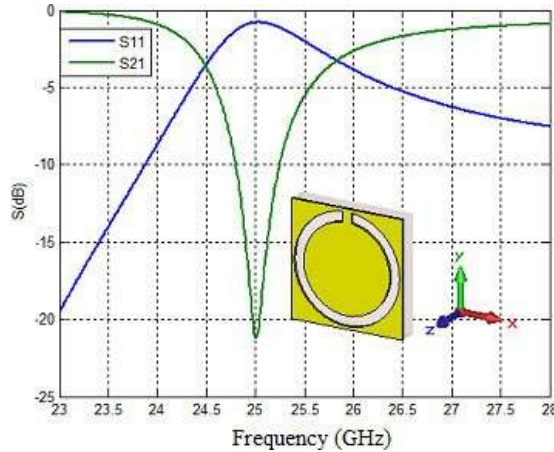


**Fig 3 :** S parameter of CSRR unit cell
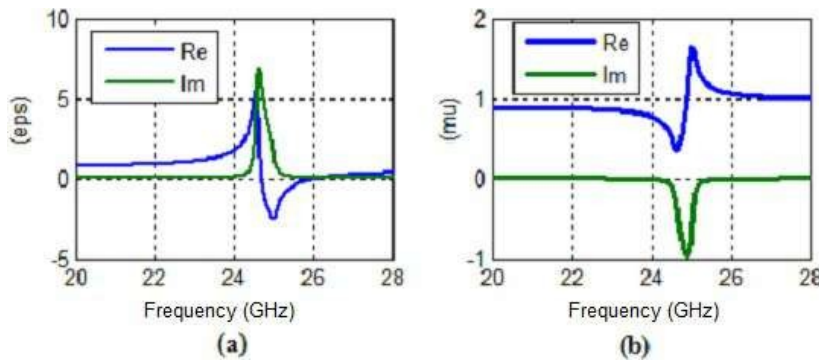


**Fig 4 :** Constitutive parameters of CSRR unit cell

### III.    IMPROVING ISOLATION MIMO ANTENNA WITH CSRR

As defined in the previous section, the isolation method using metamaterials was implemented to reduce the coupling between the circular antennas. Indeed, in order to maximize the energy radiation by a powered antenna, it is essential to ensure that all the energy supplied to it is not dissipated in the second antenna. Therefore, it is imperative to minimize the value of $S_{21}$, which is used to measure the radiated energy and characterize the decoupling between the two radiating elements. Multiple unit cell orientations in one layout array were analyzed by the researchers [24], and it was concluded that the CSRR structure provides optimal band rejection characteristics when combining two face-to-face cells with a slot, compared to a CSRR unit cell array periodicals conventional. The goal is to improve good band rejection characteristics by periodically arranging CSRRs in a network. Three case are studied, the CSRR network is placed between the patches on the surface, on the ground plane, then both on the surface and on the ground plane as illustrated in Figure 5.
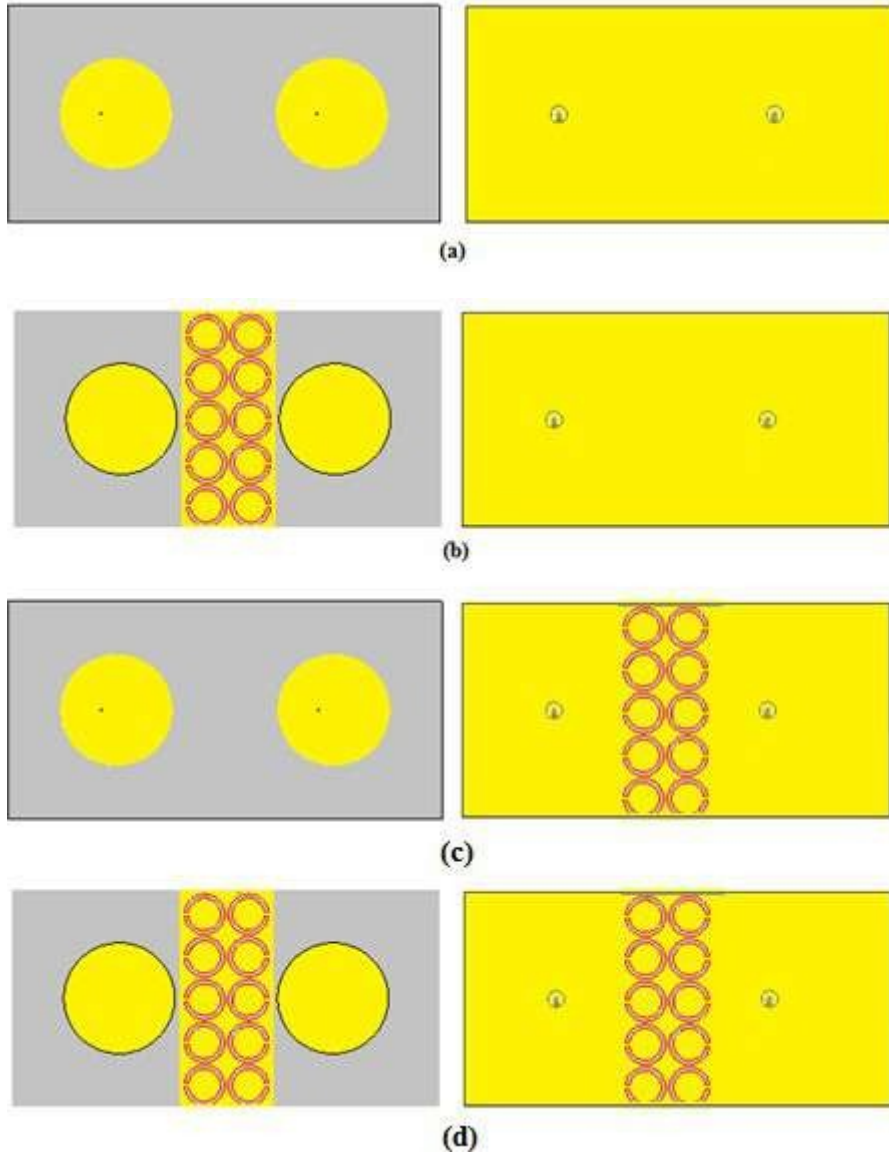
**Fig 5 :** Top and bottom views of a two-element array with and without decoupling elements. (a) Without CSRR. (b) with CSRR between the two patches. (c) With CSRR on the ground plane. (d) With CSRR both on the surface and on the ground plane.

## IV. SIMULATION RESULTS

In Figure 6, the simulated reflection coefficient (S11) and transmission coefficient (S21) of the proposed MIMO antenna are presented, both with and without the application of CSRR metamaterial. We note from these graphs that the presence of the resonator network does not have much impact on the adaptation of the antenna, if we compare it with the case where it there is no CSRR cell. Indeed, at the frequency of 25 GHz, the reflection coefficient for the four case is less than -10 dB and remains very satisfactory as illustrated in Figure 6 (a). On the other hand, referring to Figure 6 (b), the mutual coupling was reduced from -31.2 to -31.6 to -34.6 to -63.29 dB for no decoupling, CSRR on the plane ground plane, CSRR only on the patch surface, and for CSRR on both the ground plane and the patch surface, respectively. Therefore, very good insulation is obtained in the last configuration with this type of cells. The suppression of mutual coupling is therefore achieved by integrating the CSRR cells on the ground plane which is responsible for the coupling current. However, this degrades the radiation performance due to the powerful energy propagating backward. To suppress this high energy loss, CSRRs were introduced onto the patch surface, which improved the mutual coupling by reducing backward radiation. Therefore, the combination of cells from two sides of the substrate exhibits a more dominant coupling suppression response.

The behavior of the MIMO system in terms of isolation can also be explained by analyzing the surface current distribution of the antenna at the working frequency. The current distribution at 25 GHz in both cases (with and without the use of metamaterials) is shown in Figure 7. When exciting the two ports of the antenna a strong mutual coupling occurs between the two elements, the current is strongly coupled to the second patc. So, it is obvious that the CSRRs exert control over the current flow between the antenna elements. Thus, a very weak mutual coupling is obtained.



(a)



(b)
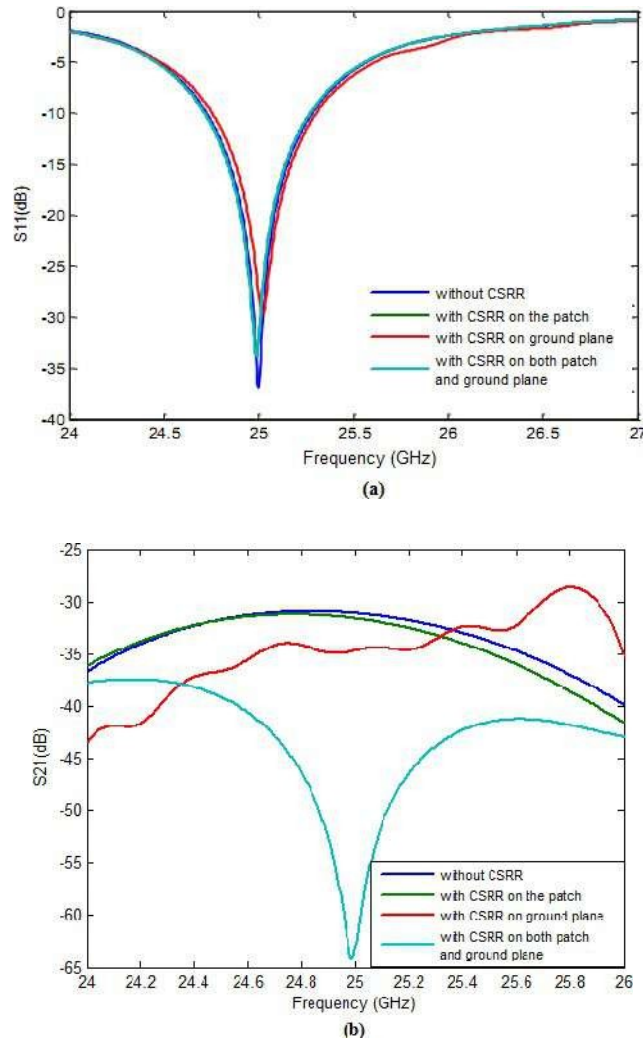
Fig 6 : S parameter of the two-element MIMO system: (a) coefficient S11, (b) coefficient S21.



(a)
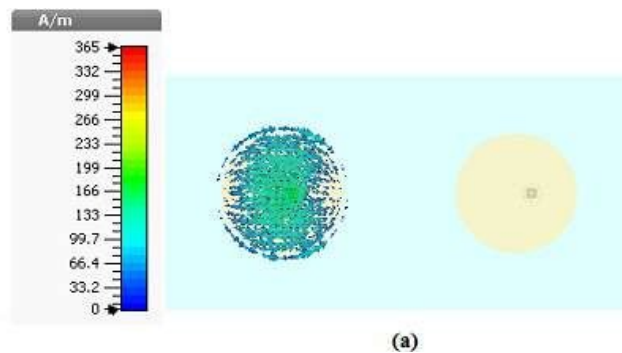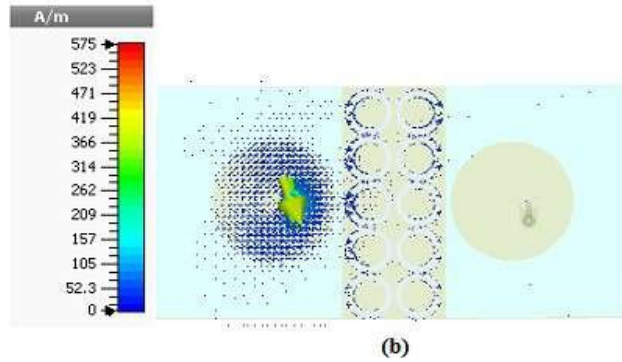
**Fig 7**: Surface current distribution of the MIMO antenna: a) Without CSRR, b) with CSRR

Further study, mainly the radiation characteristics of the MIMO antenna in both cases (with and without metamaterial), was also carried out. Figure 8 presents the simulated polar coordinate radiation patterns for the two principal planes (Phi = 0) and (Phi = 90), at 25 GHz frequency. As depicted in the figure, the inclusion of metamaterial has a minimal impact on the alteration of the radiation pattern. The simulated gain of the proposed MIMO antenna with and without metamaterial cell is shown in Figure 9. The antenna gain is improved when metamaterial unit cells are inserted at the ground plane and on the patch surface, therefore, the maximum realized gain of 7.56 dB is obtained at 25 GHz.

A comparison between the spatial radiation of the MIMO antenna with and without isolation technique at the 25 GHz frequency is shown in Figure 10. We observe a significant improvement in gain between the initial structure and that with MMTs. Indeed, the gain goes from 7.38 dB for the structure without CSRR to 7.56 dB for the antenna with CSRR. However, this result remains very satisfactory.

The parameter defining isolation and correlation in a MIMO system is the ECC (Envelop Correlation Coefficient). It is a measurement that evaluates the correlation between the radiation patterns or performance of two or more antennas in a wireless communication system. An ECC close to 1 indicates a strong correlation, meaning the antennas have similar performance and are strongly coupled. In contrast, an ECC close to 0 indicates low correlation, meaning that the antennas have different performances and are relatively independent of each other. In Figure 11, we represent the correlation coefficient of the MIMO antenna simulated at 25 GHz. The ECC is very low and close to the ideal value and it is equal to $1.48 \times 10^{-7}$ . This indicates that the proposed antenna system is capable of operating more independently, which can improve communication quality, reduce interference and increase reliability, allowing validation of the isolation technique used in this work.
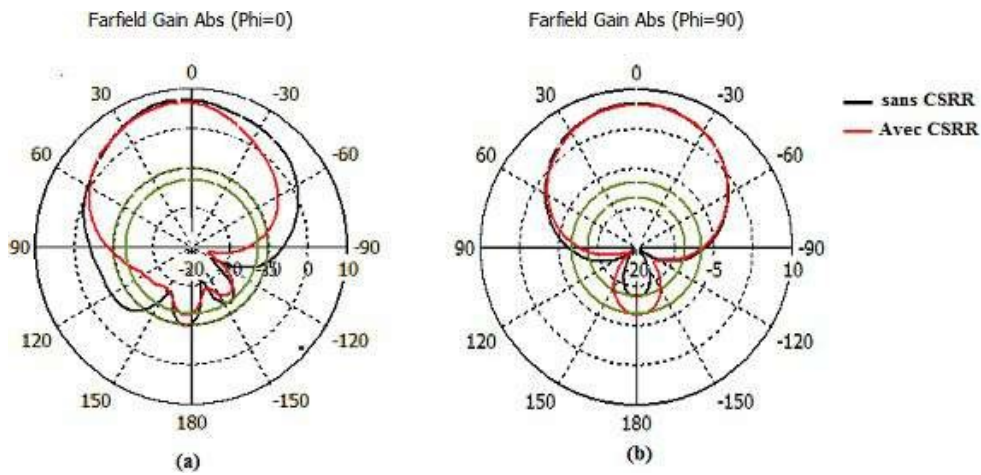


**Fig 8 :** Simulated radiation pattern (with and without CSRR) at 25 GHz (a) φ = 0°; (b) φ = 90°
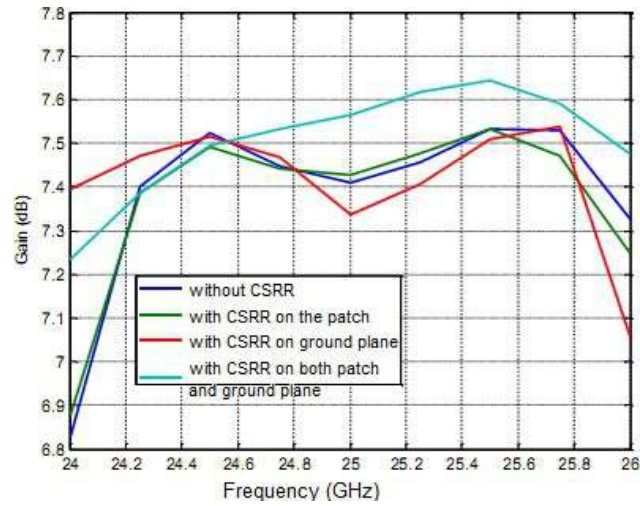
**Fig 9 :** Gain variation of the multi-antenna system with and without decoupling technique for different positions of the CSRR array
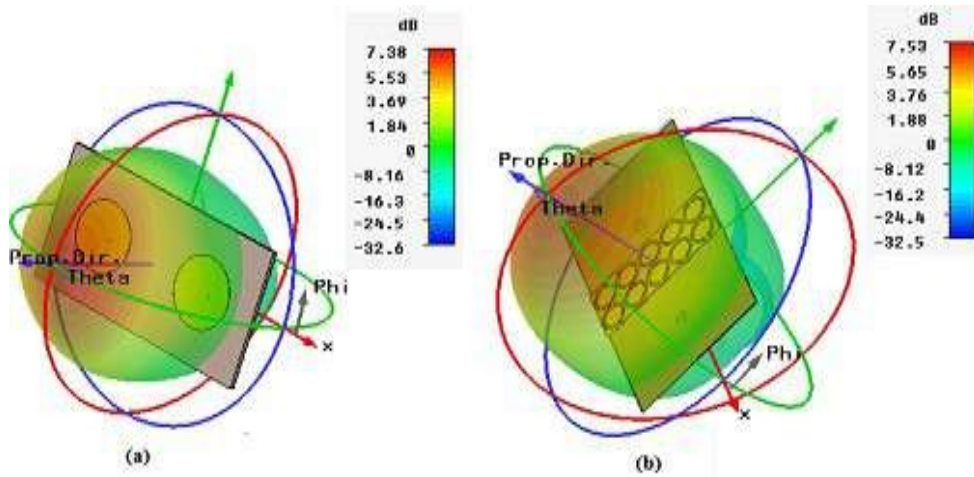


**Fig 10 :** 3D radiation patterns at 25 GHz frequency for the MIMO antenna (a) without CSRR and (b) with CSRR
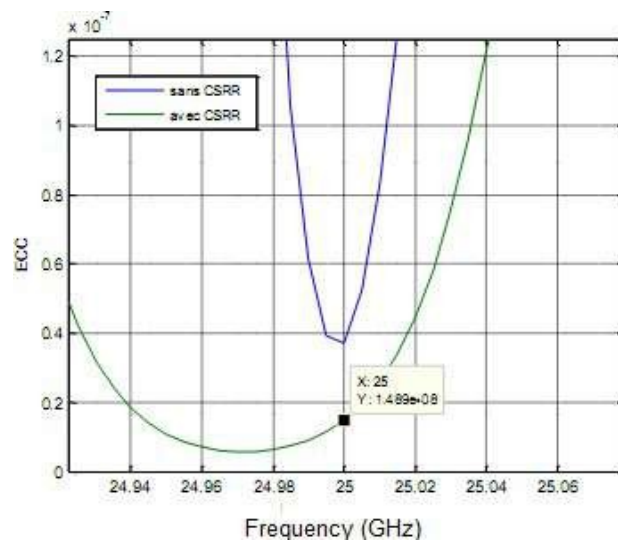


**Fig 11 :** ECC as a function of frequency for MIMO antenna without and with CSRR
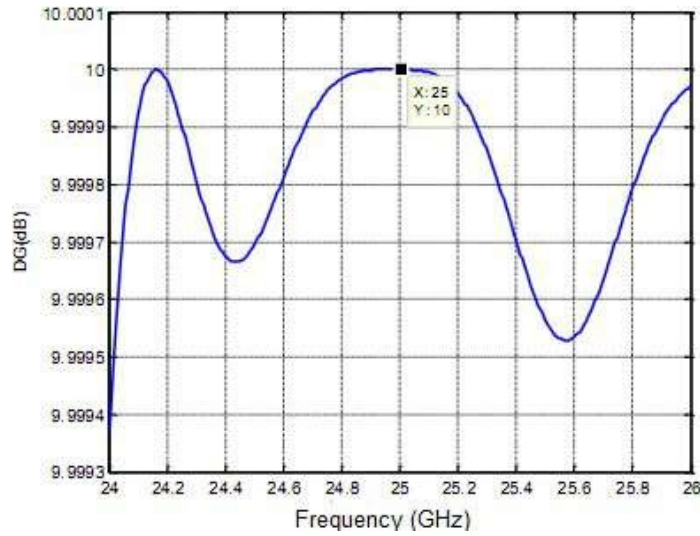
**Fig 12 :** Diversity gain as a function of frequency

Another essential parameter for characterizing the MIMO antenna is the Diversity Gain (DG), which can be computed using the equation provided in reference [24].

$$DG = 10\sqrt{1 - (ECC)^2}$$

In Figure 12, the Diversity Gain (DG) as a function of frequency is displayed. At 25 GHz, the MIMO antenna under consideration achieved a DG of 10 dB. The higher the Diversity Gain, the better in terms of reducing transmission errors and improving signal quality. Remarkably, the proposed antenna maintains a DG exceeding 9.5 dB across the entire frequency range.

Moreover, a comparison between our proposed method and several other metamaterial-based techniques is outlined in Table 3. The CSRR filtering element we suggest demonstrates superior isolation enhancement in antenna arrays compared to the other metamaterial structures detailed in Table 2.

TABLE II

PERFORMANCE COMPARAISONNIT

| Ref | Approach | Frequency (GHz) | Distance D | Improvement in isolation $S_{21}$[dB] |
|---|---|---|---|---|
| [4] | Slotted CSRR | 5 | 0.5 $\lambda$ | 10 |
| [17] | Slotted combined CSRR | 3.7 | 0.5 $\lambda$ | 10 |
| [26] | Defected ground structure | 6 | 0.3 $\lambda$ | 7.2 |
| [27] | Square CSRR | 25 | 0.67 $\lambda$ | 23 |
| | Proposed CSRR | 25 | 0.66 $\lambda$ | 32 |

## V. CONCLUSIONS

In this work, we presented a multi-antenna system designed for 5G communication antenna networks, implementing the MMTs technique to minimize the mutual coupling between their two constituent elements. The introduction of a CSRR cell array on the ground plane and patch surface helps to reduce the mutual coupling between these elements. As a result, improved isolation is provided, thereby enhancing the diversity performance and improving the overall radiation characteristics of the MIMO system. This approach has several advantages, including its simplicity, lower cost, and efficiency, making it a suitable solution for devices connected to 5G wireless applications.

## REFERENCES

[1] Balanis, C. A., *Antenna Theory: Analysis and Design*, 3rd Edition, John Wiley & Sons, 2016.

[2] Hansen, R. C., *Microwave Scanning Antennas*, R. C. Hansen (ed.), Vol. 1, Academic Press, Apertures, 1964.

[3] Gupta, I. and A. Ksienski, "Effect of mutual coupling on the performance of adaptive arrays, "*IEEE Transactions on Antennas and Propagation*, Vol. 31, No. 5, 785–791, 1983.

[4] 4. Bait-Suwailam, M. M., M. S. Boybay, and O. M. Ramahi, "Electromagnetic coupling reduction in high-profile monopole antennas using single-negative magnetic metamaterials for MIMO applications," *IEEE Transactions on Antennas and Propagation*, Vol. 58, No. 9, 2894–2902, 2010.

[5] Pozar, D., "Input impedance and mutual coupling of rectangular microstrip antennas," *IEEE Transactions on Antennas and Propagation*, Vol. 30, No. 6, 1191–1196, 1982.

[6] Bamford, L., J. James, and A. Fray, "Minimising mutual coupling in thick substrate microstrip antenna arrays," *Electronics Letters*, Vol. 33, No. 8, 648–650, 1997.

[7] Su, T. and H. Ling, "On modeling mutual coupling in antenna arrays using the coupling matrix," *Microwave and Optical Technology Letters*, Vol. 28, No. 4, 231–237, 2001.

[8] Huang, Z., C. A. Balanis, and C. R. Birtcher, "Mutual coupling compensation in UCAs: Simulations and experiment," *IEEE Transactions on Antennas and Propagation*, Vol. 54, No. 11, 3082–3086, 2006.

[9] Nasir, J., M. H. Jamaluddin, M. R. Kamarudin, Y.-C. Lo, R. Selvaraju, et al., "A four-element linear dielectric resonator antenna array for beamforming applications with compensation of mutual coupling," *IEEE Access*, Vol. 4, 6427–6437, 2016.

[10] Steyskal, H. and J. S. Herd, "Mutual coupling compensation in small array antennas," *IEEE Transactions on Antennas and Propagation*, Vol. 38, No. 12, 1971–1975, 1990.

[11] Jamaluddin, M. H., R. Gillard, R. Sauleau, and M.-A. Milon, "Perturbation technique to analyze mutual coupling in reflectarrays," *IEEE Antennas and Wireless Propagation Letters*, Vol. 8, 697–700, 2009.

[12] Huang, Q., H. Zhou, J. Bao, and X. Shi, "Calibration of mutual coupling effect for adaptive arrays composed of circularly polarized microstrip antennas," *Electromagnetics*, Vol. 34, No. 5, 392–401, 2014.

[13] Khaleel, H. R., H. M. Al-Rizzo, and A. Isaac, "Mutual coupling reduction between flexible mimo antennas," *WIT Transactions on State-of-the-art in Science and Engineering*, Vol. 82, 105, 2014.

[14] Hafezifard, R., M. Naser-Moghadasi, J. R. Mohassel, and R. Sadeghzadeh, "Mutual coupling reduction for two closely spaced meander line antennas using metamaterial substrate," *IEEE Antennas and Wireless Propagation Letters*, Vol. 15, 40–43, 2016.

[15] Ramaraj, M., S. Raghavan, S. Bose, and S. Kumar, "Elliptical split ring resonator: Mathematical analysis, HFSS modeling and genetic algorithm optimization," *PIERS Proceedings*, 631–635, Moscow, Russia, Aug. 19–23, 2012.

[16] Bait-Suwailam, M. M., O. F. Siddiqui, and O. M. Ramahi, "Mutual coupling reduction between microstrip patch antennas using slotted-complementary split-ring resonators," *IEEE Antennas and Wireless Propagation Letters*, Vol. 9, 876–878, 2010.

[17] Qamar, Z., L. Riaz, M. Chongcheawchamnan, S. A. Khan, and M. F. Shafique, "Slot combined complementary split ring resonators for mutual coupling suppression in microstrip phased arrays," *IET Microwaves, Antennas & Propagation*, Vol. 8, No. 15, 1261–1267, 2014.

[18] Shafique, M. F., Z. Qamar, L. Riaz, R. Saleem, and S. A. Khan, "Coupling suppression in densely packed microstrip arrays using metamaterial structure," *Microwave and Optical Technology Letters*, Vol. 57, No. 3, 759–763, 2015.

[19] Pendry, J. B., A. J. Holden, D. Robbins, and W. Stewart, "Magnetism from conductors and enhanced nonlinear phenomena," *IEEE Transactions on Microwave Theory and Techniques*, Vol. 47, No. 11, 2075–2084, 1999.

[20] Hsue, C.-W., Y.-W. Chang, and S.-L. Jang, "Comments on babinet's principle," *Forum for Electromagnetic Research Methods and Application Tecchnologies (FERMAT)*, Vol. 16, No. 3, Jul.–Aug. 2016.

[21] Falcone, F., T. Lopetegi, J. D. Baena, R. Marqu´es, F. Mart´ın, and M. Sorolla, "Effective negative-/spl epsiv/stopband microstrip lines based on complementary split ring resonators," *IEEE Microwave and Wireless Components Letters*, Vol. 14, No. 6, 280–282, 2004.

[22] C. A. Balanis, *Antenna Theory, Analysis and Design*. USA: John Wiley & Sons, Inc, 1997.

[23] D. R. Smith, S. Schultz, P. Markosˇ, C. M. Soukoulis, "Determination of effective permittivity and permeability of metamaterials from reflection and transmission coefficients," *Physical Review B, Vol. 65, 195104, April 2002*.

[24] Penciu, R., K. Aydin, M. Kafesaki, T. Koschny, E. Ozbay, E. Economou, and C. Soukoulis, "Multigap individual and coupled split-ring resonator structures," *Optics Express*, Vol. 16, No. 22, 18131-18144,2008.

[25] Sharawi, M.S. Printed MIMO Antenna Engineering; Artech House: Norwood, MA, USA, 2014.

[26] Xiao, S., M.-C. Tang, Y.-Y. Bai, S. Gao, and B.-Z.Wang, "Mutual coupling suppression in microstrip array using defected ground structure," *IET Microwaves, Antennas & Propagation*, Vol. 5, No. 12, 1488–1494, 2011

[27] Raghuraman S, Muhamad R, « Complementary Split Ring Resonator for Isolation Enhancement in 5G Communication Antenna Array » Progress In Electromagnetics Research C,Vol.83, 217– 228, 2018.

# Extension of the shelf life of fresh cream by the addition of *Citrus* Spp. essential oils

Nidhal SALEM[#1], Selim JALOULI[1], Ichrak MOUSSAOUI[1], Eya FEZAI [1], Souhir BELLOUMI[1], Rafika NEJI[1], Saber KHAMMASSI[2]

[1]nidhal_bio@yahoo.fr

[2]sabirouch2004@yahoo.fr

[1] *Laboratory of bioactive substances, Biotechnology Center at the Borj Cedria Technopole, BP, 901, 2050 Hammam Lif, Tunisia.*

[2]*Laboratory of medicinal plants, Centre de Biotechnologie at the Technopole de Borj Cedria, BP, 901, 2050 Hammam Lif, Tunisie.*

*Abstract*— Several countries have restricted the use of synthetic and chemical preservatives due to their harmful effect on health. Therefore, the researchers directed their study towards the exploitation of new bio-preservatives, while depending on the current trend of consumers to follow natural diets. In order to contribute to the valorization of the Tunisian flora, we proceeded to the study of the essential oils of *Citrus limon* and *Citrus aurantium* zests, from the region of Borj Cedria. These two aromatic and medicinal plants are quite rich in essential oil with higher extraction yields ranging from 0.09% to 0.22%, respectively. Limonenewas the major volatile compound for the two essential oils ((68.08%) and 93.53%, respectively). Both plants have powerful activities with $IC_{50} = 23\mu g/ml$ and $EC_{50} = 27\mu g/ml$ for *Citrus limon* and $IC_{50}= 28$ μg/ml and $EC_{50}=30$ μg/ml for *Citrus aurantium*. The results showed that creams added with essential oils do not present any contamination during the 14th day of treatment, then they begin to appear weakly from the 28th day to the 40th day of treatment in comparison to the control. *Citrus* essential oil can extend the shelf life of fresh cream and therefore make possible its application as an effective bioconservator in the food industry with higher acceptability.

*Keywords*— *Citrus limon*, *Citrus aurantium*, antioxydant power, cream, sensory analysis.

## I. Introduction

In recent years, synthetic food preservatives such as benzoate, nitrites and sulphites have become widely used and techniques have been developed to increase the shelf life of products. However, these chemicals posed problems in terms of safety and human health. The restriction imposed by the food industry and regulatory bodies has led to a renewed interest in the search for alternatives such as essential oils. They are commonly used as bio-preservatives in the food industry mainly for packaged foods sold in grocery stores such as fresh cream (Boulouri et al., 2022). Among the sources of these essential oils, *Citrus* spp weres widely used in traditional medicine as food preservatives for their antioxidant and antimicrobial potentials. It is in this perspective that this study was structured with the main objective was (**i**) to evaluate the antioxidant and antimicrobial effectiveness of *Citrus limon* and *Citrus aurantium* essential oils and (**ii**) to investigate its bioconservative effects to preserve the quality of fresh cream stored at +4 ° C for 40 days.

## II. Materials and Methods

### A. Plant material

*Citrus limon* and *Citrus aurantium* peels were collected from Borj Cedria (North Western Tunisia; latitude 36° 41' 17.22''(N); longitude 10° 22' 40.31''(E), altitude 11904 m). These species were deposited in the Herbarium of the Laboratory of bioactive substances under voucher number 28.452.

### B. Citrus essential oil extraction

The peels of *Citrus spp.* (300 g FW) were subjected to Clevenger extraction (Silva Moura et al., 2020). The plant material was placed in a Clevenger flask for 4 h. The water vapour entraining the volatile compounds was condensed in a refrigerant to be recovered in the Clevenger siphon. The resulting essential oil was stored at 4 °C in the dark, under a nitrogen atmosphere until analysis. Esential oil yield

percentage (%) was calculated as volume (ml) of essential oil per 100 g of plant dry matter. The obtained oils were analyzed by GC/MS using an Agilent GC system 7890A coupled with a mass spectrometer Agilent 5975C inert XL MSD with electron impact ionization (70 eV). An HP-5MS capillary column (30 m × 0.25 mm coated with 5% phenyl methyl silicone, 95% dimethylpolysiloxane, 0.25 μm film thickness).

### C. Antioxidant potential

Antiradical scavenging potential.

In this analysis, the purple-colored DPPH was reduced by antioxidants into pale yellow hydrazine (Najafabad and Jamei, 2014). 2000 μL of each essential oil at different concentrations (0.1−100 μg/ml) were added to 500 μl of fresh methanolic DPPH solution (0.2 mM). After 30 min of incubation in the dark at room temperature, the reading of absorbance was carried out at 517 nm using a Split Beam UV–vis spectrophotometer (T60 UV/VIS). Inhibition percentages were calculated using the following formula :

$$IP\% = ((Ac − At) / Ac] × 100$$

Where IP%: Inhibition percentage; Ac: Absorbance of control; At: absorbance of the test made. BHT was used as a positive control at the same concentrations as the tested extracts.

Ferric reducing antioxidant power.

The reducing ability of tested essential oils was determined according to the method of El Jemli et al. (2016). This method was based on the chemical reaction to reduce ferric iron ($Fe^{3+}$) present in the complex $K_3Fe (CN)6$ into ferrous iron ($Fe^{2+}$). To 1 ml of the sample at different concentrations (50, 200, 1000 and 2000 μg/ml), 2.5 ml of a phosphate buffer solution (0.2 M, pH 6.6) and 2.5 mL of $K_3Fe (CN)_6$ at 1% were added. The mixture was incubated at 50 °C for 20 min and then cooled at room temperature. 2.5 ml of TCA (10%) were added to stop the reaction, and then the tubes were centrifuged at 3000 /min for 10 min. 2.5 ml of the supernatant were added to equal volume of distilled water and 500 μl of a 0.1% solution of $FeCl_3, 6H_2O$. The absorbance was read against a blank at 700 nm using a Split Beam UV–vis spectrophotometer (T60 UV/VIS). Ascorbic acid was used as a positive control under the same conditions.

### D. Monitoring microbiological and physicochemical quality of fresh cream samples

The preliminary tests of sensory analyzes carried out at different concentrations to choose the acceptable doses of the different *Citrus* essential oil incorporated in the fresh cream. According to the sensory analysis. This application was based on adjunction of two doses (30μl/150g and 15μl/150g) of *Citrus spp* essential oil to the fresh cream to obtain treated and an untreated samples. All these were then, sampled each 3 days during refrigerated storage.

pH measurement

10 grams of fresh cream were homogenized with 90 ml of distilled water in a blender for 30s. The homogenate was filtered and the pH value of the filtrate was determined using the pH meter (Microprocessor pH meter BT-500, Boeco, Hamburg, Germany) (Boulares et al., 2017; Moradi et al., 2020).

Microbiological analysis of minced poultry meat

The microbiological quality of different samples of control and treated fresh cream, during storage at 4 °C, was monitored by determining total mesophilic aerobic flora (TMAF), total coliforms (TC), fecal coliforms (FC) and yeast molds (YM) counts over time, defined by International standards. 10 g of fresh cream, containing or free of essential oil samples were aseptically removed and homogenized with 90 ml of buffered peptone water (BPW) (Biolife, Milan, Italy) for 2 min using a Stomacher 400 Lab Blender (ISO 6887/V 08-010, 1982) and bacteriological investigations were performed from decimal prepared dilutions according to the standardized method ISO 6887/V 08-010 (1982). TMAF was enumerated on Plate Count Agar (PCA) (Biolife) after 48 h of incubation at 30 °C according to the norm NF V 08-051 (1999). TC and FC counts were determined on Violet Red Bile Glucose (VRBG) (Biokar) for 24 h respectively at 37 °C and 44 °C (NF V 08-054, 1999 and NF V 08-06, 1996 respectively). According to standard NF V08-059 (2002), YM were counted on Sabouraud medium at 25 °C for 3 days.

*E. Sensory analysis*

The sensory analysis of the fresh cream based on the essential oils of the two species of *Citrus* was carried out by 15 people who gave their opinions on the overall quality of the cream prepared. Essential oil-added cream samples randomly coded and served to individuals to rate color, odor, hardness, juiciness, and overall acceptability using a 6-point hedonic scale, where: 5 was extremely similar and 0 was extremely unpleasant (ISO13299, 2016) compared to a control cream.

## III. RESULTS AND DISCUSSION

### A. *Citrus* essential oils

The analysis of *Citrus spp* essential oils was determined by the chromatographic technique, GC-MS. The constituents had been identified (Table I) and their percentages were listed according to their elution order on the HP-5 column. The chromatographic allowed the identification of 25 and 24 volatile compounds respectively for *Citrus limon* and *Citrus aurantium*. Indeed, these essential oils were characterized by a clear dominance of monoterpene hydrocarbons with a percentage reaching up to 89.83% for *Citrus limon* and 96.12% for *Citrus aurantium*. This class of hydrocarbons is known for its antibacterial, antioxidant, anti-inflammatory, antiviral, expectorant, sedative, herbicide and insect repellent effects (Shehadeh et al., 2019). Limonene represented the major volatile compound for the two essential oils (*Citrus limon* (68.08%) and *Citrus aurantium* (86.53%)).

TABLE I
Chemical composition (%, w/w) of *Citrus Spp*. peels essential oils.

| Volatile compound* | Retention indices | | Essential oil composition | |
|---|---|---|---|---|
| | IRᵃ | IRᵇ | *Citrus limon* | *Citrus aurantium* |
| α-pinene | 939 | 1032 | 1.29±0.01 | 0.56±0.01 |
| Camphene | 954 | 1076 | 0.13 ±0.02 | 0.01±0.00 |
| Sabinene | 975 | 1132 | 6.48±0.06 | 0.09±0.00 |
| β-pinene | 980 | 1118 | 1.06±0.03 | 0.20±0.01 |
| Myrcene | 991 | 1174 | 1.54±0.02 | 1.55±0.03 |
| p-Cymene | 1026 | 1280 | 9.84±0.09 | 0.10±0.02 |
| Limonene | 1030 | 1203 | 68.08±0.11 | 86.53±1.05 |
| 1.8-Cineole | 1033 | 1193 | 0.51±0.01 | - |
| γ-terpinene | 1058 | 1255 | 0.04±0.00 | 0.43±0.01 |
| **Chemical classes** | | | | |
| **Monoterpene hydrocarbons** | | | 89.83±2.01 | 90.12±1.01 |
| **Oxygenated monoterpens** | | | 3.92±0.05 | 3.92±0.09 |
| **Sesquiterpene Hydrocarbons** | | | 0.06±0.00 | 1.92±0.02 |
| **Oxygenated sesquiterpens** | | | 0.01±0.00 | 0.3±0.01 |

*Compounds were listed in order of elution in HP-5 column. IRᵃ : retention index calculated on HP-5 column, IRᵇ : retention index calculated on HP-innowax column -: absent. The values shown in this table were the average of three replicates andgiven as mean± SD (n=3). One− way ANOVA followed by Duncan's multiple range test was used.

### B. Antioxidant potential

The evaluation of the antioxidant activity of *Citrus* essential oil was highlighted by two tests: the anti-radical capacity (DPPH test) and the reducing power (Table II). It should be noted that the lower the $IC_{50}$ and $EC_{50}$ of the sample, the higher the antioxidant activity.

TABLE II
Antioxidant properties against DPPH radical and
reducing power of *Citrus spp.* essential oils.

| *Citrus* species | IC$_{50}$ (µg/ml) | EC$_{50}$ (µg/ml) |
|---|---|---|
| *Citrus limon* | 23±1.22 | 27±1.00 |
| *Citrus aurantium* | 28±0.88 | 30±1.55 |
| Synthetic standards | | |
| BHT | 50±2.33 | - |
| Ascorbic acid | - | 70±1.44 |

The anti-radical activity of *Citrus* essential oils was higher than BHT; (IC$_{50}$ = 50 µg/ml). This can be due to the dominant chemotype, limonene (68.08 to 86.53%) which showed strong anti-radical power (Vitalini et al., 2021). *Citrus limon* essential oil showed an IC$_{50}$ = 23 µg/ml which was higher than that of *Citrus aurantium*. This potential could be linked to the synergy between major monoterpene hydrocarbons specifically; limonene, p-cymene, sabinene and α-pinene which are well known for their antioxidant potential. The EC$_{50}$ recorded for *Citrus limon* essential oil (27µg/ml) was lower than that of *Citrus aurantium* EO (30 µg/ml), resulting from the powerful reducing power of Citrus limon. This result joins that of the anti-radical activity. This could be explained by the fact that *Citrus limon* essential oil is a mixture of volatile compounds with strong antioxidant activity, more particularly a synergy between these major compounds while in *Citrus aurantium* essential oil, the activity is due exclusively to a single major compound which is limonene 93.53%.

*C. Microbiological quality variation*

*Total germs*

The results showed that creams added with essential oils didn't present any contamination during the 14th day of treatment, then they begin to appear weakly from the 28th day to the 40th day of treatment. On the other hand, untreated creams stored under the same conditions showed bacteriological growth which exceeded the standard which requires 10$^6$ CFU/ml (VignolaI et al., 2002).

*Total coliforms*

we noticed the absence of coliforms for the fresh cream added with *Citrus lemon* essential oil during storage. For the fresh cream added with *Citrus aurantium* esential oil, there is an appearance of coliforms from the 40th day, on the other hand for the control cream we observed the appearance of coliforms from the 28th day and the content of the latter does not exceed the standard which requires 10 CFU/ml but presented slight contamination.

*pH value variation*

We noticed that the pH of untreated fesh cream decreased more quickly than the pH of the treated cream (Fig.1). This decrease in pH could be justified by the acidity of *Citrus* essential oils. We thus noticed that the pH of the cream added with *Citrus limon* essential oil decreased more weakly than that added with *Citrus aurantium* essential oil.
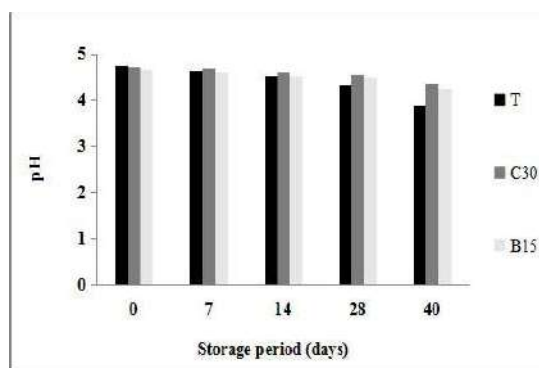
**Fig.1.** Evolution of pH in untreated (T) and treated (C30 and B15) fresh cream during storage. pH values, were significantly different at $P < 0.05$ (Duncan test).

### D. Sensory analysis

According to the bacteriological and physicochemical analyses, we choosed fresh cream added with *Citrus limon* essential oil to carry out a sensory analysis (Fig.2).
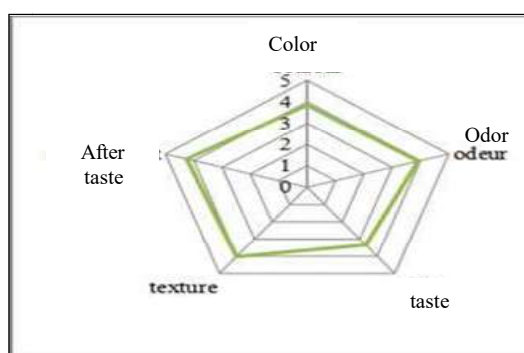


**Fig.2.** Sensory analysis of the fresh cream added with *Citrus limon* essential oil.

Obtained results showed that the treated fresh cream with *Citrus limon* essential oil had a homogeneous, good and non-oily texture which constituted a good point. The product was acceptable to most consumers based on criteria of odor, taste, aftertaste, texture and color.

### IV. CONCLUSIONS

The present study, carried out to find natural bioconservator products capable of extending the shelf life of fresh cream, showed powerful antioxidant and antmicrobial potentials of *Citrus* species. The addition of these essential oils reduced microbial load and improved fresh cream storage stability in comparison to the control. Thus, it is concluded that *Citrus* essential oils could be used as biopreservatives in fresh cream. However, toxicological tests are considered necessary to guarantee the use of these creams in complete safety for human health.

### ACKNOWLEDGMENT

### REFERENCES

[1] Parisa Bolouri, Salami Robab< /span>Javad Hadian, Behnam Asgari  Lajayer,Masoumeh  Kordi ,Shaghayegh Kouhi3 , et Tess Astatkie. (2022). Applications of essential oils and plant extracts in different industries. Molecules, 27(24), 8999.

[2] Silva Moura E, D'Antonino Faroni LR, Fernandes Heleno F, et al. (2020). Optimal extraction of *Ocimum basilicum* essential oil by association of ultrasound and hydrodistillation and its potential as a biopesticide against a major stored grains pest Molecules 25: 1–17.

[3] Najafabad MA and Jamei R. (2014). Free radical scavenging cap acity and antioxidant activity of methanolic and ethanolic extracts of plum (*Prunus domestica* L.) in both fresh and dried samples. Avicenna Journal of Phytomedicine 4(5): 343–353.

[4] El Jemli M, Kamal R, Marmouzi I, et al. (2016). Chemical composition, acute toxicity, antioxidant and anti-inflammatory activities of Moroccan Tetraclinis articulata L. Journal of Traditional and Complementary Medicine 7(3): 281–287.

[5] Boulares M, Mankai M, Sadok S, et al. (2017). Anti-Listerial inhibitory lactic acid bacteria in fresh farmed sea bass *Dicentrarchus labrax*) fillets during storage at 4 °C under vacuum-packed conditions. Journal of Food Safety 37(3): 1–14.

[6] Moradi E, Moosavi MH, Hosseini SM, ,R et al. (2020). Prolonging shelf life of chicken breast fillets by using plasma-improved chitosan/low density polyethylene bilayer film containing summer savory essential oil. International Journal of Biological Macromolecules 156: 321–328.

[7] Shehadeh Mayadah., Jaradat Nidal., Al-Masri Motasem., Zaid Abdel Naser., Hussein Fatima., Khasati Ahmad., et al. (2019), <<Rapid, cost-effective and organic solvent-free production of biologically active essential oil from Mediterranean wild *Origanum syriacum*>>, Saudi pharmaceutical journal : SPJ : the official publication of the Saudi Pharmaceutical Society.

[8] Vitalini, S. Vinciguerra, V. Iriti, M. and Garzoli, S. A comparative study of the chemical composition by SPME-GC/MS and the antiradical activity of less common citrus species.(2021). Molécules, 26(17) 5378.

[9] VignolaI C.L., et al (2002). Science et technologie du lait : Transformation du lait – Montréal : Presse internationale polytechnique 600p.

# Exploitation and control of a hybrid system for an isolated area

Azzag El bahi[#1], Ksentini Abdelhamid[*1]

[#] *Labor. Electrotechnical, Department of Electrical Engineering - Badji Mokhtar University-Annaba, Algeria*

Email 1 – azzag15@gmail.com

*Abstract*— **Fossil fuels are down sharply and negatively affect the environment. The development of clean energy sources seems increasingly necessary; in particular, renewable energy that are an attractive alternative for energy supply isolated or difficult access sites not allowing connection year national grid. We present in this paper a new proper management of a Hybrid Energy System (HES) based renewable energy to power a autonomous power grid, using a Wind Turbine Generator (WTG) and a Diesel Generator (DG), this strategy helps balance operation and management of these sources. The use of renewable energy depends first of the installed capacity of the site to power. The integration of the Battery Energy Storage System (BESS) is required to ensure energy autonomy of economic site. The economic analysis of the production of this energy and its effect on the environment and ecology will have a long term benefit.**

*Keywords*— Modelling, Hybrid network, Energy management ,coupling,Wind,Group diesel,battery, inverter.

## I. INTRODUCTION

Depletion of fossil fuels and environmental pollution caused by consumption of these fuels are two predominant energy problem faced in contemporary world. But still many communities around the world, living in remote location that lacks access to regular electric power grid supply, utilize the diesel generators for day-to-day power consumption. Since diesel generators are highly expensive option and contribute to very high carbon emission [8], an alternative energy solution is required to reduce diesel fuel consumption by integrating and operating a clean energy source in parallel.

Sustainable development, recourse to the use of renewable energy sources energy systems has become indispensable. Knowing the problems for the transport of electricity in remote areas, as well as the high cost, it would be advisable to consider the use of hybrid energies (Wind-Diesel) systems in these regions as the wind direction (wind speed) is important.

The preliminary study of this type of system is an important step, because oversized systems mean additional costs, while a system undersized would be less reliable. Southern Algeria and more particularly the Adrar site has strong wind energy potential which advocates the development of sources of renewable energy systems in these regions. It is then necessary to know the contribution of wind power source to power the load ensuring a suitable optimization.

## II. WIND MAP OF ALGERIA AND LOCATION OF HES

The city of Adrar is located south west of Algeria, about 1540 km from Algiers. The region is characterized by relatively flat topography and geomorphology by a desert. Adrar and its surroundings are characterized by a high potential of wind from the north east(**6.2 m/s**) see Fig.1.
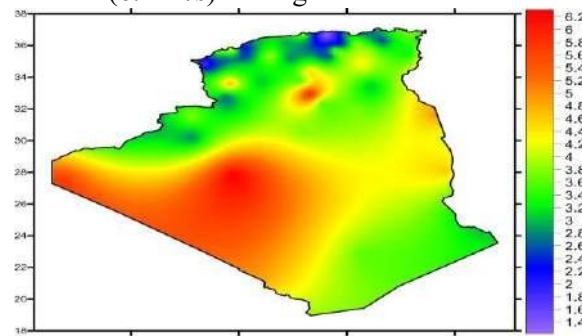


**Figure1. Annual wind map (m/s) at 10m from the ground, estimated by Dr. Boudia [11].**

Wind data from the Adrar region ranked it as the one with the best wind potential in Algeria. This site is located about 72km north of the city of Adrar near an electrical substation SONELGAZ its geographical coordinates are 27° 12'30 "N and 0° 10'30" W (Fig.2)[1].
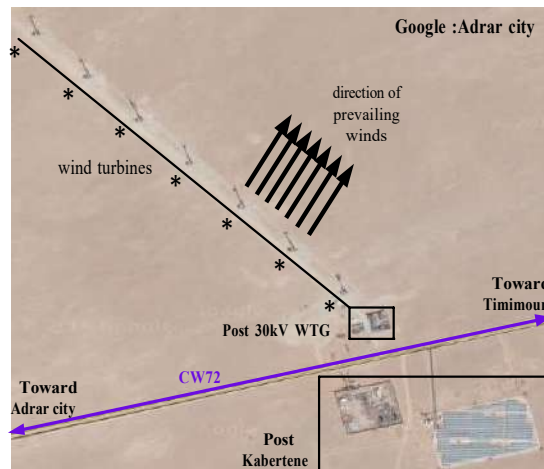


**Figure 2. Aerial view of the site**

The majority of sites in the city of Adrar could be considered as isolated sites to the vast size and distance from the city and each other. The extremely difficult Climatic conditions are another parameter to be considered. All this leads us to think of hybrid systems for powering an area in this region [2]

### III.    PROBLEMS OF THE PRODUCTION OF ELECTRICITY BY A DIESEL GROUP

Fossil energies are always used extensively today in the world. Presumably they will pose two major problems. The first is that their rarities will create geopolitical tensions in the world (eg Iraq War). The second problem is that $CO_2$ emissions that they engender, are high and strongly contributing to global warming [3].

### IV.    SYSTEM OVERVIEW

The proposed wind-diesel hybrid system shown in Fig. 3 consists of the following:
- Wind turbine (WTG) with machine double-fed asynchronous (DFIG).
- Generator diesel (GD) system.
- Battery energy storage system
- Load

The connection of these elements is carried out at the level of an AC bus. This bus has the advantage of more easily interconnected the different elements of the hybrid system.
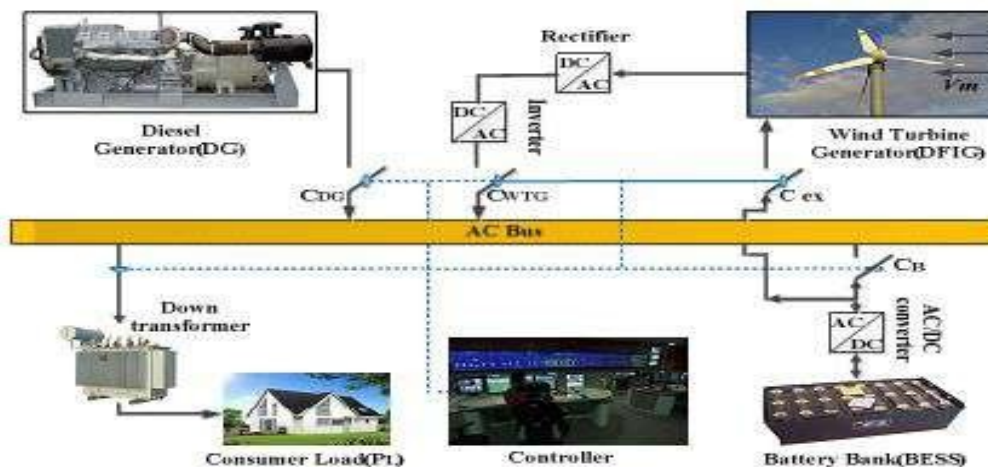


**Figure 3. Schematic of hybrid wind-diesel system supplying isolated load**

Depending on the strength of the wind, 3 operating modes can be distinguished for systems with high penetration "Fig. 4"[4].
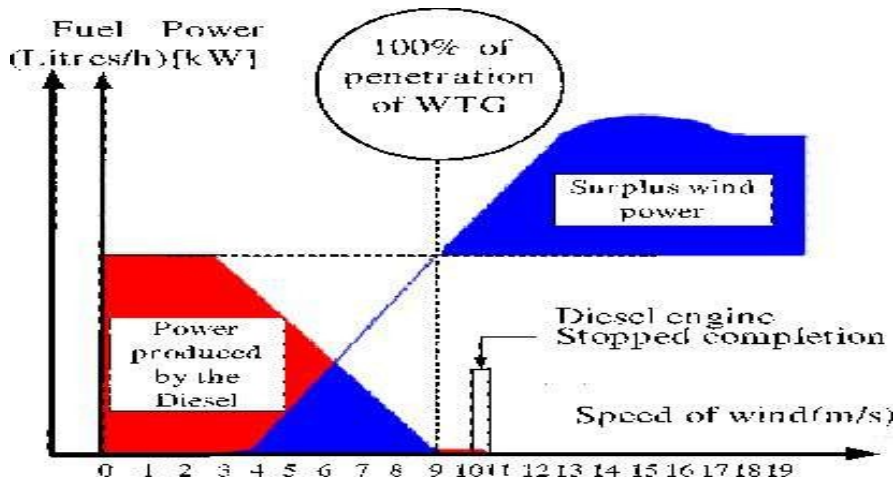


Figure 4. Variation of energy covered by a system Wind -Diesel and diesel consumption as a function of wind speed

## V. THE PROPOSED CONTROL SYSTEM STRATEGY

For a multi-source energy system, a power flow management strategy is needed. According to wind speed values ($V_m$) and the power demanded by the consumer load. The power system has three operation modes, as follows [5].

• Weak winds ($V_m \leq 3.5$)$m/s$ : Diesel Only(DO)in service.

• Moderate winds($3.5 < V_m \leq 10$)$m/s$ : Wind- Diesel (WD) in serviced

• Strong winds ($10 < V_m \leq 17$)$m/s$ : Wind Only(WO)in service

To adapt the production of the renewable source to the need for the load, we integrate a system of storage, such as the battery to ensure the continuity of service; that is necessary to feed the load, in case when the generator diesel fails and the wind is insufficient (low) for the operation of the wind turbine.

The following figure shows the simulation block diagram of the different modes of the system manager "Fig.5".
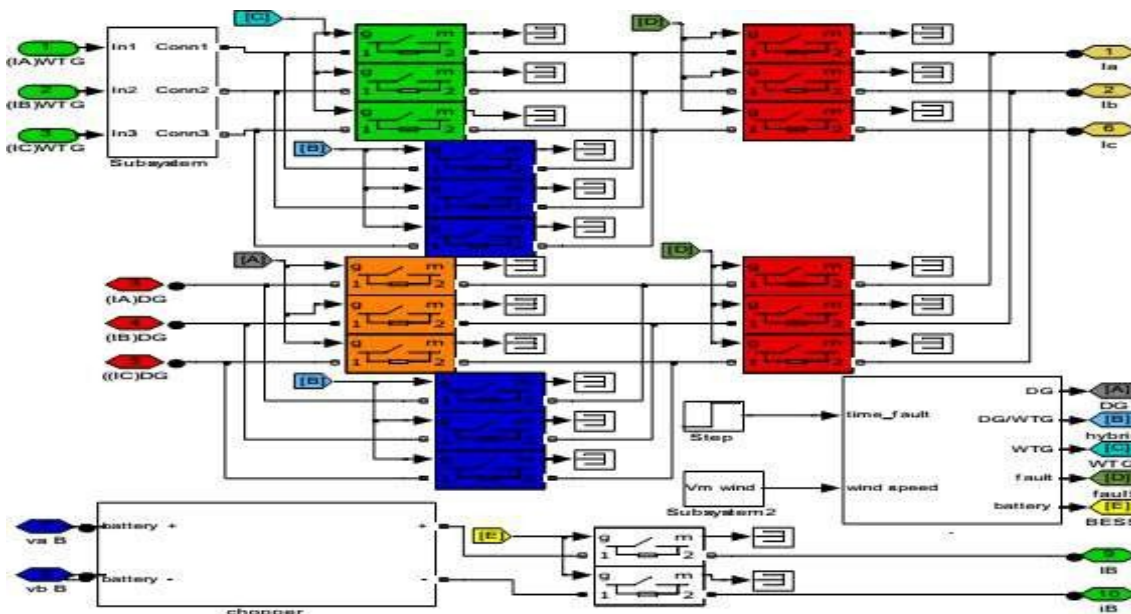


Figure 5. Diagram simulation of the management energy

For the hybrid system study (Wind-Diesel) must be modeled all the elements of this system (WTG, DG, BESS Battery, DC / AC inverter).

## VI.  MODELING OF SOURCES

### WIND TURBINE

The wind generator set consists of a wind turbine, double-fed asynchronous generator, rectifier and inverter to get an AC supply. The turbine model is based on the steady-state power characteristics of the turbine. The friction factor and the inertia of the turbine are combined with those of the generator coupled to the turbine. The output power of the turbine is given by [6]:

$$P_{mec} = \frac{1}{2}.\rho.A.Vm^3.Cp(\lambda) \tag{1}$$

where, $P_{mec}$ is the mechanical output power of the turbine, $\rho$ is the air density (Kg/m³), $A$ is the turbine swept area A= $\pi R^2$ , R is the blade radius (m), $Cp$ is the performance coefficient of the turbine, and $Vm$ is the wind speed (m/s).

The performance coefficient $(Cp)$, determines the power conversion efficiency from wind to mechanical. It is related to blade aerodynamic characteristics and turbine design. The performance coefficient is calculated from:

$$Cp(\lambda) = 0.5176 \left(\frac{116}{\lambda_i} - 0.4\beta - 5\right) e^{-\frac{21}{\lambda_i}} + 0.0068\lambda_i \tag{2}$$

Where: $\beta$ is the pitch angle (degree) and $\lambda$ is the tip speed ratio (TSR), defined by

$$\lambda = \frac{\omega_t.R}{v} \tag{3}$$

Finally, the output mechanical torque is calculated from:

$$T_{mec} = \frac{P_{mec}}{W_r} \tag{4}$$

Where $\omega_r$ is the rotor angular speed (rad/s).

### *) MPPT CONTROL AND PITCH CONTROL

In order to track an optimal rotor speed reference, the MPPT algorithm is proposed and based in PI controller .The objective of the MPPT operation mode is to maximize power extraction at low to medium wind speeds by following the maximum value of the wind power .To extract the maximum power, we need to fix the tip speed ratio at $\lambda_{opt}$, the maximum power coefficient $C_{p-max}$ and $\beta$ should be equal to 0° [9].

$$\lambda_{opt} = \frac{\omega_{opt}.R}{v} \tag{5}$$

Where $\lambda_{opt}$ and $\omega_{opt}$ are the tip speed ratio and the rotor speed optimal respectively.

The aerodynamic power optimal must be set to the following expression:

$$P_{opt} = 0.5 C_{p-max} \left[ A \left( \frac{\omega_{opt}.R}{\lambda_{opt}} \right)^3 \right] \tag{6}$$

The above equations are used to establish the servo block diagram of the turbine speed ( See Fig.6).
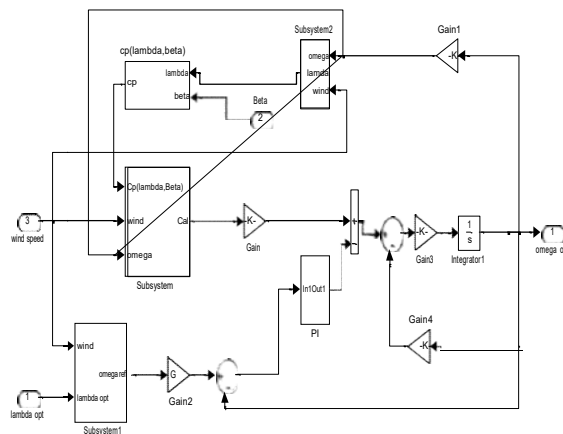


**Figure. 6  DFIG speed control loop**

To capture the maximum power of the incident wind must continuously adjust the rotational speed of the wind turbine. Optimal mechanical turbine speed is $\lambda_{opt}$ and $\beta = 0°$. The speed of the DFIG is used as a reference for a controller proportional-integral type (PI phase lead) [10].

## DIESEL GENERATOR SYSTEM

Diesel engines are the prime movers in countless small and remote power systems throughout the world. Often diesel fuel at these locations is expensive. These generators also often operate at low load, with poor fuel efficiency. The low-load operation may result in increased engine maintenance requirements. Thus, fuel use and maintenance are primary concerns in these remote locations.

Though the fuel consumption characteristic of a typical diesel generator is somewhat quadratic in nature, the linear function is used as a simplified model.

$$Consu_{fuel} = Consu_{0,\,fuel} + Consu_{speci,\,fuel}.P_{DG} \qquad (7)$$

Where:

$Consu_{0,fuel}$ : Vacum fuel consumption of DG [l/h].

$Consu_{speci,fuel}$ : Specific fuel consumption of the generator[l/kWh].

## BATTERY LEAD-ACID MODEL

The Battery block implements a generic dynamic model parameterized to represent most popular types of rechargeable batteries[7].
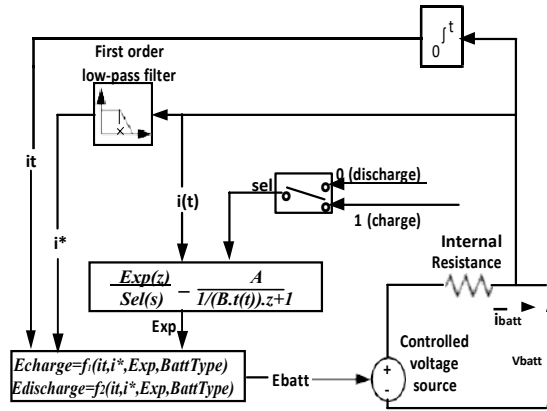


**Figure 7. Lead-Acid Model**

The parameters of the equivalent circuit can be modified to represent a particular battery type, based on its discharge characteristics as shown below(see Fig.8)[7].
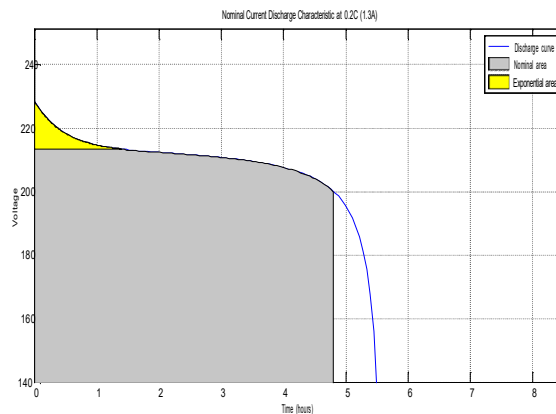


**Figure 8. Typical Discharge Strategy**

## VII.    RESULTS

This study is based on the average wind speed according to the strategy proposed in Section IV. To simulate the WDHS system we realized the simulation scheme of Fig.3 in the software Matlab- 7.8 *Simulink* for powering a

load (AC) for a low-voltage regime knowing that at the beginning. We used the WO to supply the load with a well controlled wind speed. After we use the only diesel group for the same charge and finally hybridization (WD).

*Case 1- WO: 10≤Vm <17 (m/s)*

Figure 9 shows the average active and reactive power generated by WTG
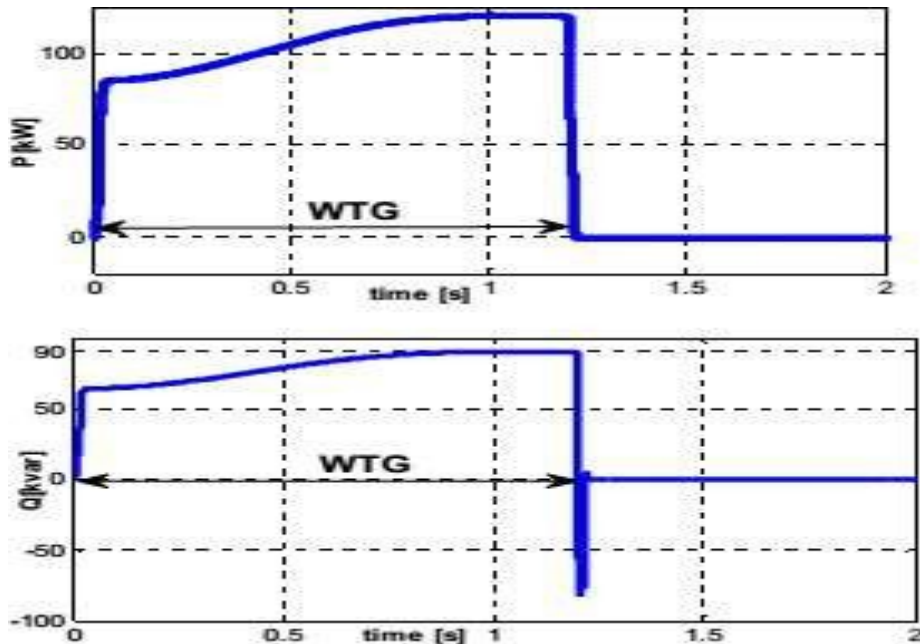


**Figure 9. Active and reactive power generated by WTG.**

Depending on wind speed, it is noted that the active and reactive power is has attained maximum(120kW), (90kVAR) respectively as the wind operate (Vm≥10).

The following figure shows the three phase voltages of the charge $P_L$ (380V) supplied by WTG view that the wind speed is sufficient (WO).
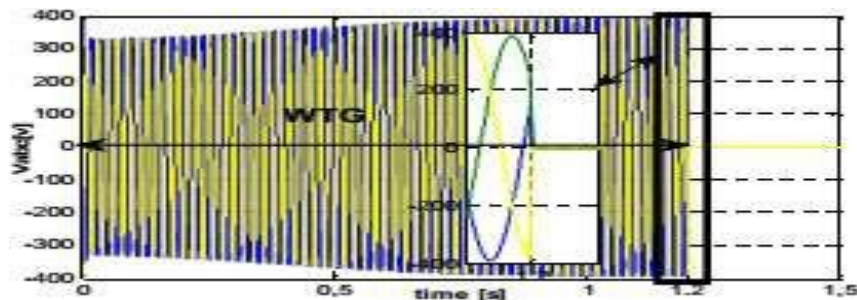


**Figure 10. Three Phase Voltage of the load when WTG operating.**

**A. Case 2-** *DO: Vm <3.5 (m/s)*

The Figure below shows the average active and reactive power generated by the DG,(see Fig.11)
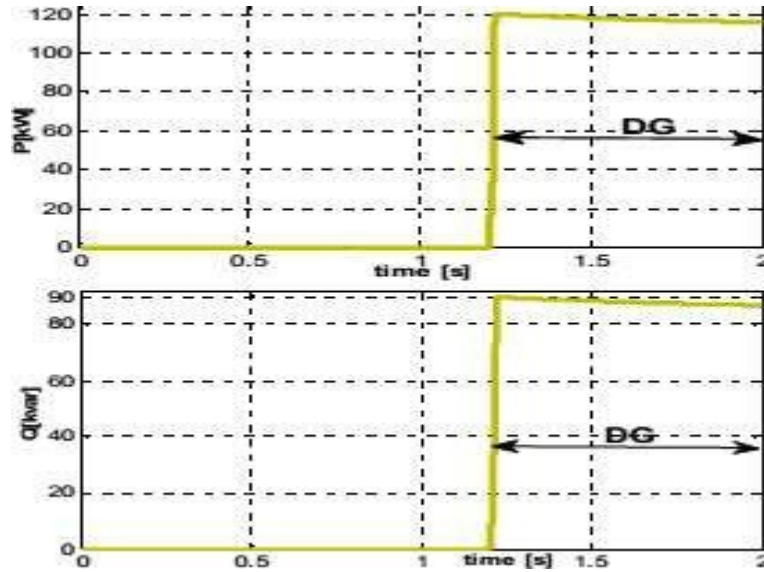
**Figure 11. Active and reactive power generated by DG**

From Fig.11, we see that the power of consumers (P_L) that are alimantés by the electric power generated by DG (DO) view that the wind speed     (*Vm* <3.5m / s) for the time [1.2 s to 2s].
The following figure shows the three phase voltages of the charge (380V) which are fed by DG (DO)
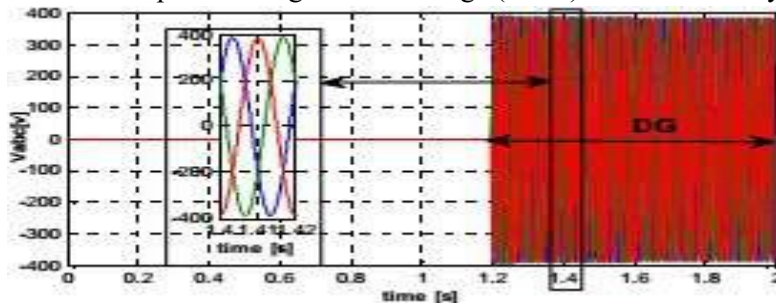


**Figure 12.Three Phase Voltage of the load when DG operating.**

**B.  *Case 3- *** *WD: 3.5 ≤V< 10(m/s)*

Figure 13 shows the timing to be established between the two energy sources (WTG, DG) at t = 1.2s with a wind speed ranging from 3.5 to 10 (m / s).
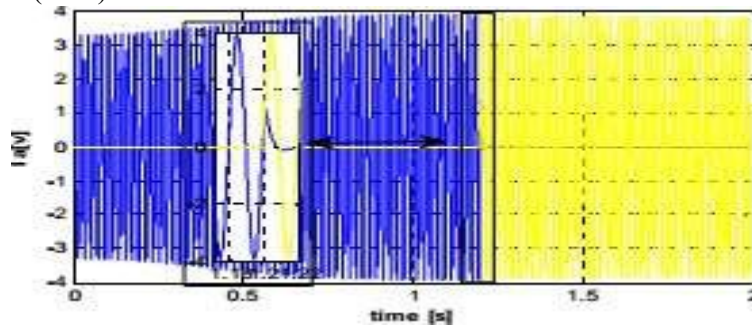


**Figure 13. Voltages produced by DG/ WTG.**

The following figure gives us a general idea about the frequency of the HES system during operation.
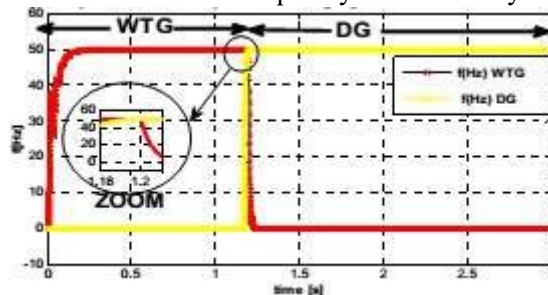


**Figure 14. Overview of frequency**

The following figure shows the amount of fuel saved through the use of a hybrid system (HES) when compared to diesel system (DG)
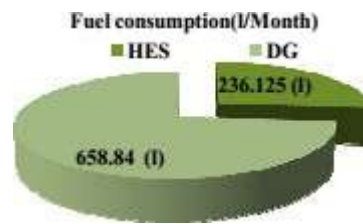


**Figure 15. Gain of the fuel saved**

According to Fig.15, we note that the quantity of fuel consumption is generated by HES **(236.125 *l*)** and vice verses less the DG system **(658.84 *l*)**.Depending on the excellent wind speed where the DG is at rest.

## VIII.   CONCLUSIONS

Through the results obtained; we be conclude the use of the command which adapts this kind of hybrid energy system (HES). We have detailed and presented the modelling of the different sources of the system (WTG, DG, storage battery''BESS") and the service of rotational speed of the turbine by optimal control MPPT(Maximum Power Point tracking) ensuring of operation of the hybrid system. The analysis of the results of this article enabled us to obtain a technical-economic gain in fuel and longevity of the generator, without forgetting to mention the ensurance of continuity of service and the elimination of a portion of the green house gas effect when operating in wind

## REFERENCES

[1] S B. Benlahbib,F.bouchafaa,N. Bouarroudj,B. Batoun ,"Aerodynamic Power Forecasting In Order To Enhance Wind Farm Supervision ADRAR Station in South Algeria",Journal of Electrical Engineering, Vol 15, issu e4, pp211-220,2015.

[2] K. Messaitfa, T. Chergui , "water, energy and the wind through the region of Adrar, Algeria".

[3] Site:http://www.energiepositive.info/fr/pourquoi/energies-fossiles.html.

[4] Kamal E, Koutb M, Sobaih A A, Abozalam B."An intelligent maximum power extraction algorithm for hybrid wind-diesel storagesystem" International journal of Electrical Power & Energy Systems, 2010,32(3): 170–177.

[5] H. Ibrahim, R. Younès, T. Basbous, A. Ilincac, and M.  Dimitrova "Optimization of diesel engine performances fora hybrid wind diesel system with compressed air energy storage" , Energy, vol.36, 3079-3091,2011.

[6] M. I. Marei, and H. S. K. El-Goharey,"Modeling and Dynamic Analysis of Gearless Variable-Speed Permanent Magnet Synchronous Generator Based Wind Energy Conversion System", International Conference on Renewable Energies and Power Quality,(ICREPQ'12), Santiago de Compostela (Spain), 28th to 30th March, 2012.

[7] T. Kranthi Kumar, Asha Tulasi, Smaranika Swain "Hybrid Wind Diesel Energy System Using Matlab Simulation" *International Journal of Engineering Science and Innovative Technology (IJESIT)*Vol 2, Issue 5, September 2013.

[8] V, Singh, Blending wind and solar into the diesel generation  market, *Renewable Energy Policy Project*, no. 12, 2011.

[9] K.H.Kim,T.L.Van,D.C.Lee,S.H.Song and E.H.Kim,"Maximum Output power Tracking Control in Variable speed Wind Turbine Systems considering Rotor Inertial Power",*IEEE Transactions On Industrial Electronics*,Vol 60,No 8,pp 3207-3217,2013.

[10] BOSSOUFI, Badre, KARIM, Mohammed, LAGRIOUI, Ahmed, *et al.*Backstepping control of DFIG generators for wide-range variable-speed wind turbines. *International Journal of Automation and Control*, 2014, vol. 8, no 2, p. 122-140.

  S.M. Boudia, "Optimisation de l'Évaluation Temporelle du Gisement Énergétique Éolien par Simulation Numérique et Contribution à la Réactualisation de l'Atlas des Vents en Algérie", Thèse de Doctorat. Université de Tlemcen, 2013

# Two phase flow of nanofluid in minichannels

BOUDOUH Mounir [#1], SAIDANI Noureddine2

[#]*University of Batna 2, Faculty of technology,LESEI Laboratory,  RN3 Fessdis 05078 ALGERIA*

```
Email 1 – m.boudouh@univ-batna2.dz
Email 2 – n.saidani@univ-batna2.dz
```

*Abstract*— **An experimental study of convective boiling heat transfer of water flowing in minichannels at low flow rate is carried out with pure de-ionised water and copper-water nanofluids. A low concentration of copper nanometer-sized particles was used to enhance the boiling heat transfer. The aim is to characterize the surface temperature as well as to estimate the local heat transfer coefficients by using the inverse heat conduction problem IHCP. The inlet water temperature is fixed at 60°C and mass fluxes operated in range of 212–573 kg/m².s in minichannels of dimensions 500×2000 µm². The maximum heat flux investigated in the tests is limited to 7000 W/m². The results show that the surface temperature and the local heat transfer coefficient are dependent on the axial location and the adding of copper nanoparticles can significantly improve the heat transfer.**

*Keywords*— **Two-phase flow, cooling, boiling, local heat transfer coefficient, nano-fluid.**

## I. INTRODUCTION

The cooling process based on miniaturization has attracted a great deal of attention in many applications; one can cite electronic devices, computing technologies and proton exchange membrane fuel cells known as (PEM fuel cells). The comprehension of the main phenomenon related to the evacuation of heat energy peaks has led to a better control and thus has helped to improve the performance of thermal systems. In this context, several research studies have been carried out, in both fundamental and industrial applications. The focus is to guaranty energy efficiency by finding a compromise between rapid high heat dissipation fluxes and cost, in such configurations of two phase cooling in order to ensure compactness, adequate and efficient functionality. The modern cooling process has evolved towards to fluid phase change, which is considered a promising approach compared to classical ones, (air and liquid) especially in fuel cells technology. Indeed, Tome [1] has reported the benefit of the two phase cooling, Garrity et al. [2] has concluded that the use of this method of cooling can be effective in the fuel cell system.

Then it appears in particular that the convective boiling heat transfer in microchannels or minichannels holds great promise to replace air-cooling and water-cooling [3], indeed cooling by ''liquid-vapor'' phase change is an effective solution [4], useful for dissipating a high amount of heat while a uniform system temperature 80-100°C is kept in the case of PEM fuel cells. It has also been noted that cooling systems using a coolant circulating in mini or micro-channels, (micro-ducts) is generally an innovative method which combines efficiency and compactness, (compactness of approximately 20 000 m².m-3) and which allows a better environmental protection, (reduction of coolant fluid amount) and a high thermal dissipation which would reach 20 000 Wm-3 as reported by M. Lallemand [5].

In addition, on the microscale, the effect of gravity forces is surpassed by that of the surface tension forces, i.e., no stratified flow exists if the channel diameter is sufficiently small [6]. The Bond number gives the ratio of these forces for a channel of hydraulic diameter $D_h$:

$$\text{Bo} = \frac{g(\rho_L - \rho_7)D_h^2}{\sigma} \qquad (1)$$

Where $\rho_L$ and $\rho_V$ are respectively, liquid density and vapor density [kg m$^{-3}$], $\sigma$ is the surface tension [N m$^{-1}$] and $g$ acceleration of gravity [m s$^{-2}$].

Cheng *et al.* [7] have proposed a classification of microchannels based on Bond number: (i) microchannel (Bo< 0.05), (ii) minichannel (0.05 < Bo <3), and (iii) macrochannel (Bo> 3), in our case (Bo = 0,089).

Studies have proven that the flow's structure, and therefore the heat and mass transfer laws are significantly altered when the diameter of the channels is reduced to values lower than 3 mm [8]. In the case of boiling in micro-channels, many studies are performed on the visualization of flow regimes [9], in order to study the behaviour of the flow regimes, the extent of pressure drop and the average heat exchange coefficients. However, the critical

heat flux (CHF), or burnout refers to the sudden decrease in the heat transfer coefficient for a surface on which evaporation or boiling is occurring, is a constraint that limits the power increase of operating cooling systems [10], indeed exceeding this heat flux causes the replacement of liquid adjacent to the heat transfer surface with a vapor blanket. This blanket acts as a barrier to heat flow from the heat dissipating device, resulting in possible failure (burnout) of the device and the identification of mechanisms and trigger areas of critical flux appears to be necessary [11] in order to act on the exchange surface and to increase the critical heat flux. In This study, the main interests are the measure of both local temperatures and flux densities in minichannels (application to PEM fuel cells) in order to reinforce the literature by this new laboratory investigation. The local surface temperature and heat flux are determined by solving inverse heat conduction problem (IHCP) using only wall temperature measurements. Experimental results presented in this paper are treated only in steady state. The local heat transfer coefficient of each axial location along the channel length is determined from the local heat flux ($q_{channel,x}$) and local surface temperature ($T_{s,x}$) as follows:

$$h_x = \frac{q_{channel,x}}{T_{s,x} - T_f} \tag{2}$$

where ($T_f$) is the bulk mean temperature, it is equal to saturation temperature ($T_{sat}$) when boiling fluid is in the saturated state. ($q_{channel,x}$) and ($T_{s,x}$) are obtained by solving IHCP. The physical model for solving IHCP is defined in previous work [12].

## II.  EXPERIMENTAL APPARATUS AND PROCEDURE

An experimental bench has been conceived and realized in this context. It is composed of: evaporator, micro pump and heat exchanger, the bench is instrumented with micro-thermocouples and accuracy pressure sensors. Fig.1 show a schematic diagram of the experimental device fully designed to investigate the two-phase-cooling in simulated bipolar-plate of a PEM fuel cell.
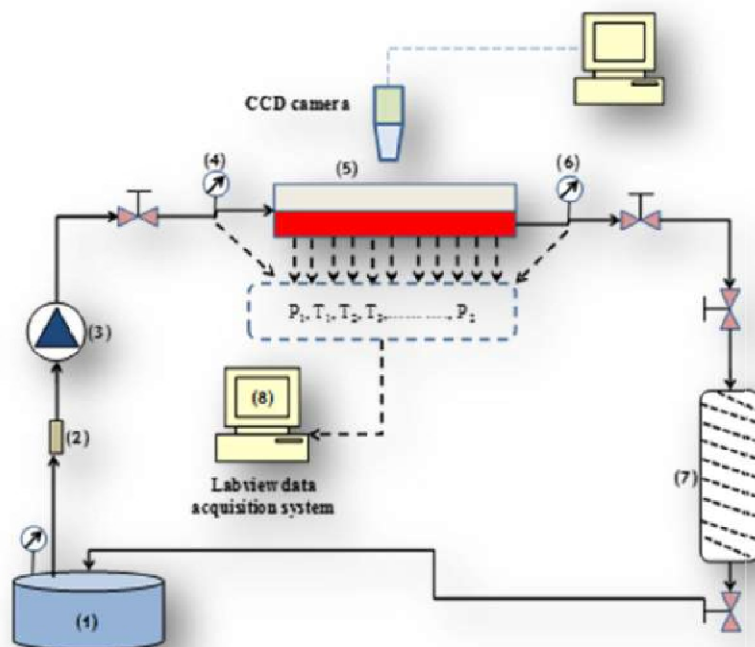


Fig.1. Schematic diagram of the experimental apparatus.

The experimental set up consists of a micro-channels test section (evaporator) and a heat transfer fluid loop. The liquid is pumped from the tank (1) by a magnetic gear pump (3) fitted with a control microprocessor of MCP-Z

standard type. The pump is also used as a flow meter. A 2 mm filter (2) is used to remove dust and micro-particles from the working fluid. The fluid passes from the tank to the test section (5). The mass flux is adjusted within the regulating valves. The working liquid passes through the micro-channels test section to become a vapor and then enters into the heat exchanger (7) where it is cooled before returning to the tank (1). The temperature of the coolant fluid in the tank (1) is controlled using an electrical heater associated with a temperature controller. The test section (the evaporator) is made of a copper plate of 250x250 mm² and 10 mm thick. On one side of the test section, 50 rectangular mini-channels with hydraulic diameter of 800 µm are performed, fig. 2a and fig. 2b. These mini-channels of 160 mm of length are parallel. On the opposite side of the exchange surface, a heating panel of a maximum power density of 7000 W/m² is placed. This panel is equipped with a PT100 sensor which keeps limiting the surface temperature level to 150°C. It distributes heat evenly over the entire surface.
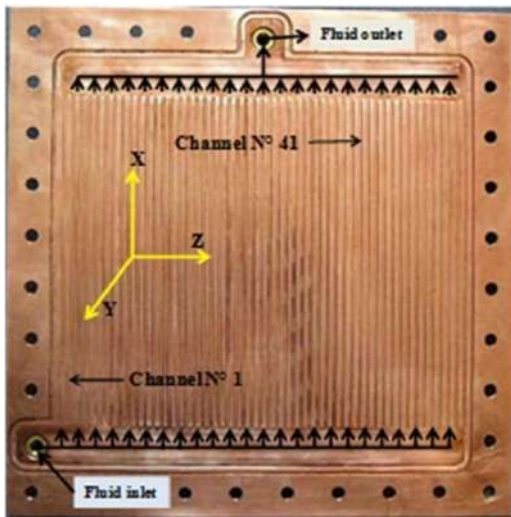


Fig. 2a. Copper plate of the test section.
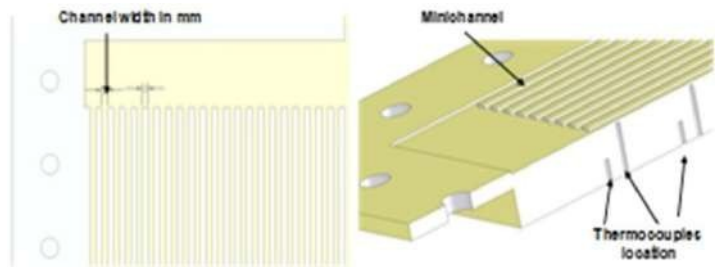


Fig. 2b. Construction of the minichannels in the test section.

A power supply is used to control the power imposed on the surface of the test section. The mini-channel surface is covered by a polycarbonate plate of 8mm thick in order to visualize the coolant during its evolution in the mini-channels. All the plates forming the test section (polycarbonate plate, copper plate and the heater panel) are tightly jointed in a nested set of plates PTFE of 45 mm thick, which serve as a support and a thermal insulator. Chromel-Alumel micro-thermocouples (K-type 75 µm) are inserted into holes of 1mm diameter on the back and the side of the plate, microthermocouples calibration is conducted by comparing the temperatures measured by microthermocouples and a precision sensor probes (±0.03°C). The calibration procedure consists to maintain the microthermocouples at a known temperature through a precision sensor probe and to record the microthermocouples responses using a labview data acquisition system. The procedure is repeated for different known temperatures. Two mini-channels are instrumented by micro-thermocouples as shown in fig. 3a. Furthermore, two micro-thermocouples are placed at the inlet and outlet of the test section in order to measure the inlet and outlet temperature of the fluid. Two pressure sensors (4) and (6) Omega PX209 (0.25 % of accuracy) are installed to measure the total pressure loss in the test section. The data acquisition is fully automated using the"Labview" software and "National Instruments" hardware (8) which allows measurements in real time. Two mini-channels have been instrumented by micro-thermocouples that are inserted in the copper plate at different depths and different positions fig. 3b along the length of the channels.
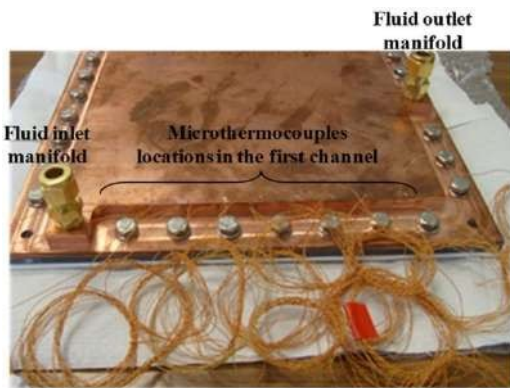
Fig. 3a. Bottom side of copper test plate.
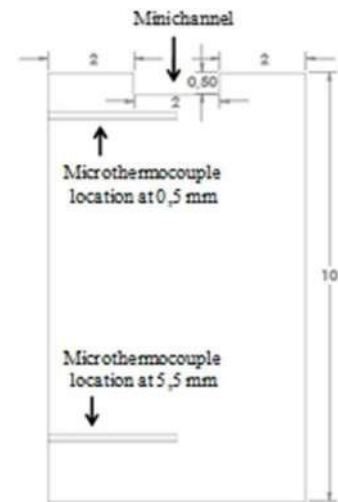


Fig. 3b. Thermocouples locations in the first minichannel

The first instrumented channel (channel 1) is located at 2 mm from the edge of the test section, near the inlet of the coolant. The second one (channel 41), situated near the outlet of the fluid, is located at160 mm from the edge of the test section. The micro-thermocouples are arranged at two or three levels deep from the exchange surface. Thus, for the first channel, 21 micro-thermocouples are placed at 0.5 mm, 5.5 mm and 8 mm from the exchange surface. However, 17 micro-thermocouples are placed at 0.5 mm and 5.5 mm from the exchange surface for the second channel. These micro-thermocouples allow us to measure the temperature at different depths of the plate.

## III. RESULTS AND INTERPRETATION

An experimental procedure is carried out to check the replicate results. Prior to testing, the micro pump flow is made constant and the power output is set to a maximum of up to 280 W in order to activate boiling. Once this latter is reached, power is then reduced by decrements of 20 W, while recording the system temperatures and pressures.

*1) Wall temperatures measured in steady and unsteady state*

During trials, the temperature time change of the two wall channels 1 and 41 are measured. The test is conducted for a total flow rate of 35 mL/min and a supply power of 200 W. Fig. 4a, 4b show the temperature time change for temperatures values given by micro-thermocouples placed at 0.5mm from the surface exchange for channels 1 and 41.
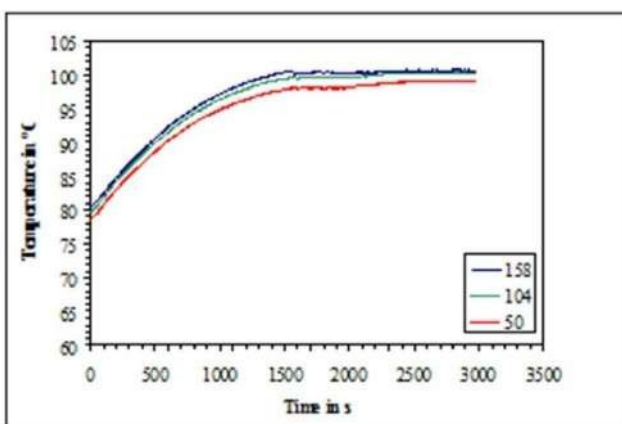


Fig. 4a. Wall temperature measured for channel 1.
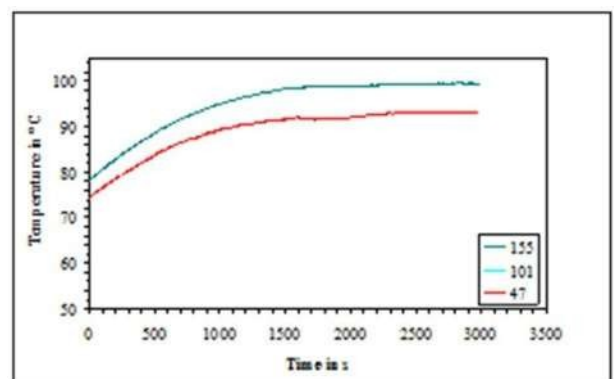


Fig. 4b. Wall temperature measured for channel 41.

These changes are related to both abscissas x = 47mm and x = 155mm for channel 1 and to both abscissas x = 22mm and x = 148mm for channel 41. For readability reasons, only two curves are presented in these figures because the behavior is comparable to that obtained by curves given by other micro-thermocouples placed in the wall. Under transient conditions, the temperatures increase continuously with substantially the same temperature change with respect to time. In steady state, temperatures stabilize and become substantially constant over time. It is noticed during testing that at given positions of the channel outlet (x = 148mm for the channel 41 and x = 155mm for channel 1), the flow is composed of large pockets of bubbles which occupy a large part of the channel. This latter observation explains the rapid increase in temperature in the specified area Fig. 4b shows the difference between the inlet and outlet temperatures. For channel 41, the difference is about 6°C in steady state, whereas, this difference is much lower in the case of channel 1, a gap of about 2°C is noticed in steady state. These temperature variations are due to the two phase flow structure in each channel that is mainly dependent upon flow rate and channel 1 is close to the entrance and the water flow in this channel is probably more important than that in other channels. In order to confirm this, the plate temperature is measured by an infrared camera as shown in fig. 5. This fact explains that the temperatures recorded in this channel are lower than those recorded in channel 41. Fig. 6 illustrates these temperature differences and shows the distribution of wall temperatures in both channels, in steady state for total flow rate. In the case of channel 1, and at the entrance of the channel, the temperatures difference of the wall measured at 0.5mm and 8mm from the exchange surface is more pronounced than that recorded at the outlet channel.
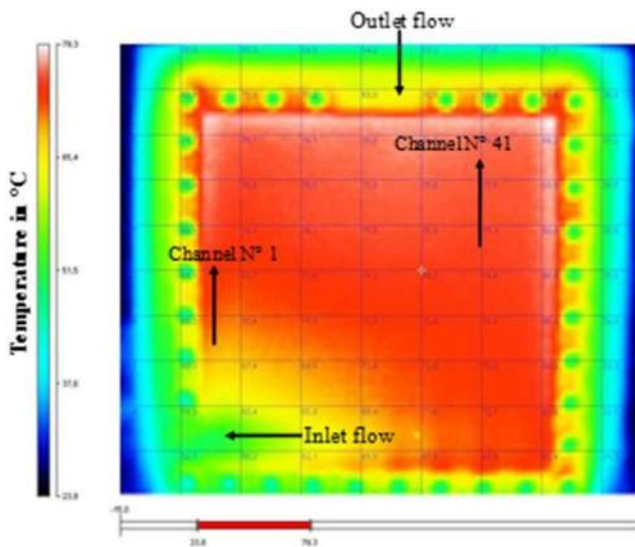


Fig.5. Temperature distribution measured with infrared camera.
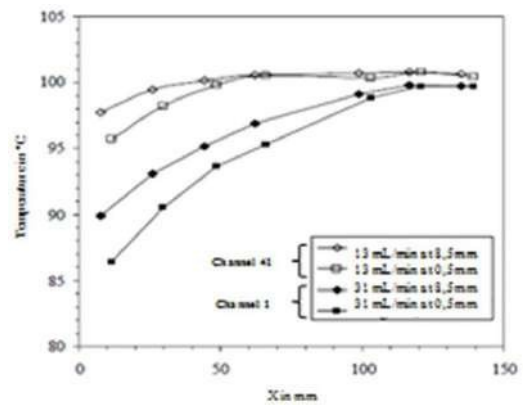


Fig. 6. Wall temperature distribution in steady state.

Along on the flow direction, the difference of temperatures of the wall decreases as far as we move away from the channel inlet where the coalescence phenomena are amplified.

This amplifies the thermal resistance between the fluid and the wall. This latter becomes less and less wetted by the liquid and the dispersed flow should tend towards a minimum value. Fig. 7 shows a typical pressure signal given by the pressure sensor located at the inlet of the test section. In the steady state the total pressure drop is 2000 Pa, fig. 8 shows the time variation of the pressures drop of the test section and it is found that the evolution of the pressure follows exactly that of the temperature as we can see in fig. 9. Other tests are conducted for power supplies of 180, 190, 210 and 230 W and for total flow variants of 20 mL/min to 36 mL/min with an increment of 1mL/min.

IV.
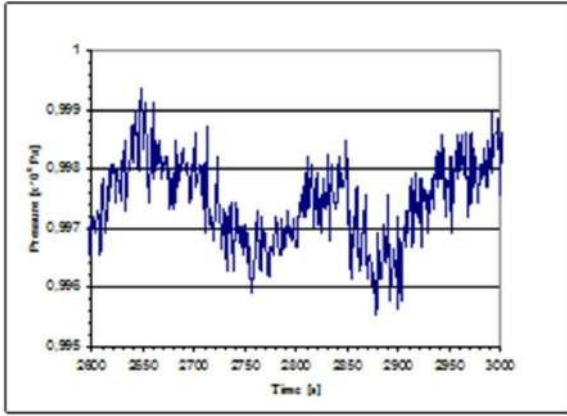
Fig. 7. Inlet typical pressure signal.          Fig. 8. Temporal variation of pressure drop.
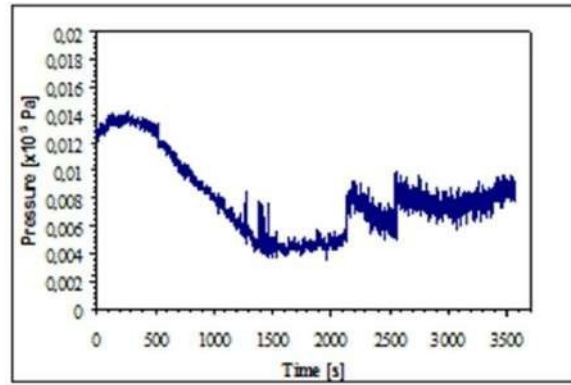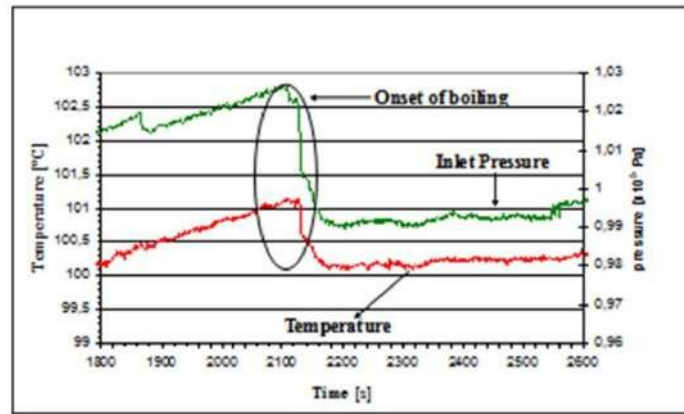


Fig. 9. Temporal variation of temperature and inlet pressure.

The shape of the curves is comparable to those presented in fig. 8 and fig. 9. The maximum temperatures recorded are always located at the outlet region of the plate because of the upward flow of bubbles which is more pronounced in the upper part of the channel than that in the lower one. Another cause is the warming of the liquid during its passage through the mini-channel. The bubble rise increases the bubbles concentration and the void rate.

### 2) Local heat transfer coefficients in steady state

Tests treated in some articles [13] have proved the benefit of nano-fluids for heat transfer enhancement,that's why these same tests are carried out here using pure dionized nano-fluid with copper nano-particles of 35 nm prepared carefully in a clean room. The concentrations of tested particles are 5 mg/L and 10 mg/L. To avoid the agglomeration of particles, an ultrasonic agitator was used. The measured electrical conductivity of nano-fluid is 4.8 µS /cm. Fig. 10a and fig.10b show respectively the changes in wall temperatures for pure water and for the nano-fluid (water loaded with nano-particles of Cu). The results presented by these two figures are obtained for a flow rate of 28 mL/min and an imposed power of 200 W.
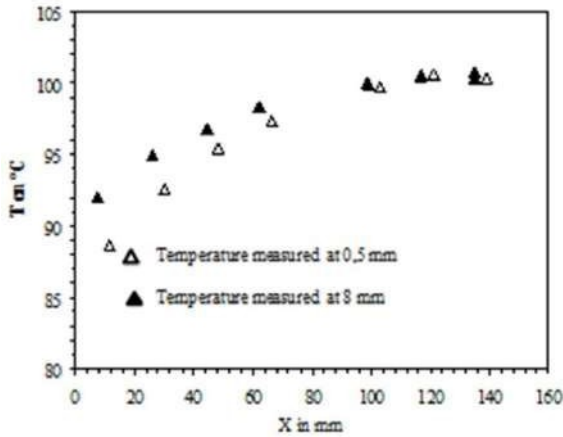
Fig. 10a. Wall temperature measured
(water cooling) channel 1.
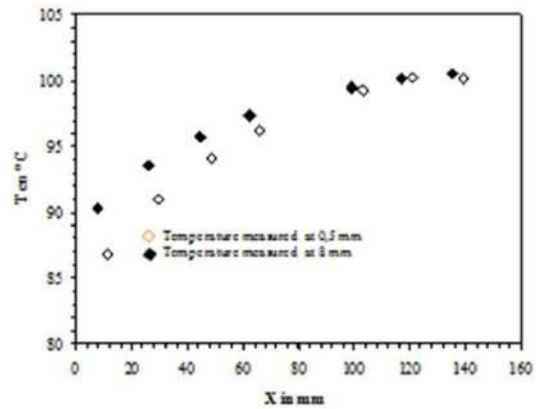


Fig. 10b. Wall temperature measured
(nanofluid cooling) Channel 1

The temperatures shown by both fig. 10a and fig. 10b are recorded in the channel 1. A slight decrease in wall temperatures is noticed using the cooling nano-fluid. This is due to the presence of copper nano-particles of thermal conductivity of 389 W/m.K which improve the heat dissipation of the wall. To quantify the effect of nano-particles on the local heat transfer coefficients, the results of measurements are treated using the inverse technique, detailed in previous work [12]. Based on the measured temperatures within the wall this technique allows the estimation of thermal conditions at the exchange surface. The used physical model takes into consideration a flat plate thermally isolated with PTFE on both of its surfaces except that which is cooled by boiling. On this surface lie the estimating parameters, namely the heat flux and surface temperature. The surface on the opposite side of the exchange surface is subjected to a known heat flux density (assessed value during the experiment). The physical model is two dimensional. The solving procedure of the inverse problem is based on the minimization of the residual function, expressed in terms of measured temperatures and those estimated by solving the direct problem. Fig.11 shows curves of the surface temperatures measured in steady state for the pure water and the nanofluid. For a same flow rate and a same imposed power, surface temperatures, during cooling by the nano-fluid, are lower than those estimated by using pure water. The variance between the temperatures of water and nano-fluid does not exceed 2.5°C at most.
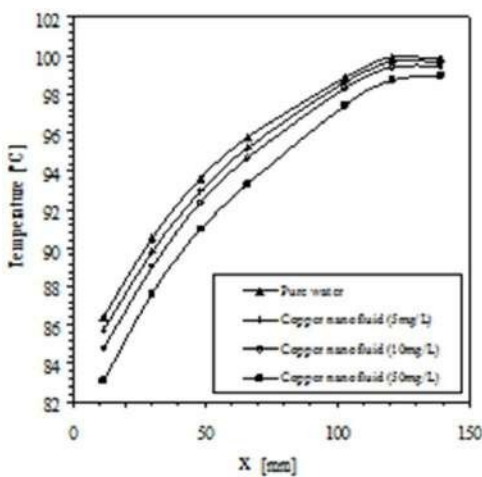


Fig. 11. Wall temperatures measured
at 0.5mm below the heat transfer surface.
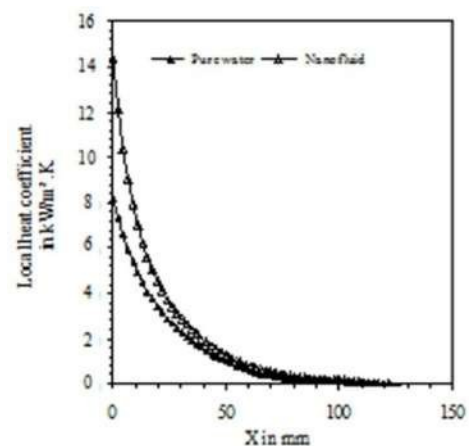


Fig. 12a. Local heat exchange coefficients.

This maximum is observed at the inlet channel. Fig.12a shows the evolution obtained for the local heat transfer coefficients. These exchange coefficients are calculated for each abscissa 'x' from the heat flux density dissipated locally in the channel and the local temperature of the heat exchange surface. The results confirm that the heat transfer rate obtained by the nano-fluid is better than that obtained by pure water. An improvement in heat transfer rate of about 40% toward the inlet channel is noticed. Fig.12b. shows the effect of copper nanoparticles concentration on the enhancement of the local heat transfer coefficients estimated inversely using equation 2. It is shown that the heat transfer coefficient enhancement increases with the copper nanoparticles concentration at low concentration of nanoaparticles. Indeed at high concentration of nanoparticles it is shown that the nanoparticles agglomerates. Fig.14 shows the results of the inverse-heat-conduction-problem (IHCP) analysis applied to the test section which enabled the evaluation of thermal boundary conditions, the surface temperature and the heat flux.
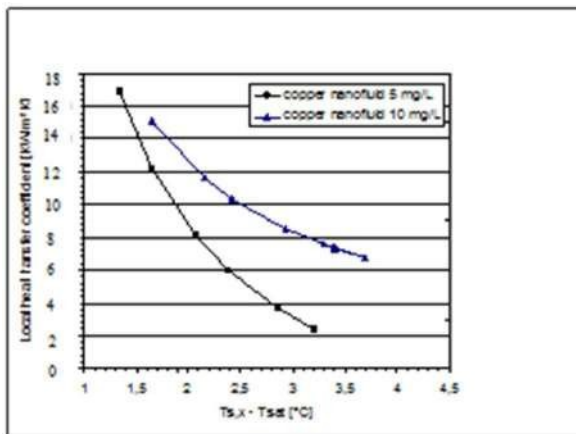


Fig. 12b. Effect of copper nanoparticles concentration on local heat transfer coefficients measured for a power supply of 200 W
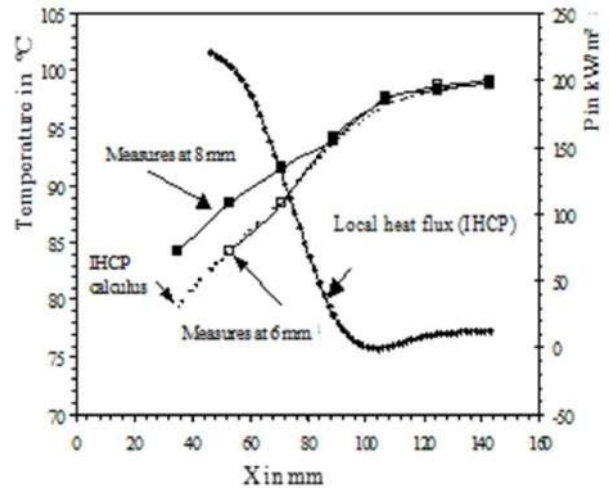


Fig. 13. Local heat flux and surface temperature

IV. CONCLUSIONS

This paper presents experimental results of a study of the phase change cooling using forced convection flow in mini-channels.

Our prototype is designed to simulate PEM fuel cells cooling. Several flow rates and powers were tested, leading to a distribution of wall temperatures which is mainly related to the flow structure and the cooling flow. The main findings can be drawn as follows:

- The amount of dissipated heat is very large in comparison to the very small amount of water used hence the interest of the two-phase cooling in mini-channels.
- It is noteworthy that heat transfer coefficients associated with boiling are typically much higher than those encountered in other forms of convection processes that involve a single phase.
- The nanofluid shows higher local heat transfer coefficient and lower surface temperature than its base fluid at the same mass flux because the copper nanoparticles contribute to increase heat transfer locally and accelerate the onset boiling.
- it is recommended to well choose the inlet and outlet port of fluid, in order to have an axisymmetric temperature distribution in the test section.

REFERENCES

[1] J.R. Thome, 2004, ''Boiling in microchannels: a review of experiment and theory'', Internationa Journal of Heat and Fluid Flow 25, 2: 128–139.
[2] P.T. Garrity, , et al., 2007, ''A flow boiling microchannel evaporator plate for fuel cell thermal Management'', Heat Transfer Engineering 28, 10: 877–884.

[3]    , J.Lee, . Mudawar, 2005, '*'Two-phase flow in high-heat flux micro-channel heat sink for refrigeration cooling applications: Part II-heat transfer characteristics''*, International Journal of Heat and Mass Transfer *48*, 5: 941–955.

*[4]*    M.B. Bowers, I. Mudawar., 1994, '*'High-flux boiling in low-flow rate, low-pressure drop mini-channel and microchannel heat sinks''*, International Journal of Heat and Mass Transfer *37*, 2: 321-332.

[5]    M. Lallemand,  2004, ''Report integrated research project 8.2'', Energy Program, France.

[6]    V. Dupont, J. R. Thome, J, 2005, *''Evaporation in microchannels: influence of the channel diameter on heat transfer''* Microfluidics and Nanofluidics 1, 2: 119–127.

[7]    P. Cheng, *et al.*, 2007, *''Phase-change heat transfer in microsystems''*, Journal of Heat Transfer, 129*, *2: 101-107.

[8]    T. Harirchian, S. V. Garimella, 2009, *''Effects of channel dimension, heat flux, and mass flux on flow boiling regimes in microchannels''*, *International Journal of Multiphase Flow 35*, 4: 349–362.

[9]    S. G. Kandlikar, *et al.*, 2005, *''Experimental evaluation of pressure drop elements and fabricate nucleation sites for stabilizing flow boiling in minichannels and microchannels''*, Proceedings, 3rd international conference on microchannels and minichannels, Canada,.

[10]    G. M. Lazarek, S. H. Black, 1982, *''Evaporative heat transfer, pressure drop and critical heat flux in small vertical tube with R-113''*, *International  Journal of Heat and Mass Transfer 25*, 7: 945- 960.

[11]    D. D. Hall, I. Mudawar, 2000, *''Critical heat flux (CHF) for water flow in tubes-I. Compilation and assessment of world CHF data''*, International Journal of Heat and Mass Transfer 43, 24: 2573-2604.

[12]    H. Louahlia-Gualous, *et al.*, 2004, *''The inverse estimation of the local heat transfer coefficient in falling film evaporation''*, Inverse Problem in science and Engineering Journal *12*, 1: 29-43.

[13]    M. Boudouh, M., *et al.*, 2010, *''Local convective boiling heat transfer and pressure drop of nanofluid in narrow rectangular channels''*,  *Applied Thermal Engineering 30*, 17-18: 2619-2631.

# A nano hexagonal terahertz antenna for medical application

Bouchra Moulfi[#1], Souheyla Ferouani [*2], Ziani Kerarti Djalal [*#3], Moussa Fatima Zahra[#4]

[#] *Department of Electronic and Telecommunications, University of Ain Temouchent ,*
*SSL laboratory of Ain Temouchent, Algeria.*

[*] *Department of Electronic and Telecommunication , University of Ain Temouchent,*
*LTT laboratory of Tlemcen,Algeria..*

[*#]*Department of post-graduated and specialities ,National institute*
*of Telecommunications and ICT of Oran,Algeria.*

[1]bouchra.moulfi@univ-temouchent.edu.dz
[2]souheyla.ferouani@univ-temouchent.edu.dz
[3]DZIANIKERARTI@INTTIC.DZ
[4]fatima.moussa@univ-temouchent.edu.dz

*Abstract*— **In this paper , we will designing a nano terahertz hexagonal antenna for very small biomedical applications radiating in two different frequencies using different type of substrate materiel such as polyimide ($\varepsilon$r =3.5)roger RO3003 ($\varepsilon$r =3), roger RO4003C ($\varepsilon$r =3.55) and Quartz ($\varepsilon$r =3.75).The best result obtained by Roger RO4003C($\varepsilon$r =3.55)substrate the antenna resonates in two deferent frequency 0.825 THz and 0.972 THz with hight Gain of 7.268 dBi and 7.703 dBi respectively. Thus, The proposed antenna can be used in the THz region for medical application.**
*Keywords*— **Medical application ; Terahertz region ; nano antenna ; Terahertz antenna ; Hight Gain ; Instructions.**

## I. INTRODUCTION

Telemedicine is a medical technique that uses information and communication technologies to deliver medical services to patients at a distance. It provides a platform for patients to consult medical professionals[1], obtain diagnoses, medical advice and even treatment, without having to physically visit a medical treatment facility[2]. Telemedicine uses different communication methods[3], such as video calls, telephone calls, e-mail messages and mobile applications, to enable remote consultations. Medical professionals can examine symptoms, ask questions, interpret test results, provide recommendations and even prescribe medication if necessary[4].

Biomedical antennas are essential devices in the field of medicine and healthcare for the transmission and reception of wireless signals for diagnostic or diagnostic-therapeutic purposes[5]. They are designed to be integrated into medical devices such as implants, sensors or portable monitors[6]. These biomedical antennas can operate at different frequencies, depending on their specific application. For example, some biomedical antennas are designed to operate in the radio frequency range[7][8], while others can use higher frequencies, such as microwaves[9].
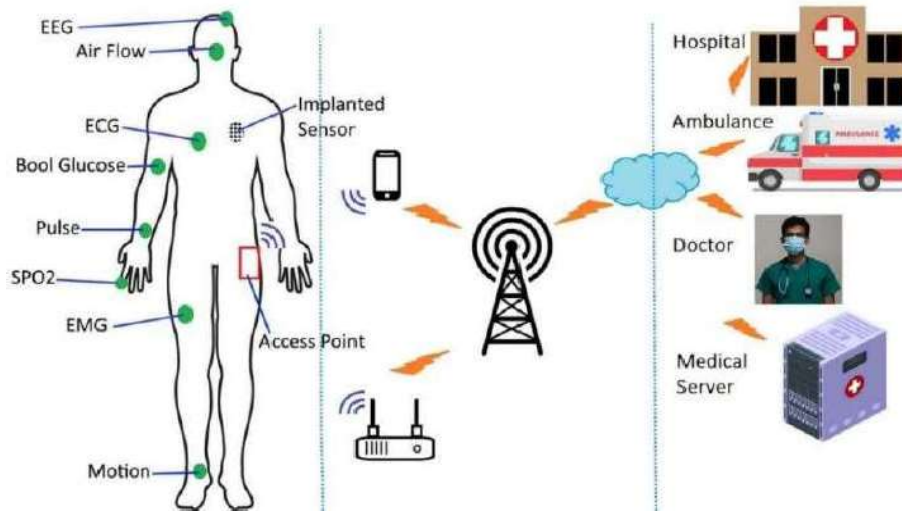
FIg 1 The biomedical application antenna .

It should be noted that the design of biomedical antennas must consider a number of factors, such as bio-compatibility, small size, transmission efficiency and resistance to interference[10]. These aspects are essential to ensure reliable and safe operation of these devices in a medical environment. The size of the terahertz antenna is a crucial factor influencing its performance and efficiency[1]. Terahertz antennas are designed to operate in the terahertz frequency range, which is situated between radio and infrared frequencies. In  terahertz antenna design, size is directly related to operating wavelength. Terahertz waves have a relatively short wavelength, on the order of a few hundred micrometers to a few millimeters[11]. Consequently, terahertz antennas need to be sized accordingly to achieve maximum performance.

In this work we will design a nano hexagon antenna for biomedical applications wide a very small size radiating in two different frequencies using polyimide($\epsilon$r=3.5) substrate, to further increase performance the antenna is simulated with different type of substrate roger RO3003($\epsilon$r =3) , roger RO4003C($\epsilon$r =3.55) and Quartz($\epsilon$r =3.75).


II.  PROPOSED HEXAGONAL ANTENNA DESIGN


with the help of CST software, we designed a hexagon terahertz antenna with 50 Ohm impedance, fed by a microstrip line. The materiel used for ground plane and the radiating element called the patch is the gold, We used polymide($\epsilon$r=3.5) for material substrates with a thickness h=9 μm (fig1) . The dimensions of the patch antenna are calculated from the equations[12]:

$$w = \frac{3*10^8}{2*fr*10^{12}*\left(\frac{eps+1}{2}\right)^{0.5}}$$  Eq.1

$$L = \left(\frac{3*10^8}{2*fr*10^{12}*(epseff)^{0.5}}\right)*10^6 - (2*\Delta l)$$  Eq.2

$$Wg = w + 6*h$$  Eq.3

$$Lg = ll + l + 6*h$$  Eq.4

where h:substrate thickness ,fr : the resonant frequency, ll:the length of the line,Lg: length of both ground plan and substrate, Wg: width of both substrate and ground plane .
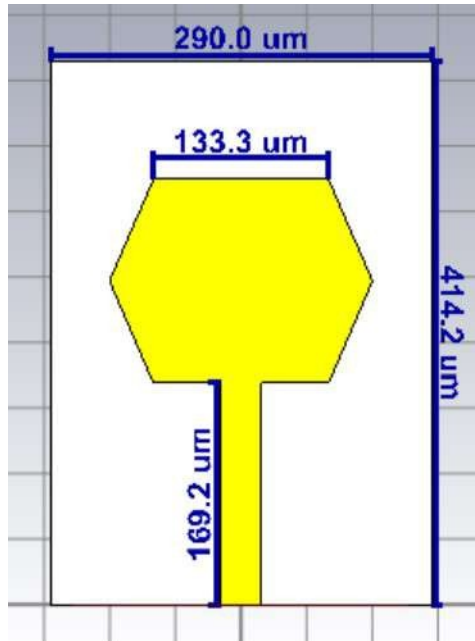
FIg 2 Proposed Nano hexagon patch antenna.

A. *Simulation and result of hexagon antenna with polymide substrate materiel*

Simulation results for the proposed nano hexagon antenna with polymide substrate ($\epsilon$r=3.5) are summarized in the figure 4 figure 5 figure 6 and figure 7 .
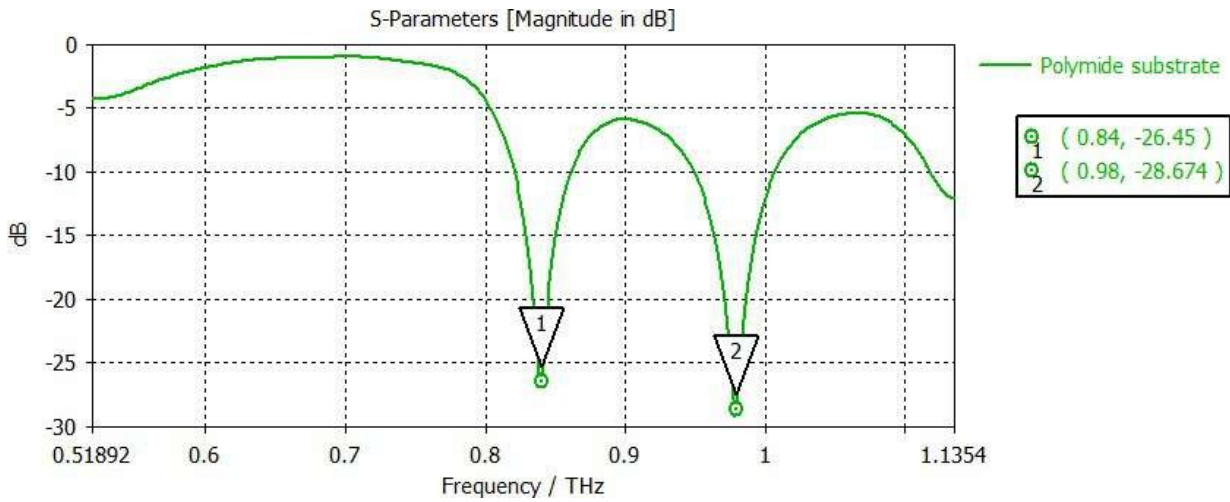


FIg 3 The Reflection coefficient parameter of the proposed nano hexagon antenna with polymide substrate.
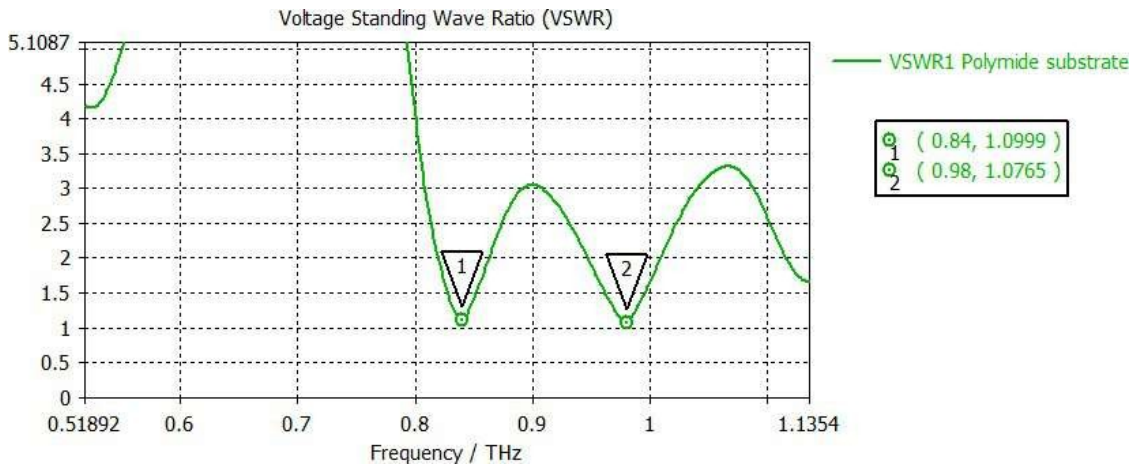
FIg 4 The VSWR parameter of the proposed nano hexagon antenna with polymide substrate.
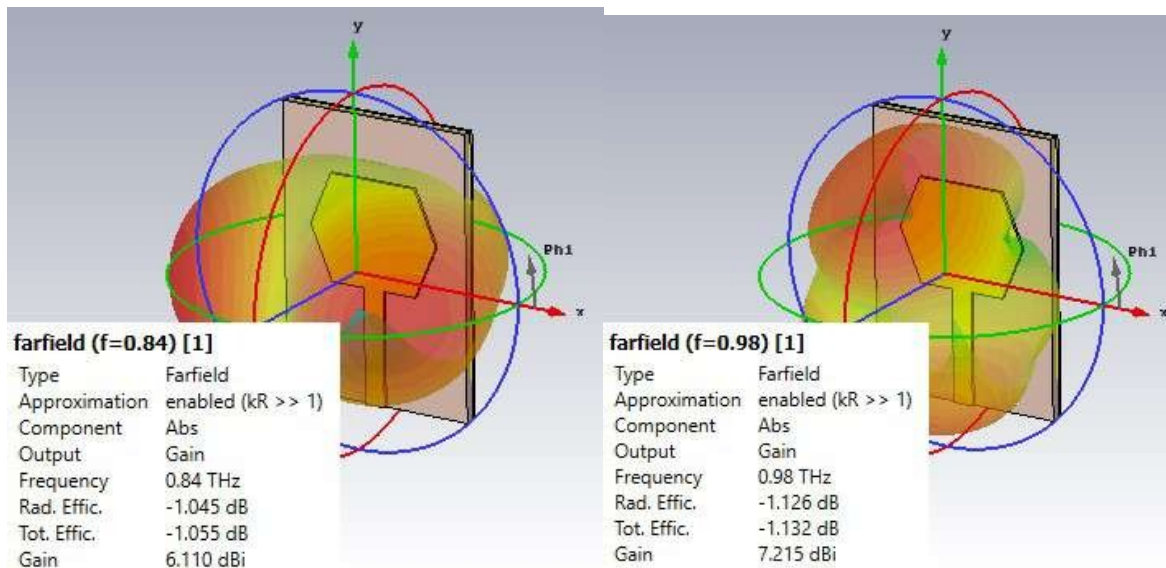


FIg 5 The 3D Gain parameter of the proposed nano hexagon antenna with polymide substrate.
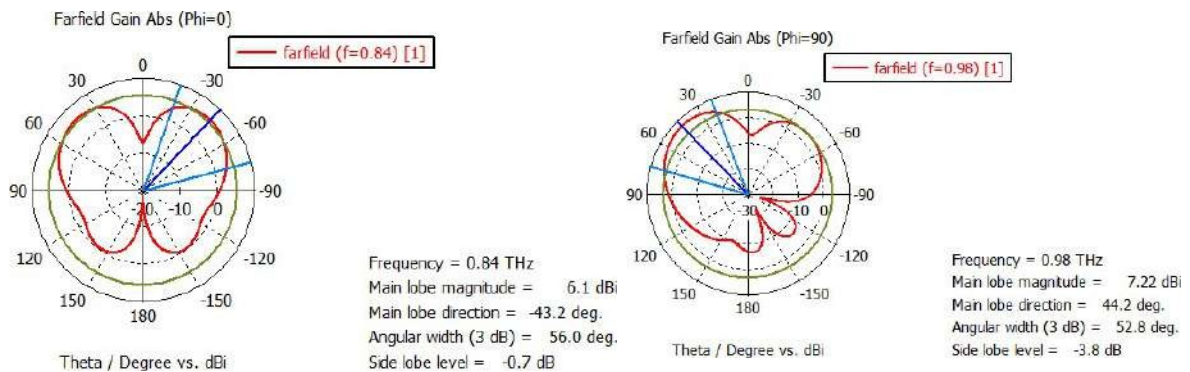


FIg 6 The polar Gain parameter of the proposed nano hexagon antenna with polymide substrate.

We have seen in figure 2 we will obtained by polymide substrate tow different frequency 0.83 and 0.979 with a return loss of -24.264 and -34.976 respectively , the figure 5 show that this frequency have Voltage Standing Wave Ratio(VSWR ) less to 2 means that there is no reflection of energy and that the antenna impedance is perfectly adapted.

B. *Simulation and result of hexagon antenna with different type of substrate materiel*

There are various other substrates that can be employed while keeping the shape of a gold patch antenna the same, such as polyimide($r$ =3.5), roger RO3003($r$ =3) , roger RO4003C($r$=3.55) and Quartz($r$ =3.75). These substrates have varying electrical characteristics the figure 8,9,10,11 show a result obtained for studying the substrate effect antenna.
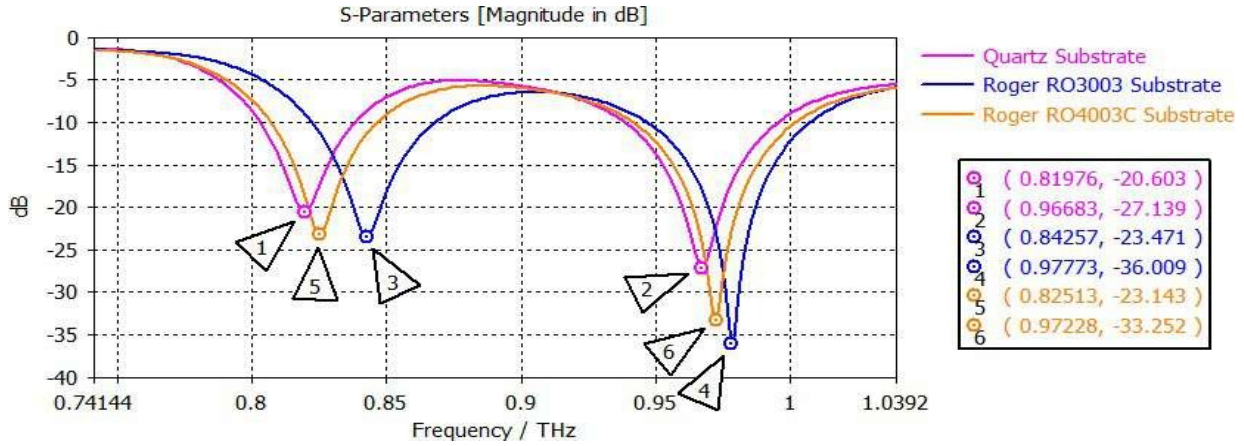


FIg 7  Reflection coefficient parameter S11 of proposed  nono hexagon antenna  for deffirent types of  substrates.
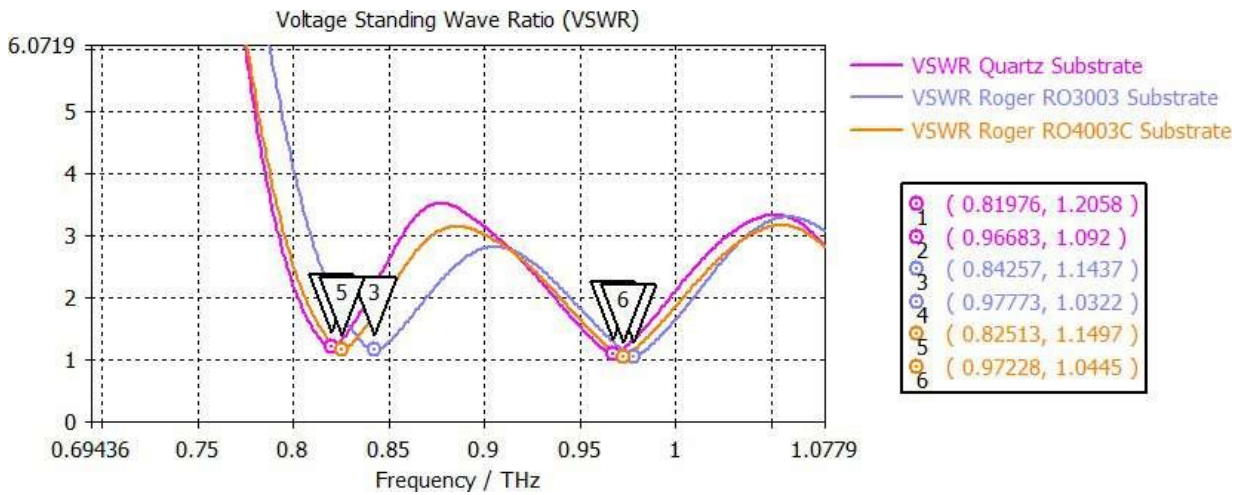


FIg 8 VSWR  of proposed  nono hexagon antenna  for deffirent types of  substrates.

As shown in Figure 8, changing the  material substrate produce a variety of frequencies 0.819 THz  and 0.966 THz with -20.603 dB and -27.139 dB by Quartz substrate , 0.842 THz and 0.977 THz with -23.471 dB and -36.009 dB by Roger RO 3003 substrate and 0.825 THz and 0.972 THz with -23.143 dB and -33.252 dB by Roger RO 4003C substrate , all these frequencies are very well adapted are VSWR less than 2.
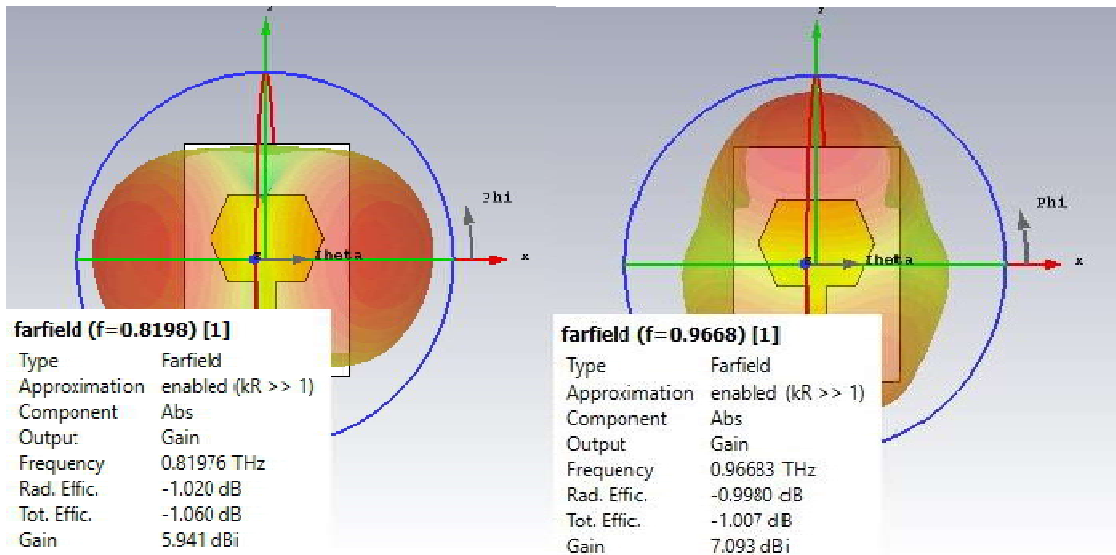
FIg 9 2D Gain of proposed nano hexagon antenna for Quartz substrates.
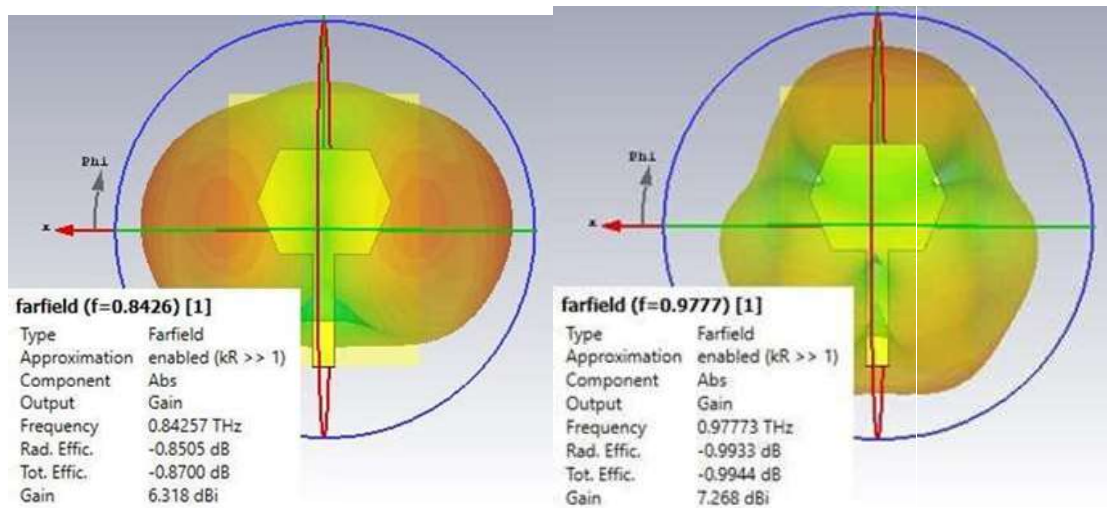


FIg 102D Gain of proposed nono hexagon antenna for Roger RO3003 substrates.
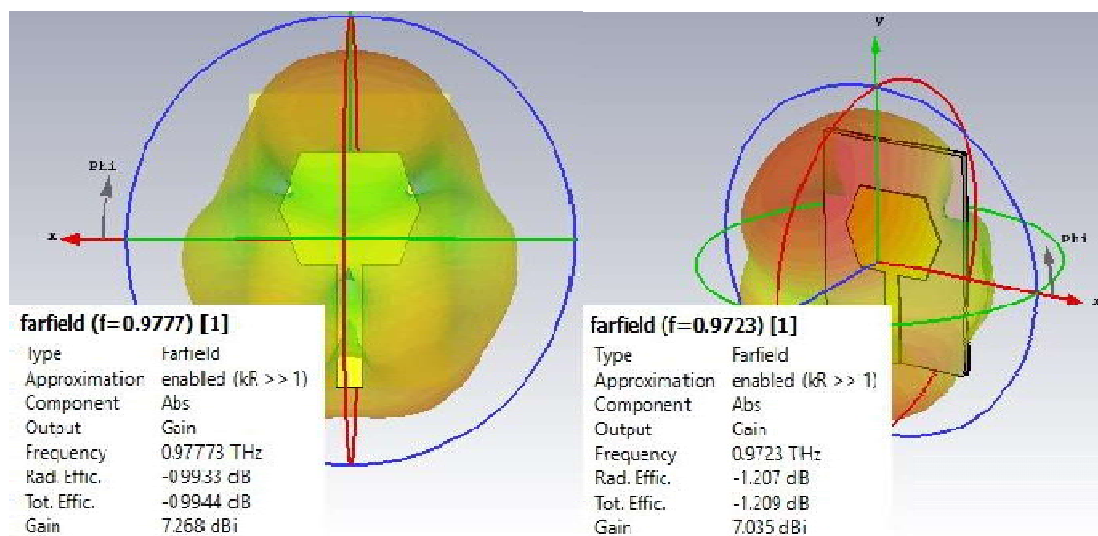


FIg 11 2D Gain of proposed nono hexagon antenna for Roger RO4003C substrates.

III. COMPARISON OF RESULTS WITH OTHER SUBSTRATES

TABLE I
COMPARISON OF RESULTS WITH OTHER SUBSTRATES

| | Substrate | Frequancy (THz) | S11(dB) | Gain (dBi) | VSWR |
|---|---|---|---|---|---|
| Proposed nano hexagone antenna | Polymide($\varepsilon_r$=3.5) | 0.84 0.98 | -26.45 -28.674 | 6.11 7.21 | 1.130 1.036 |
| | Quartz($\varepsilon_r$=3.75) | 0.819 0.966 | -20.603 -27.139 | 5.941 7.093 | 1.205 1.092 |
| | Roger RO3003($\varepsilon_r$=3) | 0.842 0.977 | -23.471 -36.009 | 6.318 7.268 | 1.143 1.032 |
| | Roger RO4003C($\varepsilon_r$=3.55) | 0.825 0.972 | -23.143 -33.252 | 7.268 7.703 | 1.149 1.044 |
| [13] | Roger RO4003C ($\varepsilon r$ = 3.55) | 0.740 1.148 1.734 | -41.408 -43.918 -29.2 | 5.32 6.21 4.815 | 1.0156 1.0146 1.0683 |
| [10] | Silicon($\varepsilon r$=11.9) | 3.930 | -54.96 | 5.4 | 1.0036 |
| | Duroid 3210($\varepsilon r$=10.8) | 4.010 | -63.1 | 5.06 | 1.0034 |
| [8] | RT Duriod 6010($\varepsilon r$=10.2) | 0.852 | -20 | 2.5 | Not mentioned |
| [14] | Quartz($\varepsilon_r$=3.75) | 1.02 | -28.76 | 1.44 | 1.07 |

Table 1 summarizes all of the results obtained with each substrate and compare them with the various works for medical applications in the terahertz band. The results obtained is very satisfactory, we have a very high gain which is more than 7 dBi.

IV. CONCLUSIONS

In this paper, a nano circular patch antenna operating at terahertz frequencies 0.1 to 10 THz is conceived for WBAN applications. The use of a Roger RO4003Csubstrate ($\varepsilon$r=3.55,h=9 μm) and the gold patch antenna with 6 μm thickness very suitable suitable for medical applications.

The antenna's size is very small with hight gain , this terahertz band is not ionized, i.e. it requires some electron volt it does not affect the human body.

REFERENCES

[1]  [1] T. Hayajneh, G. Almashaqbeh, S. Ullah, and A. V. Vasilakos, A survey of wireless technologies coexistence in WBAN: analysis and open research issues, vol. 20, no. 8. 2014.
[2]  [2] U. Tenaga et al., "WBAN System Organization , Network Performance and Access Control : A Review," IEEE, no. October, pp. 27–28, 2021.
[3]  [3] S. N. Mahmood et al., "Full ground ultra-wideband wearable textile antenna for breast cancer and wireless body area network applications," Micromachines, vol. 12, no. 3, pp. 1–16, 2021, doi: 10.3390/mi12030322.
[4]  [4] E. D. Informatique, E. Ed, and A. Makke, "Thèse Détection d ' attaques dans un système WBAN de surveillance médicale à distance," no. Ed 130, 2014.
[5]  [5] M. Kumar, S. Goel, A. Rajawat, and S. H. Gupta, "Design of optical antenna operating at Terahertz frequency for In-Vivo cancer detection," Optik (Stuttg)., vol. 216, p. 164910, 2020, doi: 10.1016/j.ijleo.2020.164910.
[6]  [6] B. Latré, B. Braem, I. Moerman, C. Blondia, and P. Demeester, "A survey on wireless body area networks," Wirel. Networks, vol. 17, no. 1, pp. 1–18, 2020, doi: 10.1007/s11276-010-0252-4.

[7]     [7] Q. Rubani, S. H. Gupta, and A. Rajawat, "Optik A compact MIMO antenna for WBAN operating at Terahertz frequency," Opt. - Int. J. Light Electron Opt., vol. 207, no. January, p. 164447, 2020, doi: 10.1016/j.ijleo.2020.164447.

[8]     [8] Q. Rubani, S. H. Gupta, and A. Kumar, "Design and analysis of circular patch antenna for WBAN at terahertz frequency," Optik (Stuttg)., vol. 185, pp. 529–536, 2019, doi: 10.1016/j.ijleo.2019.03.142.

[9]     [9] X. Tong, C. Liu, X. Liu, H. Guo, and X. Yang, "Switchable ON-/OFF-Body Antenna for 2.45 GHz WBAN Applications," IEEE Trans. Antennas Propag., vol. 66, no. 2, pp. 967–971, 2018, doi: 10.1109/TAP.2017.2780984.

[10]    [10]       M. Bouchra, S. Ferouani, and Z. K. Djalal, "Design of Optical Gold Printed Antenna in Terahertz Band for ON Body WBAN Applications," Microw. Rev., vol. 28, no. 1, pp. 9–13, 2022.

[11]    [11]       B. Moulfi, S. Ferouani, and D. Ziani Kerarti, "WIDE BAND NANO CIRCULAR GRAPHENE PRINTED ANTENNA FOR TERAHERTZ TRANSMISSION WITH DGS," vol. 81, no. 2, pp. 37–48, 2022.

[12]    [12]       M. Bouchra, F. Souheyla, Z. K. Djalal, and M. Wassila, "Design of a Novel Nanometric Graphene Pentagone Patch Antenna Array for Terahertz Transmission," pp. 1–5, 2022, doi: 10.1109/icisat54145.2021.9678495.

[13]    [13]       B. Moulfi, S. Ferouani, and D. Ziani-Kerarti, "Nanorectangular Printed Gold Antenna for on-Human Body Wireless Body Network Applications," Telecommun. Radio Eng., vol. 82, no. 1, pp. 1–8, 2023, doi: 10.1615/telecomradeng.2022043621.

[14]    [14]       A. T. Devapriya and S. Robinson, "Investigation on metamaterial antenna for terahertz applications," J. Microwaves, Optoelectron. Electromagn. Appl., vol. 18, no. 3, pp. 377–389, 2019, doi: 10.1590/2179-10742019v18i31577.

# Dual-band Butterfly Patch Antenna Based on CSRR for 5G Mobile and C-band Applications

MOUSSA Fatima Zahra[#1], FEROUANI Souheyla[#2], BELHADEF Yamina[*3], MOULFI Bouchra [#4]

[#]*Dept. of Electronic and telecommunications, SSL Laboratory (of Ain temouchent University),LTT Laboratory (of Tlemcen University)*

*Ain temouchent University Belhadj Bouchaib*
*Ain temouchent, Algeria*

[1]fatima.moussa@univ-temouchent.edu.dz
[2]souheyla.ferouani@univ-temouchent.edu.dz
[4]bouchra.moulfi@univ-temouchent.edu.dz

[*]*Dept of Telecommunications (of Tlemcen University), LTT Laboratory (of Tlemcen University)*

*Tlemcen University Abou Bekr Belkaid.*
*Tlemcen, Algeria*

[3]yamina.belhadef@univ-tlemcen.dz

*Abstract*—**The objective of this work is the design of a new form of dual-band butterfly patch antenna based on Complementary Split Ring Resonators (CSRRs) addressing the needs of users in the frequency ranges [3.4-3.8] GHz for 5G mobile applications and [4-8] GHz for C-band. The antenna consists of two symmetrical triangles fed by a microstrip line, with 15 CSRRs etched on the ground plane which is modified by DGS in order to improve the gain and to increase the bandwidth. The DGS technique used allowed us to achieve gains of the order of 5.28 and 5.88 dB for the two frequency bands [3.5-3.8] and [4-8] GHz respectively.**

*Keywords*— **Dual-band, butterfly patch antenna, CSSR, ,5G, gain, DGS.**

## I. INTRODUCTION

The new 5G cellular technology will provide major benefits in terms of high data rates, highly reliable communications and low latency, and will use different frequencies including high frequencies: (1GHz<f<6GHz) where it is allocated as intermediate spectrum [1]. Fifth generation (5G) systems suggest a lower band of 3.5 GHz and multiple beams with high gain and capacity for 5G mobile applications.[2-3]. In addition, in satellite communications, real-time satellite television networks and satellite power supplies, the C-band of the microwave frequency range is used. This C-band is frequently used in rainy tropical regions because it is less sensitive to evaporation caused by rain than the Ku-band. Its frequency range is between 4 and 8 GHz[4][5]In the last two decades, antennas have become very necessary in many mobile applications such as wireless networks, which have given rise to intense research, due to their many advantages and better prospects, including ease of design, low cost, light weight.[6]Metamaterials have a variety of advantages in different applications for different frequency ranges such as shape geometry, dimensions, alignment, arrangement of inclusions determine the nature of the interaction between the metamaterial on the host medium and an applied electromagnetic field.[7]. To meet the increasing need for wireless communication demands, broadband antennas with appropriate radiation properties are needed where metamaterials can be used to improve their characteristics and performance [8]. A split-ring resonator (SRR) [9-10]. A complementary split-ring resonator (CSRRs) [11-12], periodic array structures [13], and spiral resonators (SR) [14] have been proposed for the miniaturization of antennas [15], creating multi-band operation and improving gain and bandwidth [16].This work focuses on the design of a new form of patch antenna using complementary CSRR metamaterials on the ground plane in order to maintain the performance in terms of gain and bandwidth at the [3.4-3.8] GHz and [4-8] GHz frequency bands for 5G mobile and C-band applications. Rogers RT 5880 substrate material is used with relative permittivity of $\varepsilon r = 2.2$, the DGS technique is introduced on the ground plane of the proposed antenna for improving the gain and bandwidth.

## II. ANTENNA DESIGN

In this paper, a new form of patch antenna composed of two symmetrical triangles fed by a 50 Ω microstrip line is presented. A Rogers RT 5880 substrate with a relative permittivity of $\varepsilon r = 2.2$ and a thickness of 1.57 mm is used. The proposed antenna simulated using CST MiroWave Studio software; resonates at 3.5 GHz whose size Wg x Lg

is 61.71 x 60.45 mm. The final geometry of the initial antenna is presented in Fig.1 and TABLE I presents their dimensions.



*A. Results and Discussion*
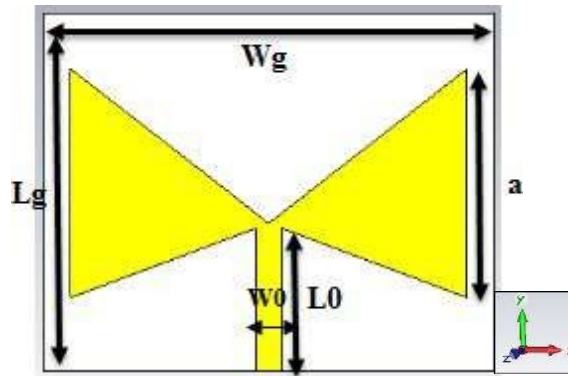
Fig. 1 Geometry of the proposed antenna

TABLE I

DIMENSIONS OF THE PROPOSED ANTENNA

| Parameters | Dimensions |
|---|---|
| Wg | 61.71 mm |
| Lg | 51.82 mm |
| a | 30.4 mm |
| L0 | 24 mm |
| W0 | 4.30 mm |

- Return loss [S11]

The reflection coefficient of the initial antenna obtained in the simulation is shown in Fig.2, with a match of about -4.91 dB at 3.14 GHz. This does not meet the conditions for use in the desired frequency band [3.4-3.8] GHz .
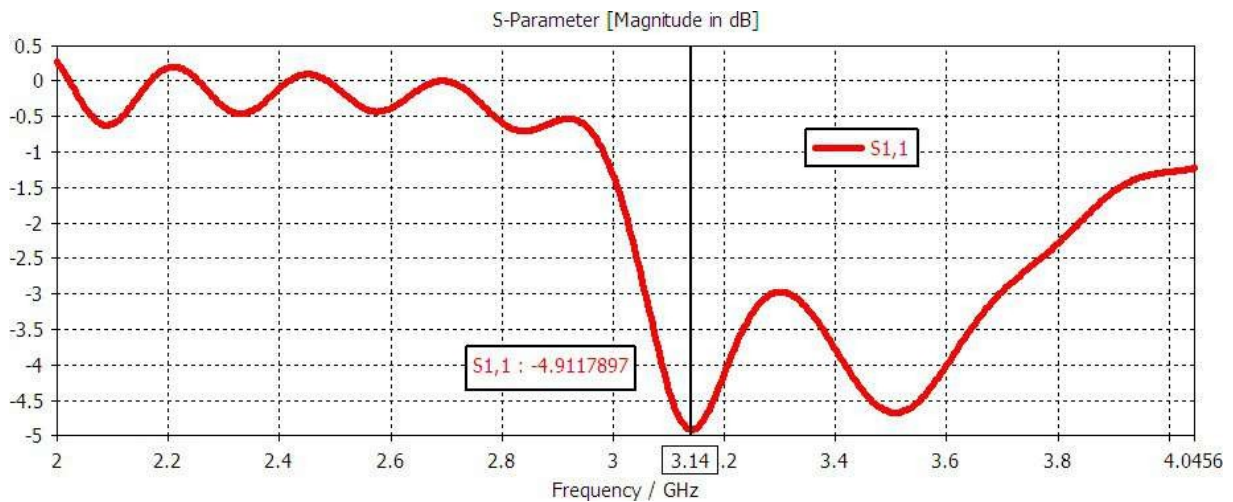


Fig. 2   Return loss of the proposed initial antenna.

III.  ADAPTATION OF THE ANTENNA TO THE 3.5 GHZ FREQUENCY

*A. The CSRR Cell*

In order to determine the resonance frequency of the CSRR cell with the above parameters. The simulation software CST was used. The geometry of this cell is composed of three-square shaped rings with dimensions of W1= 5.81 mm, W2 =4.86 mm, W3=3.86 mm down and a gap of g=0.8 mm, were adjusted to match the desired resonant frequency 3.5 GHz.  These dimensions resulted in the CSSR design as shown in Fig. 3
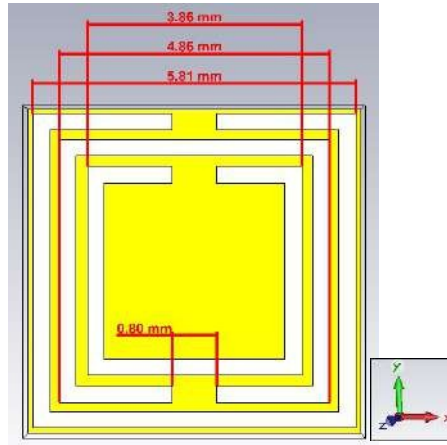
Fig. 3 CSRR cell.

The simulation results in terms of reflection coefficient S11 and transmission coefficient S21 of the proposed CSRR cell are shown in Fig.4.
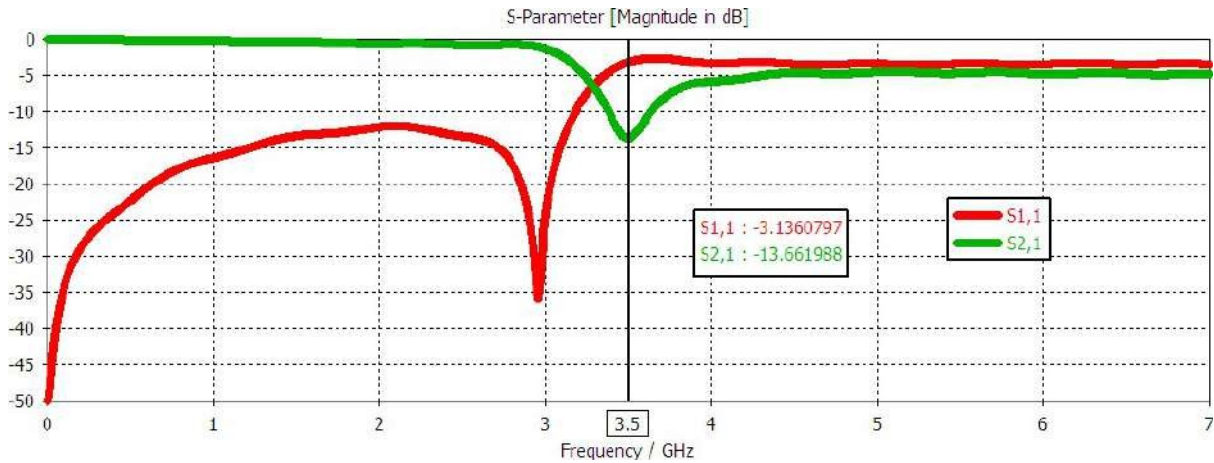


Fig. 4 Reflection and transmission coefficients of the proposed CSRR cell.

## B. Insertion of CSRR Cells

In this study, we added a CSSR structure to the ground plane of 5 x 3 (15) cells to have better performance in terms of reflection coefficient matching, gain and bandwidth. The Fig.5 shows the final geometry of the proposed microstrip patch antenna loaded with 15 CSRRs cells etched on the metallic ground plane. The final dimensions are given in TABLE II.



(a)

(b)
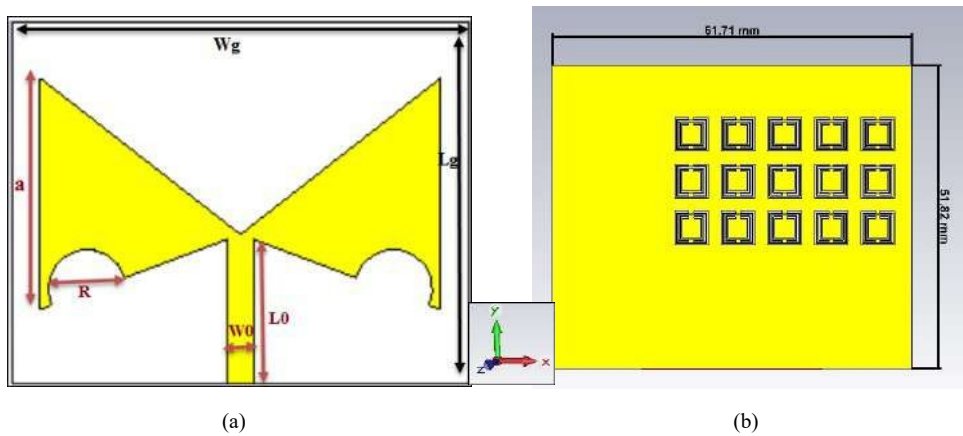
Fig. 5 Patch antenna matched by two circular slots on the radiating element and 15 CSRRs etched on the ground plane (a) Top view, (b) Bottom view.

TABLE II

DIMENSIONS FOR THE 3.5 MATCHED ANTENNA

| Parameters | Dimensions |
|------------|------------|
| Wg | 61.71 mm |
| Lg | 51.82 mm |
| a | 30.4 mm |
| R | 10 mm |
| L0 | 24 mm |
| W0 | 4.30 mm |

### C. Simulation Results

- With inserting of 15 CSRR cells
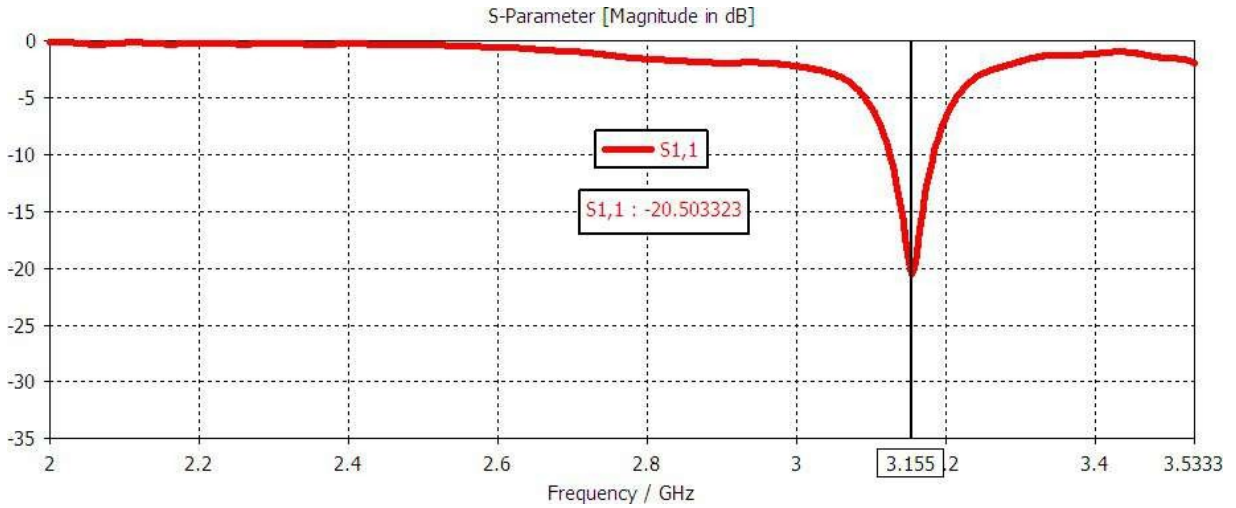


Fig. 6 The reflection coefficient after the insertion of 15 CSRR cells on the ground plane of the proposed antenna.

As shown in Fig.6, after inserting 15 complementary CSRR metamaterial cells on the ground plane of our proposed antenna; we had a good match in terms of reflection coefficient at the frequency of 3.155, which does not satisfy the requirements of the 5th generation mobile applications between 3.4-3.8 GHz.

- With inserting slits

Fig.7 shows the final reflection coefficient obtained is -35.39 dB at the resonant frequency of 3.5 GHz which is very satisfactory.
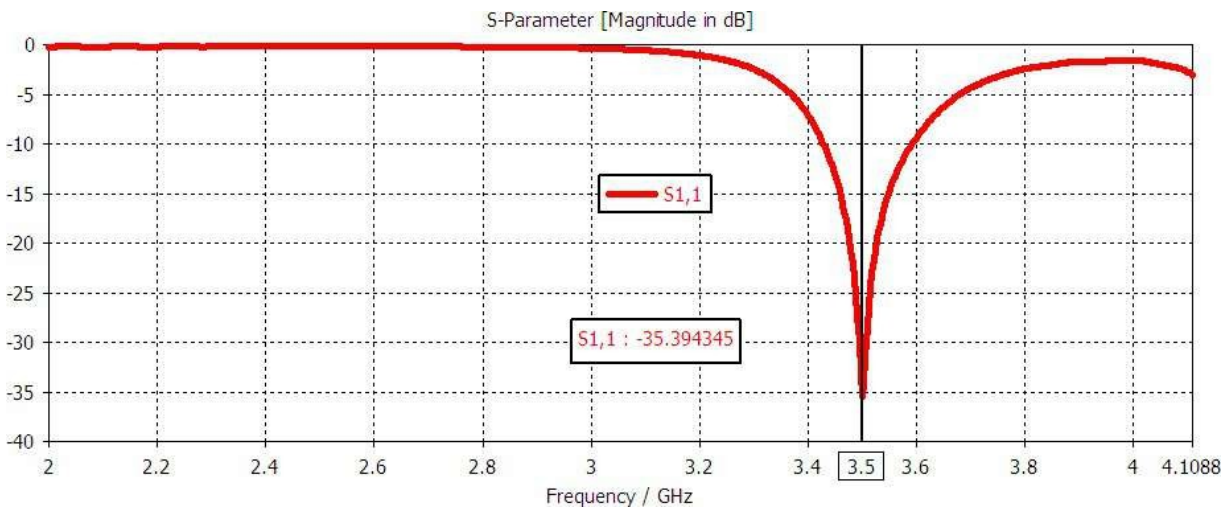


Fig. 7 Reflection coefficient of the proposed miniature antenna.
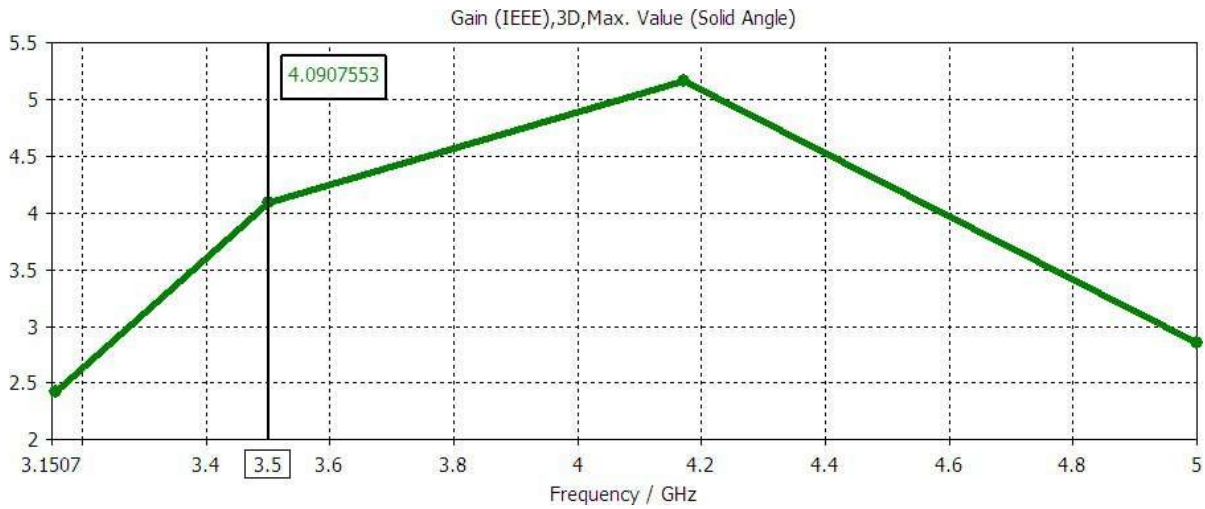
Fig. 8 Gain of the proposed antenna at 3.5 GHz resonant frequency.

The resulting gain of the patch antenna is 4.09 dB at the resonant frequency of 3.5 GHz.
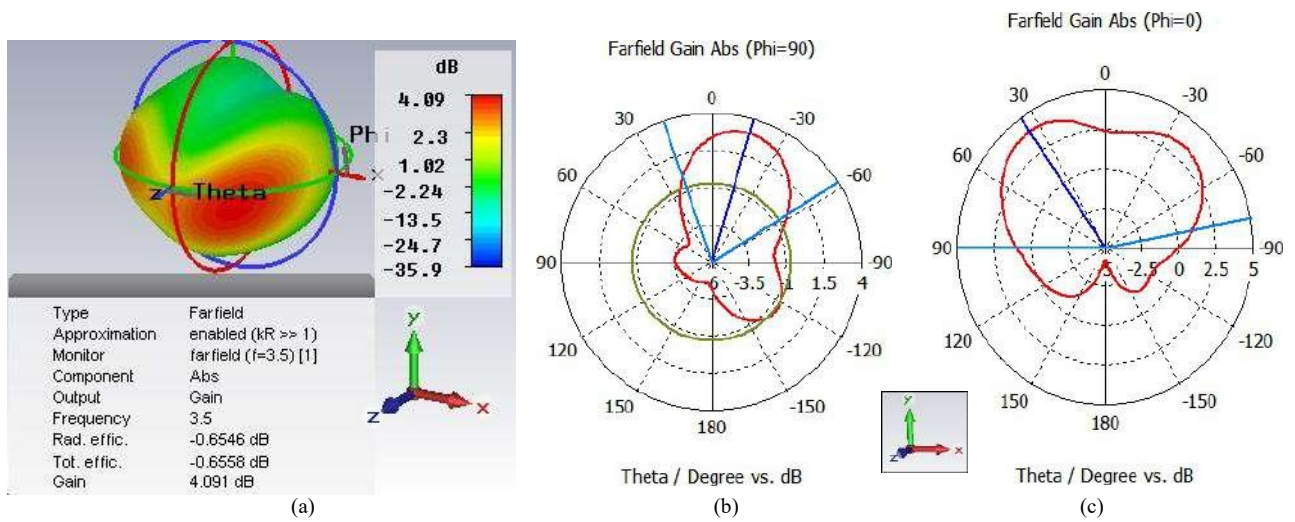


Fig. 9 Radiation patterns of the proposed antenna: (a) in 3D, (b) and (c) polar in 2D at the resonant frequency 3.5 GHz.

The 3D and polar radiation patterns obtained are presented in Fig.9 which is omnidirectional.

### D. Defected Ground Structure DGS For Proposed Antenna

The DGS is applied to the ground plane with the aim of improving the gain and widening the bandwidth. The final geometry obtained after using the ground plane modification technique is shown in Fig.10
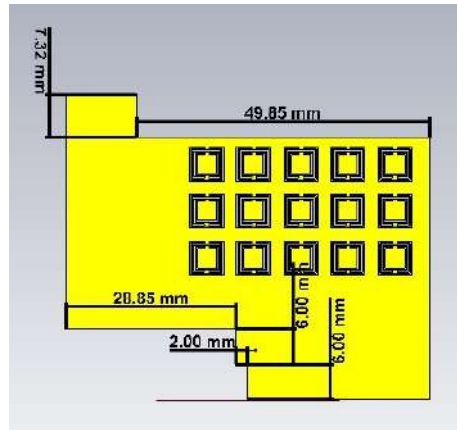
Fig. 10 Proposed final antenna with DGS inserted on the ground plane.

Fig.11 below shows the reflection coefficients of the final antenna after using the DGS. From the graph, we deduce that the antenna has two operating zones at resonant frequencies 3.509 and 4.166 respectively.
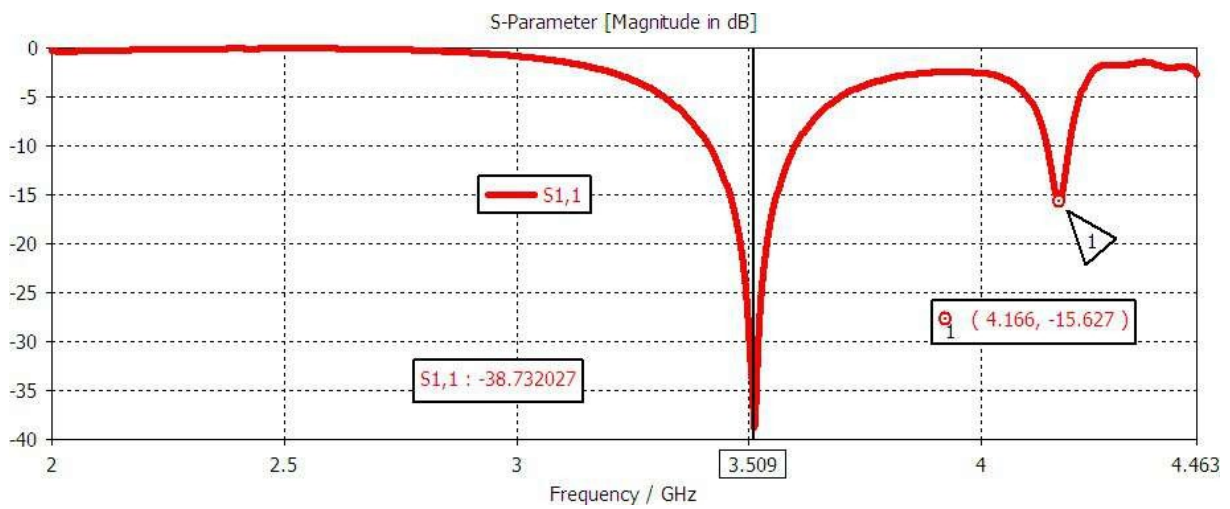


Fig. 11 Reflection coefficients of the final antenna at resonant frequencies 3.509 and 4.166 respectively.



Fig. 12 Gain of the final proposed antenna at resonant frequencies 3.509 and 4.166 GHz respectively.

The Fig.12 shows the gain of the proposed final antenna in the [3.4-3.8] GHz frequency band is about 5.28 dB, while that in the [4-8] GHz frequency band is about 5.88 dB. As can be seen, the radiation gain is thus improved by the DGS used on the ground plane.

(a)                                        (b)                                        (c)
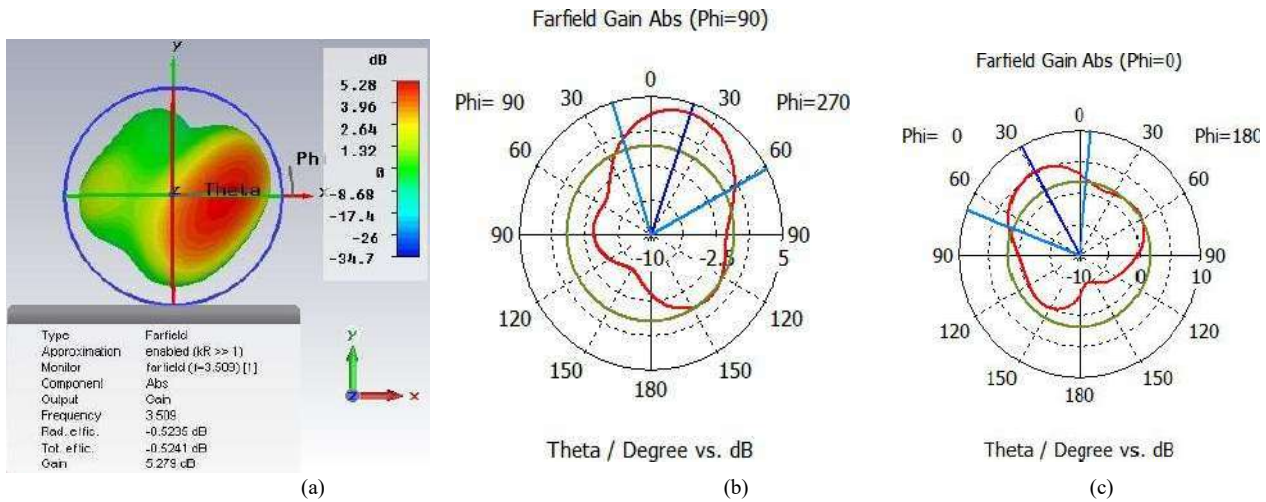
Fig. 13 Radiation patterns of the proposed miniature antenna: (a) in 3D, (b) and (c) polar in 2D at the resonant frequency 3.509 GHz.



(d)                                        (e)                                        (f)
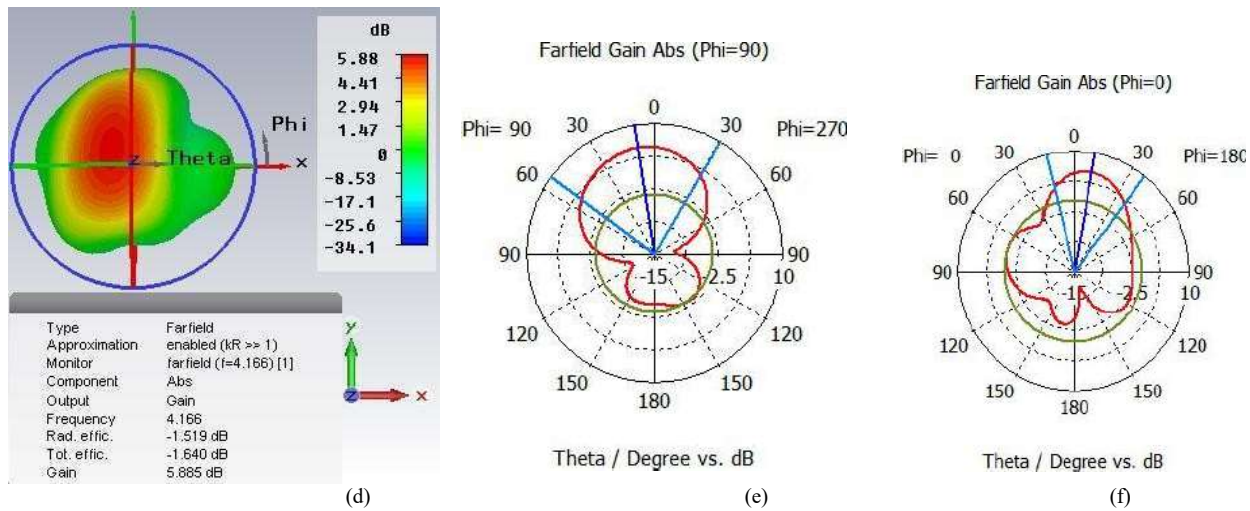
Fig. 14 Radiation patterns of the proposed miniature antenna: (d) in 3D, (e) and (f) polar in 2D at the resonant frequency 4.16 GHz

The radiation patterns of the proposed final antenna studied and calculated in terms of gain are shown in Figures 13 and 14. From the 3D and 2D polar radiation patterns for the E ($\varphi=0°$) and H ($\varphi=90$) planes, we can deduce that the proposed antenna has a semi-omnidirectional pattern for the two resonant frequencies, i.e., 3.509 GHz and 4.166 GHz.

TABLE III

COMPARED RESULTS TO OTHER REFERENCES RESEARCHERS

| References | Fr (GHz) | Reflection coefficient S11 (dB) | Gain (dB) | Dimensions Wg*Lg ($mm^2$) |
|---|---|---|---|---|
| [17] | 3.52 | -29.77 | 3.66 | 50 x 40 |
| [18] | 3.5 | -20.5 | 6.74 | 78.6 x 42.5 |
| [19] | 3.78 | -23 | 3.48 | 48 x 48 |
| Proposed antenna | 3.509 4.166 | -38.73 -15.62 | 5.28 5.88 | 61.71 x 51.82 |

From TABLE III, we can say that our proposed antenna has a good performances compared to the works, we achieved a gain of 5.28 and 5.88 dB for 3.5 GHz and 4.16 GHz frequency respectively.

## IV. CONCLUSIONS

A new form of dual-band butterfly patch antenna based on CSRR cells, fed by a microstrip line, has been studied. CSRR complementary metamaterial cells have been used for antenna matching while keeping their performance under the conditions of use for 5th generation applications and C band. The simulation results show

that with the use of 15 CSRR cells, Slits and DGS, the gain and bandwidth are in the order of 5 dB and 180 MHz respectively. The butterfly antenna is easy to fabricate and to be used for 5G mobile and C-band applications respectively.

REFERENCES

[1] M. F. Rafdzi and S. Y. Mohamad, "Study for Microstrip Patch Antenna for 5G Networks," no. September, pp. 27-28, 2020.

[2] T. Z. Fadhil et al, "A Beam-Split Metasurface Antenna for 5G Applications," IEEE Access, vol. 10, pp. 1162-1174, 2022, doi: 10.1109/ACCESS.2021.3137324.

[3] T. Aathmanesan, "NOVEL SLOTTED HEXAGONAL PATCH ANTENNA FOR SUB-6 GHZ 5G WIRELESS APPLICATIONS," pp. 1010-1013, 2021, doi: 10.21917/ijme.2021.0176.

[4] P. Deb, T. Moyra, and P. Bhowmik, "Dual Band Multilayer E-Shape Microstrip Patch Antenna for C-Band and X-Band," pp. 30-34, 2015.

[5] T. Bhandari and S. Baudha, "An UWB compact microstrip antenna for S band, C band and X band applications," 12th European Conference on Antennas and Propagation (EuCAP 2018), London, UK, 2018, pp. 1-5, doi: 10.1049/cp.2018.1014.

[6] H. Elftouh, N. A. Touhami, M. Aghoutane, S. El Amrani, A. Tazon, and M. Boussouis, "Miniaturized Microstrip Patch Antenna with Defected Ground Structure Reproduced courtesy of The Electromagnetics Academy Reproduced courtesy of The Electromagnetics Academy," vol. 55, no. September, pp. 25-33, 2014.

[7] Y. Ali et al, "Analysis of Compact Dual-Band Metamaterial-Based Patch Antenna Design for Wearable Application," Arab. J. Sci. Eng, 2021, doi: 10.1007/s13369-021-06365-1.

[8] Kumari, E.K., Kumar, M.V., Sharma, P.K., Murugan, S. (2021). Double-Sided Split Ring Resonator-Based Probe Feed Patch Antenna with Enhanced Bandwidth for 5G and Ku Band Applications. In: Sharma, H., Gupta, M.K., Tomar, G.S., Lipo, W. (eds) Communication and Intelligent Systems. Lecture Notes in Networks and Systems, vol 204. Springer, Singapore. https://doi.org/10.1007/978-981-16-1089-9_37

[9] HASAN, Md Mehedi, RAHMAN, Maskia, FARUQUE, Mohammad Rashed Iqbal, et al. Electrically compact SRR-loaded metamaterial inspired quad band antenna for bluetooth/WiFi/WLAN/WiMAX system. Electronics, 2019, vol. 8, no 7, p. 790, https://doi.org/10.3390/electronics8070790.

[10] R. Li and X. Chen, "Design of a Miniaturized Antenna Based on Split Ring Resonators for 5G Wireless Communications," 2019 Cross Strait Quad-Regional Radio Sci. Wirel. Technol. Conf. pp. 1-4.

[11] F. Z. Moussa, S. Ferouani, and Y. Belhadef, "New Design of Metamaterial Miniature Patch Antenna with DGS for 5G Mobile Communications," Microwave Review, 2022, vol. 28, no 2.

[12] D. Pal, R. Singhal, and A. Kumar, "Parametric Optimization of Complementary Split - Ring Resonator Dimensions for Planar Antenna Size," Wirel. Pers. Commun, vol. 123, no. 2, pp. 1897-1911, 2022, doi: 10.1007/s11277-021-09220-6.

[13] B. Y. Dong and T. Itoh, "Metamaterial-Based Antennas," vol. 100, no. 7, pp. 2271-2285, 2012.

[14] C. Zhu, J. Ma, and H. Zhai, "Characteristics of Electrically Small Spiral Resonator Metamaterial With Electric and Magnetic Responses," vol. 11, pp. 1580-1583, 2012.

[15] M. Gupta, V. Mittal, J. Saxena, and S. Gupta, "Miniaturized Microstrip Patch Antenna Array for ISM Band Using Complementary Split Ring Resonator," Wirel. Pers. Commun. no. 0123456789, 2019, doi: 10.1007/s11277-019-06679-2.

[16] M. Islam, M. T. Islam, M. Rashed, I. Faruque, N. Misran, and M. F. Mansor, "A Miniaturized Antenna with Negative Index Metamaterial Based on Modified SRR and CLS Unit Cell for UWB Microwave Imaging Applications," pp. 392-407, 2015, doi: 10.3390/ma8020392.

[17] D. Paragya and H. Siswono, "3 . 5 GHz Rectangular Patch Microstrip Antenna with Defected Ground Structure for 5G," vol. 8, no. 1, pp. 31-42, 2020.

[18] S. S. Al-bawri, S. Islam, H. Y. Wong, and M. F. Jamlos, "Bandwidth and Gain Enhancement of Quad-Band CPW-Fed Antenna for Wireless Applications," pp. 1-14, 2020.

[19] M. Ameen and R. K. Chaudhary, "Dual-layer and Dual-polarized Metamaterial Inspired Antenna using Circular-Complementary Split Ring Resonator Mushroom and Metasurface for Wireless Applications," AEUE - Int. J. Electron. Commun. p. 152977, 2019, doi: 10.1016/j.aeue.2019.152977.

# Density, speed of sound, refractive index and related derived/excess properties of binary mixtures comprising 2-benzylaminoethanol with alcohols ($C_1 - C_3$) at different temperatures

**Aouicha Belabbaci[1], Amal Ayad[1], Amina Negadi[1], Ariel Hernández[2], Bakusele Kabane[3], Indra Bahadur[4], Latifa Negadi[1,5,*]**

[1] LATA2M, Laboratoire de Thermodynamique Appliquée et Modélisation Moléculaire, University of Tlemcen, Office Box 119, Tlemcen 13000,Algeria

[2] Departamentode IngenieríaIndustrial, FacultaddeIngeniería, Universidad Católicadela Santísima Concepción, Post AlonsodeRibera2850, Concepción, Chile

[3] Department of Physical Chemistry laboratories, Faculty of Applied Sciences, Durban University of Technology, Durban-4001, South Africa

[4]Department of Chemistry and Materials Science Innovation & Modelling Research Focus Area, School of Physical and Chemical Sciences, Faculty of Natural and Agricultural Sciences, North-West University (Mafikeng Campus), Private Bag X2046, Mmabatho 2735, South Africa

[5]Thermodynamics Research Unit, School of Engineering, University of KwaZulu-Natal, Howard College

**ABSTRACT: The densities, speeds of sound and refractive indices of binary mixtures 2-Benzylaminoethanol (2-BAE) with methanol, ethanol, 1-propanol, or 2-propanol were measured in the temperature range from 293.15 to 323.15 Kover the whole composition range and atmospheric pressure. Experimental data were used to calculate the isentropic compressibility, $m_s$. From this data, excess molar volumes, $V_m^E$, deviation in isentropic compressibilities, $\Delta m_s$, deviation inspeed of sound,$\Delta u$ and deviation in refractive indices, $\Delta n_D$, for all studied mixtures were calculated and correlated as function of temperature using Redlich-Kister polynomial equation. The excess properties of binary mixtures were found to be negative or positive curves as a function of the composition. The results were interpreted in terms of molecular interactions and molecular structures occurring in the binary mixtures.**

**Keywords: density; excess properties; Redlich-Kister equation; refractive index; speed of sound.**

## I. INTRODUCTION

The understanding of the thermodynamic and transport properties of liquid mixtures has been used to resolve numerous challenging engineering issues, including heat and mass transfer, fluid flow, and energy transformations [1-4].

Intermolecular interactions are one of the most interesting areas, and therefore the applications of experimental data and theoretical models combined together are used to investigate the behavior

of liquid mixtures. In this regard, several transport and thermophysical properties of liquid mixtures comprising 2-Benzylaminoethanol + Methanol, Ethanol, 1-Propanol, or 2-Propanol were explored in this research to aid in the investigation of the nature and extent of intermolecular interactions.

In this study, density, speed of sound and refractive index of binary mixtures of 2-Benzylaminoethanol (2-BAE) with methanol, ethanol, 1-propanol or 2-propanol were measured at the temperature range of T=293.15 to 323.15 K and atmospheric pressure. The excess or deviation properties: excess molar volumes, $V^E_m$, deviation in isentropic compressibilities, $\Delta \kappa_s$, deviation inspeed of sound,$\Delta u$ and deviation in refractive indices, $\Delta n_D$ are also calculated and correlated with the Redlich-Kister (RK) equation [5].

## II.    METHODS

Density and speed of sound of the pure liquids (2-benzylaminoethanol, methanol, ethanol, 1-propanol, and 2-propanol) and their binary mixtures were measured using Anton Paar (DSA 5000 M) digital vibrating tube densimeter and a sound velocity analyzer at a temperature range of 293.15 to 323.15 K and an atmospheric pressure of P = 0.1 MPa

Refractive indices of pure liquids and their binary mixtures were measured using an Anton Paar Abbemat 300 digital refractometer at temperature range of 293.15 to 323.15 K. The apparatus was calibrated with distilled water before each series of measurements.

## III.    RESULTS

The plots of $V^E$, $\Delta ks$, $\Delta u$ and $\Delta n$ versus the mole fraction of 2-Benzylethanolamine $x_1$ have been presented in Figs. 1.

The negative excess molar volume values reveals that there is a strong interaction between the investigated alcohols resulting to a well-organized packing effect when mixed with 2-benzylaminoethanol resulting to volume contraction. The other contributing factor towards negative values is due to unlike molecular interactions resulting to the charge transfer. The observed negative values for the deviation in isentropic compressibilities show that there are strong interactions between the investigated binary systems which contributes towards a limited free space in the molecules of the binary mixtures. It can be seen that the values of $\Delta u$ are positive for studied systems at different temperatures and decrease in chain length of alcohol increases according to order: (2-BAE + Methanol) > (2-BAE + Ethanol) > (2-BAE + 2-Propanol) > (2-BAE + 1-Propanol) as shown Figure 1(c). The calculated data for the deviation in refractive indices are positive and decrease with an increase in temperatures.

## IV.     CONCLUSIONS

In this work, new experimental data comprising thermophysical properties measurements including densities, speed of sound, refractive indices of the binary mixtures of 2-benzylaminoethanol with alcohols (C$_1$ – C$_3$) at T = (293.15 – 323.15) K and at atmospheric pressure. This was conducted at an entire range of mole fraction ($x_{2-BAE} = 0 \ to \ 1$). The results are interpreted in terms of molecular interactions between the binary systems by computing excess properties such as excess molar volume, isentropic compressibilities, and deviation in refractive indices. These were computed from the measured data of densities, refractive indices, and speed of sound data. The excess properties were correlated with the application of Redlich-Kister polynomial equation and a great correlation for the investigated binary mixtures was obtained. Negative differences were observed in the derived properties reaving the strong intermolecular interactions between 2-benzylaminoethanol and methanol, ethanol, 1-propanol, or 2-propanol. Large negative values were observed in 2-benzylaminoethanol and methanol suggesting that 2-benzylaminoethanol can easily accommodate methanol with high packing effect. The magnitude of strong intermolecular interactions was observed to be methanol > ethanol >2-propanol >1-propanol
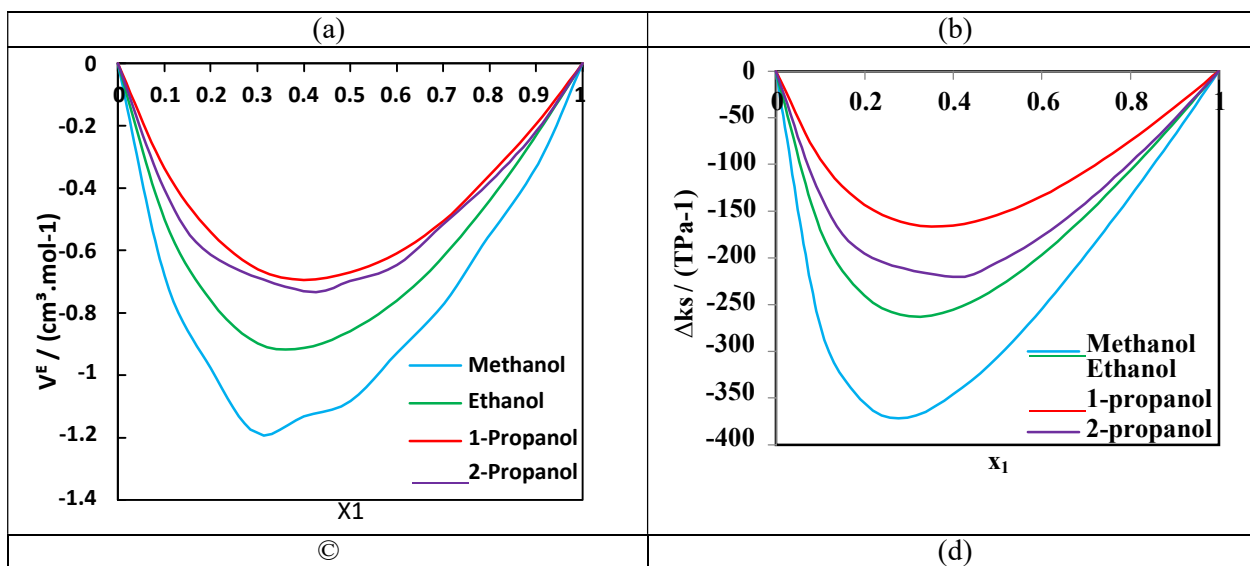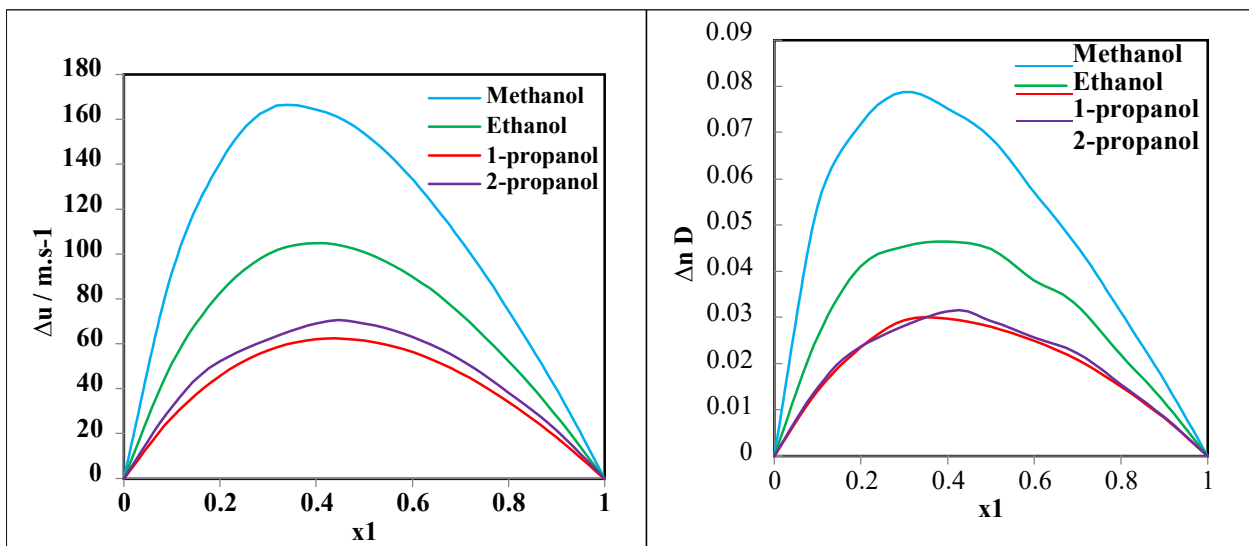
**Fig.1.**Plot of excess or deviation properties, for the binary mixtures: {2-Benzylethanolamine ($x_1$) + Methanol + Ethanol + 1-Propanol or 2-Propanol ($x_2$)} as function of the composition expressed in the mole fraction of 2 -Benzylethanolamine at 313,15 K .(a) excess molar volumes,$V^E$ ,(b) Deviation in isentropic compressibility, $\Delta\kappa_s$. (c): deviation in speed of sound,$\Delta u$ , (d): deviation in refractive index, $\Delta n_D$.

# REFERENCES

[1]     V.K. Pandey, V. Verma, R. Srivastava, A. Awasthi, A. Awasthi, Refractive Indices and Their Related Properties for Binary Mixtures Containing 2-Diethylethanolamine with 1-Propanol and 1-Butanol, J. Solution Chem. 49 (2020) 1459-1472.

[2]     Z.R. Master, N.I. Malek, Molecular interaction study through experimental and theoretical volumetric, acoustic and refractive properties of binary liquid mixtures at several temperatures 1. N, N-dimethylaniline with aryl, and alkyl ethers, J. Mol. Liq. 196 (2014) 120-134.

[3]     M. Aftabuzzaman, M.M. Islam, F.R. Rima, M.N. Islam, M.A. Ali, Volumetric and transport properties of binary liquid mixtures of sulfolane with aniline, N, N-dimethylaniline and N, N-diethylaniline at different temperatures and atmospheric pressure, J. Chem. Thermodyn. 96 (2016) 181-186.

[4]     D.S. Kumar, K. Srikanth, D.K. Rao, Molecular interactions in the mixtures of 2-chloroaniline with equimolar mixture of methanol and isopropanol/isobutanol, J. Mol. Liq. 136 (2007) 90-93.

[5]     Redlich, O.; Kister, A. T. Algebraic Representation of Thermodynamic Properties and the Classification of Solutions. Ind. Eng. Chem. 1948, 40, 345−348.

# Performance enhancement of the improved P&O-MPPT strategy using Proteus software equipped with an Arduino board

Menasria Azzeddine[#1], Moussa Sedraoui [*2], Bechouat Mohcene[#3], Bourouba Hocine[#4], Doghmane Hakim[#5], Boualleg Abdelhalim[#6]

[#1-2-4-5-6] *Département d'Électronique & Télécommunications,Université 8 Mai 1945 Guelma, Algeria,*

[#3] *Université of Ghardaïa, Algeria*

menasria.azzeddine@univ-guelma.dz

sedraoui.moussa@univ-guelma.dz

bechouat.mohcene@univ-ghardaia.dz

bourouba.hocine@univ-guelma.dz

doghmane_hakim@univ-guelma.dz

boualleg.abdelhalim@univ-guelma.dz

## Introduction:

This paper proposes an enhanced maximum power extraction of a solar system consisting of a KC200GT photovoltaic generator that feeds a variable resistive load via a DC-DC boost converter. The corresponding PV control loop has two distinct steps. In the first, the Perturb and Observe P&O algorithm is directly implemented to provide the reference PV current according to the change in absolute temperature and solar irradiance. This last one is compared by the actual measured PV current, in which a discrepancy current is generated at each sampling time. As the minimization of the last one must be carried out in the second stage, the synthesis of a PID current controller becoming indispensable regardless the internal functioning of the solar system. According, the controller tuning parameters requires a prior linear model that describing the actual solar system behavior around the Standard Test Conditions STC where a linearization step occurred as a key success for improving the power extraction ratio. This step is established by applying the small-signal principle on the nonlinear state space representation of the actual solar system. On the basis of the resulting small-signal model, the parameters of the current PID controller are tuned using the existing guidelines available in Matlab®'s *pidTuner* function. This controller provides an optimal duty cycle variation which must then be added to the existing value of the existing control, given previously at STC. This allows optimally updating the duty cycle control which in turn leading to provide the power output without any ripple issue. The proposed preceding to steps leads highlighting the improved P&O-MPPT control strategy where its real-time implementation in the control loop becoming the important challenge in most scholars interesting by the renewable conversion system based on solar systems. This can be due to the modeling uncertainties that are unavoidable during the linearization step of the actual solar system behavior. It is also due the existing of some unmodelled dynamics occurring in real-world applications such as a dissipated power in the DC-DC boost converter diodes, nonlinearity of the current-voltage characteristic of the KC200GT PV module, and so on. To resolve these drawbacks, the solar system modeling is carried out using the existing electrical components in the Proteus software where all existing electrical devices in the control loop must be established component-by-component. Afterwards, the real-time implementation of the resulting optimal duty cycle control is ensured using the Arduino UNO card which including the required programs of standard and improved P&O-MPPT control strategies. Finally, the performance assessments of the

proposed improved P&O-PID control strategy including the preceding two distinct stage are demonstrated under different climatic conditions and some resistive load variations. The given simulation results are compared by those provided by the standard P&O control in terms of the trade-off between reference MPP tracking dynamic and closed loop robustness against the exogenous conditions affecting the control loop. Consequently, the proposed control loop based on the Proteus software and equipped with the Arduino UNO board offer a new gate for other industrial applications sur as optimal driving of solar water pumps, entrained  by permanent magnet asynchronous motors, ensuring a stable electrical power feed, located as far from public grid and so on

## Results:

Fig.1. shows the proposed control loop that will be used for the current regulation of the solar system, including the KC200GT PV module, the DC-DC boost converter  and  the variable resistive load. It is used for either standard and improved P&O control strategy where the main goal is to provide a smooth electrical power with  oscillation-free  tracking of the desired *MPP* and without ripple issue. This aim must be achieved, regardless of the change in climatic conditions such as solar irradiance and absolute temperature.
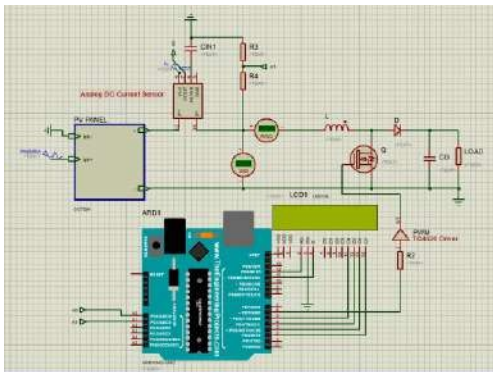


Fig.1. Proposed control loop established by Proteus software and equipped with Arduino board
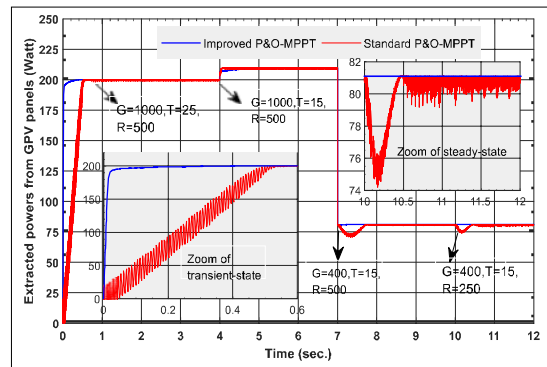


Fig.2. Comparison between the power outputs, given by standard and improved P&O strategies

| • Nonlinear model describing the actual solar system: | | • Linear small-signal model: | |
|---|---|---|---|
| $\frac{a}{dt}i_{pv}(t) = \frac{1}{L}v_{pv}(t) - \frac{1-a}{L}v_o(t)$<br>$\frac{d}{dt}v_o(t) = \frac{1-d}{C}i_{pv}(t) - \frac{1}{R.C}v_o(t)$ | (1) | $\begin{bmatrix} \frac{d}{dt}i_{pv}(t) \\ \frac{d}{dt}v_o(t) \end{bmatrix} = \begin{bmatrix} -\frac{R_{MPP}}{L} & -\frac{1-D_{MPP}}{L} \\ \frac{1-D_{MPP}}{C} & -\frac{1}{RC} \end{bmatrix}\begin{bmatrix} i_{pv}(t) \\ v_o(t) \end{bmatrix} + \begin{bmatrix} \frac{V_{oMPP}}{L} \\ -\frac{I_{pvMPP}}{C} \end{bmatrix}d(t)$ | (2) |

## Conclusion:

The synthesis of the current PID controller, based on the small-signal model, has been investigated in this paper in order to increase the power extraction ratio of the standard P&O-MPPT control strategy. This improvement was achieved in two distinct stages. In the first step, the P&O algorithm was modified to generate the reference current using the existing the measured PV power and measured PV voltage of the KC200GT PV panel. This reference current was compared with the one measured from the PV panel, where the control loop based on the PID current controller was performed in the second step. The proposed control loop was set up using Proteus software equipped with the Arduino board, in order to overcome some drawbacks occurring in the modeling of the solar system as well as in the real-time implementation of optimal duty cycle control. Simulation results confirmed the effectiveness of the proposed control strategy in terms of

MPP reference tracking and robustness trade-off against model uncertainties, the existence of certain exogenous effects caused by meteorological changes, the presence of resistive load variations and so on. Finally, the proposed control loop, established by Proteus software and equipped with the Arduino UNO board, will offer a new gateway to other industrial applications, such as controlling solar water pumps, ensuring a stable power source, especially for systems located so far away from the public grid.

## Références :

[1]  A.Dehghanzadeh, , G.Farahani, , H.Vahedi, &K.Al-Haddad, (2018). Model predictive control design for DC-DC converters applied to a photovoltaic system. International Journal of Electrical Power & Energy Systems, 103, 537-544.

[2]  Aissani, S., Kahla, S., Bechouat, M., Amieur, T., & Sedraoui, M. (2023). A Voltage PID Controller Synthesis Based on a New Small-Signal Linear Model to Enhance the Performance of the Standard P &O Algorithm Employed in Photovoltaic Panels. *Arabian Journal for Science and Engineering*, *48*(5), 6615-6630.

[3]  Taibi, D., Amieur, T., Laamayad, T., & Sedraoui, M. (2023). Improvement of the Standard Perturb & Observe MPPT control strategy by the proposed Fuzzy Logic Mechanism for a Cascade Regulation of a PMSM-based PV pumping system. *Arabian Journal for Science and Engineering*, *48*(5), 6631-6647.

# Tuning Functions Based Adaptive Backstepping Control of Uncertain Non-Affine Nonlinear Systems

Yassine Soukkou[1,*], Ammar Soukkou[2], Hicham Khebbache[3], Mohamed Tadjine[4], Mokhtar Nibouche[5]

[1]*Research Center in Industrial Technologies CRTI, P. O. Box. 64, Cheraga 16014, Algiers, Algeria*
[2]*Renewable Energy Laboratory, Faculty of Science and Technology, Department of Electronics, University of MSB Jijel, BP. 98, Ouled Aissa, 18000, Jijel, Algeria*

[3]*LAJ, Faculty of Science and Technology, Department of Automatic Control, University of MSB Jijel, BP. 98, Ouled Aissa, 18000, Jijel, Algeria*

[4]*LCP, Department of Automatic Control, National Polytechnic School of Algiers (ENP), 10, Av. Hassen Badi, BP. 182, Algiers, Algeria*

[5]*Department of Engineering Design and Mathematics, University of the West of England, Frenchay Campus, Coldharbour Lane, Bristol BS16 1QY, UK*

Email 1 - *y.soukkou@gmail.com; y.soukkou@crti.dz
Email 2 - soukkou.amr@gmail.com
Email 3 - khebbachehicham@yahoo.fr
Email 4 - tadjine@yahoo.fr
Email 5 - mokhtar.nibouche@uwe.ac.uk

## Introduction:

The adaptive backstepping control techniques are well known methods for uncertain nonlinear systems [1-8].

On the other hand, compared with strict-feedback systems, a few results were obtained for nonlinear systems in non-affine form [9-12].

This paper presents a tuning functions based adaptive backstepping control scheme for uncertain non-affine nonlinear systems. The tuning functions design is introduced to overcome the problem of the overparametrisation in the adaptive backstepping control method. Lyapunov stability theory is used to establish the boundedness of all the signals in the closed-loop system and the tracking errors can converge to zero. Simulation results for an arc length in gas metal arc welding (GMAW) process are provided to demonstrate the effectiveness of the proposed adaptive control approach.

## Controller design:

We consider a class of uncertain non-affine nonlinear systems of the form:

$$
\begin{aligned}
\dot{x}_1 &= \Box^T f_1\left(x_1\right) + g_1\left(x_1, x_2\right) \\
\dot{x}_i &= \Box^T f_i\left(\underline{x}_i\right) + g_i\left(\underline{x}_i, x_{i+1}\right), i = 2, \ldots, n \Box 1 \\
\dot{x}_n &= f_0\left(x\right) + \Box^T f_n\left(x\right) + \Box_0\left(x\right) u \\
y &= x_1
\end{aligned}
\tag{1}
$$

where, $x = \begin{bmatrix} x_1 & x_2 & \cdots & x_n \end{bmatrix}^T \Box \mathbb{R}^n$ is the system state vector and $\underline{x}_i = \begin{bmatrix} x_1 & x_2 & \cdots & x_i \end{bmatrix}^T \Box \mathbb{R}^i$, $u \Box \mathbb{R}$ is the control input, $y \Box \mathbb{R}$ is the system output and $\Box \Box \mathbb{R}^p$ is an unknown constant parameter vector.

The nonlinear functions $f_0$, $f_i$ and $g_i$ are known and continuous with $\Box_0 \Box 0$. We define coordinate transformation as follows:

$$
\begin{cases}
e_1 = x_1 \Box x_{1d} \\
e_i = g_{i\Box1} \Box \Box_{i\Box1}, \quad i = 2, \cdots, n
\end{cases}
\tag{2}
$$

where, $e_i$, $i = 1, \cdots, n$ are called the tracking errors and $\alpha_{i-1}$ are the virtual control functions.

The virtual control signals $\alpha_i$, the actual control input $u$ and the adaptive law $\dot{\hat{\theta}}$ are chosen as:

$$\alpha_1 = -k_1 e_1 - \hat{\theta}^T f_1 + \dot{x}_{1d} \tag{3}$$

$$\tau_1 = -e_1 f_1 \tag{4}$$

$$\alpha_i = \frac{1}{\frac{\partial g_{i-1}}{\partial x_i} g_{i-1}}\left[-ke_i - \frac{\partial g_{i-2}}{\partial x_{i-1}} e_{i-1} - \frac{\partial \alpha_{i-1}}{\partial x_i}\hat{\theta}^T f_i + \sum_{k=1}^{i-1}\frac{\partial \alpha_{i-1}}{\partial x_k}\left(\hat{\theta}^T f_k + g_k\right)\right. \tag{5}$$

$$\left. + \frac{\partial \alpha_{i-1}}{\partial \hat{\theta}}\tau_i + \sum_{k=1}^{i}\frac{\partial \alpha_{(i-1)}}{\partial x_{1d}^{(k)}} x_{1d}^{(k)} - \sum_{k=1}^{i}e_{k+1}\frac{\partial \alpha_k}{\partial \hat{\theta}}\Gamma\left(-\frac{\partial \alpha_{i-1}}{\partial x_i} f_i + \sum_{k=1}^{i-1}\frac{\partial \alpha_{i-1}}{\partial x_k} f_k\right)\right]$$

$$\tau_i = \tau_{i-1} - e_i \Gamma\left(-\frac{\partial \alpha_{i-1}}{\partial x_i} f_i + \sum_{k=1}^{i-1}\frac{\partial \alpha_{i-1}}{\partial x_k} f_k\right) \tag{6}$$

$$u = \frac{1}{\frac{\partial g_{n-1}}{\partial x_n} g_0}\left[-k_n e_n - \frac{\partial g_{n-2}}{\partial x_{n-1}} e_{n-1} - \frac{\partial \alpha_{i-1}}{\partial x_i}\left(f_0 + \hat{\theta}^T f_n\right) + \sum_{k=1}^{n-1}\frac{\partial \alpha_{n-1}}{\partial x_k}\left(\hat{\theta}^T f_k + g_k\right)\right. \tag{7}$$

$$\left. + \frac{\partial \alpha_{n-1}}{\partial \hat{\theta}}\tau_n + \sum_{k=1}^{n}\frac{\partial \alpha_{n-1}}{\partial x_{1d}^{(k-1)}} x_{1d}^{(k)} - \sum_{k=1}^{n}e_{k+1}\frac{\partial \alpha_k}{\partial \hat{\theta}}\Gamma\left(-\frac{\partial \alpha_{n-1}}{\partial x_n} f_n + \sum_{k=1}^{n-1}\frac{\partial \alpha_{n-1}}{\partial x_k} f_k\right)\right]$$

$$\dot{\hat{\theta}} = \tau_n = \tau_{n-1} - e_n \Gamma\left(-\frac{\partial \alpha_{n-1}}{\partial x_n} f_n + \sum_{k=1}^{n-1}\frac{\partial \alpha_{n-1}}{\partial x_k} f_k\right) \tag{8}$$

## Simulation results:

The dynamics of a GMAW are described as follows [13]:

$$\dot{l}_a = K_1 I + K_2 I^2 - \left(l_r - l_c\right) v_e \tag{9}$$

$$\dot{I} = -\frac{1}{\tau_i} I + \frac{1}{\tau_i} I_r$$

where the definitions of $l_a$, $I$, $K_1$, $K_2$, $\tau_r$, $l_c$, $v_e$, $\tau_i$, and their values can be seen in [13]. Denote, $x_1 = l_a$, $x_2 = I$ and $u = I_r$, then, (9) can be rewritten as:

$$\dot{x}_1 = K_1 x_2 + K_2 x_2^2 - \left(l_r - x_1\right) v_e \tag{10}$$

$$\dot{x}_2 = -\frac{1}{\tau_i} x_2 + \frac{1}{\tau_i} u$$

The unknown parameter $\theta^T$ is set as $\theta^T = \frac{1}{\tau_i}$, where, $f_2 = -x_2$. The objective is to design our

controller $u$ such that $x_1$ tracks the desired trajectory $x_{1d} = 3 \cdot 10^{-3} m$. The simulation results are shown in Figure 1.
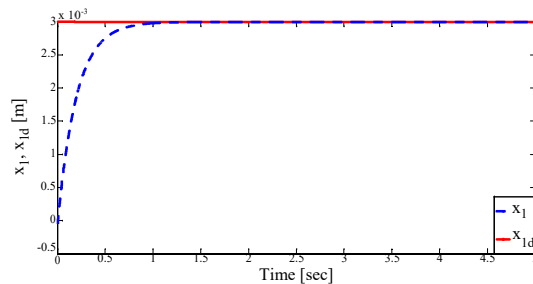


**Fig. 1.** Response of arc length: desired $x_{1d}$ ("-") and actual $x_1$ ("--").

## Conclusion:

In this paper, a tuning functions based adaptive control scheme has been presented for a class of uncertain non-affine nonlinear systems. By using tuning functions, the overparametrisation problem is avoided. Based on the Lyapunov stability theory, the proposed adaptive control scheme can guarantee that all the signals in the closed-loop system are bounded and the convergence of the tracking errors to zero is achieved. Simulation results of an arc length in GMAW process have been studied, where the results show the effectiveness of the proposed control scheme.

## References:

[1] M. Krstić, I. Kanellakopoulos, and P. V. Kokotović, "Nonlinear and adaptive control design," John Wiley & Sons, New York, 1995.

[2] Y. Soukkou, M. Tadjine, A. Soukkou, M. Nibouche, and H. Nouri, "Tuning functions based adaptive backstepping control for uncertain strict-feedback nonlinear systems using barrier Lyapunov functions with full state constraints," European Journal of Control, vol. 70, pp. 100783:1-100783:10, 2023.

[3] Y. Soukkou, M. Tadjine, M. Nibouche, and Q. Zhu, "Robust adaptive dynamic surface control scheme for a class of single-input and single-output uncertain nonlinear systems in strict-feedback form," International Journal of Adaptive Control and Signal Processing, vol. 36, no. 11, pp. 2938-2952, 2022.

[4] Y. Soukkou, S. Labiod, and M. Tadjine, "Composite adaptive dynamic surface control of nonlinear systems in parametric strict-feedback form," Transactions of the Institute of Measurement and Control, vol. 40, no. 4, pp. 1127-1135, 2018.

[5] P. P. Yip, and J. K. Hedrick, "Adaptive dynamic surface control: a simplified algorithm for adaptive backstepping control of nonlinear systems," International Journal of Control, vol. 71, no. 5, pp. 959-979, 1998.

[6] W. Dong, J. A. Farrell, M. M. Polycarpou, V. Djapic, and M. Sharma, "Command filtered adaptive backstepping," IEEE Transactions on Control Systems Technology, vol. 20, no. 3, pp. 566-580, 2012.

[7] Y. Soukkou, M. Tadjine, A. Soukkou, and M. Nibouche, "Immersion and invariance based adaptive command filtered backstepping control design for a class of SISO uncertain nonlinear systems in strict-feedback form," Transactions of the Institute of Measurement and Control, pp. 1-11, 2023. DOI: 10.1177/01423312231166435

[8] Y. Soukkou, M. Tadjine, and M. Nibouche, "Adaptive finite time command filtered backstepping control design for a class of uncertain full state constrained strict-feedback nonlinear systems," International Journal of Robust and Nonlinear Control, vol. 33, no. 17, pp. 10647-10661, 2023.

[9] Y.-H. Liu, "Adaptive tracking control for a class of uncertain pure-feedback systems," International Journal of Robust and Nonlinear Control, vol. 26, no. 5, pp. 1143-1154, 2016.

[10] Y.-H. Liu, L. Huang, D. Xiao, and Y. Guo, "Global adaptive control for uncertain nonaffine nonlinear hysteretic systems," ISA Transactions, vol. 58, pp. 255-261, 2015.

[11] X. Liang, B. Xu, and L. Gong, "ADT-based adaptive back-stepping control for the switched non-affine nonlinear system with uncertain parameters," Nonlinear Dynamics, vol. 110, pp. 467-777, 2022.

[12] Y.-H. Liu, L. Huang, and D. Xiao, "Adaptive dynamic surface control for uncertain nonaffine nonlinear systems," International Journal of Robust and Nonlinear Control, vol. 27, no. 4, pp. 535-564, 2017.

[13] J. S. Thomsen, "Control of pulsed gas metal arc welding," International Journal of Modelling, Identification and Control, vol. 1, no. 2, pp. 115-125, 2006.

# Optimizing the Energy Efficiency of InGaP/GaAs Double Junction Solar Cells

H. Zeboudj[#1], A. kharoua[#2], S. M. Makrelouf[#3]W. Nasri[#4], B. Hadri[#5]

*#Département de Génie Electrique, Université Abdelhamid Ibn Badis Mostaganem
Route de Belhacel 27000, Faculté des Sciences et de la Technologie, MOSTAGANEM*

[#1]zeboudj47@gmail.com
[#2]amirakharoua@gmail.com
[#3]makrelouf2020@gmail.com
[#4]n.wissem@yahoo.com
[#5]hadriba@yahoo.fr

*Abstract*: **The goal of this research is to improve the performance of InGaP/GaAs solar cells by evaluating the effectiveness of two distinct tunnel junctions. The aim is to surpass the efficiency achieved by InGaP/GaAs and GaAs/GaAs tunnel junction solar cells.To achieve this aim, adjustments to the thickness and concentration of the tunnel junction were made using the TCAD Atlas program.The simulation data indicated that InGaP/GaAs exhibited the top power conversion efficiency at 42.77%, closely trailed by GaAs/GaAs with 41.10%.High fill factors and external quantum efficiency were observed across all two configurations. The study culminates in a comparative analysis of the InGaP/GaAs tunnel junction against the other one, offering significant insights into the optimization of InGaP/GaAs solar cells.**

*Keywords*— **Solar cell,efficiency,Double Junction InGaP/GaAs, diode tunnel, TCAD Atlas**

## Introduction

In recent years, the costs of photovoltaic (PV) solar panels have seen a substantial decrease, while their efficiency continues to improve, thereby enhancing their cost-competitiveness relative to conventional energy sources[1,2].The performance of technologies utilizing crystalline silicon (c-Si) and thin-film technologies like Cadmium Telluride (CdTe) and Copper Indium Gallium Selenide (CIGS) has stabilized at approximately 26% and 23%, respectively [3,4,5] These efficiencies are, however, restricted by the fundamental Shockley-Queisser (SQ) limit, which falls in the range of 31% to 33% for single-junction solar cells. Consequently, researchers are increasingly focusing on multi-junction devices, comprising two or more stacked sub-layers [6,7,8]. Double-junction solar cells are designed with the concept of improving energy conversion efficiency by capturing a broader spectrum of solar light more efficiently. In this design, the first junction absorbs high-energy photons (short wavelengths) as sunlight passes through, while the second junction absorbs low-energy photons (long wavelengths). This sequential absorption of light optimizes energy utilization, resulting in a higher electricity yield from a single cell [9,10,11].

Materials frequently employed in the construction of InGaP/GaAs double-junction solar cells include combinations of semiconductors. Specifically, InGaP (Gallium-Indium Phosphide) is utilized for the first junction, which absorbs higher-energy photons, while GaAs (Gallium Arsenide) is employed for the second junction, responsible for absorbing lower-energy photons. The selection of these material combinations is based on their respective bandgaps, ensuring the optimal absorption of solar light [12,13].

Double-junction solar cells find common application in high-efficiency settings, such as space satellites or concentrated solar power systems, where solar light is concentrated onto the cell to amplify efficiency. While these cells provide superior efficiencies compared to conventional single-junction solar cells, their manufacturing can be more costly due to the intricacy of their structure and the utilization of specific materials. Nevertheless, technological progress and economies of scale are progressively rendering double-junction solar cells more competitive in the solar energy market [14,15,16].

In the context of double-junction solar cells, InGaP serves as the material for the first junction due to its proficiency in absorbing low-energy photons, specifically the longer wavelengths of solar light such as red and

infrared. Consequently, InGaP can efficiently produce electric current from red and infrared light [17]. GaAs is selected for the second junction in double-junction solar cells owing to its effectiveness in absorbing high-energy photons, which corresponds to the shorter wavelengths of solar light like blue and green. This attribute enables GaAs to generate electric current from blue and green light.

A tunnel junction denotes the boundary between two semiconductor materials characterized by distinct properties. At this interface, charge carriers, either electrons or holes, can traverse the potential barrier existing between the two materials through a quantum tunneling phenomenon. This enables particles to overcome a potential barrier without possessing adequate energy, as per the principles of classical physics [18,19].

In a tunnel junction, the energy bands of the two semiconductor materials are misaligned, resulting in the formation of a potential barrier. Nevertheless, the quantum tunneling effect comes into play, allowing electrons or holes to traverse this barrier, overcoming their lower energy levels. This phenomenon facilitates the flow of current through the junction. Tunnel diodes harnessing this principle can be utilized to improve overall performance.

Utilizing tunnel diodes can optimize the performance of multilayer solar cells by reducing series resistance and augmenting the short-circuit current. The selection of a tunnel diode for a III-V tandem solar cell is contingent upon various factors, including electrical resistivity, optical transparency, and the structural characteristics of the tunnel junctions.

Our research involves refining the InGaP/GaAs tandem double-junction solar cell and determining the appropriate tunnel junction type between InGaP and GaAs. A meticulous selection and optimization of the InGaP/GaAs tunnel junction have resulted in remarkably high energy conversion efficiencies of 42.77% under a 1.5G spectrum. Additionally, we explored the influence of factors such as layer thickness and doping concentration in the multilayer solar cell (InGaP/GaAs) on key cell parameters like (FF), ($V_{OC}$), ($J_{SC}$), and ($\eta$)

## I. Tandem configuration

The tandem configuration (InGaP/GaAs) consists of InGaP as the top cell and GaAs as the bottom cell, with the InGaP/GaAs tunnel diode used to connect the top and bottom cells in this model[20].

To optimize power absorption, the top cell (InGaP) should have a bandgap energy (Eg) of approximately 1.84 eV. This upper cell is designed to capture high-energy photons, effectively absorbing shorter wavelengths. Consequently, longer wavelengths are transmitted to the bottom cell. The bottom cell, operating with low-energy photons, is engineered with a bandgap energy (Eg) ranging from 1.42 to 1.43 eV[21,22].

In this configuration, the window layer and back surface field (BSF) layer are both composed of InAlGaP. The window layer, typically made of materials with a broad bandgap, is chosen to facilitate the passage of maximum solar irradiance to the device. Figures 1 and 2 depict the initial schematic structure of the simulated tandem cell
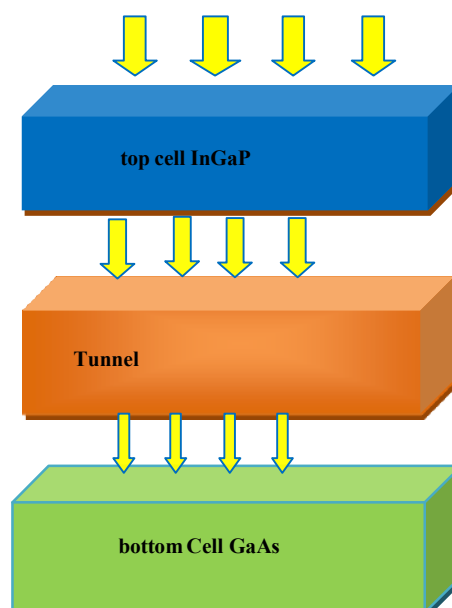
Fig1: A schematic illustration of the studied structure

| | | Anode contact | |
|---|---|---|---|
| 0.011 µm | Window | In(0.3)Al(0.09)Ga(0.7)P(0.91) | 3e21 cm-3 (p-type) |
| 0.059 µm | Emitter | In(0.99)Ga(0.01)P | 4e20 cm-3 (p-type) |
| 0.550 µm | Base | In(0.98)Ga(0.02)P | 2e21 cm-3 (n-type) |
| 0.030 µm | BSF | In(0.2)Al(0.1)Ga(0.8)P0.9 | 1e21 cm-3 (n-type) |
| 0.020 µm | Tunnel Diode | InGaP | 2e21 cm-3 (n-type) |
| 0.001 µm | Tunnel Diode | GaAs | 8e20 cm-3 (p-type) |
| 0.032 µm | Window | In(0.49)Ga(0.51)P | 1e21 cm-3 (p-type) |
| 0.680 µm | Emitter | GaAs | 2e17 cm-3 (p-type) |
| 3.650 µm | Base | GaAs | 4e16 cm-3 (n-type) |
| 0.0099 µm | BSF | Al(0.69)Ga(0.31)As | 2e18 cm-3 (n-type) |
| 0.90 µm | Substrate | GaAs | 9e18 cm-3 (n-type) |
| | | Cathode contact | |

Fig 2: Design of the optimized InGaP/GaAs cell with InGaP/GaAs tunnel junction



Top cellInGaP

Diode

Bottom cell GaAs
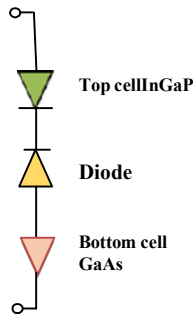
Fig 3: Equivalent circuit of the double-junction InGaP/GaAs solar cell with a tunnel junction[23]
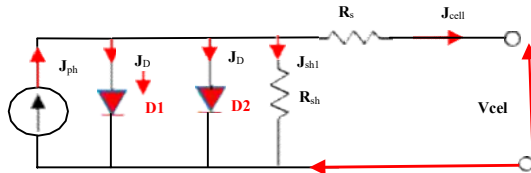


Fig4: Equivalent circuit of the two-diode model for possible exact modeling of the one junction of the double-junction InGaP/GaAs solar cell

From a circuit perspective, it is apparent that a solar cell can be modeled by an ideal current density source ($I_{ph}$) inparallel with two diodes, one with an ideality factor of "1" and the other with an idealityfactor of "2", as shown in Figure 3. Diode D1 represents the recombination current in the quasi-neutral regions, while diode D2 represents recombination in the depletion regionThe series resistance Rs accounts for ohmic losses in materials, metallization, and semiconductor contact. The parallel resistance $R_{sh}$ represents the leakage current between the top and bottom of the cell.

The current density equation for the two-diode model of the PV cell is as follows [24,25]:

$$J_{cell} = J_{ph} - J_{D1} - J_{D2} - \frac{V_{cell} + R_S J_{cell}}{R_{sh}} \quad (1)$$

Where

$$J_{ph}(T,G) = \frac{G}{G0} J_{ph}\, T_0\, G_0\, (1 + C^{T}_{J_{ph}}(T - T_0)) \quad (2)$$

$$J_{D1} = J_{sat1}(T)(exp^{\frac{q(V_{cell}+R_S J_{cell})}{n_1 KT}} - 1) \quad (3)$$

Where $J_{cell}$ is the current density delivered by the cell, $J_{ph}$ is the photocurrent density, $J_D$ is the diode current density, and $J_{sh}$ is the shunt current density, $V_{cell}$ is the cell voltage, $J_{D1}$ is the current density of the first diode due to the diffusion of minority carriers and recombination in the depletion region, RS and RP are the series and shunt resistances of the cell, $J_{satl}$ is the reverse saturation current density, n is the ideality factor, T is the temperature, and G is the received solar irradiance energy.

The top and bottom cells are connected in series with the tunnel diode and carry the same current

The tunnel-junction interconnect between the InGaP and GaAs subcells serves an important electrical purpose. It provides a low-resistance connection path joining the p-type back surface field (BSF) layer of the top InGaP cell to the n-type window layer of the bottom GaAs cell. Without this conductive tunnel junction, the opposing polarity p-n layers would form a junction with its own photovoltage under illumination. This photovoltage would act in opposition to the useful photovoltages generated by the top and bottom cells above and below the junction. So the tunnel junction functions to effectively short out or bypass this counterproductive middle junction, allowing the total voltage generated by the multi-junction stack to equal the sum of the top and bottom cell photovoltages. This connects the subcells in series electrically using a low-resistance interface optimized for multijunction operation.

Vcell is the algebraic sum of the top and bottom cell voltages, including the tunnel junction voltage.

$$V_{cell} = V_1 - V_{DT} + V_2 \quad (4)$$

The functional form of $J_{DT}$ is dominated by an exponential term of the form:

$$J_{DT}\, \alpha\,(- \frac{E_g^{3/2}}{\sqrt{N}}) \quad (5)$$

where $E_g$ is the band gap and $N = N_A N_D/(N_A + N_D)$ is the effective doping concentration [110]. The value of $J_{DT}$ must be larger than the photocurrent of the tandem cell. If $J_{DT} < J_{SC}$, the behavior of the tunnel junction current switches to that dominated by the usual thermionic emission and the voltage drop across the tunnel junction increases to that of a typical *p-n* junction.

Numerical device simulations were conducted to model the structure shown in Figure 2. These simulations employed technology computer aided design (TCAD) software using ATLAS modules. The ATLAS simulation engine solves the fundamental semiconductor equations that govern carrier transport and electrostatics in semiconductor devices. Specifically, the Poisson equation is solved to determine the electric potential distribution based on space charge density. Additionally, the continuity equations for electrons and holes are solved to find the carrier concentrations throughout the device under bias. These coupled physical models enable simulation of electrical and optical characteristics based on the physics of carrier dynamics, allowing investigation of the Figure 2 device without the need for fabrication.

$$\frac{\partial n}{\partial t} = \frac{1}{q}\nabla J_n + G_n - R_n \quad (6)$$

$$div(\varepsilon \nabla T) = -\rho \quad (7)$$

$$\frac{\partial p}{\partial t} = \frac{1}{q}\nabla J_p + G_p - R_p \quad (8)$$

Where $\varepsilon$ is the dielectric permittivity, $\rho$ is the local charge density, q is the elementary charge, $\psi$ is the electric potential, $G_n$, $R_n$, $G_p$, and $R_p$ express the generation and recombination rates for electrons and holes, and $J_n$ and $J_p$ are the electron and hole current densities, respectively

I. THE TUNNEL JUNCTION EFFECT

A tunnel junction interconnect is utilized between the InGaP top cell and GaAs bottom cell to provide a low resistance electrical connection path linking the p-doped back surface field (BSF) layer of the InGaP top cell to the n-doped window layer of the GaAs bottom cell. The tunnel junction functions as a conductive bridge serving to connect the two subcells in series, thereby avoiding a high resistance or rectifying junction between the disparate p- and n-type polarity layers of the adjacent multijunction subcells.

Tunnel junctions composed of GaAs/GaAs, InGaP/GaAs, or InGaP/InGaP semiconductor layers are most prevalent in high efficiency multijunction solar cells. These materials offer suitable band alignments to facilitate low resistance tunneling current flow. To optimize the tunnel junction design and further improve efficiency in our simulated InGaP/GaAs tandem device, we computationally modeled a range of layer doping concentrations and materials. Advanced numerical simulation enables systematic optimization of the multilayer tunnel junction interconnect by accounting for carrier transport physics across the full solar cell stack. Leveraging these simulations, presented in detail in references [24] and [26], we pursued performance gains through refined tunnel junction calibration. This approach shows promise for guiding design of next-generation InGaP/GaAs-based tandem cells with potentials beyond existing limits.Through extensive numerical device simulations investigating a range of tunnel junction materials and designs, we determined an optimal configuration yielding maximum tandem solar cell efficiency. The modeling results indicated that an InGaP/GaAs tunnel junction interconnect structure provides superior performance in the InGaP/GaAs dual-junction stack. This specific low-resistance tunnel diode achieved the highest simulated efficiency among the candidate tunnel junction options considered. The optimized carrier transport and reduced optical absorption losses in the InGaP/GaAs tunnel junction boost current matching and voltage yield of the complete device structure. We have identified an InGaP-based tunnel junction that sets a new performance standard for the class of III-V multijunction photovoltaics targeted in this work.

the results are illustrated in Table 1

Table 1: Simulation Results for Each Type of Tunnel Junction Used

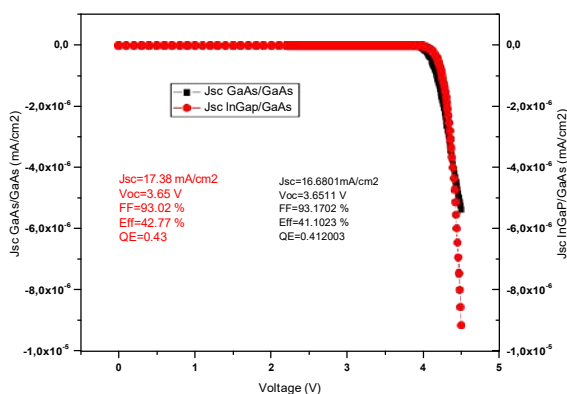| type of tunnel junction | efficiency (%) | FF(%) | $V_{oc}$ (V) | $J_{sc}$ (mA/cm$^2$) |
|---|---|---|---|---|
| InGaP/GaAs | 42.77 | 93.02 | 3.65 | 17.38 |
| GaAs/GaAs | 41.10 | 93.17 | 3.65 | 16.68 |



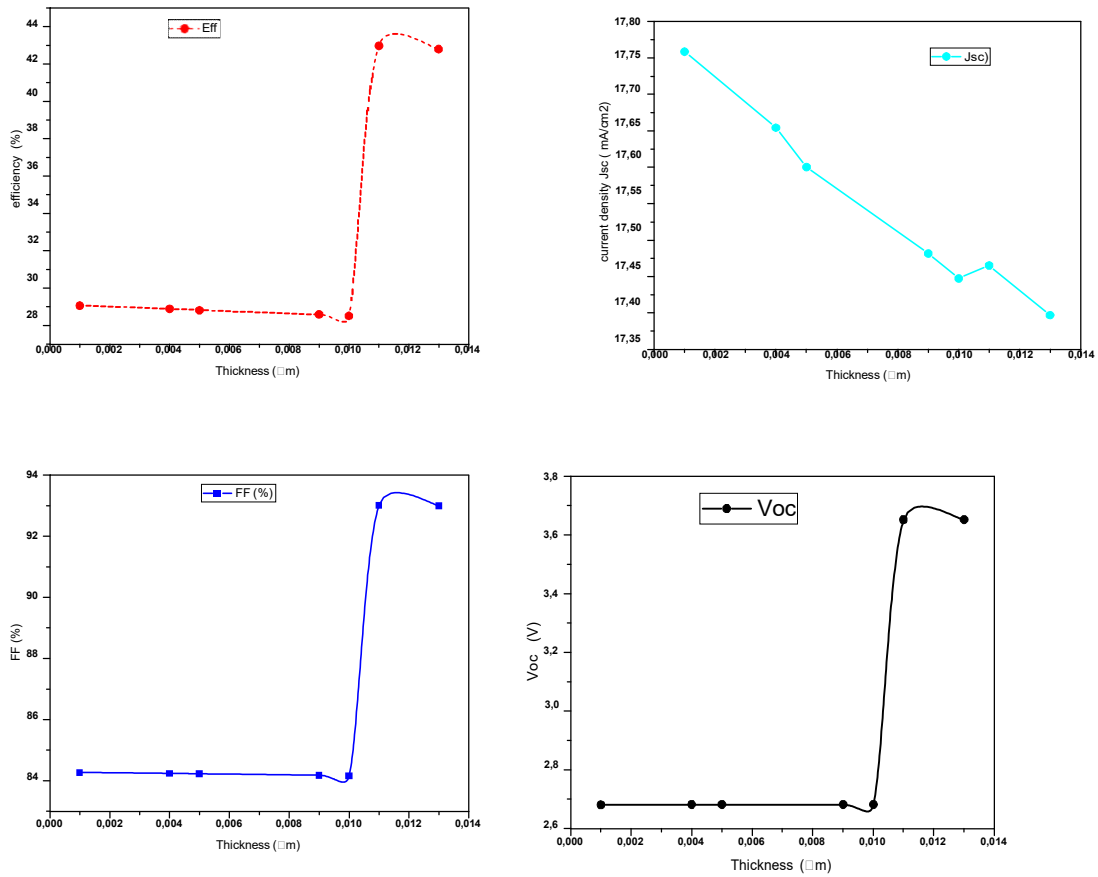Fig 5: J-V Characteristics with Tunnel Junction InGaP/GaAs and GaAs/GaAs

Fig. 7: Effects of Window InAlGaPlayer thicknessvariation on dual-junction solar cell performance, (a) efficiency, (b) open-circuit voltage (c)Fill factor d) short circuit current density,
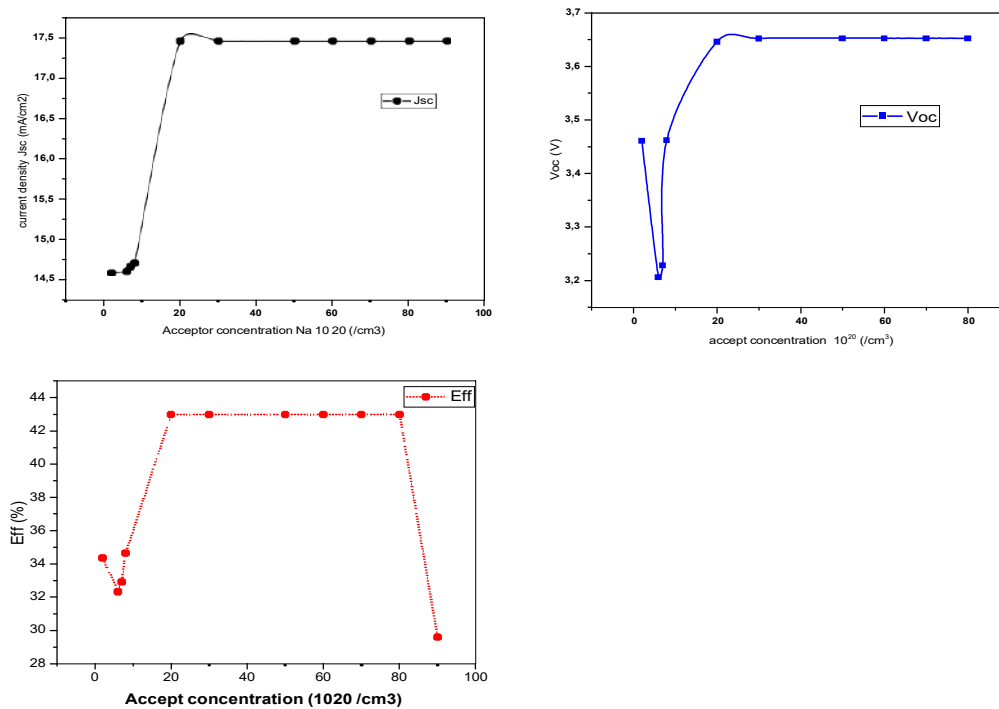


Fig 8: The window layer doping concentrationvariation effect on a) current densityJsc b) Voc c) efficiency .

## II. Effect of Window InAlGaP layer thickness

The impact of thickness on performance parameters is depicted in Figure 7. Examining the diverse performance graphs reveals that the optimal efficiency is achieved at a thickness of 0.011 nm. Figure 7 illustrates that both the efficiency (Jsc - short-circuit current density) and the Voc (open-circuit voltage) follow a parallel trend. Concerning the open-circuit voltage (Voc) parameter, it remains relatively constant across the range of thickness variations. The Voc values consistently hover around 2.68 V for thicknesses spanning from 0.001 nm to 0.011 nm. In contrast, the short-circuit current density (Jsc) is influenced by the escalating thickness.

### The impact of changing doping density for the window InAlGaP layer of the top cell on the dual junction cell

Another step involves adjusting the doping density of the window layer from $Na=2 10^{20}$ $cm^{-3}$ to $Na=9 10^{21}$ $cm^{-3}$. Efficiency reaches its maximum value η=42,77% and Fill factor reaches its minimum value of 93.01%. when theacceptor concentration (Na) is $3 10^{21} cm^{-3}$ Figures 8 illustrate the impact of variation of the doping density of the top cell window InAlGaPlayer versus on the efficiency of InGaP/GaAs dual junction, FF, $V_{OC}$, and $J_{SC}$.

Table 3 Comparison between the proposed structure with other works

| Tandem cells | InGaP/GaAs [21] | InGaP/GaAs [26] | InGaP/GaAs [27] | Proposed structure |
|---|---|---|---|---|
| Jsc mA/cm² | 14.54 | 16.4999 | 19:84 | 17.38 |
| Voc V | 2.62 | 2.2340 | 2:32 V | 3.65 |
| FF(%) | 90.61 | 87.9201 | 83:9% | 93.02 |
| Eff(%) | 34.53 | 36.8608 | 38:53% | 42.77 |

The table presented above unmistakably demonstrates a notable enhancement in conversion efficiency for the current structure, reaching an impressive 42.77%—a substantial leap from previous design iterations. This noteworthy progress underscores the triumph and efficacy of the novel structure in optimizing the transformation of input energy into the desired output.

## III. CONCLUSIONS

In this study, the refinement of the proposed InGaP/GaAs dual junction structure with a tunnel junction InGaP/GaAs involved meticulous adjustments to the doping concentration and thickness of the top cell's window layer. These strategic modifications were implemented with the aim of elevating the overall performance and efficiency of the structure.Through meticulous adjustment of these parameters, our objective was to enhance the overall performance and optimize the power conversion efficiency of the device. This fine-tuning process afforded us greater control over the electrical and optical properties of the structure, culminating in improved performance characteristics.Based on simulation outcomes, the dual junction cell yielded impressive results, with a short-circuit current density (Jsc) of 17.38 mA/cm2, an open-circuit voltage (Voc) of 3.65 V, a fill factor (FF) of 93.02%, and an overall efficiency (η) of approximately 42.77%. All assessments were conducted under standard AM1.5 illumination. Notably, the proposed structure outperformed previous research, showcasing superior performance across key parameters.

### References

[1] GoksinKavlak,JamesMcNerney,Jessika E.Trancik "Evaluating the causes of cost reduction in photovoltaic modules Energy Policy"Volume 123, , Pages 700-710  December 2018

[2] Brittany L. Smith,1 Michael Woodhouse,1 Kelsey A. W. Horowitz,1 Timothy J. Silverman,1 Jarett Zuboy,2 and Robert M. Margolis1 Photovoltaic (PV) Module Technologies: 2020 Benchmark Costs and Technology Evolution Framework Results NREL/TP-7A40-78173 November 2021

[3] Jeyakumar Ramanujan and U dai.P.Singh Copper indium gallium selenide based solar cells – a review Energy & Environmental Science  Issue ,2017

[4] Hervé Joël Tchognia Nkuissi, Fransisco Kouadio Konan, Bouchaib Hartiti and Jean-Marie NdjakaToxic Materials Used in Thin Film Photovoltaics and Their Impacts on Environment Books Reliability and Ecological Aspects of Photovoltaic Modules08 January 2020

[5] Kam Hoe Ong, Ramasamy Agileswari, Biancamaria Maniscalco, Panagiota Arnou, Chakrabarty Chandan Kumar, Jake W. Bowers, and Marayati Bte MarsadekReview on Substrate and Molybdenum Back Contact in CIGS Thin Film Solar Cell international journal of photoenergy Volume 2018 | Article ID 9106269

[6] Kashif Hussain, Alessio Gagliardi Modelling tandem/multi-junction hybrid perovskite–organic solar cells: A combined drift–diffusion and kinetic Monte Carlo study Solar EnergyVolume 243, 1 September 2022, Pages 193-202

[7] Masafumi Yamaguchi Frank Dimroth John F. Geisz Nicholas J. Ekins-DaukesMulti-junction solar cells paving the way for super high-efficiencyJ. Appl. Phys. 129, 240901 (2021)

[8] Adil Baiju and Maksym Yarema Status and challenges of multi-junction solar cell technologyFrontiers in Energy Research Volume 10 - 2022

[9] Zhen Li and Kai ZhuUltra-High Efficiency Perovskite–Perovskite Tandem Solar CellsPhotovoltaics & Solar Cells

[10] Andrea Cordaro*Ralph Müller Stefan Wil Tabernig Nico Tucher Patrick Schygulla Oliver Höhn Benedikt Bläsi and Albert Polman Nanopatterned Back-Reflector with Engineered Near-Field/Far-Field Light Scattering for Enhanced Light Trapping in Silicon-Based Multijunction Solar Cells  ACS Photonics 2023, October 26, 2023

[11] Abdulaziz S.R.Bati, Yu Lin Zhong Next generation application for integrated perovskite solar cells, communication Materials,4 , Article number 2(2023)

[12] Senthilarasu Sundaram, David Benson, Tapas Kumar Mallick chapter 3.4.3 Multijunction Solar Cells Solar Photovoltaic Technology Production, 2016

[13] Simon P. Philipps, Andreas W. BettChapter I-4-B High-Efficiency III–V Multijunction Solar Cells, in McEvoy's Handbook of Photovoltaics (Third Edition), 2018

[14] Rosaria Verduci, Valentino Romano, Giuseppe Brunetti, Narges Yaghoobi Nia, Aldo Di Carlo, Giovanna D'Angelo, Caterina Ciminelli Solar Energy in Space Applications: Review and Technology Perspectives 22 June 2022

[15] Sara SabriRachid MalekKhalil Kassmiimprovement Efficiency of Solar Cells Using III-V Dual Junction: InGap/GaAsAugust 2023 Key Engineering Materials 954(12):97-109

[16] Fatima Zahra KharchichAbdellatif KhamlichiOptimizing efficiency of InGaP/GaAs dual-junction solar cells with double tunnel junction and bottom back surface field layers Nov 2022 OPTIK

[17] F.Djaafar, B. Hadri, and G. Bachir, "Optimal parameters for performant heterojunction InGaP/GaAs solar cell," International Journal of Hydrogen Energy, vol. 42, no. 13, pp. 8644–8649, 2017

[18] N. Moulin, Mohamed Amara, F. Mandorlo, M. Lemiti Tunnel junction I (V) characteristics: Review and a new model for p-n homojunctions  Journal of Applied Physics, 2019, 126 (3), pp.033105. ff10.1063/1.5104314ff. ffhal-03035269f

[19] Mike Schwarz, Tom D Vethaak, Vincent Derycke , Anaïs Francheteau , Benjamin Iniguez, Satender Kataria, Alexander Kloes , Francois Lefloch , Max Lemme, John P Snyder , Walter M Weber and Laurie E Calvet The Schottky barrier transistor in emerging electronic devices  Nanotechnology 34 (2023) 352002 (35pp)

[20] Marwa S. Salem ,Omar M. Saif,Ahmed Shaker ,Mohamed Abouelatta ,Abdullah J. Alzahrani,Adwan Alanazi ,M. K. Elsaid,and Rabie A. RamadanPerformance Optimization of the InGaP/GaAs Dual-Junction Solar Cell Using SILVACO TCAD International Journal of PhotoenergyVolume 2021, Article ID 8842975

[21] F.Djaaffar Etude et Modélisation des Performances des Cellules Photovoltaïques à Multi Couches à Base des Semi-conducteurs Inorganiques. thèse de doctorat Soutenue le : 30-10-2018 Oran Algeria

[22] M. Babar, E.A. Al-Ammar & N. H Malik, «Numerical simulation model ofmultijunction solar cell», Journal of Energy Technologies and Policy (2012), 2(7), 44-53

[23] Nour El I. Boukort, Alamera Nouran Alquennah, Amal M. AlAmri, Photogeneration losses from interface trap density in Passivated Ultrathin CIGS Solar Cell IECON 2022 Annual Conference of the IEEE Industrial Electronics Society | 978 -1-6654-8025-3/22 IEEE Xplore.January 08,2023

[24] Marwah M. Salim Khalid Kh. Mohammed Al-Rafidain Simulation of High Efficiency Tandem Solar Cell using InGaP/GaAs Engineering Journal (AREJ) Vol.26, No.2, October 2021,pp.171-178

[25] Fatima Zahra Kharchich, Abdellatif Khamlichi Optimizing efficiency of InGaP/GaAs dual-junction solar cells with double tunnel junction and bottom back surface field layers OptikVolume 272, February 2023, 170196

[26] M. Babar, E.A. Al-Ammar & N. H Malik, «Numerical simulation model ofmultijunction solar cell», Journal of Energy Technologies and Policy (2012), 2(7), 44-53

[27] Nemat azimi1, Sara ghari , Hassan Rasooli Saghai Modeling Arc less Ingap/Gaas Double Junction Solar Cell with Tunneling Junction and Bsf Layer Stem Cell Research International Stem Cell Res Int, Volume 6 | Issue 2 | 100 2022

.

# Thermal performance enhancement of parabolic trough collector: a new generalized correlation of the absorber's optimum diameter

Anissa GHOMRASSI[#1], Hatem MHIRI[#2] and Philippe BOURNOT*[3]

[#] *Thermal and Thermodynamics Laboratory in Industrial Processes, National Engineering School of Monastir, Tunisia*
[1]ghomrassi.anissa@hotmail.com
[2]hatem.mhiri@enim.rnu.tn
[*]*IUSTI, UMR CNRS 6595, Château-Gombert technopole, 5 Enrico Fermi street, Marseille 13013, France*
[3]philippebournot@yahoo.fr

*Abstract*– **The purpose of this paper is to optimize absorber geometry in order to enhance parabolic trough collector's performance. A series of numerical simulations performed by Soltrace software and CFD code are performed. Indeed, it is shown that the outlet temperature can be improved by receiver diameter raise. Yet, there is a receiver optimum diameter from which the outlet temperature diminishes. A new correlation of the receiver tube optimum diameter is deduced to generalize this latter finding. Absorber tube with external layer can also enhance its performance. That is why, a new receiver tube surrounded by a metal thickness is tested.**

*Keywords*– **PTC; MCRT method; Receiver tube optimum diameter; Empirical correlation; external layer.**

## I. INTRODUCTION

Solar energy is regarded as an unlimited and clean future energy source. Since solar energy is abundant, it seems interesting to focus it by reflectors in order to acquire high temperatures needed for electricity production. The most approved technology of concentrating solar power is parabolic-trough-collector (PTC) compared to other existing technologies (solar-tower-system, reflector-Fresnel-mirrors and solar-dish) (Mao Q G et al. 2014; Cherif H et al. 2019, Codd, D S. et al. 2020).

The PTC is principally constituted of an absorber, mirrors and a support structure (Bellos E et al. 2016). The absorber is a copper or steel tube coated by a black paint.

Optical study is developed by MCRT method by Cheng et al. (2014). PTC were designed, manufactured and tested experimentally by Ghomrassi et al. (2017). The MCRT is coupled to CFD models to suitably reproduce the experimental results (Wang et al. (2010)).

## II. METHODOLOGY

The adopted numerical procedure consists of two key steps. In the first step, Solar Heat Flux (SHF) focused in a focal line is determined by Soltrace software. In the second step, receiver thermal performances are optimized by Computational Fluid Dynamic (CFD) modeling.

## III. RESULTS AND DISCUSSIONS

The studied Parabolic Trough collector is represented in figure 1. The receiver diameter enhances the PTC system's optical performance by raising the SHF on its inferior periphery (figure 2).
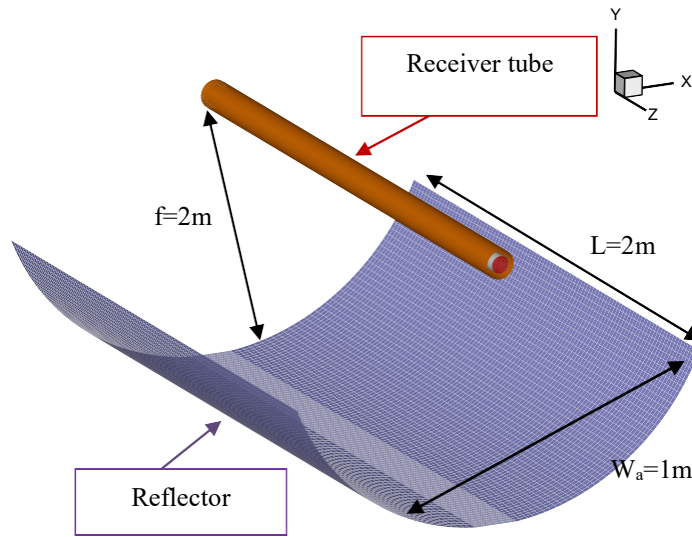
Fig.1 PTC system studied
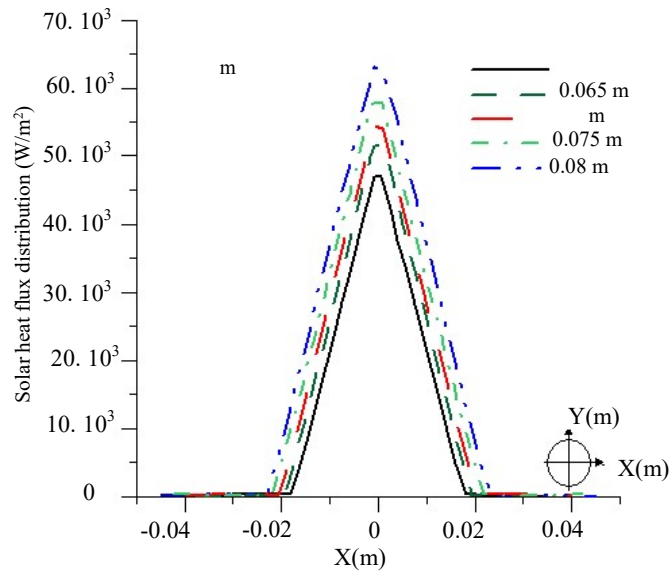


Fig. 2 SHF distributions for different absorber tube diameters

Based on the Soltrace software results, we found that as the absorber tube diameter rises, the SHF concentrated on the tube inferior half increases. Furthermore, raising the tube diameter implies a growth in the exchange surface with the environment and this can cause a rise in heat losses to the exterior.

The raise in the absorber diameter brings on a growth in SHF concentrated, therefore an augmentation in the working fluid outflow temperature (figure 3).
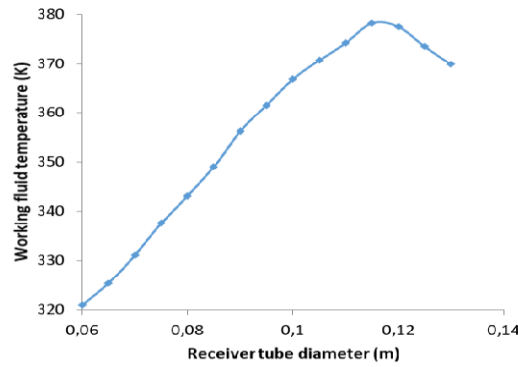
Fig. 3 Temperature evolutions

However, there is doubtless an absorber tube optimum diameter ($d_{ri}$ = 0.115 m) beyond that fluid temperature at exit section reduces.

To generalize this outcome, a mathematical expression is established to determine the absorber tube optimum diameter for any PTC's dimension.

Different aperture widths ($W_a$) are tested for diverse absorber tube diameters. SHF for different aperture widths and for different absorber tube diameters are estimated by Soltrace. Then, the SHF distribution in each case is introduced in ANSYS software as User defined functions written in C++ program. After that, thirty-five CFD simulations are launched.

Temperature fluid evolutions for diverse receiver diameters and for various opening widths are shown in Figure 4. Then, the optimum tube diameter for each configuration is then determined. This lets us deduct a generalized expression of the receiver optimum diameter from which the PTC system's performance reduces. We have established that the optimum diameter pursues a linear law: optimum diameter (dop) in function of the opening width Wa (see Figure 5) and can be written as follows:

$$d_o = 0.006 W_a + 0.088 \tag{1}$$

This new correlation is statistically meaningful with an $R^2$ =0.95. This generalized expression will be advantageous for any configuration of the PTC system.
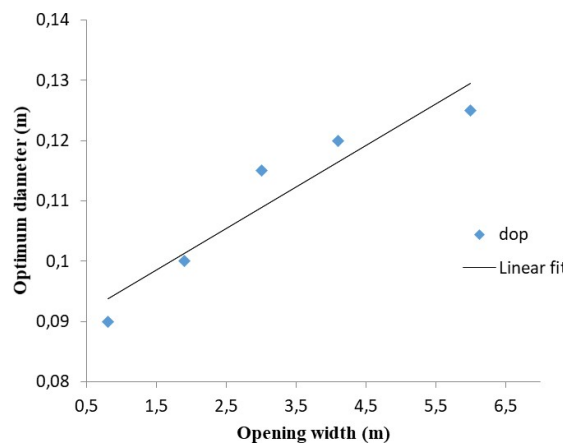


Fig. 5 Evolution of the optimal diameters as a function of the opening widths Wa

## IV. CONCLUSIONS

Finally, we can announce that the MCRT method combined to the CFD model give satisfactory results. Diverse receiver tube diameters were tested to acquire a PTC's optimum diameter. A new correlation has been developed. This finding avoids future researches to conduct experiments or numerical simulations trying to calculate tube diameter for different reflector configurations. In order to improve the PTC system performance by increasing the

heat transfer fluid energy absorbed and by the thermal losses reduction to the outside, a new type of receiver tube is tested. The latter is surrounded by a metal thickness.
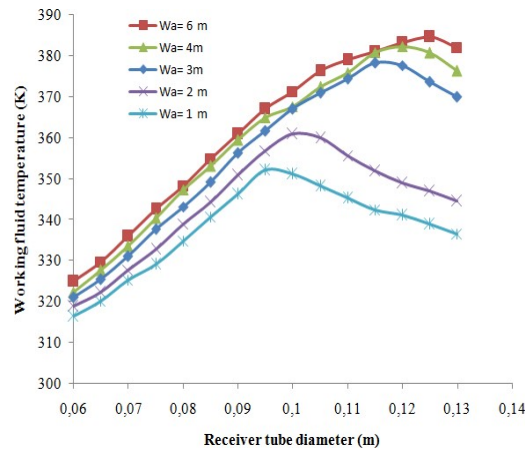


Fig. 4 Average temperatures at the outlet section for different dri and for different Wa

## REFERENCES

[1] Q.G. Mao, Y. Shuai, and Yuan. Y., *Study on Radiation Flux of the Receiver with a Parabolic Solar Concentrator System.* Energy Conversion and Management, Vol. 84, pp. 1–6, 2014.

[2] H. Cherif, A. Ghomrassi, J. Sghaier, H. Mhiri and P. Bournot*, A receiver geometrical details effect on a solar parabolic dish collector performance.* Energy Reports, Vol. 5, pp. 882-897, 2019.

[3] D.S. Codd, A. Gil, M.T. Manzoor, *Concentrating solar power (CSP)—thermal energy storage (TES) advanced concept development and demonstrations.* Sustainable and Renewable Energy, Vol. 7, pp. 17-27, 2020.

[4] E. Bellos and C. A Tzivanidis, *Detailed working fluid investigation for solar parabolic trough collectors.* Applied Thermal Engineering, 10.1016/. 11.201, 2016.

[5] Z. D. Cheng, Y. L. He. and Cui. F. Q. *Numerical Study of Heat Transfer Enhancement by Unilateral Longitudinal Vortex Generators Inside Parabolic Trough Solar Receivers.* Int. J. Heat Mass Transfer, vol. 55, pp. 21–22, 2012.

[6] A. Ghomrassi, H. Mhiri, and P. Bournot, *Experimental study of the PTC tilt angle's variation on its performance under a Tunisian desert climate*. International Conference on Engineering & MIS (ICEMIS), DOI: 10.1109/ICEMIS.2017.8273071, 2017.

[7] F. Wang, Y. Shuai, Y. Yuan, G. Yang, and H. Tan. *Effects of Material Selection on the Thermal Stresses of Tube Receiver Under Concentrated Solar Irradiation.* Material Dessalination, vol. 33, pp. 284–291, 2010.

# Experimental study of a thermal comfort in cells impregnated by a phase change materiel

M. Dehmous[#1], N. Lamrous[#2], E. Franquet [*3]

[#] *LMSE, Université Mouloud Mammeri de Tizi Ouzou, Algérie*
[1]*nacer.lamrous@gmail.com*

[*]*Université de Pau & Pays de l'Adour, LaTEP, 64000 Pau, France*

*Abstract*—**The purpose of this study is to combine lightness and architectural aesthetics with the thermal and energetic qualities of concrete walls. Lightweight concrete with high thermal energy storage capacity was manufactured by mixing a composite phase change material (PCM), namely coconut oil (GV23-26), with sepiolite (S). Cells formed with these panels are subject to the vagaries of the summer climate over a few days at the same time as another cell, of the same dimensions, with ordinary concrete walls for comparison purposes. The measurements focused on the air temperature inside and outside the cells, the temperature of the walls as well as the heat fluxes exchanged at the walls and the amount of heat absorbed by these walls. Particular attention is paid to the internal temperature, an essential parameter of the thermal comfort of the cells. Our experiments have shown an increase in the thermal capacity of the cell envelope by the addition of PCMs, which by storing an additional part of the incident heat fluxes, leads to a reduction in cells inner temperature. This effect, positive for the thermal comfort, is accompanied by a reduction in the thickness and therefore the weight of the wall panels compared to ordinary concrete wall panel.**

*Keywords*—**Experimental study, Thermal comfort in cells, Panels with PCM, Coconut oil**

## I. INTRODUCTION

As the industrial and transport sectors, the building (residential together with tertiary sectors) has become the largest consumer of energy in the world with 29% of total energy consumption. In France, the proportion of the final consumption of the residential sector reaches over 24% mainly due to the excessive use of mechanical heating and cooling systems in the building to guarantee the thermal comfort of the occupants [International Energy Agency (IEA) Data and statistics of 2018 (iea.org)]. Thermal comfort can be obtained in the building by passive or active means. Active means relate to the transfer of energy, stored or not, with mechanical or thermal systems, while passive means are mainly linked to thermal storage in the building envelope itself. [1]. Thermal energy storage (TES) in the building envelope in particular is one of the passive means put forward to reduce the energy consumption of buildings. The use of phase change materials (PCM) in the building envelope has been widely studied to take advantage of the latent heat stored during the phase change. The implementation of PCM has become a means of providing thermal inertia to the building [2].

For example, according to the manufacturer BASF-Micronal, a wall containing 2 cm of PCM manufactured by BASF has the same performance in terms of thermal inertia as a brick 36 cm thick or a concrete wall of 24 cm thick or solid wood 38 cm thick [3]. Several criteria exist for the classification of PCMs according to their chemical composition, their melting temperature, their latent heat of fusion, etc. The most frequent categorization divides them into three groups: organic, inorganic and eutectic [4]. Comparisons made by several authors [5], [6] present the advantages and disadvantages of organic and inorganic materials. A large number of materials have been used and studied as PCM for thermal energy storage. These are mainly hydrated salts, paraffin waxes, fatty acids and eutectics of organic and inorganic compounds. Furthermore, a non-exhaustive list of commercially available PCMs can be found in [6]–[9]. The phase change temperature as well as the melting range remain important criteria in choosing the type of PCM to use. Their meltingrange can be determined depending on the desired application (building, nuclear, transport, food, textile, etc.). On the other hand, these materials must exhibit a high latent heat of fusion. Other criteria should also be considered (see [1], [10]). PCMs are often encapsulated before being added to the material. There are two types of encapsulation, microencapsulation and macroencapsulation. However, it is common to find in certain research works a mix between microencapsulation and macroencapsulation of MCP [11]–[14]. Encapsulated PCMs are generally prepared using industrial techniques. The capsules are most often made from inert materials (natural or synthetic polymer), which allows them not to chemically interact with the materials with which they are in contact (PCM or matrix). In addition, these capsules must have high thermal conductivity for optimal melting of the PCM and must be strong to withstand the mixing process. In addition, several authors have opted for the use of lightweight aggregates with a porous structure (LWA) as PCM containers. They are generally

mineral aggregates that are perfectly compatible with most building materials, especially concrete. They allow a higher content of PCM and are produced easily and at low cost. Most clayey mineral materials have a porous structure and a considerable specific surface. Thus, the adsorption capacity of the clay mineral is excellent and the PCM can easily be impregnated therein. On the other hand, clayey mineral materials having a small specific surface and a small spacing between the layers are not very conducive to the loading of the PCM. The interactions between PCM and mineral clay materials are mainly capillary force, surface tension, hydrogen bonding, Van der Waals force, etc. These interactions may limit PCM leakage from TESAs [8]. Commonly used clay mineral materials are kaolin [15], diatomite [16]–[24], sepiolite [25]–[27], bentonite [28]–[32], perlite [33]–[38], le $SiO_2$[39]–[41], attapulgite [42], vermiculite [33], [34], [43], etc. mineral materials have relatively high thermal conductivity and excellent adsorption, which successfully remedies the shortcomings of MCP. Most of the work available in the literature that deals with the thermal analysis of composites incorporating TESAs indicates the same result; higher thermal storage capacity and lower thermal conductivity [15], [44]–[46]. Special coating materials were used to prevent leakage of PCM from the LWA but also to improve the thermal conductivity of the final composite material. Thus, it is possible to integrate it into a metal matrix [47], [48] or to manufacture a composite having better thermophysical properties by dispersing particles of high thermal conductivity in the PCM such as graphite, graphene or again aluminum (incompatible with concrete) [49]. When no precautions are taken, the technique of impregnating light mineral aggregates with PCM has the main drawback of leaking PCM in the liquid state. After a few cycles of fusion solidification, the structure of the composite is destabilized and the effectiveness and role of PCM are called into question. To prevent any PCM leakage, most of the studies available in the literature use a protective coating generally comprising epoxy resin, graphite powder and silica fume [15], [32], [44]–[46], [50], [51]. Another solution is to limit the maximum degree of filling to 80 %v in order to minimize the risk of leakage [52].

When used in buildings, PCMs can be integrated into walls, windows, sunscreens and window shutters, ceilings and floors [53]. This integration essentially depends on the different target applications, thus making use of unique configurations and characteristics. In most of the existing studies related to the integration of PCMs in the building envelope, it is in walls that PCMs are mainly applied. This part of the envelope represents the area where the heat exchange is greatest and efficient, but also where the implementation is practical and simple [10].

The different modes of integrating MCP into walls can be categorized into two main families, namely immersion and attachment. Immersion is the introduction of PCMs into building materials by means of microencapsulation, macroencapsulation or direct immersion techniques, while attachment is the addition of one or more layers of PCM to a wall. This addition remains independent of the main wall.

**Error! Reference source not found.**shows a sample of research work integrating a variety of PCM products into walls by different methods. In some buildings, especially those used as offices, the outer envelope is made of light and transparent elements and the internal partitions are often absent and give way to an open configuration (open spaces).

TABLE 1.

RESEARCH INTEGRATING PCM PRODUCTS INTO WALLS USING DIFFERENT METHODS

| Authors | Integration mode | PCM | Wall materiel containing the PCM | Résultats essentiels |
|---|---|---|---|---|
| [1] | Attach | PEG 600 | Fiber cement, VIP panels, PCM pannels, Wooden plywood | - Decrease of the amplitude of the interior temperature by about 20 °C in summer. Storage and significant heat release in winter. |
| [70] | Mic | Micronal® | PCM concrete | - The thermal comfort time is increased by at least 10% and the maximum temperature is reduced by 6%. |
| [73] | Mic-Attach | Inertek | PCM concrete | - Significant reduction in thermal conductivity. Reduction of peak internal surface temperature up to 1.7 ° C. Thermal phase shift of about 2 hours. |
| [57] | Attach | BioPCM$^{TM}$ Energain | PCM panels, Plaster panels | - Lower temperature fluctuations for longer periods, shifting the temperature peak and reducing temperature extremes. |
| [2], [69] | Mic | Micronal® | PCM concrete | - (2007) Increase in thermal inertia, thermal phase shift of about 2 hours. Other monthly suggestions.<br>- (2019) Reduction of surface temperatures. Large thermal phase shift of internal ambient temperatures and |

| | | | | smoother fluctuations between day and night. Same thermal response and mechanical resistance same after ten years. |
|---|---|---|---|---|
| [72] | Mac | Fatty acid Paraffin Salt hydrated | Glass bricks | - Significant increase in temperatures with the use of PCM but remaining lower than those without using PCM. Necessary for systems with PCM coupled with efficient night ventilation and strict limitation of solar gain. |
| [13] | Mac-Attach | RT27 SP-25 A8 | Polyurethane, Bricks, PCM panels | - The use of PCM reduces the temperature peak by 1 ° C and the electrical energy consumption by 15%. |
| [64] | Mic | Eutectic : capric Acid myristic Acid | PCM concrète | - Decrease in mechanical resistance. The microcapsules retained their spherical shape after addition to concrete. A 2 ° C damping is achieved at midday, or 13% energy savings according to ASHRAE standards. PCM thermally stable after 2 years. |
| [63] | Mac-Attach | Energain | Plaster, Polystyrene Wood panels, PCM panels | - Reduction of air temperature fluctuations in the room. Lower overheating with the use of PCM. Reduction of wall surface temperatures with PCMs. Improvement of thermal comfort by radiative effects. |
| [61] | Mac-Attach | SP29 RT18 | Polystyrene, PCM panels | - Temperature drop of approximately 4.28 to 7.7 ° C during the summer day and a temperature increase of 2.02 to 2.71 ° C during the summer night. Temperature drop for the winter day from 11.21 to 14.12 ° C and the temperature rise from 6.93 to 9.48 ° C for the winter night. Reduction of temperature fluctuation from 17.7 to 25.4% in winter and from 28.8 to 67.8% in summer. |
| 86 | | RT-27 SP-25 A8 Ester | Cement mortar, Bricks, Polyurethane, Plaster, Concrete, Asphalt, Stone | - The use of the ester as PCM improves thermal results. The use of salt or ester hydrates as PCM in cells results in an impact reduction of 9% and 10.5% respectively, compared to paraffin. Adding polyurethane to any cell increases the total impact score by approximately 20%. |
| 74 | Attach | Energain | Cement mortar, Bricks, PCM panels | - The thermal phase shift reaches up to 7.3 ° C. Reduction of thermal losses through the ceiling by approximately 50%. More efficient PCM in the ceiling. 6h shift in the passage of calories through the PCM layer. Reduction of energy consumption by 20%. |
| 87 | Attach | BioPCM Q23 M51 | Aluminum panels, Plaster panels, PCM | - Significant passive cooling can be achieved with 17 m² of PCM. A moderate temperature drop is observed when the PCM is covered with aluminum ceiling panels and plasterboard. |
| 16 | Mac | RT18® | Bricks, Cement, PCM | - The PCM significantly increases the heat storage capacity of the tested wall samples. The thermal amplitude has been reduced by 80%, when the PCM is combined with external insulation. |

In this specific case and in many other situations, it is difficult to find vertical surfaces where we can integrate PCMs in order to boost the thermal energy storage of the structure. This is one of the reasons for choosing roofs and / or false ceiling elements for loading with MCP. Many authors have published research where PCMs have been integrated using different methods in the roof or under ceilings [13], [53]–[58]. PCMs are also integrated into glazed surfaces such as glass bricks and air gaps in double glazing [59], [60].

In the construction industry, the trend is now to reduce the thickness of the walls to reduce their weight, transport costs and construction time. Lightweight envelopes are used more and more frequently in modern buildings; however, they have the drawback of insufficient thermal inertia. One of the solutions advocated by many specialists is to incorporate PCM in the envelope [1].

TABLE 2.

LITERATURE REVIEW OF CELL-TEST INTEGRATING PCM

| Author | Location / Period | Material / PCM | Dimension (m) | Main results |
|---|---|---|---|---|
| [53] | Casablanca Morocco, | Brick, PCM : Energain | 3 x 3 x3 | - Temperature increase of approx. 6 °C during the night, increase of the thermal mass of the room, reduction of heat |

| | | | | |
|---|---|---|---|---|
| | Winter spring | | | flows, up to 20 % savings in heating energy. |
| [61] | China, Winter summer | EP, PCM : SP 29, RT 18 | 1 x 1 x 1 | - Summer: Reduction of the indoor temperature by approx. 4.28 to 7.7 °C and reduction of the fluctuation of the indoor air temperature by up to 28.8 to 67.8%. Winter: Temperature rise from 6.93 to 9.48 °C during the night and the fluctuation of the indoor air temperature decreases from 17.7 to 25.4%. |
| [62] | Lleida Spain, Winter | PCC, Brick, PCM : RT 21 | 2.4×2.4×5.8 | - The efficiency of the PCM depends on the weather conditions, with 20% energy savings achieved with a partial melting of the MCP and 55% when the melting is complete, 25% energy savings in hard winter and 40% in medium winter. |
| [63] | Lyon France, Summer, Climatic chamber | Concrete, Plaster, Ps, Wood, PCM : Energain | 3.1x3.1x2.5 | - Reducing of the air temperature fluctuations in the PCM-cell, lower overheating effect, reducing of the wall surface temperatures, improvement of the thermal comfort. 5 mm PCM panel is equivalent to a concrete layer of about 8 cm, increasing of the thermal inertia of the PCM-cell, available storage energy is twice as high with PCM. |
| [64] | Adana Turkey, Winter summer | PCC, PCM : (75% capric acid - 25% myristic acid) | 2 x 2 x 2 | - Maintain of the thermal comfort of the buildings, indoor air temperature gain of up to 2°C corresponding to 13% energy savings, difference of 5°C between the internal surface temperatures of the two cells (due to the storage effect of the PCM) observed using thermal cameras, thermal stability of the PCM after two years of monitoring. |
| [65] | Brno-sever Czechia, Summer | Plaster, Ps, SP, MW, PCM : RT 27 | 3x2.43x3.09 | - The effect of latent heat storage in the PCM and its release is highly dependent on the intensity of overall solar radiation and the temperature of the outside air. The optimum response of the façade occurred under a maximum total solar radiation of 600 W/m² and an outside air temperature of up to 26 °C. |
| [66] | Hefei China, Summer, mid-season (Sep-Oct) | Brick, Cement, Ps, PCM : RT 28HC | 1 x 0.95 x 1 | - The maximum temperature of the interior surface of the south wall is 40.7 °C (Cell A, Brick walls) 34.9 °C (Cell B, PCM walls) and 32.5 °C (Cell C, RC walls -PCM). The corresponding daily indoor average temperature is 27.8 °C, 27.3 °C and 27.0 °C, respectively. The PCM fusion time in cell C is approximately 16 hours per day, which is approximately 2.3 hours longer than that of cell B. The southern wall cooling loads for cell C are reduced by 47.9% and 23.8% relative to cells A and B, respectively. |
| [37] | Shanghai China, Summer mid-season (March) | Ps, Concrete, Brick, PCM : GH 20 (paraffin-SSPCM) | 3.25x3.86x2.91 | - Reduction in the fluctuation and maximum value of the surface temperature of the interior face of the PCM-composite wall in mid-season, insufficient melting of the PCM observed during certain days and absence of phase change after a given date, approximately 43.23% increase in heat transferred to the cell for a representative sunny day. |
| [67] | Lleida Spain, NC | Brick, Plaster, Cement, Concrete, PU, PCM : SP 25, RT 27, Ester | 2.4×2.4×2.4 | - Better impact of the ester used as PCM compared to salt hydrates. The use of salt hydrates or ester as PCM in cells results in a 9% and 10.5% reduction in impact, respectively, compared to the case of the use of paraffin. |
| [68] | Perugia Italy, Summer | SR, Plaster, Concrete, Brick, Sans MCP | 3.78×4.00×2.85 | - Reduction of the interior temperature, the analytical model shows an acceptable accuracy in the representation of the building cladding behavior. |
| [58] | Oslo Norway (In laboratory), Summer | Plaster, Others, PCM : Q23 M51 | 15 m² | - A significant passive cooling effect can be obtained by using 17 m² of PCM, the most significant effect obtained when the PCM is uncoated and directly exposed to the climatic conditions, a decrease in temperature observed when the PCM was covered with aluminum false ceiling panels and plasterboard. |
| [69] | Lleida Spain, Summer, mid-season (Mar-May) | Concrete, PCM : Micronal DS 5001 | 2 x 2 x 3 | - The cell without PCM has a maximum temperature 1 °C higher than that with PCM and a minimum temperature 2 °C lower. The maximum temperature in the wall with PCM appears about 2 hours later compared to the wall without PCM, i.e. the thermal inertia is higher, this thermal inertia appears in the afternoon due to the freezing of the PCM and earlier in the morning due to its melting. |

| [1] | Grenoble France, Winter mid-season (Sep-Nov) All the year | VIP, PW, Fiber cement, PCM : PEG 600 | Environ : 1 x 1 x 1 | - In summer: 20°C decrease in the amplitude of the interior temperature of the cell with PCM on a daily cycle. In winter: negative indoor temperature avoided when the cell temperature without PCM is -9°C and the outdoor temperature is below -6°C. |
|---|---|---|---|---|
| [70] | Lleida Spain, Summer | Concrete, PCM : Micronal DS 5001 | 2.64×2.64×2.52 | - Reduction in maximum temperatures of approximately 6%, the PCM remained active for at least 4% of overtime, increase in comfort time by at least 10% in cells with awnings, the effect of high outside temperatures and solar radiation was not completely overcome because the PCM did not undergo complete phase change cycles every day. |
| [71] | Lleida Spain, Mid-season (April) | PU, Plaster, MW, PCM : Paraffin | NC | - The inclusion of PCM decreases the interior ambient temperature by up to 3 °C and the temperature on the southern part of the intermediate wall. |
| [57] | Toronto Canada, Summer | PW, Ps, Plaster, PCM : BioPCM$^{TM}$, Energain | NC | - Improvement of the thermal performance of the PCM cell, stabilization and reduction of the maximum interior and surface temperatures up to 6 °C, damping of 9% of the high peak temperatures in the west orientation and 22% of the low peak temperatures in the south orientation equivalent to an average temperature of 4.1 °C and 4.6 C°, respectively. |
| [72] | Grenoble France, Summer, Mid-season (May) | Glass brick, VIP, PCM : (Capric acid – Myritic acid), Paraffin, Hydrated salt | Environ : 1 x 1 x 1 NC | - For the three different glass brick walls, the interior maximum temperature of the PCM cell is lower than that of the test cell without PCM. The temperature attenuation varies between 3.5 and 4 °C for fatty acid, 2 and 3 °C for paraffin and 3.5 and 5 °C for hydrated salt. |
| [2] | Lleida Spain, Summer | Concrete, PCM : Micronal DS 5001 | 2.4×2.4×2.4 | - Reduction of facade surface temperatures with PCM, greater thermal phase shift and smoother temperature fluctuations between day and night. Ten years later, the cell with PCM showed the same thermal response obtained in 2005 and the mechanical performance of concrete with PCM remains the same. |
| [13] | Lleida Spain, Summer | Brick, Concrete, Cement, PU, PCM : RT-27, SP-25 A8 | 2.4×2.4×2.4 | - Reduction of peak temperatures up to 1 °C and smoothing of daily fluctuations, in summer 2008, electrical energy consumption was reduced in PCM cells by about 15% resulting in a reduction in $CO_2$ emissions from About 1-1.5 kg/year/m², some PCM solidification problems were observed overnight. |

EPs: Expanded polystyrene. PCC: Precast concrete. Ps: Polystyrene. PU: Polyurethane. OSB: Oriented strand board. SP: Solar panel. Mineral wool. SR: Sedimentary rock. PW: Polywood.

To do this, a significant number of works have been carried out on test cells in several countries including China, France and Italy, but the majority of these studies are located in the municipality of Puigverd de Lleida located (Lérida in Catalonia). , Spain). The **Error! Reference source not found.** summarizes the characteristics of the test cells as well as the main results obtained.

This study is devoted to the evaluation of the thermal performance of a test cell called TESC-S25-b-Cell designed with lightweight concrete wall panels in which the sand, which represents 25% of the total volume, is replaced by the same volume of sepiolite impregnated with vegetable fat (Coprah oil). This cell is subjected to the vagaries of climatic variations over a few days at the same time as another cell, of the same dimensions, with ordinary concrete walls called C-R-Cell, for comparison purposes. The measurements focused on the air temperature inside and outside the cells, the temperature of the walls as well as the heat fluxes exchanged at the walls and the amount of heat absorbed by these walls. Particular attention is paid to the internal temperature, an essential parameter of the thermal comfort of the cells. Our experiments, carried out mainly in the summer period, have shown an increase in the thermal capacity of the cell envelope by the addition of PCMs, which by storing an additional part of the incident solar energy, leads to a reduction in cells inner temperature. This effect, positive for the thermal comfort of the cells, is accompanied by a reduction in the thickness and therefore the weight of the wall panels compared to ordinary concrete wall panels.

## II. EXPERIMENTAL

The TESC-S25-b is a mixture of 75 %v of an ordinary concrete and 25 %v of TESA. In the preparation of the concrete, a mixture of three different normal-weight aggregates is used, namely sand and medium and coarse gravels. The cement used as a binder is a commercially available certified NA442 CEM II / B-L 42.5 N Portland limestone cement, compliant with the Algerian and French standards (true class greater or equal to 42 MPa). TESA was obtained by direct impregnating the sepiolite LWA (S) with the PCM (VF 23-26 : a low-cost Coprah oil furnished by Mewaholeo industries, Malaysia) at 60 °C during 30 mn and the maximum impregnation rate was about 48,20 %wt. The properties of the C-R and TESC-S25-b and each component are given in *Table 3*3,

*Table 4*4, *Table 5*5 and *Table 6*.

TABLE 3.

CHARACTERISTICS OF LWA (SEPIOLITE)

| LWA | $\rho$ (kg/m$^3$) | $\alpha$ maxat 60°C (%wt) | D(mm) | Price (€/kg) | Origin |
|---|---|---|---|---|---|
| Sepiolite (S) | 759 | 48.20 | 0 - 7 | $\approx 0.50$ | Spain |

TABLE 4.

PROPERTIES OF PCM (VF 23-26)

| Melting range (°C) | $\rho$ à 30 °C (kg/m$^3$) | H (j/g) | Price (€/kg) | Origin |
|---|---|---|---|---|
| $\approx 15$-26 | 700 | $77 \pm 13$ | $\approx 1$ | Malaysia |

The panels of 77 x 77 x 3 cm$^3$, 8 in total for the two cells, are fixed to a framework formed from wooden rods of section 5x5 cm². The cells thus formed can be geometrically assimilated to cubes with sides of 87 cm. To allow a comparative study, one of the cells has only ordinary concrete panels (C-R), this is the "control" cell, while the second is formed from the composite concrete panels TESC-S25-b.

TABLE 5.

THERMAL AND MECHANICAL PROPERTIES OF TESTED SAMPLES AND PANELS (TESC-S25-B AND C-R)

| 1) Sample | D (cm) | Component | %$_V$ | $\rho$ (kg/m$^3$) | T (°C) | Cp (J/kg.K) | $\lambda$ (W/m.K) | Qs (kJ/kg) | L (kJ/kg) | R 28 (MPa) |
|---|---|---|---|---|---|---|---|---|---|---|
| TESC-S25-b | 20x20x3.3 | TESA-S Concrete | 25 75 | 1898 | 10-15 30-35 10-35 | Cs = 1093 Cl = 1151 Ct = 1145 | $\lambda_s$ = 1.09 $\lambda_l$ = 0.72 - - - | 4.88 5.48 29.43 | - - - - - - 19.07 | 15.44 ± 0.97 |
| C-R | 20x20x3.3 | Concrete | 100 | 2195 | 30-35 | C= 1132 | $\lambda$ = 1.26 | 5.71 | - - - | 26.32 ± 0.69 |

a large area fully exposed to the sun, without any physical obstacles in the vicinity, with a north-south orientation and sufficiently far from each other. The lower faces and the north faces are fitted with 5 cm thick polystyrene panels. The north-facing posterior panels feature a 35x30 cm² opening that can be kept open or closed depending on the requirements of each experiment. The experiments are carried out in the enclosure of the former institute of architecture of the University of Tizi-Ouzou (Algeria). The Tizi-Ouzou region, located in northern Algeria, is representative of the typical Mediterranean climate. It is characterized by wet and cold winters and hot and dry summers, marked by fairly large temperature amplitudes between day and night. *Figure 1*shows the monthly averages of maximum and minimum temperatures recorded by the local meteorological station of the National Meteorological Office (ONM). The melting and solidification temperature ranges of TESA are compatible with the climatic conditions of the summer period excluding periods of heat waves, that is to say daytime temperatures above 25 °C and nighttime temperatures below 16 °C.

TABLE 6.

COMPOSITION OF THE SAMPLES AND PANELS TESTED (TESC-S25-b AND C-R)

| Sample | Mass (kg) for 1 m³ ofconcrete | | | | | | |
|---|---|---|---|---|---|---|---|
| | Sand | Gravel 3/8 | Gravel 8/16 | Water | Cement | TESA including PCM | |
| C-R | 623 | 228 | 991 | 200 | 400 | 00 | 00 |
| TESC-S25-b | 00 | 228 | 991 | 200 | 400 | 281 | 90 |

In view of the outside temperatures in the Tizi-Ouzou region (see *Figure 1*) and the thermodynamic characteristics of the PCM used in the concrete of the cells, the cycles of energy storage-release by latent heat remain fully active during the months of May, June and October and partially during the months of April and September. But for the months of July and August which are as shown in *Figure 1* the hottest months of the year, nighttime temperatures are too high to allow the coprah oil to solidify.
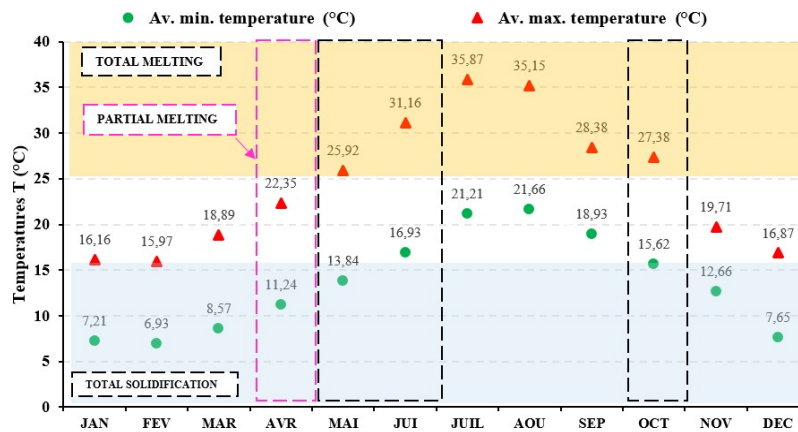


Figure 1. PCM performance according to time of year and climate

The test cells are equipped with six K-type thermocouples and two fluxmeters connected to a data acquisition system for the simultaneous saving of measurements. The computer and the data acquisition are placed throughout the experimental campaign in a weather shelter. 4 thermocouples and a fluxmeter are provided for the TESC-S25-b-Cell, a thermocouple and a fluxmeter for the C-R-Cell and finally 1 thermocouple for the measurement of the
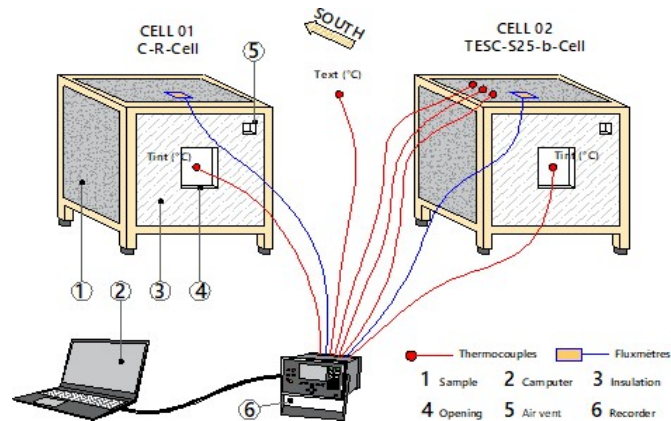


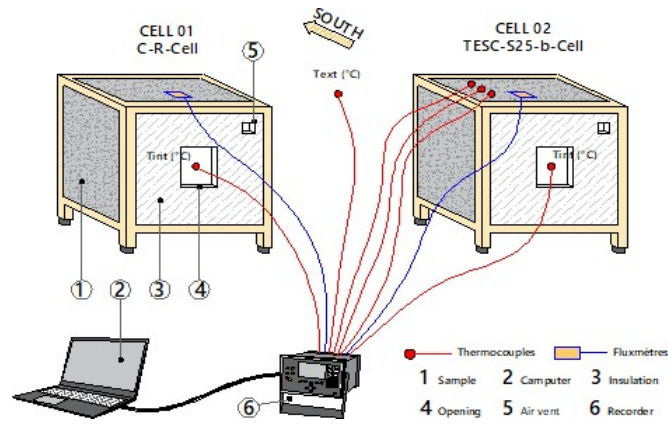temperature of the external environment (see *Figure* 2).

Figure 2. Schematic representation of the experimental set-up of the test cells

The temperature inside the two test cells is measured by thermocouples placed in the center of the cells. Thermocouples and fluxmeters intended to measure the internal and surface temperature of the top panels, as well as the heat flows passing through them, are fixed on the surface using aluminum tape. The choice to make these flux measurements by limiting oneself to the upper panels is motivated by the fact that the thermal contributions on the roofs of the cells represent in summer approximately 70% of the total contributions. The device as a whole is
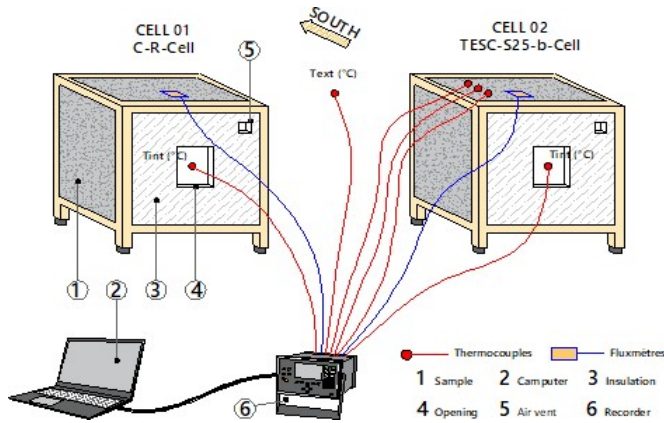


illustrated in
*Figure* 2.

Figure 3. Composition of the walls of the test cells in the 5 scenarios

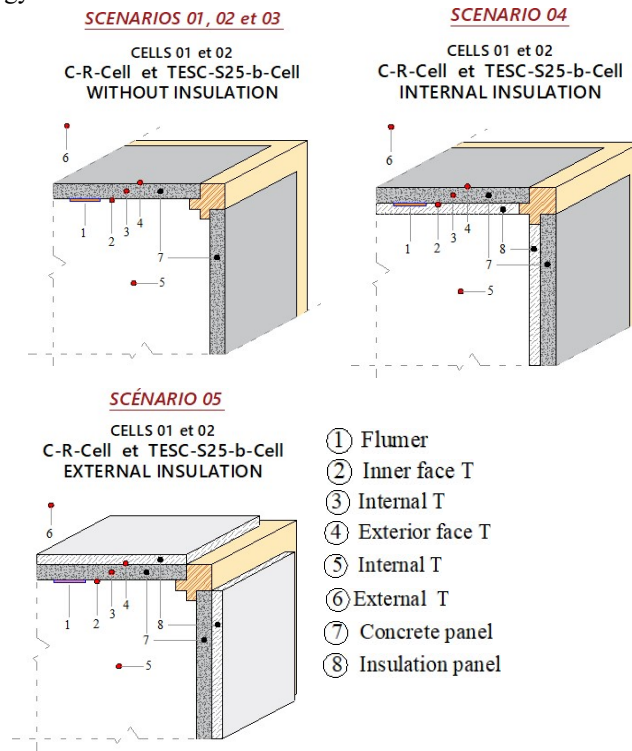III. EXPERIMENTAL PROTOCOL

The two test cells are subjected for several days to external climatic conditions according to five different scenarios (see the composition of the walls in the five scenarios in *Figure 3*). In the first two scenarios, the cells have no thermal insulation with windows closed in the first case and open in the second. In the third test, the wall panels have no insulation boards and the windows are closed during the day and open at night. Finally, the panels are insulated by adding a 1.5 cm thick sheet of polystyrene, inner side in the fourth test and outer side for the fifth and final experiment by keeping the windows closed during the day and open at night.



Figure 4. External and internal appearance of the two test cells in the 5 scenarios

To further characterize the thermal behavior of TESC-S25-b panels, including its performance in terms of phase shift and thermal damping, experiments are conducted in the laboratory under controlled conditions. The experimental set-up, shown in *Figure 5*, comprises two exchanger plates on which are placed the two square samples of TESC-S25-b and C-R, 20 cm square and 3 cm thick. The exchangers are permanently supplied with

water, coming from two thermostatically controlled circulating baths. The outlines of the two samples are carefully isolated by sufficiently thick polystyrene plates, the upper faces (noted face 2) being left free. Before any experiment, we checked the consistency of the temperature measurements made on the two exchangers. We fed them with the bath water by imposing two heating-cooling cycles of 40 minutes each from 10 °C to 50 °C. The temperatures and flows at the surface of the exchangers are measured. The values are very similar for the two parameters, which makes it possible to conclude positively on the reliability of the set-up. The samples being placed on the exchangers, an experiment of three cycles of 100 min each is carried out with temperatures varying from 10 °C to 50 °C. Thermocouples measure the temperatures in the middle and on the surface of the samples, on the exchanger side, while a fluxmeter placed on the upper face (face 2) of the samples measures the heat flows passing through them. These eight sensors are connected to a data acquisition center connected to a computer.
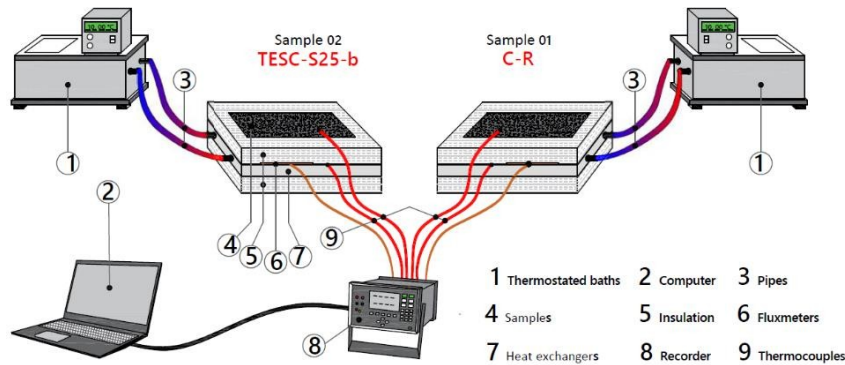


Figure 5. Schematic representation of the experimental setup planned for the evaluation of the phase shift and thermal damping of the C-R and TESC-S25-b samples under controlled conditions
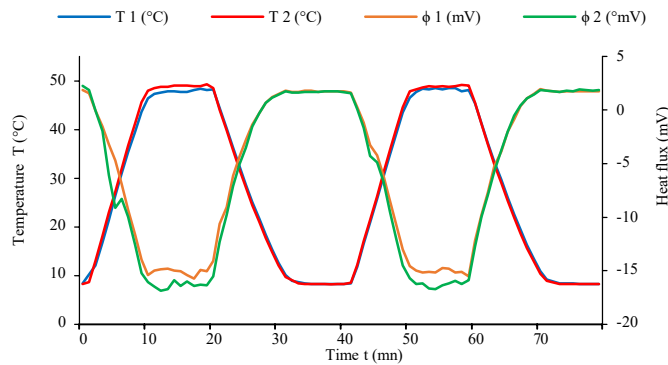


Figure 6. Verification of the agreement of the temperatures and heat flows emitted by the two exchangers

## IV. RESULTS AND DISCUSSION

### A. The testing scenarios

#### i. Scenario 1: 31/08-02/09/2019, closed window, without insulation

During the three successive days of the experiment, the outside temperature has a similar evolution and reaches the same maximum value of 34 ° C. Inside the cells, the maximum reached temperature varies between 40 and 43 °C for TESC-S25-b-Cell and between 41 and 44 °C for C-R-Cell. With the exception of a short period between 8 a.m. and 10 a.m., the temperature remained slightly higher in the C-R-Cell and the range reached 1 °C at midday. Closing the windows resulted in significant overheating (S). It evolves during the day in phase with the outside

temperature and reaches a maximum of around 10 °C in the C-R-Cell and 9 °C in the TESC-S25-b-Cell
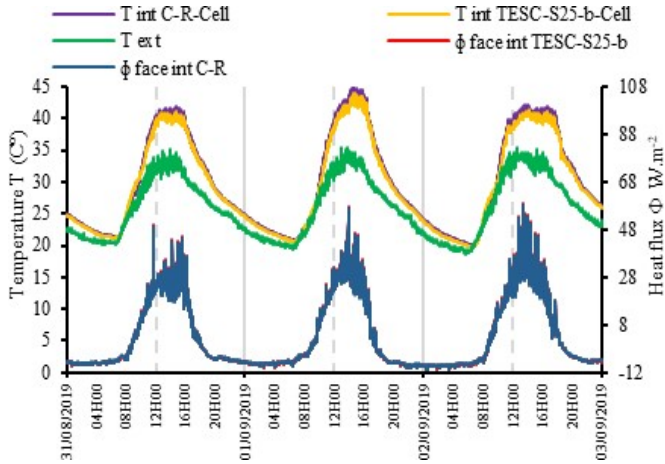


(*Figure* 7). The cells' lack of thermal insulation and their small size, combined with the lack of ventilation, further accentuate this overheating phenomenon. Estimated from
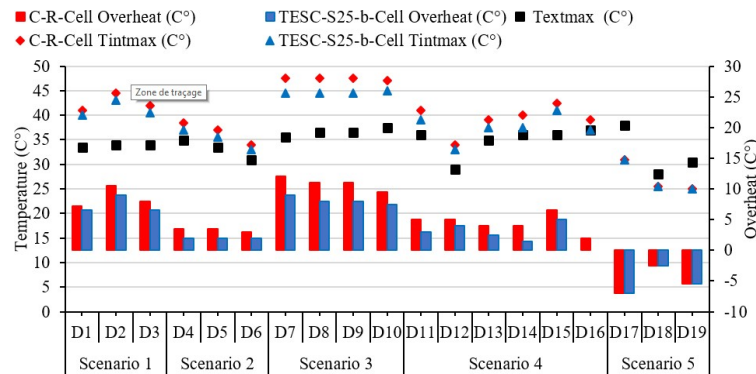


*Figure* 12, the thermal phase shift in the two cells is almost identical (D ≈ 1 hour). Thus, it is about 59 min in the C-R-Cell and it is 69 min in the TESC-S25-b-Cell, the PCM being in the liquid phase for the duration of the experiment. During these days, nighttime outdoor temperatures never dropped to a level low enough to solidify the PCM and activate the latent heat storage-release cycle. Overall, the flows recorded on the two cells are very close and follow the same daily evolution. The numerical values of the flows are very slightly different, greater in the CR-Cell during periods of underheating, at the end of the day and during the night, and higher in the TESC-S25-b-Cell between 6 a.m. and 2 p.m.

Figure 7. Variation of inside and outside temperatures of the test cells and heat flow through the upper walls (Sc1)



Figure 8. Variation of inside and outside temperatures of the test cells and heat flow through the upper walls (Sc2)

## ii.  Scenario 2: 03-05/09/2019, opened window, without insulation

During the three days of the measurement campaign, the weather was sunny with a moderately high maximum outside temperature (31 °C - 35 °C). Inside the cells, the maximum temperature during the 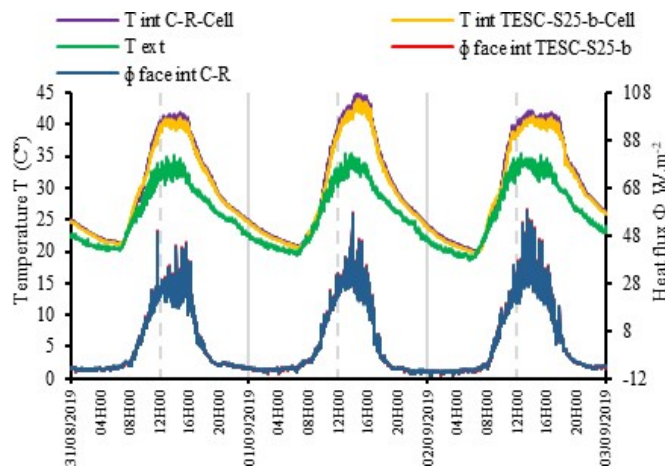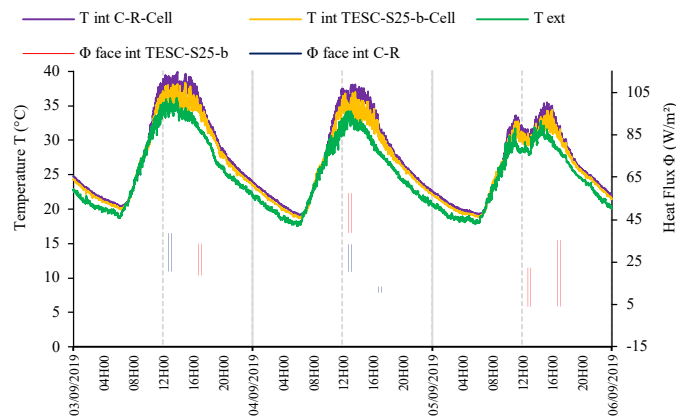day reaches a value higher  than the ambient temperature with approximately 33 to 37 ° C for the TESC-S25-b-Cell and 34 to 38.5 ° C for the CR-Cell (see **Error! Reference source not found.**). Tempered by ventilation, the overheat, 2 °C for the TESC-S25-b-Cell  and  between  3 °C and 3.5  °C in  the  C-R-Cell, is much  less (see
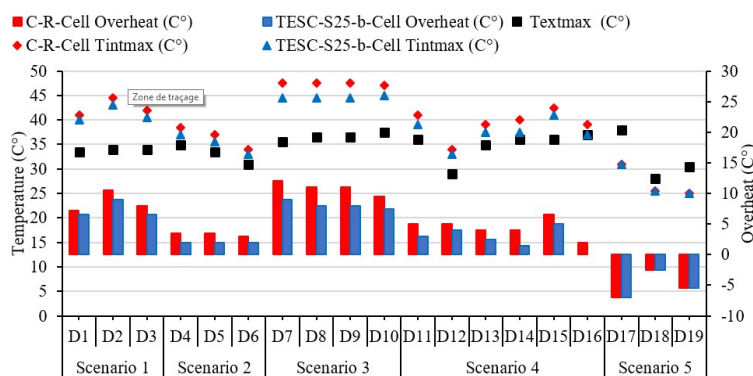


*Figure* 12). The temperature remains higher in the C-R-Cell, with the exception of the 8 am-10 am period, with an average deviation at midday of 1.5 °C for the first two days and 1 °C on the third. The heat flow is greater, in the C-R-Cell at the end of the day and during the night and in the TESC-S25-b-Cell from 6 a.m. to 2 p.m. As in the first scenario, the thermal phase shift is around 60 minutes for the two cells. Here too the nighttime outdoor temperatures are not low enough, the PCM has remained in the liquid domain and the latent heat storage is not  activated. The most interesting result remains the relative improvement in the thermal damping factor in the TESC-S25-b-Cell, which seems to be better insulated, especially since this is combined with a decrease in the average density of the panels synonymous with panels lighter. Opening the windows refreshed the interior ambience of the cells and reduced overheating, but without ensuring an acceptable level of thermal comfort. To obtain more information on these cells and to analyze the contribution of the MCP with an activated phase change cycle, additional experiments were carried out under more favorable climatic conditions (Scenarios 3, 4 and 5).

## iii.  Scenario 3: 27/09-01/10/2019, windows closed the day, opened at night, without insulation

During the measurement campaign carried out over a period of 5 days (from 09/27 to 10/01), the weather was sunny until the fourth day, then very rainy on the fifth; daytime temperatures were high, well above the melting temperature of coconut oil, and during the nights they dropped to 15 °C to 25 °C allowing it to solidify. In other

words, the weather conditions were favorable for the MCP phase change cycle. The curves drawn from the measurements of temperature and heat flux in the test cells have similar shapes with, however, some differences in relation to their thermal insulation. During the first four days, the temperature is approximately 3 °C lower in the TESC-S25-b-Cell. However, temperature levels remain excessively high, with a maximum of around 45 ° C for TESC-S25-b-Cell and 48 °C for C-R-Cell. Between 6 a.m. and 9:30 a.m., when the window is closed, the internal temperature rises more slowly than the outside temperature. After 9:30 am, the temperature rises rapidly in the cells giving overheating reaching 9 °C for the TESC-S25-b-Cell and 12 °C for the C-R-Cell. *Figure 9* and
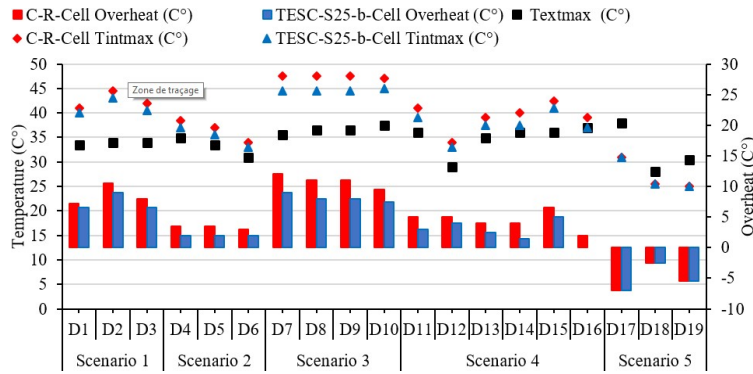


*Figure* 12, it can be seen that the average difference in maximum temperatures between the inner and outer faces of the top panel of the TESC-S25-b-Cell is 3 °C. It becomes insignificant for minimum temperatures (around 0.15 °C). The average thermal phase shift noted on the graph of the two cells (*Figure 9*) is approximately 1.5 hours. So, about 2 hours earlier, the temperature in the C-R-Cell has already reached the same value as the maximum temperature of the TESC-S25-b-Cell. Regarding the heat fluxes recorded in the two test cells, the evolution is generally the same, with lower values on the inner face of the roof of the TESC-S25-b-Cell.



Figure 9. Variation of inside and outside temperatures of the test cells and heat flow through the upper walls (Sc3)

Indeed, the examination of the heat flow and temperature curves of the test cells makes it possible to detect a relative efficiency of the process with a drop in the values for the temperature in the TESC-S25-b-Cell and in the heat flows exchanged. It is a result of the storage of part of the heat received in the form of latent heat. During the night, this flux is higher in the TESC-S25-b-Cell, which is explained by the release of the thermal energy absorbed by its walls during the day, which is greater compared to that which was stored by the CR-Cell panels.

In view of these results, the TESC-S25-b-Cell cell showed very promising behavior. An improvement compared to the C-R-Cell is observable, this despite the average amount of MCP used. Note that in these experiments, the internal temperature in the TESC-S25-b-Cell however remains quite high. The thermal phase shift and damping can be increased with a greater wall thickness, a greater amount of MCP incorporated as well as by the addition of an

insulating plate on the panels. It is for this and to have a simulation that best approaches the reality of the building that two other experiments were carried out on these cells where polystyrene sheets are added on the interior faces of the concrete panels for the first experiment then on their outer faces for the second.

iv.  *Scenario 4: 05-11/10/2019, windows closed the day, opened at night, interior insulation*

With the exception of the second day marked by bad weather and a temperature that fluctuates below 30 ° C, the other days were under perfectly clear skies with high temperatures during the day and quite low at night, oscillating
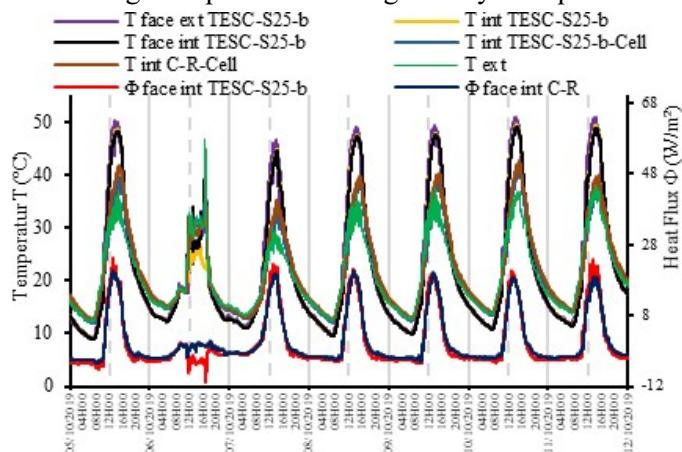


between 12 °C and 41 °C. According to *Figure* 10, the maximum temperatures recorded inside the concrete slabs and on their two faces are between 43 °C and 51 °C during the day and between 8 °C and 12 °C at night; a final temperature range, from 8 °C to 51 °C, favorable to phase changes, total melting and solidification of the MCP contained in the concrete. Although the flow and temperature curves follow similar patterns, the thermal performance of the two cells is slightly different. At night, the internal temperature curves meet and merge for the two cells. During the day, overheating, quite significant in both cells. The thermal phase shift is in the 30-80 minute interval with greater superheating (S) as the outside temperature increases. It reaches a maximum of around 5 °C for TESC-S25-b-Cell and 6.5 °C for C-R-Cell. Overall, the curves of the fluxes measured on the two test cells follow the same pattern with similar values. It should be noted at night that on the roof panel of the TESC-S25-b-Cell, the heat flow exchanged on the exterior side is greater than that which is exchanged with the interior of the cell. The internal thermal insulation device was not enough to lower the internal temperature of the two test cells below the external temperature. In fact, the temperatures recorded on the roof are very high and cause the cells to heat up when the windows are closed.

During the night period when temperatures are low and below the melting range of the MCP, the temperatures of the concrete panels are much lower than the outside temperature due to the nighttime radiation, while the temperatures inside the two cells- test are almost similar to the outside temperature because of the exchanges by convection through the windows left open. The position of the insulating plate on the interior side reduces the transfer to the cell of heat stored during the day by the panels. Regarding the heat fluxes measured by the fluxmeters installed between the concrete panels and the polystyrene sheets (see *Figure 3*), they reach average maximum values of around 20 W.m$^{-2}$ during the daytime period coinciding with the storage phase of heat by the concrete panels, and 4 W.m$^{-2}$ during the night period corresponding to the phase of restitution of this heat. When we take a closer look at the flux curves, we see a slight superiority of the flux recorded in the TESC-S25-b-Cell at midday and overnight.
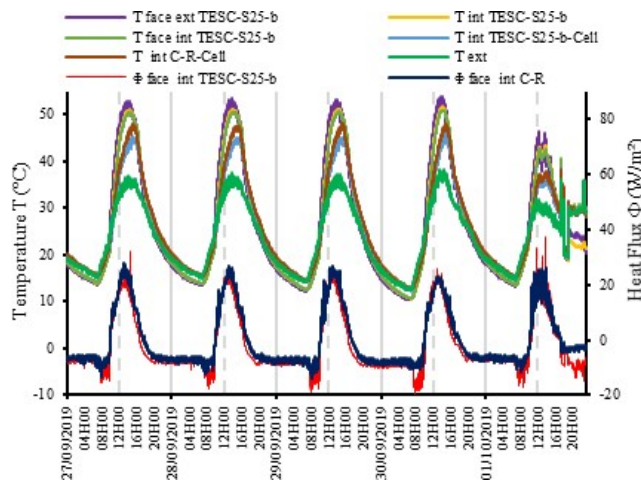
Figure 10. Variation of inside and outside temperatures of the test cells and heat flow through the upper walls (Sc4)

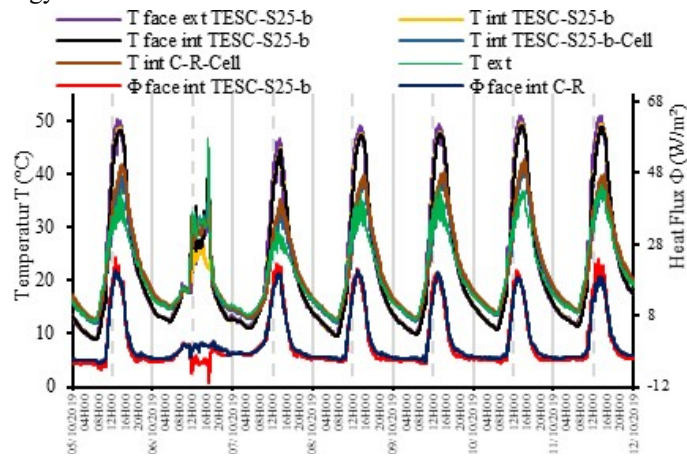The results obtained during these experiments lead to conclusions similar to those in the literature. That is, PCMs used in concrete as a thermal dopant can cause temperature gains between 1 °C to 7 °C [10], [69].

v. *Scenario 5: 13-15/10/2019, windows closed the day, opened at night, exterior insulation*

These experiments, carried out from October 13 at midnight to October 15, at midnight, show certain differences
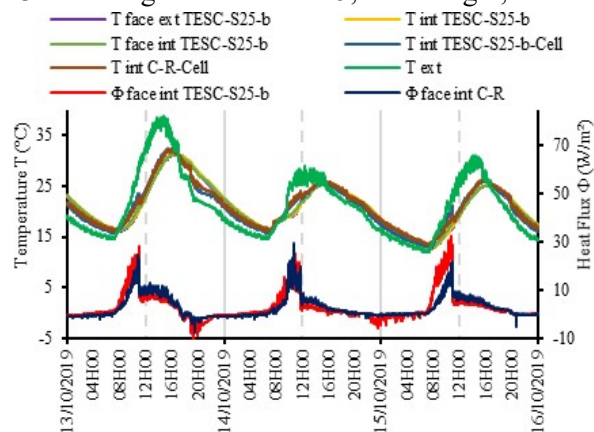


in the thermal behavior of the two test cells (see
*Figure* 11). A refined analysis of the temperature curves makes it possible to distinguish three phases: a first period which lasts 2 to 3 hours and begins in the early hours of dawn; the windows are still open at this time of day, and the ambient temperature outside quite low (around 15 ° C). In this phase, the temperature in TESC-S25-b-Cell is slightly higher than that of CR-Cell. A second phase follows during the diurnal period of the day, which lasts about ten hours; the windows are in the closed position. In this phase which ends at the end of the afternoon around 6 p.m., the two curves almost merge, the two temperatures being quite close. In the evening and after opening the windows, the third phase begins, characterized by a temperature curve of the TESC-S25-b-Cell which passes little by little and slightly below that of the CR-Cell, this until to achieve a temperature difference of about 1 °C. Still from these two curves, we can see that putting insulation on the outside of the panels has an effect on the damping rate (A). It becomes more important than in the case of internal insulation. Indeed, thanks to this arrangement, the temperatures in the two cells fell, and even remained lower than the ambient temperature during the hottest period of the day. The temperature attenuation increases as the outside temperature increases and reaches a maximum of around 7 °C. The phase shift between the two curves is on average 2.5 hours. Regarding the weather conditions, it should be noted that from the second day, the climate became relatively milder with temperatures not exceeding 30 °C and a completely clear sky on the first day and then partially cloudy. The measurement campaign ended at the end of the third day under the constraint of heavy rains which occurred at midday of the fourth day.

As previously indicated, the solidification limit temperature of the PCM used in the panels, coconut oil, is around 15 °C, the minimum temperature to be reached to ensure that the PCM solidifies completely, and restores all the

heat stored to melt. During our experiments, these conditions were not always reached, which somewhat reduced the impact of this phenomenon on the thermal comfort of the test cell, the efficiency of the panels being conditioned by the rate of melting and solidification. of the PCMs they contain.
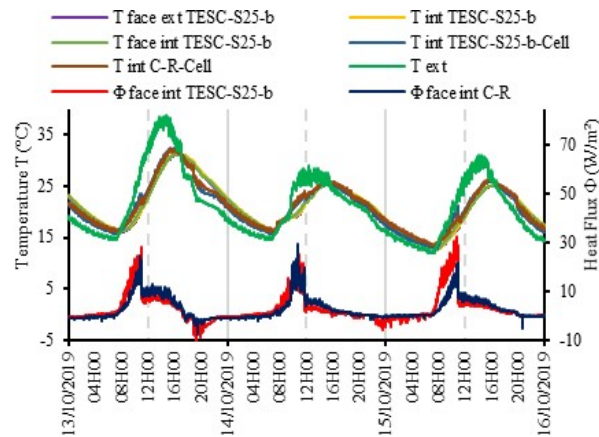


Figure 11. Variation of inside and outside temperatures of the test cells and heat flow through the upper walls (Sc5)

Regarding the heat fluxes exchanged between the internal faces of the panels with the interior of the cells and the comparative study of their evolution in the two cells, there are three zones as for temperatures. A first phase in the early morning in which the flow of the TESC-S25-b-Cell panels is greater, followed by a second where the trend is reversed and which lasts until the end of the afternoon. The third phase, nocturnal, is marked by flows which tend to equalize. Note that the direction of flow is imposed by the sign of the temperature gradients between the interior of the cells, the wall of the panels and the external ambient environment. The maximum flux exchanged and transferred by the external environment is of the order of 30 W/m², it is reached in the middle of the day. The flows evolve in a bell and decrease significantly at the end of the day. In this time interval, the temperature of the walls becomes higher than those of the cells and the external environment and the flow is thus directed from the wall to the interior. During the first two days, during the night period, it reaches a maximum value of -10 $W.m^{-2}$. For TESC-S25-b-Cell panels, which show a slightly higher heat release potential than C-R-Cell panels. This is explained by the fact that the PCM begins to solidify following the drop in temperatures, the latent heat flux being added to the sensible flux. The value of these flows is negative, indicating that the flows have changed direction, the temperature of the panels having exceeded that of the cells. When the solid-liquid phase change is complete, which happens when temperatures are high enough in the middle of the day, the flux exchanged by the CR-Cell panels becomes greater, due to better thermal conductivity, the TESC- panels S25-b being more insulating.
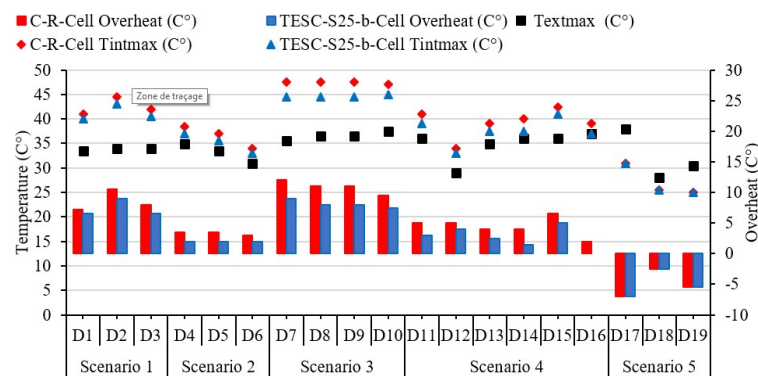


Figure 12. Temperature outside and inside the cells and superheating value in the 5 scenarios
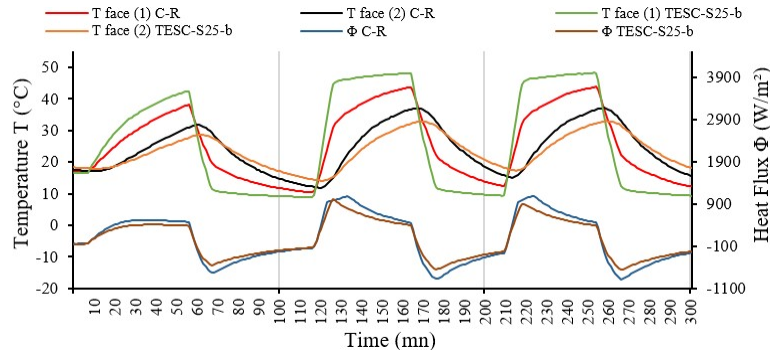
Figure 13. Thermal tests on TESC-S25-b and C-R under controlled conditions; temperature and heat flux variation
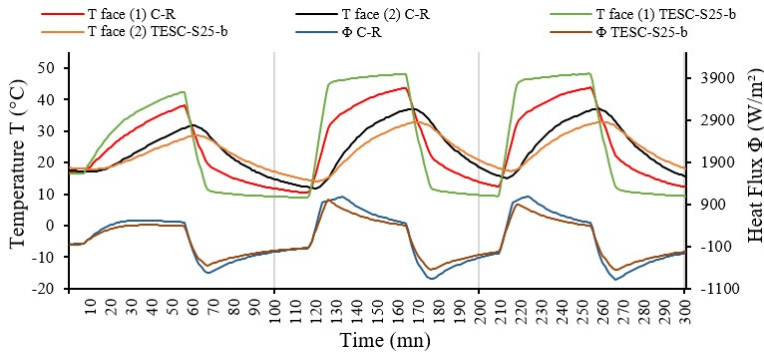
*B. Controlled conditions tests*



*Figure* 13 shows that the temperature at the interface of the exchanger with the sample (T face 1) is higher for the TESC-S25-b reaching a maximum of 48.3 °C against 43.89 °C for the C-R, with temperatures in this sample which change more rapidly both in the temperature rise phase and in cooling. During cooling, we see lower temperatures on the TESC-S25-b with a minimum of 8.81 °C against 10.38 °C on the C-R. This is due to its lower heat capacity ρ.Cp compared to that of the sample of C-R, (TESC-S25-b: 2173 kJ/kg.K <C-R: 2485 kJ/kg.K). The heat fluxes are greater for the C-R plate in the heating phase due to a larger temperature difference than for the TESC-S25-b at the exchanger-sample contact surface; Conversely, and for the same reasons of temperature differences rather favorable to TESC in this phase, the flows in this sample prevail. Subject to the same conditions (temperature and cycle time, etc.), the two samples TESC-S25-b and C-R exhibit different phase shift and thermal damping values. The recorded average phase shift is 9 minutes for the TESC-S25-b and 6 minutes for the C-R. In addition to the low value of the conductivity of the TESC-S25-b, this phase shift is to be related to the phase change of the MCP contained in the TESC-S25-b, an effect which delays the evolution of the temperature in this medium. An interesting result to note is the average temperature difference observed between the two faces of the samples. Equal to about 15 °C, it is twice as important in TESC-S25-b than in C-R with 7 °C. The damping of the external thermal signal, characteristic of the insulating property of the constituent materials of the panels, is therefore more efficient for the TESC-S25-b, result in accordance with the thermal conductivity measurements carried out, 0.72 W/m.K against 1.26 W/m.K for the C-R. Thus, all the results of these experiments, carried out in the laboratory on the two plates subjected to controlled conditions, fully confirm and support the conclusions drawn from the performance of the test cells placed in external climatic conditions.

## V. CONCLUSION

This study was a verification of the thermal properties of TESC-S25-b and its effects on indoor thermal comfort when it is used as panels. Two 87 cm$^3$ test cells, made up of four TESC-S25-b panels for the first and four ordinary concrete (C-R) panels for the control cell were designed. Interior temperatures and walls, as well as heat flows passing through the wall panels were measured in real situations. Five scenarios were tested and made it possible to

carry out a comparative study of the thermal environment inside the two cells. Without insulation in the first two scenarios, windows closed then open, a third scenario where the windows are closed during the day and open at night and finally two last scenarios, with interior insulation then exterior by polystyrene plates, the windows being open at night and closed during the day. In addition to these outdoor tests, laboratory measurements are performed on C-R and TESC-S25-b plates to assess the thermal phase shift and thermal signal damping for these plates. The energy efficiency of the cell isolated from the outside was evident; this configuration is that which achieves the best conditions of thermal comfort. When their wall panels are not insulated, there is any noticeable difference in the behavior of the two cells and a significant overheating has been noted in the interior. When insulation is applied from the inside, greater thermal damping is seen in the TESC-S25-b-Cell.

In addition, the following points were noted as a result of these experiences:

• The importance of night-time ventilation in the summer to promote the completion of the melting/solidification cycle. In fact, closing the windows at night prevents the walls from cooling below the melting point of the PCM. By remaining in the liquid state, PCM cannot contribute to thermal comfort the next day and remains without any effect;

• Full or no ventilation is not recommended;

• The importance of choosing the PCM according to its melting/solidification range in accordance with the thermal amplitude of the target period;

• The case with external insulation is the most efficient and would be even more interesting in winter;

• The additional thermal inertia provided by the addition of PCM allows for better thermal performance than ordinary concrete, in addition to the advantage of being a lighter and less expensive composite material.

## VI. REFERENCES

[1] M. Ahmad, A. Bontemps, H. Sallée, et D. Quenard, « Thermal testing and numerical simulation of a prototype cell using light wallboards coupling vacuum isolation panels and phase change material », Energy and Buildings, vol. 38, no 6, p. 673‑681, juin 2006, doi: 10.1016/j.enbuild.2005.11.002.

[2] L. F. Cabeza et al., « Behaviour of a concrete wall containing micro-encapsulated PCM after a decade of its construction », Solar Energy, déc. 2019, doi: 10.1016/j.solener.2019.12.003.

[3] S. E. Ango, « Contribution au stockage d'énergie thermique en bâtiment: développement d'un système actif à matériaux à changement de phase », p. 180.

[4] N. Stathopoulos, « Numerical and experimental optimization of peak power reduction control strategies », p. 251.

[5] B. Zalba, J. M. Marín, L. F. Cabeza, et H. Mehling, « Review on thermal energy storage with phase change: materials, heat transfer analysis and applications », Applied Thermal Engineering, vol. 23, no 3, p. 251‑283, févr. 2003, doi: 10.1016/S1359-4311(02)00192-8.

[6] L. F. Cabeza, A. Castell, C. Barreneche, A. de Gracia, et A. I. Fernández, « Materials used as PCM in thermal energy storage in buildings: A review », Renewable and Sustainable Energy Reviews, vol. 15, no 3, p. 1675‑1695, avr. 2011, doi: 10.1016/j.rser.2010.11.018.

[7] A. Abhat, « Low temperature latent heat thermal energy storage: Heat storage materials », Solar Energy, vol. 30, no 4, p. 313‑332, 1983, doi: 10.1016/0038-092X(83)90186-X.

[8] P. Lv, C. Liu, et Z. Rao, « Review on clay mineral-based form-stable phase change materials: Preparation, characterization and applications », Renewable and Sustainable Energy Reviews, vol. 68, p. 707‑726, févr. 2017, doi: 10.1016/j.rser.2016.10.014.

[9] P. K. S. Rathore et S. K. Shukla, « Potential of macroencapsulated PCM for thermal energy storage in buildings: A comprehensive review », Construction and Building Materials, vol. 225, p. 723‑744, nov. 2019, doi: 10.1016/j.conbuildmat.2019.07.221.

[10] S. Guichard, « Contribution à l'Étude des Parois Complexes intégrant des Matériaux à Changement de Phase: Modélisation, Expérimentation et Évaluation de la performance énergétique globale », p. 245.

[11] A. D'Alessandro, A. L. Pisello, C. Fabiani, F. Ubertini, L. F. Cabeza, et F. Cotana, « Multifunctional smart concretes with novel phase change materials: Mechanical and thermo-energy investigation », Applied Energy, vol. 212, p. 1448‑1461, févr. 2018, doi: 10.1016/j.apenergy.2018.01.014.

[12] R. Vicente et T. Silva, « Brick masonry walls with PCM macrocapsules: An experimental approach », Applied Thermal Engineering, vol. 67, no 1‑2, p. 24‑34, juin 2014, doi: 10.1016/j.applthermaleng.2014.02.069.

[13] A. Castell, I. Martorell, M. Medrano, G. Pérez, et L. F. Cabeza, « Experimental study of using PCM in brick constructive solutions for passive cooling », Energy and Buildings, vol. 42, no 4, p. 534‑540, avr. 2010, doi: 10.1016/j.enbuild.2009.10.022.

[14] E. Y. Tuncel et B. Y. Pekmezci, « A sustainable cold bonded lightweight PCM aggregate production: Its effects on concrete properties », Construction and Building Materials, vol. 181, p. 199-216, août 2018, doi: 10.1016/j.conbuildmat.2018.05.269.

[15] S. A. Memon, H. Z. Cui, H. Zhang, et F. Xing, « Utilization of macro encapsulated phase change materials for the development of thermal energy storage and structural lightweight aggregate concrete », Applied Energy, vol. 139, p. 43-55, févr. 2015, doi: 10.1016/j.apenergy.2014.11.022.

[16] A. Sarı, A. Bicer, F. A. Al-Sulaiman, A. Karaipekli, et V. V. Tyagi, « Diatomite/CNTs/PEG composite PCMs with shape-stabilized and improved thermal conductivity: Preparation and thermal energy storage properties », Energy and Buildings, vol. 164, p. 166-175, avr. 2018, doi: 10.1016/j.enbuild.2018.01.009.

[17] S.-G. Jeong, J. Jeon, J.-H. Lee, et S. Kim, « Optimal preparation of PCM/diatomite composites for enhancing thermal properties », International Journal of Heat and Mass Transfer, vol. 62, p. 711-717, juill. 2013, doi: 10.1016/j.ijheatmasstransfer.2013.03.043.

[18] K. Acurio, A. Chico-Proano, J. Martínez-Gómez, C. F. Ávila, Á. Ávila, et M. Orozco, « Thermal performance enhancement of organic phase change materials using spent diatomite from the palm oil bleaching process as support », Construction and Building Materials, vol. 192, p. 633-642, déc. 2018, doi: 10.1016/j.conbuildmat.2018.10.148.

[19] S. Benayache, S. Alleg, A. Mebrek, et J. J. Suñol, « Thermal and microstructural properties of paraffin/diatomite composite », Vacuum, vol. 157, p. 136-144, nov. 2018, doi: 10.1016/j.vacuum.2018.08.044.

[20] D. Guo et al., « Diatomite precoat filtration for wastewater treatment: Filtration performance and pollution mechanisms », Chemical Engineering Research and Design, vol. 137, p. 403-411, sept. 2018, doi: 10.1016/j.cherd.2018.06.036.

[21]  S. Cunha, J. B. Aguiar, V. Ferreira, et A. Tadeu, « Influence of Adding Encapsulated Phase Change Materials in Aerial Lime Based Mortars », Advanced Materials Research, vol. 687, p. 255-261, avr. 2013, doi: 10.4028/www.scientific.net/AMR.687.255.

[22]  J. A. C. Costa, A. E. Martinelli, R. M. do Nascimento, et A. M. Mendes, « Microstructural design and thermal characterization of composite diatomite-vermiculite paraffin-based form-stable PCM for cementitious mortars », Construction and Building Materials, vol. 232, p. 117167, janv. 2020, doi: 10.1016/j.conbuildmat.2019.117167.

[23]  B. Xu et Z. Li, « Paraffin/diatomite composite phase change material incorporated cement-based composite for thermal energy storage », Applied Energy, vol. 105, p. 229-237, mai 2013, doi: 10.1016/j.apenergy.2013.01.005.

[24]  B. Xu et Z. Li, « Paraffin/diatomite/multi-wall carbon nanotubes composite phase change material tailor-made for thermal energy storage cement-based composites », Energy, vol. 72, p. 371-380, août 2014, doi: 10.1016/j.energy.2014.05.049.

[25]  J. H. Deng, W. B. Li, et D. H. Jiang, « Study on Binary Fatty Acids/ Sepiolite Composite Phase Change Material », AMR, vol. 374-377, p. 807-810, oct. 2011, doi: 10.4028/www.scientific.net/AMR.374-377.807.

[26]  Q. Shen, J. Ouyang, Y. Zhang, et H. Yang, « Lauric acid/modified sepiolite composite as a form-stable phase change material for thermal energy storage », Applied Clay Science, vol. 146, p. 14-22, sept. 2017, doi: 10.1016/j.clay.2017.05.035.

[27]  A. Sarı, R. K. Sharma, G. Hekimoğlu, et V. V. Tyagi, « Preparation, characterization, thermal energy storage properties and temperature control performance of form-stabilized sepiolite based composite phase change materials », Energy and Buildings, vol. 188-189, p. 111-119, avr. 2019, doi: 10.1016/j.enbuild.2019.02.008.

[28]  C. Li, L. Fu, J. Ouyang, et H. Yang, « Enhanced performance and interfacial investigation of mineral-based composite phase change materials for thermal energy storage », Sci Rep, vol. 3, no 1, p. 1908, déc. 2013, doi: 10.1038/srep01908.

[29]  M. Li, Z. Wu, H. Kao, et J. Tan, « Experimental Investigation of Preparation and Thermal Performances of Paraffin/Bentonite Composite Phase Change Material », Energy Conversion and Management - ENERG CONV MANAGE, vol. 52, p. 3275-3281, oct. 2011, doi: 10.1016/j.enconman.2011.05.015.

[30]  C. Chen, X. Liu, W. Liu, et M. Ma, « A comparative study of myristic acid/bentonite and myristic acid/Eudragit L100 form stable phase change materials for thermal energy storage », Solar Energy Materials and Solar Cells, vol. 127, p. 14-20, août 2014, doi: 10.1016/j.solmat.2014.03.057.

[31]  A. Sarı, « Thermal energy storage characteristics of bentonite-based composite PCMs with enhanced thermal conductivity as novel thermal storage building materials », Energy Conversion and Management, vol. 117, p. 132-141, juin 2016, doi: 10.1016/j.enconman.2016.02.078.

[32]  X. Huang, G. Alva, L. Liu, et G. Fang, « Preparation, characterization and thermal properties of fatty acid eutectics/bentonite/expanded graphite composites as novel form–stable thermal energy storage materials », Solar Energy Materials and Solar Cells, vol. 166, p. 157-166, juill. 2017, doi: 10.1016/j.solmat.2017.03.026.

[33]  A. Sarı et A. Biçer, « Thermal energy storage properties and thermal reliability of some fatty acid esters/building material composites as novel form-stable PCMs », Solar Energy Materials and Solar Cells, vol. 101, p. 114-122, juin 2012, doi: 10.1016/j.solmat.2012.02.026.

[34]  A. Sarı, « Preparation and thermal energy storage properties of building material-based composites as novel form-stable PCMs », Energy and Buildings, p. 11, 2012.

[35]  D. Sun et L. Wang, « Utilization of paraffin/expanded perlite materials to improve mechanical and thermal properties of cement mortar », Construction and Building Materials, vol. 101, p. 791-796, déc. 2015, doi: 10.1016/j.conbuildmat.2015.10.123.

[36]  Z. Lu, B. Xu, J. Zhang, Y. Zhu, G. Sun, et Z. Li, « Preparation and characterization of expanded perlite/paraffin composite as form-stable phase change material », Solar Energy, vol. 108, p. 460-466, oct. 2014, doi: 10.1016/j.solener.2014.08.008.

[37]  T. Li, Y. Yuan, et N. Zhang, « Thermal  properties of phase change cement board with capric acid/expanded perlite form-stable phase change material », Advances in Mechanical Engineering, vol. 9, no 6, p. 168781401770170, juin 2017, doi: 10.1177/1687814017701706.

[38]  Y. He, X. Zhang, et Y. Zhang, « Preparation technology of phase change perlite and performance research of phase change and temperature control mortar », Energy and Buildings, vol. 85, p. 506-514, déc. 2014, doi: 10.1016/j.enbuild.2014.09.023.

[39]  D. Shin et D. Banerjee, « Enhanced thermal properties of SiO2 nanocomposite for solar thermal energy storage applications », International Journal of Heat and Mass Transfer, vol. 84, p. 898-902, mai 2015, doi: 10.1016/j.ijheatmasstransfer.2015.01.100.

[40]  X. Zhou, Q. Yu, S. Zhang, C. Zhang, et J. Feng, « Porous silica matrices infiltrated with PCM for thermal protection purposes », Ceramics International, vol. 39, no 5, p. 5247-5253, juill. 2013, doi: 10.1016/j.ceramint.2012.12.025.

[41]  Y. Zhang, S. Zheng, S. Zhu, J. Ma, Z. Sun, et M. Farid, « Evaluation of paraffin infiltrated in various porous silica matrices as shape-stabilized phase change materials for thermal energy storage », Energy Conversion and Management, vol. 171, p. 361-370, sept. 2018, doi: 10.1016/j.enconman.2018.06.002.

[42]  S. Song, L. Dong, S. Chen, H. Xie, et C. Xiong, « Stearic–capric acid eutectic/activated-attapulgiate composite as form-stable phase change material for thermal energy storage », Energy Conversion and Management, vol. 81, p. 306-311, mai 2014, doi: 10.1016/j.enconman.2014.02.045.

[43]  B. Xu, H. Ma, Z. Lu, et Z. Li, « Paraffin/expanded vermiculite composite phase change material as aggregate for developing lightweight thermal energy storage cement-based composites », Applied Energy, vol. 160, p. 358-367, déc. 2015, doi: 10.1016/j.apenergy.2015.09.069.

[44]  H. Cui, S. A. Memon, et R. Liu, « Development, mechanical properties and numerical simulation of macro encapsulated thermal energy storage concrete », Energy and Buildings, vol. 96, p. 162-174, juin 2015, doi: 10.1016/j.enbuild.2015.03.014.

[45]  G. Kastiukas, X. Zhou, et J. Castro-Gomes, « Development and optimisation of phase change material-impregnated lightweight aggregates for geopolymer composites made from aluminosilicate rich mud and milled glass powder », Construction and Building Materials, vol. 110, p. 201-210, mai 2016, doi: 10.1016/j.conbuildmat.2016.02.029.

[46]  R. Wang, M. Ren, X. Gao, et L. Qin, « Preparation and properties of fatty acids based thermal energy storage aggregate concrete », Construction and Building Materials, vol. 165, p. 1-10, mars 2018, doi: 10.1016/j.conbuildmat.2018.01.034.

[47]  Z. Dong, H. Cui, W. Tang, D. Chen, et H. Wen, « Development of Hollow Steel Ball Macro-Encapsulated PCM for Thermal Energy Storage Concrete », Materials, vol. 9, no 1, p. 59, janv. 2016, doi: 10.3390/ma9010059.

[48]  R. Velraj, R. V. Seeniraj, B. Hafner, C. Faber, et K. Schwarzer, « HEAT TRANSFER ENHANCEMENT IN A LATENT HEAT STORAGE SYSTEM1Paper presented at the ISES Solar World Congress, Taejon, South Korea, 24–29 August 1997.1 », Solar Energy, vol. 65, no 3, p. 171-180, févr. 1999, doi: 10.1016/S0038-092X(98)00128-5.

[49]  A. Soupart-Caron, « Stockage de chaleur dans les matériaux à changement de phase », p. 291.

[50]  E. Mohseni, W. Tang, et S. Wang, « Development of thermal energy storage lightweight structural cementitious composites by means of macro-encapsulated PCM », Construction and Building Materials, vol. 225, p. 182-195, nov. 2019, doi: 10.1016/j.conbuildmat.2019.07.136.

[51]  Q. Ma et M. Bai, « Mechanical behavior, energy-storing properties and thermal reliability of phase-changing energy-storing concrete », Construction and Building Materials, vol. 176, p. 43-49, juill. 2018, doi: 10.1016/j.conbuildmat.2018.04.226.

[52]  C. Mankel, A. Caggiano, et E. Koenders, « Thermal energy storage characterization of cementitious composites made with recycled brick aggregates containing PCM », Energy and Buildings, vol. 202, p. 109395, nov. 2019, doi: 10.1016/j.enbuild.2019.109395.

[53]  A. Mourid, M. El Alami, et F. Kuznik, « Experimental investigation on thermal behavior and reduction of energy consumption in a real scale building by using phase change materials on its envelope », Sustainable Cities and Society, vol. 41, p. 35-43, août 2018, doi: 10.1016/j.scs.2018.04.031.

[54] A. Pasupathy, L. Athanasius, R. Velraj, et R. V. Seeniraj, « Experimental investigation and numerical simulation analysis on the thermal performance of a building roof incorporating phase change material (PCM) for thermal management », Applied Thermal Engineering, vol. 28, no 5-6, p. 556-565, avr. 2008, doi: 10.1016/j.applthermaleng.2007.04.016.

[55] H. J. Alqallaf et E. M. Alawadhi, « Concrete roof with cylindrical holes containing PCM to reduce the heat gain », Energy and Buildings, vol. 61, p. 73-80, juin 2013, doi: 10.1016/j.enbuild.2013.01.041.

[56] M. Koschenz et B. Lehmann, « Development of a thermally activated ceiling panel with PCM for application in lightweight and retrofitted buildings », Energy and Buildings, vol. 36, no 6, p. 567-578, juin 2004, doi: 10.1016/j.enbuild.2004.01.029.

[57] U. Berardi et A. A. Gallardo, « Properties of concretes enhanced with phase change materials for building applications », Energy and Buildings, vol. 199, p. 402-414, sept. 2019, doi: 10.1016/j.enbuild.2019.07.014.

[58] T. A. Vik, H. B. Madessa, P. Aslaksrud, E. Folkedal, et O. S. Øvrevik, « Thermal Performance of an Office Cubicle Integrated with a Bio-based PCM: Experimental Analyses », Energy Procedia, vol. 111, p. 609-618, mars 2017, doi: 10.1016/j.egypro.2017.03.223.

[59] K. Zhong, S. Li, G. Sun, S. Li, et X. Zhang, « Simulation study on dynamic heat transfer performance of PCM-filled glass window with different thermophysical parameters of phase change material », Energy and Buildings, vol. 106, p. 87-95, nov. 2015, doi: 10.1016/j.enbuild.2015.05.014.

[60] K. A. R. Ismail et J. R. Henríquez, « Thermally effective windows with moving phase change material curtains », Applied Thermal Engineering, vol. 21, no 18, p. 1909-1923, déc. 2001, doi: 10.1016/S1359-4311(01)00058-8.

[61] E. Meng, H. Yu, et B. Zhou, « Study of the thermal behavior of the composite phase change material (PCM) room in summer and winter », Applied Thermal Engineering, vol. 126, p. 212-225, nov. 2017, doi: 10.1016/j.applthermaleng.2017.07.110.

[62] L. Navarro, A. de Gracia, A. Castell, et L. F. Cabeza, « Experimental study of an active slab with PCM coupled to a solar air collector for heating purposes », Energy and Buildings, vol. 128, p. 12-21, sept. 2016, doi: 10.1016/j.enbuild.2016.06.069.

[63] F. Kuznik, J. Virgone, et J.-J. Roux, « Energetic efficiency of room wall containing PCM wallboard: A full-scale experimental investigation », Energy and Buildings, vol. 40, no 2, p. 148-156, janv. 2008, doi: 10.1016/j.enbuild.2007.01.022.

[64] K. Cellat et al., « 2 years of monitoring results from passive solar energy storage in test cabins with phase change materials », Solar Energy, vol. 200, p. 29-36, avr. 2020, doi: 10.1016/j.solener.2019.01.045.

[65] J. Čurpek et M. Čekon, « Climate response of a BiPV façade system enhanced with latent PCM-based thermal energy storage », Renewable Energy, vol. 152, p. 368-384, juin 2020, doi: 10.1016/j.renene.2020.01.070.

[66] W. He et al., « Experimental study on the performance of a novel RC-PCM-wall », Energy and Buildings, vol. 199, p. 297-310, sept. 2019, doi: 10.1016/j.enbuild.2019.07.001.

[67] K. Menoufi, A. Castell, M. M. Farid, D. Boer, et L. F. Cabeza, « Life Cycle Assessment of experimental cubicles including PCM manufactured from natural resources (esters): A theoretical study », Renewable Energy, vol. 51, p. 398-403, mars 2013, doi: 10.1016/j.renene.2012.10.010.

[68] A. L. Pisello, V. L. Castaldo, C. Piselli, C. Fabiani, et F. Cotana, « Thermal performance of coupled cool roof and cool façade: Experimental monitoring and analytical optimization procedure », Energy and Buildings, vol. 157, p. 35-52, déc. 2017, doi: 10.1016/j.enbuild.2017.04.054.

[69] L. F. Cabeza, C. Castellón, M. Nogués, M. Medrano, R. Leppers, et O. Zubillaga, « Use of microencapsulated PCM in concrete walls for energy savings », Energy and Buildings, vol. 39, no 2, p. 113-119, févr. 2007, doi: 10.1016/j.enbuild.2006.03.030.

[70] P. Arce, C. Castellón, A. Castell, et L. F. Cabeza, « Use of microencapsulated PCM in buildings and the effect of adding awnings », Energy and Buildings, vol. 44, p. 88-93, janv. 2012, doi: 10.1016/j.enbuild.2011.10.028.

[71] C. Barreneche, L. Navarro, A. de Gracia, A. I. Fernández, et L. F. Cabeza, « In situ thermal and acoustic performance and environmental impact of the introduction of a shape-stabilized PCM layer for building applications », Renewable Energy, vol. 85, p. 281-286, janv. 2016, doi: 10.1016/j.renene.2015.06.054.

[72] A. Bontemps, M. Ahmad, K. Johannès, et H. Sallée, « Experimental and modelling study of twin cells with latent heat storage walls », Energy and Buildings, vol. 43, no 9, p. 2456-2461, sept. 2011, doi: 10.1016/j.enbuild.2011.05.030.

[73] M. Bahrar, Z. I. Djamai, M. EL Mankibi, A. Si Larbi, et M. Salvia, « Numerical and experimental study on the use of microencapsulated phase change materials (PCMs) in textile reinforced concrete panels for energy storage », Sustainable Cities and Society, vol. 41, p. 455-468, août 2018, doi: 10.1016/j.scs.2018.06.014.

# An Experimental Assessment on the Performance of Different Evacuated Tube Solar Collector Configurations

Sana Said[#1], Sofiene Mellouli[*2], Ridha Ajjel[#3]

[#]*Laboratory of Metabolic Biophysics and Applied Professional and Environmental Toxicology(LR12ES02),*

*Ibn El Jazzar Faculty of Medicine*
*Street Mohamed Karoui Sousse 4002, Tunisia*

[1] sanasaid022@gmail.com
[3]ajjelridha@gmail.com

[*]*Mechanical Engineering Department, College of Engineering, Jazan University*
*Jazan,45142, Saudi Arabia*

[2] sofiene.mellouli81@gmail.com

*Abstract*— **An experimental study has been conducted to evaluate the performance of two types of evacuated tube solar collectors (ETSC) – Heat Pipe and Direct Flow. The investigation, focused on the operational parameters, explored the impact of the incident solar intensities and HTF mass flow rate on the overall performance of the Heat Pipe ETSC. Additionally, the study examined the performance of a heat pipe with four direct flow configurations (U-tube, Double U-tube, Coaxial tube, and Helical tube). The comparative analysis, conducted under uniform experimental conditions with water as the heat transfer fluid (HTF), revealed that the Helical tube configurationenhanced overall ETSC performancedemonstrating a remarkable 69% increase in thermal efficiency and achieving an HTF temperature of 27.5°C.**

*Keywords*— Evacuated tube solar collector; helical tube; heat pipe; U-tube; coaxial tubes; double U-tube.

## I. INTRODUCTION

With the rapid growth of the population over the years, the demand for energy sources and supplies has increased, as well as the reliance on limited fossil fuels, leading to an increase in global warming. Therefore, the search for new ways to obtain energy is extremely important. The use of solar thermal collectors is one of the most promising methods of harvesting solar energy in order to fulfill rising energy needs and reduce greenhouse gas emissions [1]. In general, there are two kinds of solar thermal collectors: a flat-plate solar collector (FPSC) and an evacuated tube solar collector (ETSC). There are two main categories of ETSCs [2]–[4]: (i)Direct-flow ETSC; and (ii) Heat-pipe ETSC. The ETSCs are the most promising solar collector outperforming FPSCs in term of efficiency and operational temperatures. An ETSC is a solar collector comprising two highly durable glass tubes fused together and filled with vacuum inorder to reduce losses through convection. The outer tube, known for itshigh transmissivity and low reflection, allows efficient radiation passage. The inner surface of the glass tube is coated with a selective material, maximizing solar energy absorption and minimizing reflection to effectively capture and retain heat.[5] Furthermore, the upper tube enhances thermal efficiency by inducing a greenhouse effect. Different researchers have focused their attention on several elements, including construction, design, heat transfer fluid type, radiation capture techniques, and tilt angle, which have a substantial impact on the ETSC's performance[5], [6].

## II. EXPERIMENTAL SET UP AND METHODOLOGY

### A. Design of the ETSC with heat pipe configuration

The ETSC with heat pipe studied in this work consists of 10 evacuated tubes connected to a manifold. The evacuated tubes are made of high borosilicate glass. A heat pipe is placed within each tube with geometric parameters presented in Table I. The surface of the inner evacuated tubes is covered by a selective coating material, in contact with circular aluminium fins, designed to absorb the incident radiation collected as thermal energy. The HTF circulated inside the heat pipes is water.
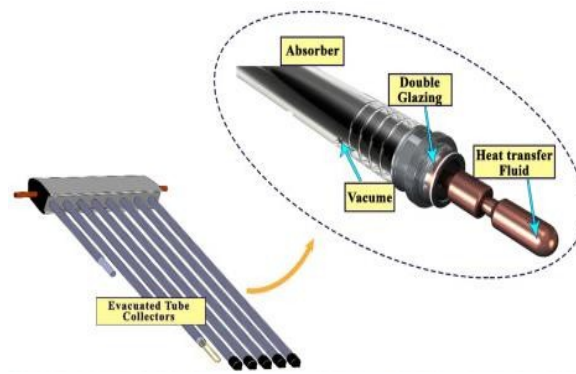
Fig. 1 Cross section of the Heat pipe ETSC system[7]

*B. Design of the direct flow ETSCs*

The direct flow ETSC consist of two glass tubes enclosed in vacuum. The inner glass tube is covered with a selective coating and linked to the heat exchanger with water circulating within it. Four heat exchanger configurations were proposed and studied in this work as seen in Fig 2: U-tube, double U-tube, helical tube and coaxial tube. The geometric parameters of the four configurations are presented in Table I.

- U-Tube configuration

The U-tube shaped design enhances the absorption of the of sunlight and facilitates the flow of the HTF circulating inside the tube. The U-Tube which is shown in Fig 2a is made up of copper material and enrolled with aluminium fin with a thickness of 0.8 mm.

- The double U-tube configuration

The ETSC with double U-tube configuration represented in Fig 2b, consist of two U-shaped tubes made of copper. The two tubes are attached to an aluminium fin.

- The Coaxial tube configuration

The coaxial heat exchanger consists of tube inside tube, the two coaxial tubes are welded at the bottom and attached to an aluminium fin. The HTF circulated within the inner tube. This type of heat exchanger helps reducing heat loss. The present configuration is presented in Fig 2c.

- The helical tube configuration

The helical tube heat exchanger, presented in Fig 2d, consists of a spiral tube, which maximizes the surface area exposed to sunlight allowing for a maximum capture of solar radiation. The helical tube configuration makes a direct contact with the inner glass tube.
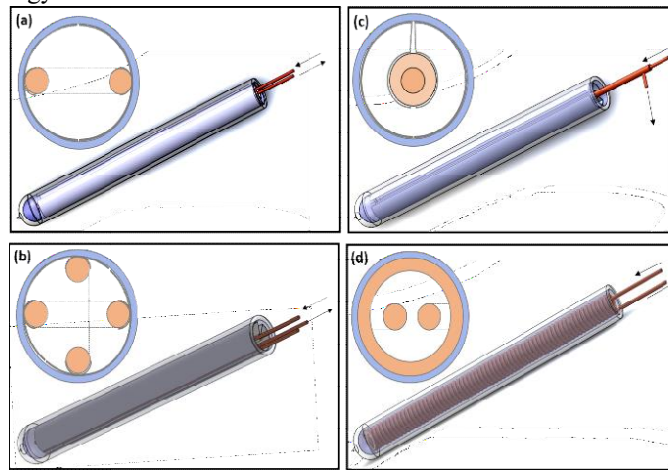
Fig. 2  Configuration of the direct flow ETSC: (a) U-tube, (b) double U-tube, (c) Coaxial tube and (d) helical tube

TABLE I:
GEOMETRIC PARAMETERS OF THE DIRECT ETSCS

| Parameters | Heat Pipe | Direct Flow ETSCs | | | |
|---|---|---|---|---|---|
| | | U- Tube | Double U-Tube | Helical Tube | Coaxial Tube |
| Pipe length (mm) | 680 | 1360 | 2720 | 5730 | 680 |
| Pipe Diameter (mm) | 15.88/25.4 | 7.94 | 7.94 | 7.94 | 7.94 |
| Glass tube Length (mm) | 700 | 700 | 700 | 700 | 700 |
| Glass Tube diameter (mm) | 58/54 | 58/54 | 58/54 | 58/54 | 58/54 |

### C. The experimental procedure

A purpose-built indoor experimental test rig was developed to assess the thermal performance of a typical ETSC featuring a heat pipe.The experiments involved facing the ETSC to a solar simulator.The initial phase of the study focused on examining the impact of received solar irradiance and mass flow rate on the ETSC's performance.Subsequently, a comparative investigation was conducted to assess the performance of the typical ETSC against direct-flow ETSCs, each configured differently:with a U-tube, a double U-tube with a  helical tube, and a coaxial tube. Fig 3 depicts the experimental setup of the 10 evacuated tubes exposed to a solar simulator.



Fig. 3 The experimental setup of the ETSC with heat pipe configuration

### D. Performance analysis

The thermal efficiency of an ETSC is a measure of how effectively the collector converts solar energy into usable heat.It is typically expressed as the ratio of the actual heat gain or output energy from the ETSC to the solar radiation that is incident on the collector. The formula for thermal efficiency is represented as bellow[8]:

$$\eta = \frac{Q_{gain}}{A.I} \quad (1)$$

With A is the area of the solar collector and I is the solar irradiance received by the solar simulator.

The heat gained from the ETSC can be calculated from the expression bellow[8]:

$$Q_{gain} = \dot{m}C_p(T_{out} - T_{in}) \quad (2)$$

With $\dot{m}$ represents the mass flow rate of the water circulating inside the heat exchanger.

## I. RESULTS

### A. Study of the conventional Heat pipe ETSC system

#### 1) Effect of the solar irradiance

In order to investigate the influence of solar irradiation on the performance of the heat pipe ETSC, three intensities were specifically selected: 300, 500, and 1000 W/m$^2$.Throughout this experiment, the flow rate and the inlet water temperature were consistently set at 0.6 LPM and 36 °C, respectively.The process involved heating the inlet water through the manifold connected to the heat pipes within the ETSC system.
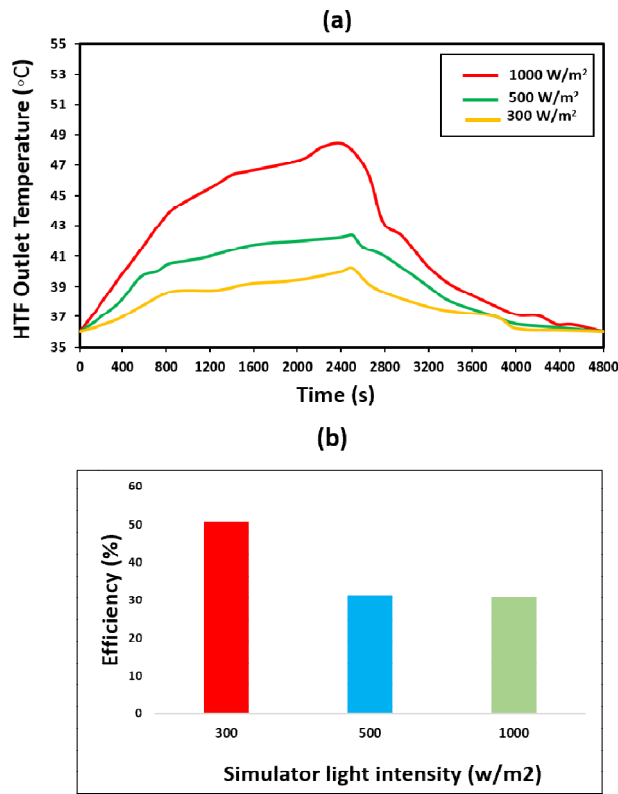


Fig. 4 The impact of solar intensity on the overall performance of the ETSC

The influence of the incident solar intensities on the overall performance of the ETSC during 80 minutes is depicted in fig.4. The evolution of the HTF outlet temperature for three different solar intensities (300W/m$^2$, 500W/m$^2$ and 1000W/m$^2$) is presented in Fig 4a. The results indicated that elevating solar intensity led to higher HTF outlet temperatures for the ETSC,reaching a peak of 48°C after 2400 seconds.Specifically, the HTF achieved outlet temperatures of 42°C and 39°C when exposed to solar intensities of 500 W/m$^2$ and 300 W/m$^2$, respectively. It is noted that the ETSC receives solar irradiance for the first 2400 seconds after that the solar radiation remains at zero W/m$^2$. Figure 4b illustrates the impact of solar intensities on the efficiency of the ETSC. The findings indicate a

notable influence of solar irradiance on the ETSC efficiency.Higher solar intensities resulted in a lower efficiency of 30.76%, whereas, with solar intensities of 500 W/m$^2$ and 300 W/m$^2$, the efficiency increased to 31.38% and 50.71%, respectively.This finding can be explained by the fact that the solar collector reached a point where its heat output exceeds it saturation limit, leading to the observes impact on the efficiency.

### 2) Effect of the mass flow rates

An experimental investigation took place to study the influence of the HTF mass flow rate on the behavior of the heat pipe ETSC. The experiment is set under different mass flow rates of 0.6 LPM, 1.2LPM and 2.4 LPM, with a higher incident solar intensity of 1000 W/m$^2$ and for an initial temperature of 22°C.
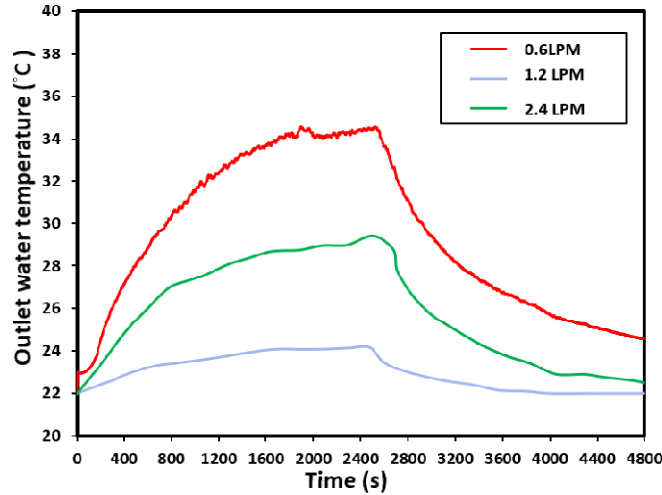


Fig. 5 The impact of mass flow rate on the HTF outlet temperature

Figure 5 illustrates the evolution of the HTF outlet temperature over an 80-minute period, employing three distinct mass flow rates (0.6 LPM, 1.2 LPM, and 2.4 LMP).The results indicate a continuous rise in HTF temperature for the initial 2400 seconds, reaching peaks of 34.1°C, 29.5°C, and 24.1°Cwith mass flow rates of 0.6 LPM, 1.2 LPM, and 2.4 LPM, respectively. As the solar irradiance diminishes after the first 2400 seconds and remains at 0 W/m$^2$,the HTF outlet temperature for all three cases starts to decrease, eventually stabilizing at the inlet water temperature at the end of the experiment. The findings highlight that the ETSC achieves higher HTF temperatures when employing lower mass flow rates of 0.6 LPM. This outcome can be explained by the fact that diminishing HTF mass flow rates prolong the contact time between the HTF and the condenser inside the heat pipe. The slower movement of water allows for more extended contact with the heat exchanging surfaces, resulting in a higher outlet temperature provided by the ETSC. Conversely, when employing higher mass flow rates, the circulation time of the HTF diminishes, leading to a lower HTF temperature.

### B. Effect of the heat exchanger design

In the second part of the study, a comparative analysis was undertaken to evaluate the performance of an ETSC specifically focusing on the design of its heat exchanger.
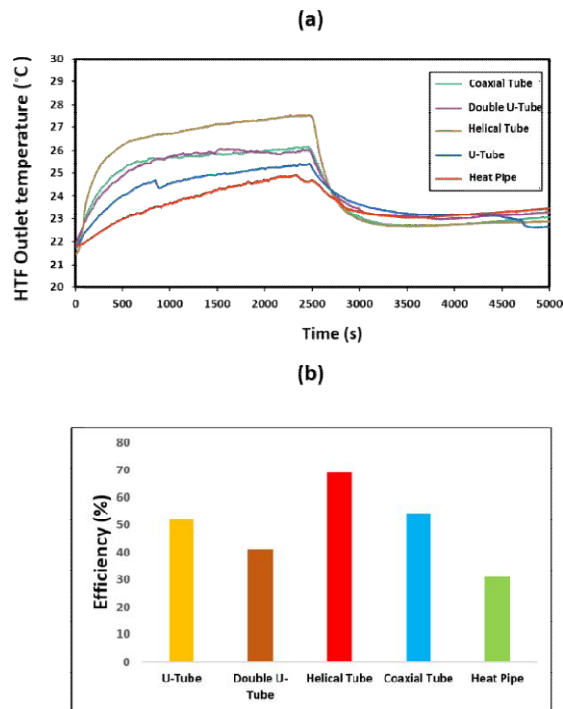
**(a)**



**(b)**



Fig.6 Effect of the ETSC configuration (a) on the HTF outlet temperature (b) and on the thermal efficiency

Four distinct single direct-flow ETSC configurations were subjected to testing and compared against a single ETSC featuring a heat pipe configuration, as illustrated in Fig. 6. These assessments were conducted under identical experimental conditions, involving a higher solar irradiance of 1000 W/m² and a HTF low mass flow rate of 0.6 LPM with an initial HTF inlet temperature set at 22°C. As depicted in Fig. 6a, the temporal evolution of HTF outlet temperatures for various ETSC configurations over a 5000 second duration revealed notable distinctions. The helical tube heat exchanger consistently outperformed other configurations, achieving a peak temperature of 27.5°C at the 2500-second mark. Additionally, the temperature of the coaxial configuration reached a maximum of 26.1°C, while the U-tube, double U-tube, and heat pipe configurations peaked at 26°C, 25.4°C, and 24.8°C, respectively. Moreover, in the absence of solar irradiance, temperatures gradually declined, reaching 23.5°C, 23.4°C, 23.3°C, 23°C, and 22.8°C for the Heat Pipe, double U-tube, coaxial tube, helical tube, and U-tube cases. Noteworthy is the superior performance of the helical tube heat exchanger under heightened solar irradiance, attributed to its design that augments the surface area, facilitating increased the contact of the HTF to be heated. Furthermore, the direct connection of the helical tube to the inner area of the glass tube without an aluminium fin enhances its efficiency. In Fig. 6b, the efficiency of the five ETSC types is presented. The helical tube configuration exhibited the highest efficiency at 69%, followed by the coaxial tube ETSC at 54%. The U-tube, double U-tube, and heat pipe configurations demonstrated efficiencies of 52%, 41%, and 31%, respectively, indicating the notable impact of heat exchanger design on overall ETSC performance. The elevated thermal efficiency observed in the helical tube ETSC underscores its superior capability in converting sunlight into usable heat, a critical factor when assessing the performance of solar thermal systems. Enhancing thermal efficiency stands as a primary objective in the design and optimization of solar collectors, aiming to maximize the utilization of solar energy for heating purposes.

## II. CONCLUSIONS

This paper work experimentally studies the parametric effect of a conventional heat pipe evacuated tube solar collector used as water heater and compare it with different configuration of a direct flow evacuated tube solar collector. Two experiment tests were presented. The first test focused on the influence of the solar irradiation and water mass flow rate on the effectiveness of the ETSC. Four single direct flow ETSC were studied in the second experiment in order to compare it with heat pipe evacuated tube collector, including helical tube, coaxial tube, U tube, and double U tube. The following conclusion were obtained from the study.

- The ETSC provides higher temperature reaching
48°C when received higher solar irradiance of 1000 W/m².
- The deployment of lower mass flow rates enhances the effectiveness of the ETSC.
- The comparison of the five types of ETSC configurations proved that the ETSC with helical tube configuration performed better compared to the other configurations, by generation higher temperatures of 27.5°C and a higher efficiency of 69%.

REFERENCES

[1]     N. L. Panwar, S. C. Kaushik, and S. Kothari, "Role of renewable energy sources in environmental protection: A review," *Renewable and Sustainable Energy Reviews*, vol. 15, no. 3, pp. 1513–1524, 2011, doi: 10.1016/j.rser.2010.11.037.

[2]     A. Kumar, Z. Said, and E. Bellos, "An up-to-date review on evacuated tube solar collectors," *Journal of Thermal Analysis and Calorimetry*, vol. 145, no. 6. Springer Science and Business Media B.V., pp. 2873–2889, Sep. 01, 2021. doi: 10.1007/s10973-020-09953-9.

[3]     M. A. Sabiha, R. Saidur, S. Mekhilef, and O. Mahian, "Progress and latest developments of evacuated tube solar collectors," *Renewable and Sustainable Energy Reviews*, vol. 51. Elsevier Ltd, pp. 1038–1054, Jul. 27, 2015. doi: 10.1016/j.rser.2015.07.016.

[4]     M. Aramesh and B. Shabani, "On the integration of phase change materials with evacuated tube solar thermal collectors," *Renewable and Sustainable Energy Reviews*, vol. 132. Elsevier Ltd, Oct. 01, 2020. doi: 10.1016/j.rser.2020.110135.

[5]     S. Said, S. Mellouli, T. Alqahtani, S. Algarni, and R. Ajjel, "New Evacuated Tube Solar Collector with Parabolic Trough Collector and Helical Coil Heat Exchanger for Usage in Domestic Water Heating," *Sustainability (Switzerland)*, vol. 15, no. 15, 2023, doi: 10.3390/su151511497.

[6]     V. Dabra, L. Yadav, and A. Yadav, "The effect of tilt angle on the performance of evacuated tube solar air collector: experimental analysis," *International Journal of Engineering, Science and Technology*, vol. 5, no. 4, pp. 100–110, Mar. 2018, doi: 10.4314/ijest.v5i4.9.

[7]     Y. Peng *et al.*, "Investigation of energy performance in a U-shaped evacuated solar tube collector using oxide added nanoparticles through the emitter, absorber and transmittal environments via discrete ordinates radiation method," *J Therm Anal Calorim*, vol. 139, no. 4, pp. 2623–2631, Feb. 2020, doi: 10.1007/s10973-019-08684-w.

[8]     S. Said, S. Mellouli, T. Alqahtani, S. Algarni, R. Ajjel, and K. Ghachem, "An Experimental Comparison of the Performance of Various Evacuated Tube Solar Collector Designs," 2023.

# Printed High-Gain Yagi Antenna for 5G Applications

Khouloud Mohammed Belhadj [#1], Ziani Kerarti Djalal [*2], Souheyla ferouani [#3]

[#] *Dept.of Electronic and Telecommunication ,SSL Laboratory of Ain Temouchent University , LTT laboratory of Tlemcen University*

*Ain temouchent University Belhadj Bouchaib*

*Ain temouchent, Algeria*

[1] khouloud.mohammedbelhadj@univ-temouchent.edu.dz

[3] souheyla.ferouani@univ-temouchent.edu.dz

[*] *Department of Post-graduated and Specialties, LARATIC Laboratory at National Institute of Telecommunications and ICT*

*Oran, Algeria*

[2] Dzianikerarti@inttic.dz

*Abstract*— **A Yagi printed antenna is designed in this work to achieve a high gain for using in mobile communication. The proposed antenna operates at 3.59 GHz between [3.4-3.8] GHz. The use of four directors exhibits a good return loss of -34.56 at 3.59 GHz wi th a bandwidth of 149.1 MHz between 3.5229 GHz and 3.672 GHz, directional energy patterns and linearly increasing gain ranging of 10.35 dB over the entire bandwidth. The results are very satisfactory and the Yagi antenna can be integrated for 5 G applications enabling its usability for point-to-point and point-to-mul tipoint communication links.**

*Keywords*— **Microstrip antenna, yagi-uda antenna, mobile communications, 5G applications, directional radiation pattern.**

## I. INTRODUCTION

Over the past ten decades, wireless communications have developed exceptionally. Today's communications systems are evolving at breakneck speed. Antennas play an essential role as the eyes and ears of our world, establishing our links with the space around us. These antennas are indispensable to wireless communications, and they also ensure OEM transmission and reception in space. Despite this, their integration into systems requires small sizes and high performance. Microstrip antennas are widely used compared with other types of antennas, due to their lightweight, low cost and ability to be integrated into mobile devices. However, they have drawbacks such as low gain and narrow bandwidth. These limitations can be overcome by using the Yagi-Uda antenna, which was invented in 1926 by Dr. H. Yagi and Shintaro Uda. Its configuration normally consists of a number of directors and reflectors that enhance radiation in one direction when properly arranged on a supporting structure [1] that offers both. high bandwidth and efficient radiation performance. Micros trip YAGI Antenna is an antenna consisting of driven elements and some parasitic elements, including a reflector and director [2]. YAGI antenna, one of the most common antennas to achieve high gain, has been used successfully over decades due to its easy design structure and low cost with a single feed. However, the YAGI antenna needs a sizable volume/area. The parasitic elements called the reflector and the directors, are usually spaced approximately 0.25λ away from the driver. Additionally, each element, including the driver and parasitic elements, has a length of close to λ/2 [1].
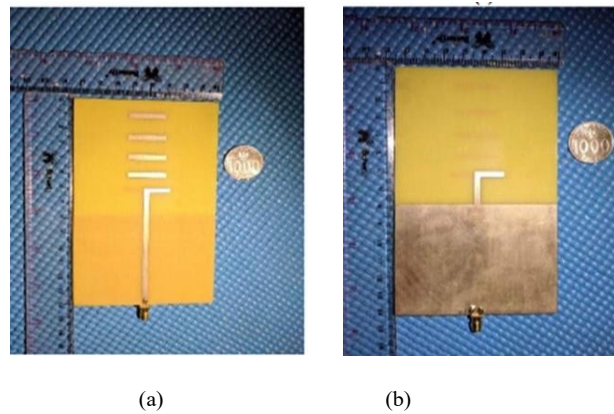
(a)　　　　　　　　(b)

Fig. 1 Fabricated Yagi antenna by [3] (a) top view and (b) bottom view

YAGI microstrip antennas have been the subject of several research papers. In a study by [4], the first YAGI microstrip antenna was presented. It comprises driven elements and parasitic patches (reflector and director elements) located on the same plane, used for the mobile satellite system (MSAT). YAGI-Uda dipole antenna operating at [3.4-3.8] GHz was designed and built for 5G applications [3]. A presentation was given on the design and results obtained with single-beam and dual- beam dipole antennas. First, the authors designed a printed dipole antenna with a single director. A printed dipole antenna with four directors was then studied to increase antenna gain. Finally, they developed a special dual-beam antenna for the node in a linear configuration. This antenna was designed as part of the ANR project called CAPNET, dedicated to site security (autonomous sensor network). In conclusion, they simulated, realized, and characterized all the antennas , measuring their return loss, radiation patterns, and gain. They noted very favorable results in terms of gain and obtained an accurate comparison between simulations and measurements [5]. Further work was presented by [6] ; They have developed a Yagi-Uda 5G linear array antenna specifically for vehicular applications. This array consists of two radiating elements with eight parasitic elements each, and its overall dimensions are $110\times60\times1.6$mm3. Their[7] presented a modified broadband Quasi-Yagi microstrip antenna. This antenna consists of an insulated microstrip acting as director, a microstrip dipole acting as driver, and a truncated ground plane at the rear of the substrate serving as a reflector. The two arms of the driver dipole are positioned on opposite sides of the substrate. One arm is fed by the tapered strip of the 50-$\Omega$ microstrip feedline, while the other is fed by the tapered strip of the truncated ground plane. There have been several generations since the advent of mobile technology. Among them, the first was 1G, followed by 2G, 3G, 4G, and finally 5G. Throughout history, communication systems have evolved significantly with each new iteration [8]. The Fifth-generation (5G) technology[8], which is developing rapidly to meet the growing demand for mobile communications [9], has been designed to overcome the limitations of fourth-generation (4G) technology [8]. The key aspect of 5G is the ability to achieve and maintain data rates around 10 Gbps, delivering a superior customer experience by speeding up downloads and uploads[10].5G frequencies are grouped into three categories: low frequencies, medium frequencies, and high frequencies [11]. 5G mobile networks are extending their reach to enable higher data rates. In 2015, the World Radio Communication Conference (WRC) allocated frequency bands below 6 GHz, sparked debate. Several frequency bands were proposed, including 470-694 MHz, 1427-1518 MHz, 3300-3800 MHz, and 4500-4990 MHz Of these, the 3.5 GHz frequency band was preferred, as it is recognized by most countries [12]. Printing antennas for 5G technology is the subject of a number of research projects. In a paper by [13], a microstrip antenna for 5G, operating at 3.5 GHz with a gain of 3.661 dB, was designed and implemented. In another work [14], the aim was to design and simulate an antenna based on metamaterials in order to miniaturize the dimensions of planar antennas. Firstly, they modelled and designed a rectangular patch antenna with notches. This was used to better adapt the antenna to the resonant frequency of 3.5 GHz, with a gain of 6.2 dB. This study preceded the design of a four-element antenna. This research demonstrates commitment to the development ofof printed antennas optimized for 5G technology in a variety of geometric configurations.

In this work, we simulate a printed Yagi antenna between [3.4-3.8] GHz printed on an FR-4 substrate, having permittivity εr = 4.3, thickness h = 1.5 mm, and dielectric loss tangent of 0.025. We used four directors to achieve a high gain for using in 5G applications enabling its usability for point-to-point and point-to-multipoint communication links.

## II.  ANTENNA DESIGN

In figure 2, a printed Yagi dipole antenna with a permittivity of 4, 35 and a thickness of 1.5 mm was simulated on FR4 substrates. We calculated the antenna dimensions using [1] to operate between [3.4 - 3.8] GHz for 5G applications.

$$Lde = 0.47\lambda \tag{1}$$

$$Ldi = 0.406\lambda \tag{2}$$

$$Lr = 0.76\lambda \tag{3}$$

$$Sr = 0.25\lambda \tag{4}$$

$$Sdi = 0.34\lambda \tag{5}$$

The width of the feed line from the following equation (6) [3]:

$$W = 2h/\pi \ \{B-1 - \ln(2B-1) + (\varepsilon r - 1)/2\varepsilon r \ [\ln(B-1) + 0.39 - 0.61/\varepsilon r]\} \tag{6}$$
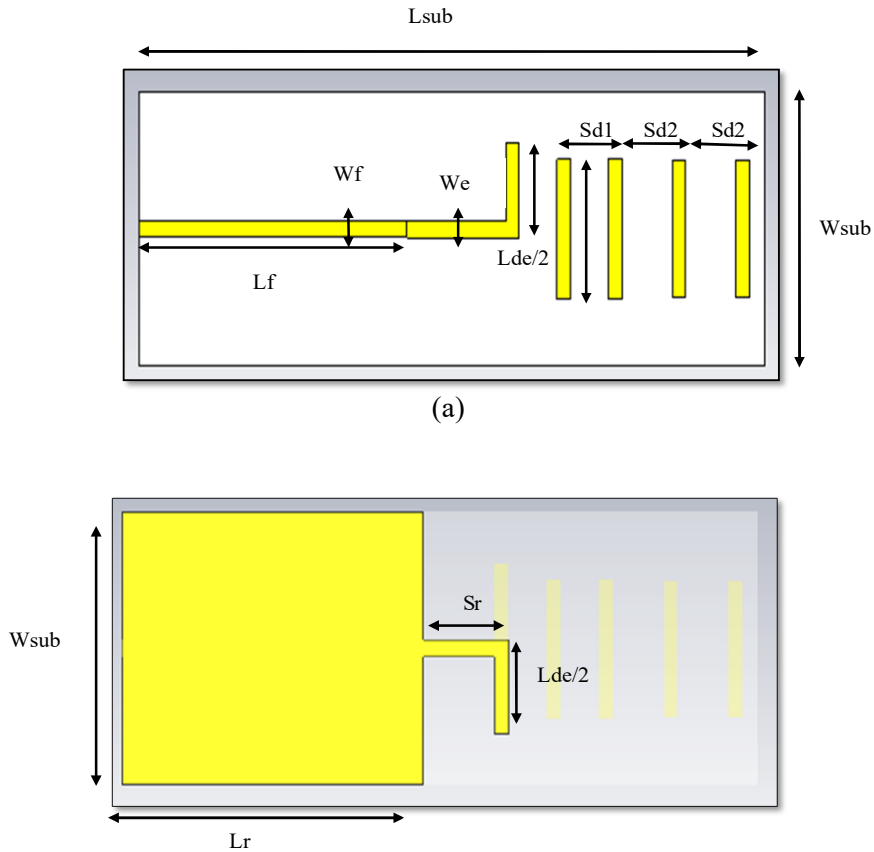


(a)



Fig. 2 Yagi dipole printed antenna, (a) top view, (b) bottom view

All numerical dimensions can be detailed on table I as below:

TABLE .I

DIMENSIONS OF THE PROPOSED YAGI ANTENNA

| Parametres | Value |
|---|---|
| $\lambda 0$ | 85.71mm |
| Wsub | $\lambda 0$+5mm |
| Lsub | Lr+Sr+5*Sd+5mm |
| h | 1.5 |
| $\varepsilon r$ | 4.35 |
| Sr | $\lambda 0$*0.25 |
| Lr | $\lambda 0$*0.76 |
| mth | $\lambda 0$*0.001 |
| We | $\lambda 0$*0.003 |
| Lde | $\lambda 0$*0.478 |
| Sdi | $\lambda 0$*0.34 |
| Ldi | $\lambda 0$*0.406 |
| C0 | C Light*1E-06 |
| Wf | 2.89mm |
| Lf | Lr-1mm |
| frequency minimum | 0.8*frequency |
| frequency maximum | 1.2*frequency |
| frequency center | 3.5 |

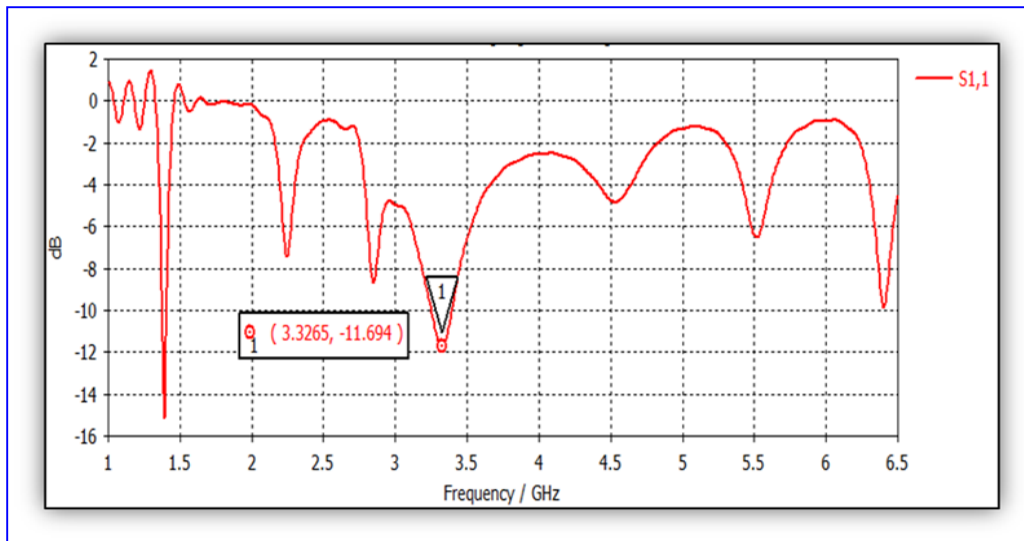## III. SIMULATION RESULTS

A. *Return Loss  |S11|*



Fig. 3 Return loss of proposed Yagi printed antenna

Figure 3 shows the 1st simulation with the initial Yagi antenna parameter values proposed from Table 1, the reflection coefficient obtained is equal to -11.694dB with a frequency of 3.3265 GHz wish is not satisfactory for 5G applications.

We have carried out a parametric study of the length of the components of the Yagi antenna, which have a profound influence on return loss and the formation of its radiation pattern. To obtained more performances of our proposed antenna, the parameters chosen for the study are: L_de= [40.28: 0.5: 33], L_di2= [33.80 : 0.5: 23.9], L_di=[34.80 : 0.5: 24.5].

Simulation results are given in figure 4 (a):
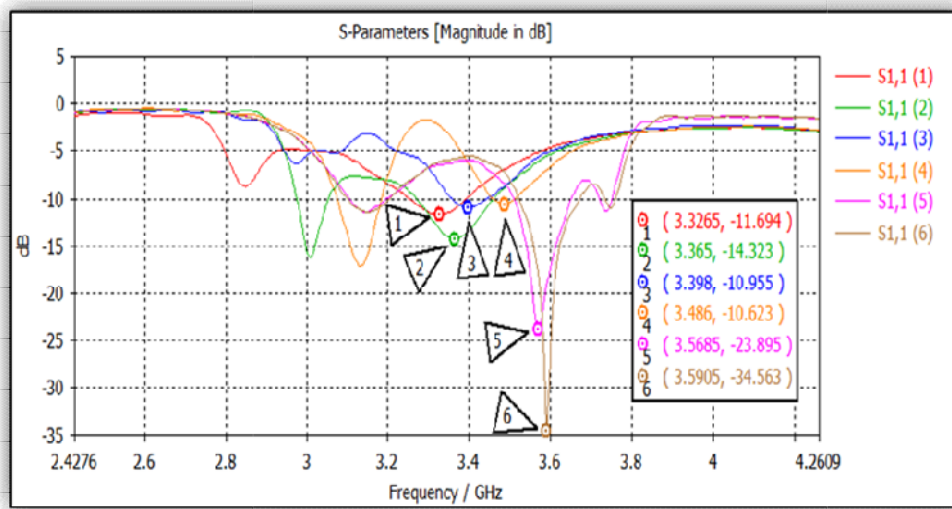


(a)
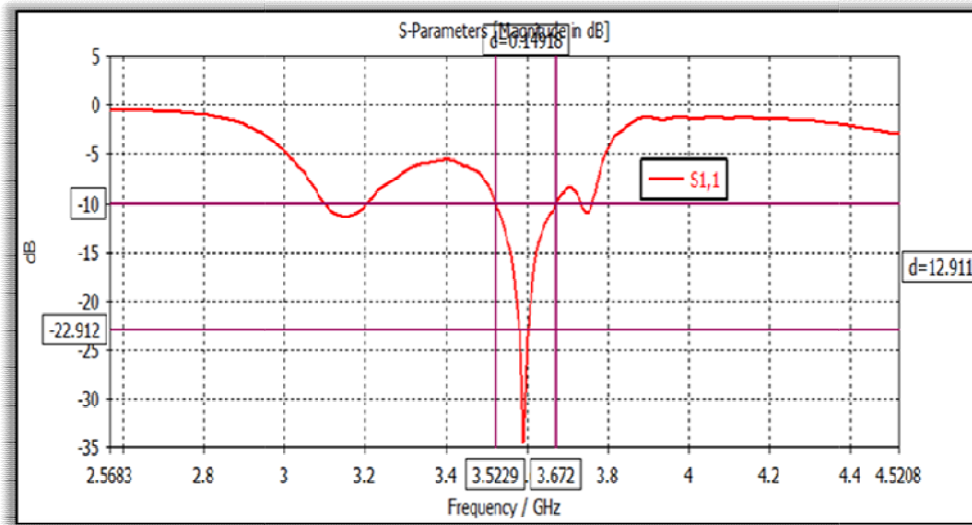


(b)

Fig.4 Return loss S11 of YAGI printed antenna

In figure 4, we obtained with four directors a high gain of 10.385 dB, a reflection coefficient |S11| of -34.563 dB at 3.5905 GHz and a bandwidth equivalent to 149.1 MHz between 3.5229 GHz and 3.672 GHz. The results are very satisfactory for 5G applications.
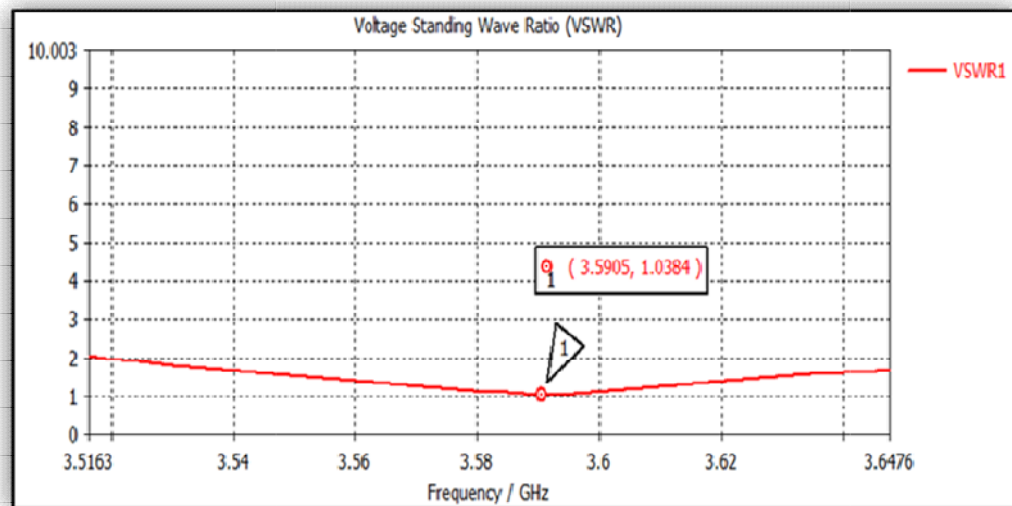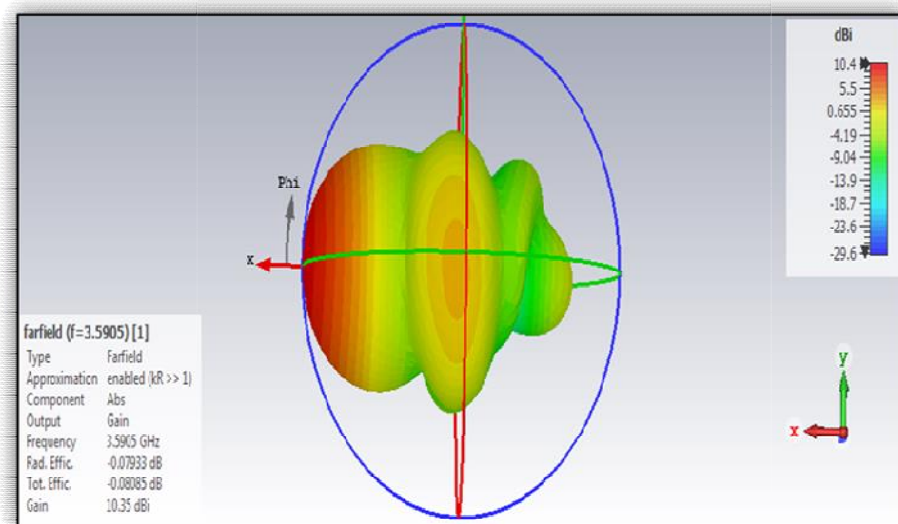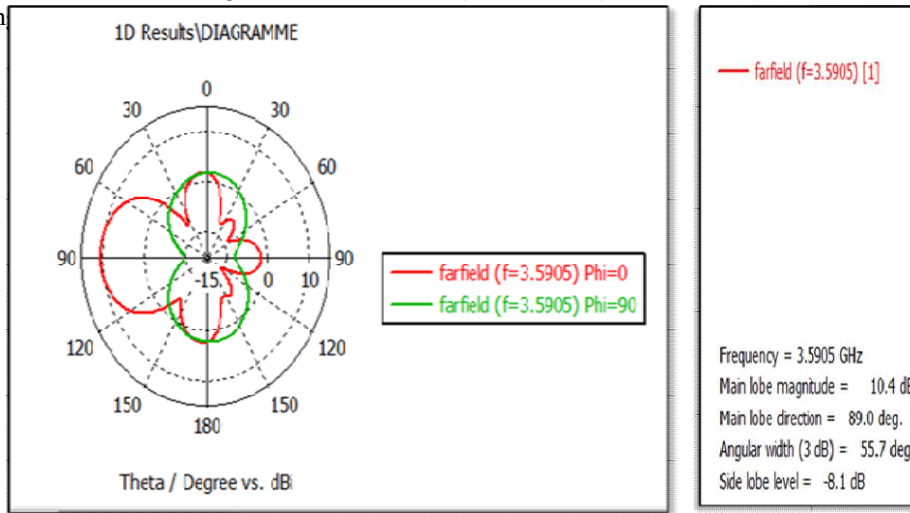
B. *The Voltage Standing Wave Ratio| VSWR |*



Fig.5   VSWR of Yagi antenna

As shown in figure 5, the Voltage Standing Wave Ratio is 1.0384.

C. *Radiation Pattern*



(a)

Fig.6 Simulated radiation pattern of the proposed YAGI antenna (a) 3D, (b) polar

Figure 6 plots both E and H plane radiation patterns of the Yagi printed antenna at 3.59 GHz. The angular width at 3 dB is 55.7 degrees in the H plane (Phi=90°) wish gives a directional and stable radiation pattern.
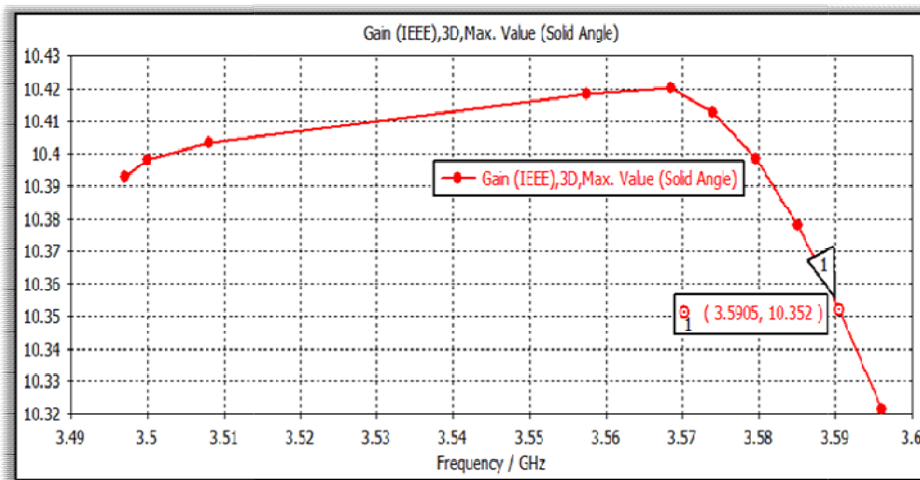
*D. Gain*



Fig.7 Gain of the proposes YAGI antenna

We obtained a high gain equal to 10.352dB at 3.5905GHz frequency.
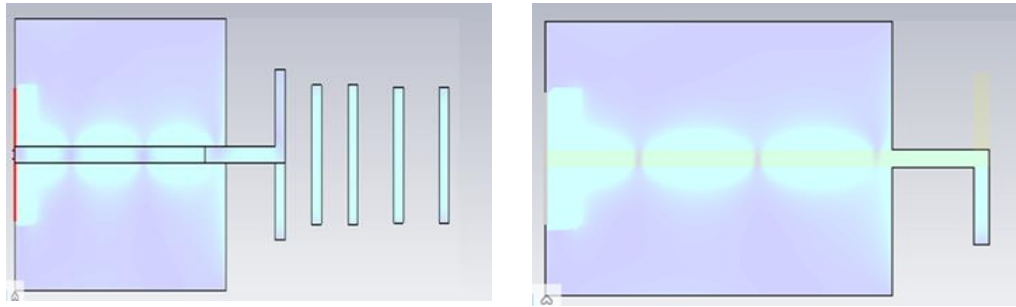
*E. Current Distribution*



Fig.8 Current distribution of the proposed antenna

Figure 8 shows the current distribution of our YAGI antenna

*F. Comparison Results With Other Works*

We compared in Table II Our Proposed Yagi antenna with others research's.

TABLE II
COMPARAISON WITH OTHER RESEARCHES RESULTS

| Ref | Freq (GHz) | \|S 11\| (dB) | Gain (dB) | L*W (mm) | VSWR | Bandwith (Mhz) |
|---|---|---|---|---|---|---|
| [3] | 3.6 | -28.65 | 10.01 | 140.1* 84.66 | / | 250 |
| [13] | 3.5 | -29.77 | 3.661 | 45*35 | 1.0671 | 233.2 |
| [14] | 3.51 | -29 | 6.2 | 71.76*42 | / | / |
| This work | 3.5905 | -34.563 | 10.352 | 138*48 | 1.0384 | 149.1 |

Table II compares our antenna with various researches studies on printed antennas. The results obtained from our proposed antenna were highly satisfactory in terms of gain. The use of Yagi printed antenna in this paper, especially with 4 directors, we obtained a gain of 10.01dB compared to the other works. The results are very satisfactory for several applications in mobile communications.

IV. CONCLUSIONS

Four directors are used in Yagi-Uda printed antenna to achieve a high gain of 10.35 dB for using in mobile communications especially for 5G applications. This will significantly improve signal strength and range in areas where 5G coverage is weaker. Simulation results give a good return loss of -34.56 at 3.59 GHz with a bandwidth of 149.1 MHz between 3.5229 GHz and 3.672 GHz. The proposed antenna gives a directional radiation pattern with angular wide of 55.7° and linearly increasing gain ranging of 10.35 dB over the entire bandwidth.

REFERENCES

[1]     Peter P Viezbicke, Yagi Antenna Design, US Government Printing Office.vol. 688, Washington DC, 1976.

[2]     N. Ismail, F. Oktafiani, and D. Permana, "The two-levels rectangular microstrip Yagi antenna for Wi-Fi application," *J. Phys. Conf. Ser.*, vol. 1402, no. 3, doi: 10.1088/1742-6596/1402/3/033105,2019.

[3]     M. F. Abdus Salam, S. T. Setiyono, Y. Mukhlis, and T. Sepdiansah, "Microstrip-Fed Yagi-Uda Dipole Array Antenna At 3.6 GHz Frequency For 5G Application," *Proc. 2019 4th Int. Conf. Informatics Comput. ICIC 2019*, pp. 0–4, 2019, doi: 10.1109/ICIC47613.2019.8985846,IEEE , 2019.

*[4]*     J. Huang and A. C. Densmore, "Microstrip yagi array antenna for mobile satellite vehicle application," *IEEE Trans. Antennas Propag.*, vol. 39, no. 7, pp. 1024–1030 , doi: 10.1109/8.86924,1991.

[5]     J. M. Floc'H, A. El Sayed Ahmad, and Y. Kokar, "Dual-beam antenna design for autonomous sensor network applications," *Int. J. Antennas Propag.*, vol. 2012, no. Figure 1, doi: 10.1155/2012/289681, 2012.

[6]     K. Sreelakshmi, P. Bora, M. Mudaliar, Y. B. Dhanade, and B. T. P. Madhav, "Linear array Yagi-Uda 5G antenna for vehicular application," *Int. J. Eng. Technol.*, vol. 7, no. 1.1, pp. 513–517, doi: 10.14419/ijet.v7i1.1.10158,2018.

[7]     S. Y. Chen and P. Hsu, "Broadband microstrip-fed modified quasi-Yagi antenna," *2005 IEEE/ACES Int. Conf. Wirel. Commun. Appl. Comput. Electromagn.*, vol. 2005, pp. 208–211, 2005, doi: 10.1109/wcacem.2005.1469563,April.2005.

[8]     N. Ramli, S. K. Noor, T. Khalifa, and N. H. Abd Rahman, "Design and performance analysis of different dielectric substrate based microstrip patch antenna for 5G applications," *Int. J. Adv. Comput. Sci. Appl.*, vol. 11, no. 8, pp. 77–83, doi: 10.14569/IJACSA.2020.0110811, 2020.

[9]     R. Li, Q. Zhang, Y. Kuang, X. Chen, Z. Xiao, and J. Zhang, "Design of a Miniaturized Antenna Based on Split Ring Resonators for 5G Wireless Communications," *2019 Cross Strait Quad-Regional Radio Sci. Wirel. Technol. Conf. CSQRWC 2019 - Proc.*, pp. 1–4, 2019, doi: 10.1109/CSQRWC.2019.8799332, IEEE ,2019.

[10]    R. A. A. Kamaruddin *et al.*, "Return looss improvement of radial line slot array antennas on closed ring resonator structure at 28 GHz," *Prz. Elektrotechniczny*, vol. 97, no. 5, pp. 65–69, 2021, doi: 10.15199/48.2021.05.10, 2021.

[11]    Huawei.: 5G Spectrum Public Policy Position. Shenzen: Huawei ,2017.

[12]    A. J. A. Al-Gburi, Z. Zakaria, I. M. Ibrahim, and E. B. A. Halim, "Microstrip Patch Antenna Arrays Design for 5G Wireless Backhaul Application at 3.5 GHz," *Lect. Notes Electr. Eng.*, vol. 865, pp. 77–88, 2022, doi: 10.1007/978-981-16-9781-4_9, ICCEE, Springer, Singapore.2022.

[13]    D. PARAGYA and H. SISWONO, "3.5 GHz Rectangular Patch Microstrip Antenna with Defected Ground Structure for 5G," *ELKOMIKA J. Tek. Energi Elektr. Tek. Telekomun. Tek. Elektron.*, vol. 8, no. 1, p. 31, 2020, doi: 10.26760/elkomika.v8i1.31,2020.

[14]    B. Fayza,"Design of Miniature Planar Antennas for 5G Systems",Adv Wirel. Commun. Networks, vol. 7, no. 1, p. 1doi: 10.11648/j.awcn.20210701.11,2021

# First principles calculations of structural, electronic and optical properties of AgGaTe₂ chalcopyrite compounds for applications in optical devices and solar cells

**N. Boucerredj[1], K. Beggas[2], S. Ghemid[3], and H. Meradji[3]**

[1,3] Radiations Physics Laboratory, Physics department, Faculty of sciences, Badji Mokhtar Annaba University, B. O. 12, 23000 Annaba. Algeria
[2] Semiconductor laboratory, Physics department, Faculty of sciences, Badji Mokhtar Annaba University, B. O. 12, 23000 Annaba. Algeria.
Email: boucerredj@yahoo.fr

## Abstract

We investigate the structural, electronic and optical properties of AgGaTe₂ chalcopyrite compounds. The calculation were performed in the framework of density functional theory (DFT) using the Full-potential augmented plane wave (FP-LAPW) method within Tran-Blaha Becke-Johnson potential (TB-mBJ) plus local density approximation (LDA). We have found that our results have a good agreement with previous reported experimental and theoretical data.

## Introduction

The ternary chalcopyrite compounds have been extensively studied due to their various applications in solar cells, tunable optical filters, photodetectors, electro-optics, light emitting diodes, photovoltaic, linear and nonlinear optical devices.[1-3]. These compounds of this family crystallize in tetragonal structure with space group $I\bar{4}2d$. The combination of Tran-Blaha modified Becke-Johnson (TB-mBJ) exchange and the local density approximation (LDA) correlation potentials gives accurate gaps for these chalcopyrite compounds.

In this work, a first principles study of structural, electronic and optical properties of AgGaTe₂ using the density functional theory (DFT) [4] with TB-mBJ potential] and LDA correlation potential implemented in wien2k code [5] are studied. All of our results are compared with available theoretical and experimental data reported previously.

## Results

We perform our study using the Full Potential Linearized Augmented Plane Wave (FP-LAPW) method within DFT [6, 7-10] as implemented in wien2k package that has been proved to yield reliable results for electronic, optical and structural properties of various solids [11, 12-15]. We use TB-mBJ approximation [4, 16] as the exchange potential plus LDA correlation potentials to do calculation. The self consistent calculations are considered to be converged when energy and charge are less than 0.0001Ry and 0.001|e|, where e is the electron charge, respectively.

AgGaTe$_2$ has a chalcopyrite structure, figure 1, with space group $I\overline{4}2d$ and a=b=6.28A°, c=11.96A° and the distortion parameter u=0.268 [17]. In order to get optimum values of the equilibrium crystal structure, we have performed full structural optimization by minimizing the total energy with respect to cell volume including lattice parameters and distortion parameter (u) using LDA exchange correlation potential.
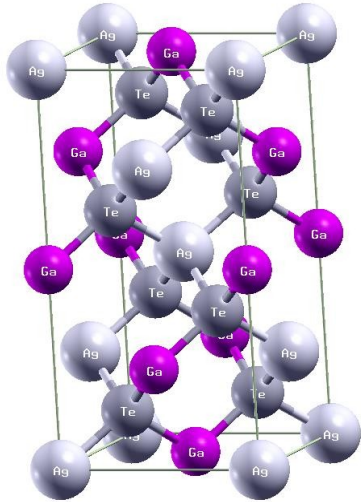


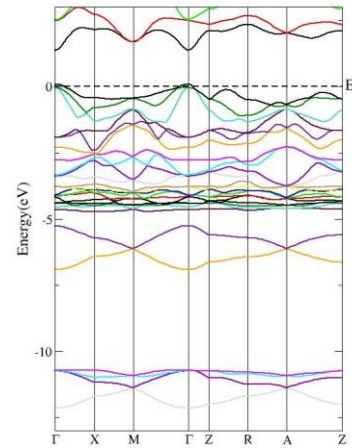**Figure 1.** Crystal structure of AgGaTe$_2$      **Figure2.** Calculated band structures.

We have found that the lattice parameters are ,a=b=6.219A°, c=12.010A° and u=0.2626, which are in good agreement with previous reported results.

In order to study the electronic properties, calculated band structure of AgGaTe$_2$ is represented in Figure 2. The maximum of the valence band and minimum of the conduction band are situated at the same high symmetry $\Gamma$ point, indicating that our compounds has a direct band gap with band gap energy of order of $E_g$=1.49eV.

The optical properties of the studied compounds is determined by frequency dependent of the dielectric function ε(w) given by:

$$\varepsilon(w) = \varepsilon_1(w) + i\varepsilon_2(w) \qquad\qquad (1)$$

The real and imaginary parts dependence of energy are shown in figure 3. The static value of ε at 0ev is about 7.18 in xx and zz directions but the maximum values of Im.ε are different in xx and zz directions.
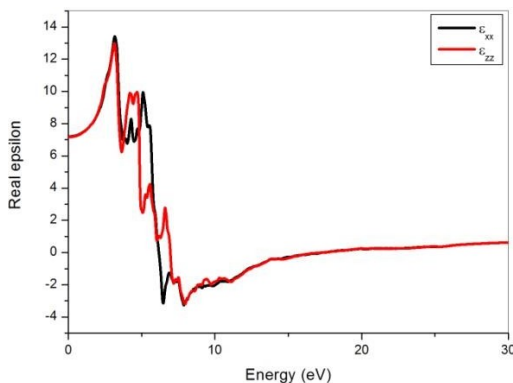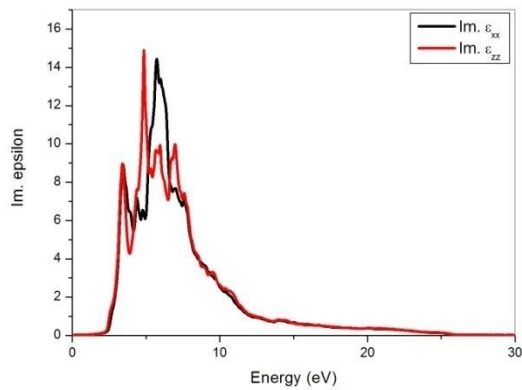
**Figure 3.** Real and imaginary parts of the dielectric function.



## Conclusion

The structural, electronic and optical properties of AgGaTe$_2$ chalcopyrite compound have been study successfully using TB-mBJ(LDA) in wien2k code. The obtained results for structural parameters and band gap energy are in good agreement with previous reported data. Further, it is observed that AuGaTe$_2$ has a direct band gap located at Γ point. The optical results show that the studied compounds have applications in solar cell and optical devices.

## References

[1] S. Chandra, Anita Sinha and V. Kumar, International Journal of Modern Physics B Vol. 33, No. 28 (2019) 1950340.

[2] J. Filipowicz, N. Romeo and L. Tarricone, Solid State Commun. 38, 619 (1981).

[3] MacKinnon, Numerical Data and Functional Relationships in Science and Technology (Springer-Verilag, Berlin, 1985), p. 124.

[4] F. Tran, P. Blaha, Phys. Rev. Lett. 102 (2009) 226401.

[**5**] W. Kohn, L. J. Sham, Phys. Rev. 140 (1965) A 1133.

[6] S. Cottenier, Density Functional Theory and the family of (L)APW-methods: a step-by-step introduction, 2002-2013 (2$^{nd}$ edition), ISBN 978-90-807215-1-7.

[7] R. Dreizler, E. K. U. Gross,Density functional Theory, Springer, New York (1995).

[8] F. Kootstra, P. L. de Boeij, J. G. Snijders, Efficient real-space approach to time-dependent density functional theory for the dielectric response of nonmetallic crystals, J. Chem. Phys. 112 N°15 (2018) 6517-6531.

[9] C. Li, R. Requist, E. K. U. Gross, Density functional theory of electron transfer beyond the Born-Oppenheimer approximation: case study of LiF, J. Chem. Phys. 148 (2018) 084110(1-10).

[10] K. Schwarz, P. Blaha, G. K. H. Madsen, Electronic structure calculations of solids using the WIEN2k package for material sciences, Comput. Phys. Commun. 147 (2002) 71-76.

[11] S. A. Khandy, I. Islam, Z. S. Ganai, D. C. Gupta, K. A. Parrey, J. of Elec. Materi. 47 N°1 (2018) 436-442.

[12] R. Khemici, Z. Chouahda, L. Tairi, F. Semari, B. Amimoura, S. Benlameri, H. Meradji, S. Ghemid, Chinese J. Phys. 56 (2018) 1033.

[13] C. Sifi, F. Chouit, H. Bendjeddou, H. Meradji, S. Ghemid, Comput. Condens. Matt. 21 (2019) e00398

[14] S. Gagui, B. Zaidi, Y. Meghdoud, B . Hadjoudja, B. Chouial, H. Meradji, S. Ghemid, C. Shekhar, Comput. Condens. Matt. 22 (2020) e00433.

[15] F. Zami, L. Djoudi, M. Merabet, S. Benalia, M. Boucharef, R. Belacel and D. Rached, Optik-International J. for light and Electron. Opt. 180 (2019) 873-883.

[16] D. Koller, F. Tran, P. Blaha, Improving the modifief Becke-Johnson exchange potential, Phys. Rev. B 85 (2012) 155109(1-8).

[17] S. Sharma, A. S. Verma, R. Bhandari, S. Kumari and V. K. Jindal, Material science in Semiconductor Processing 26, (2014) 187-198.

# Modeling, Design and Performance Study of a Linear Fresnel Plant: Application in Sahelian Rural Areas

## Sory Diarra[1, a],

[1] *Laboratoire d'Énergétique Appliquée, École Supérieure Polytechnique de Dakar, BP: 5085, Dakar-Fann, Sénégal*

[a]Corresponding author: sory.diarra@ucad.edu.sn; sorydiarra47@gmail.com;

**Abstract.** The aim of this work is to study a Linear Fresnel Plant (LFP) in rural Sahelian areas. An analytical method is used to model optical transfers in the system, followed by a sizing using MATLAB software. Then, the analytical method is compared with the Monte Carlo method using TONATIUH rays trace software. And finally, the optical characteristics of the LFP over the period from December to April are studied by simulation using TONATIUH. The design gives for a thermal power of 51.01 $kW_{th}$ an opening area of the LFP field equal to 109.04 m$^2$ with a coverage rate of 75.41%. The comparison of the analytical method with that of ray tracing confirms the validity of the analytical method for the calculation of power. As expected, numerical simulations show for each day a peak of the power received around 13 h, and optical efficiency of the field increase from December to April.

## INTRODUCTION

In countries of sub-Sahelian Africa only about 32% of the population have access to energy, among people having no access to electricity, 80% live in rural areas [1]. These regions are generally very sunny which makes solar technologies, in particular solar concentrators, very good alternatives for energy production. Among the solar-concentrating technologies, the most suitable for these mostly poor areas, are the Fresnel Linear Reflectors. These are simple to design, affordable and can achieve the performance of parabolic trough concentrators [2]. However, little work of this type of concentrator has been carried out in this area. Our main objective is to preform the modeling, sizing and numerical analysis of a Linear Fresnel Plant for geographic coordinates 14.7° North and 17.4°West of Dakar, Senegal.

.

## MODELING OF THE LINEAR FRESNEL PLANT

### Description of the Linear Fresnel Plant (LFP)

The LFP consists of a field of flat plate reflectors of equal widths arranged in a row, and a monotube receiver with a glass tube to cover it and reduce heat losses by radiation (Figure 1 and Figure 2). Geometric characteristics of the system are : the number of reflectors on both sides of the receiver (k), the length and width of reflectors (L and w), the position of each reflector and the spacing between reflectors (s), the height and length of the receiver ($f$ and $L_p$), the Outside diameters of the absorber tube and the glass tube. The main physical characteristics are the optical properties of reflectors and receiver elements, as well as the thermo-physical properties of the heat transfer fluid.
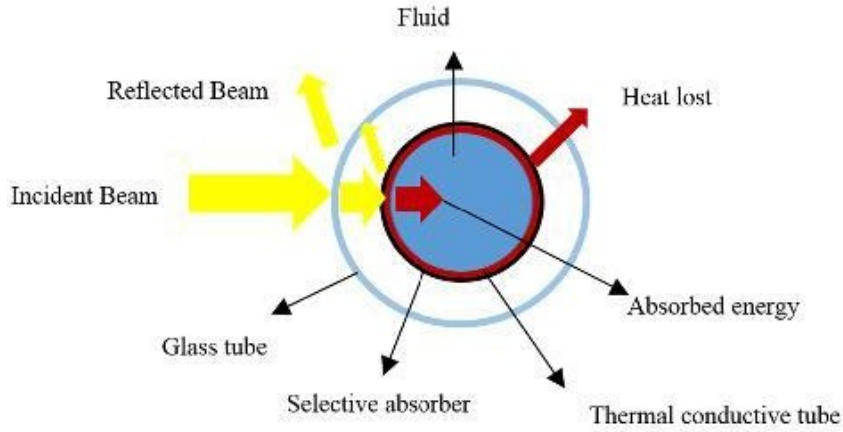
**Figure 1**: Tubular receiver

## Equations of the Model

*Modeling Radiative Optical Transfers*

Our objective is to determine the total power received by the absorber tube and to be able to evaluate the optical efficiency. The analytical method developed by Mathur et al. [3] will be used. This method gives the position (Q), inclination (θ) of each reflector and spacing (s) between the reflectors. It has the particularity, as illustrated in Figure2, to avoid blocking and shading when the sun's rays have an incidence perpendicular to the plane containing the opening surface.
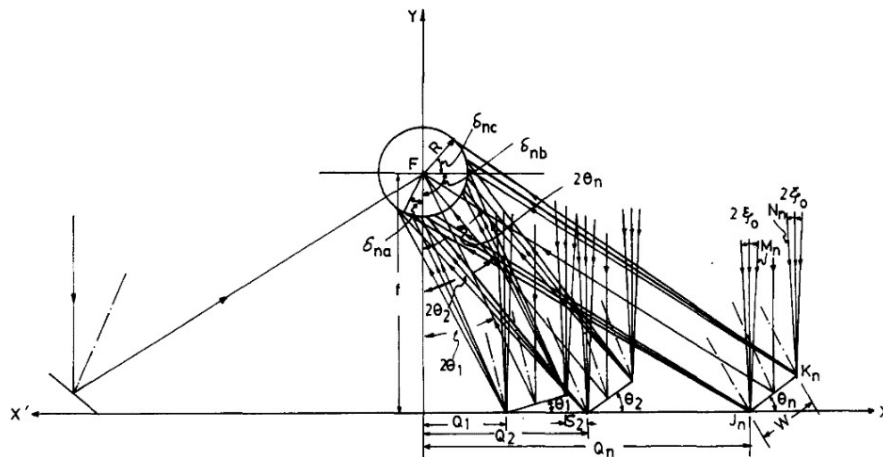


**Figure 2**: LFP with tubular absorber [3]

For a reflector "n" located on either side of the receiver (n = 1,2, ..., k), the optical design gives its offset with respect to the center ($Q_n$), its inclination ($\theta_n$), its offset with respect to the reflector which precedes it ($S_n$), the diameter of absorber tube needed to intercept all the reflected radiation ($D_p$) and the total width of field (D).

$$Q_n = Q_{n-1} + W \cos \theta_{n-1} + S_n$$

(
1)

$$\theta_n = \frac{1}{2}\left[\tan^{-1}\left(\frac{Q_n + \frac{W}{2}\cos\theta_n}{f - \frac{W}{2}\sin\theta_n}\right)\right] \tag{2}$$

$$S_n = W\sin\theta_{n-1}\tan(2\theta_n + \xi_0) \tag{3}$$

$$D_p = 2\left[w\sin\theta_k + \frac{Q_k + W\cos\theta_k}{\tan(2\theta_k - \xi_0)} - f\right]\sin(2\theta_k - \xi_0) \tag{4}$$

$$D = 2Q_1 + 2\sum_{n=1}^{k}(W\cos\theta_n + S_n) \tag{5}$$

Once the solar rays are reflected, the appearance of several zones with different concentration ratios is observed on the surface of the absorber tube. Indeed, more a reflector moves away from the center, more its image onthe surface of the absorber tube will be large. Therefore, the greatest concentration ratio will be at the center of the tube. For a number of reflectors on both sides of the receiver equal to "k", the number of zones on the surface of the tube will be "q = k + 1".

Each reflector (n) contributes to the surface of the tube. This contribution $(CI_n)$ is defined by [3] equal to:

$$CI_n = \frac{W\cos\theta_n}{r_n} \tag{6}$$

With $(r_n)$ the width of the image of reflector on absorber tube:

$$r_n = (\delta_{na} + \delta_{nb} + \delta_{nc})\frac{D_p}{2} \tag{7}$$

Each area on surface of the absorber tube has its concentration ratio. The central part of the absorber tube which intercepts the contribution of all reflectors of the field has a local concentration ratio $(LCR_1)$ equal to [3]:

$$LCR_1 = 2\sum_{n=1}^{k} CI_n \tag{8}$$

The local concentration ratio of the other zones of the absorber tube surface is given by:

$$LCR_i = \sum_{n=i-1}^{q-1} CI_n \tag{9}$$

With (i=2, …, q)

To determine the power received by the absorber tube, we need in addition the surface of each zone. Thus, the areaof the central zone 1 noted $(C_1)$ is given by:

$$C_1 = 2 * \delta_{a1} * \frac{D_p}{2} * L_p \tag{10}$$

The area of the second zone with the second largest concentration ratio $(C_2)$ is given by:

$$C_2 = 2\left(\frac{\pi}{2} + \delta_{c1} - \delta_{a1}\right)\frac{D_p}{2} * L_p \tag{11}$$

From the third zone, the surfaces $(C_j)$ are given by:

$$C_i = 2(\delta_{c(i-1)} - \delta_{c(i-2)}) \frac{D_p}{2} * L_p \tag{12}$$

With (i=3, …, q)

The absorbed radiation ($\emptyset$) from the reflectors per unit aperture area ($A_c$) is given by [4]

$$\emptyset = I_b \rho_r \alpha_p \gamma r_g \tag{13}$$

$I_b$: The Direct Normal Irradiance of site (DNI)

$\rho_r$: The specular reflectance of reflectors

$r_g$: Glass cover transmittance

$\alpha_p$: Absorber absorptance

$\gamma$: The intercept factor

And the aperture area is equal to:

$$A_c = 2L \sum_{n=1}^{k} (W \cos \theta_n) \tag{14}$$

Thus, the flux density of each zone ($\emptyset_i$)is given by:

$$\emptyset_i = \emptyset * LCR_i \tag{15}$$

With (i=1, …, q)

Finally, the total solar power received by the absorber tube ($P_p$) is given by:

$$P_p = \sum_{i=1}^{q} \emptyset_i C_i + I_b r_g \pi \frac{D_p}{2} L_p \tag{16}$$

The optical efficiency ($\eta_0$) and the intercept factor ($\gamma$) are given by:

$$\eta_0 = \frac{P_p}{A * I_b} \tag{17}$$

$$\gamma = \frac{P_p}{A_c I_b} \tag{18}$$

With A the total area of the field equal to:

$$A = D \times L \tag{19}$$

*Modeling of Thermal Transfers within the Receiver*

In this part, our objective is to determine the thermal power lost by the receiver and the useful thermal power.

The power lost by the receiver ($Q_{Loss}$) can be determined by iteration from its three expressions [4]:

$$Q_{Loss} = \frac{2\pi\lambda_{eff}L_p}{ln(\frac{D_p}{d_g})}(T_p - T_{gi}) + \frac{\pi D_r L_r \sigma(T_p^4 - T_{gi}^4)}{\frac{1}{s_p} + \frac{1-s_g}{s_g}(\frac{D_p}{d_g})} \tag{20}$$

$$P_{Loss} = \frac{2\pi\lambda_c L_p(T_{gi} - T_{ge})}{ln(\frac{D_g}{dg})} \tag{21}$$

$$Q_{Loss} = \pi D_g L_p h_a (T_{go} - T_a) + \varepsilon_g \pi D_g L_p \sigma(T_{go}^4 - T_{Sky}^4) \tag{22}$$

where the subscript p represents the absorber tube and subscripts a, *gi* and *go* represent the external environment, the glass inside and the glass outside. The cover thermal conductivity is $k_c$ and $k_{eff}$ is an effective conductivity for convection between the receiver.

In the same way, the useful power recovered by the fluid ($Q_u$) is given by [4]:

$$Q_u = E[P_p - A_p U_L(T_{fi} - T_a)] \tag{23}$$

With E the Flow Factor

$$E = \frac{\dot{m} C_p}{A_p U_L}[1 - \exp(-\frac{A_p U_L F^F}{\dot{m} C_p})] \tag{24}$$

$U_L$ the Thermal Loss Coefficient

$$U_L = \frac{P_{Loss}}{A_p(T_p - T_a)} \tag{25}$$

And $F'$ the Collector Efficiency Factor

$$F' = \frac{\frac{1}{U_L}}{\frac{1}{U_L} + \frac{Dp}{h_f dp} + \frac{Dpln(\frac{D_p}{dp})}{2\lambda p}} \tag{26}$$

where the subscript f represents the fluid.

# SIZING OF THE LFP

The sizing of the LFP ensures the operation of a 3 $kW_e$ micro-ORC plant studied by Bouhamadi [5]. The necessary thermal power is 51 $kW_{th}$. The sizing is carried out for the locality of Dakar with annual average climate data. A number of parameters has been set as shown in table 1. These choices are justified by studies that have been carried out. Singh [6] found that the optimal width of the reflectors (W) should be between 10 and 12 cm for better fixation and manipulation and the number of reflectors on both sides of the receiver (k) between 10 and 15 to have optimal overall performance. Xiao [7] shows that for latitudes less than 25 °, an orientation of north-south Tracking axis offers better efficiency. Finally, Duffie and Beckman[4] recommends a spacing between the absorber tube and the glass tube between 10 mm and 15 mm to minimize the thermal losses of the receiver. In addition, water was chosen as a thermal fluid.

**Table 1**: Geometrical parameters fixed for sizing

| Parameter | Value |
|---|---|
| Number of reflectors | 30 |
| Width of reflectors | 12 cm |
| Width of the annular space between the absorber tube and the glass tube | 15 mm |
| Orientation of tracking axis | North-South |

.

Sizing consists of determining the total area of the field and its geometric characteristics. The sizing methodology is presented in the form of the algorithm in figure 3. The methodology is first to fix all the input parameters such as the length of the reflectors and the receiver, the number of reflectors and the thermo-physical properties of the different constituting elements of the LFP. From this data, the geometric characteristics of the LFP are calculated such as the positions, inclinations and spacings of the reflectors and the diameters of the absorber tubes and the glass cover. The thermal power received by the absorber tube, the useful power recovered by the thermal fluid and the thermal losses of the receiver are then calculated. Finally, a comparison is made to check if the calculated thermal power output is equal to the one desired. If this is the case, the algorithm ends. Otherwise, the length of the reflectors from that of the receiver is increased and the calculations are resumed.
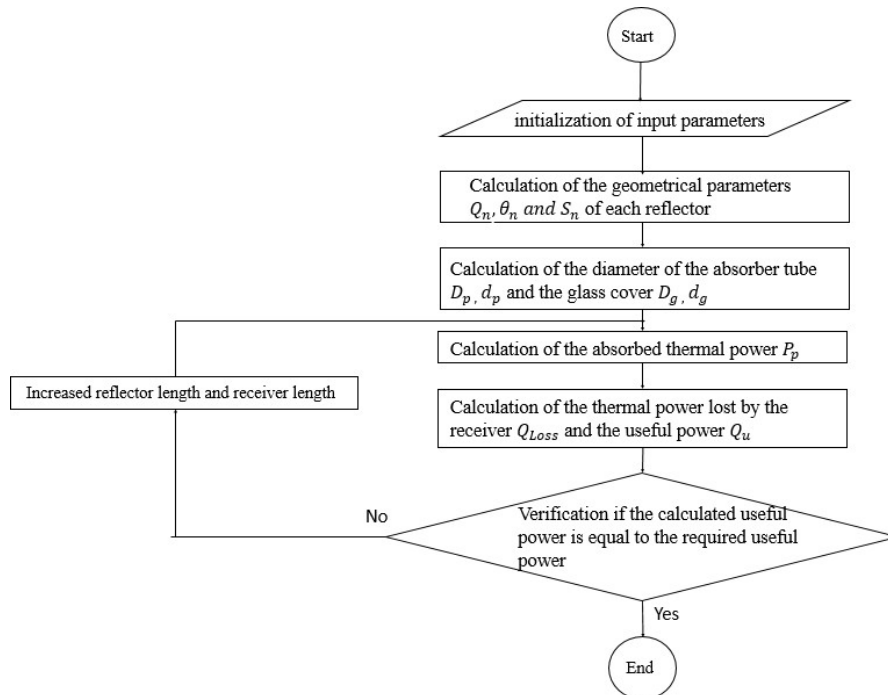


**Figure 3**: Sizing methodology

Since the equations of the model are almost all interdependent, they can only be solved iteratively. To solve the algorithm, a MATLAB program was written and the sizing results are presented in table 2.

**Table 2**: Sizing results

| Parameter | Value |
|---|---|
| LFP field total area | 109.64 $m^2$ |
| LFP field aperture area | 82.68 $m^2$ |
| Coverage rate | 75.41 % |
| LFP field width | 3.44 m |
| LFP field length | 24.023 m |
| Receiver height | 1.82 m |
| Outside diameter of the absorber tube | 0.1431 m |

## COMPARISON OF THE ANALYTICAL METHOD AND THE MONTE CARLO RAYTRACING METHOD

In this part, the dimensioned LFP is modeled in the Tonatiuh rays tracing software to perform a flux map analysison the absorber tube and determine the power received by the absorber tube. These results are compared with those obtained by the analytical method using MATLAB software.

Figure 4 represents the distribution of the incident flux on the surface of the absorber tube obtained by the Monte Carlo rays tracing method and Figure 5, the one obtained by the analytical method.

The analyzes show that the fluxes of different zones are more important with the Monte Carlo method than with the analytical method. However, the surfaces of different zones on the surface of the absorber tube are larger with the analytical method than with the Monte Carlo method. Knowing that the Monte Carlo method is the most accurate, the conclusion is that the analytical method tends to overestimate the area of the zones and to minimize their flux. On the other hand, the total powers that reach the absorber tube are quite close with a relative error of 4%. This is explained by the fact that the two errors made with the analytical method is compensated when it comes to calculating the power received by the absorber tube. This analysis shows that the analytical method can be used for the calculation of powers.
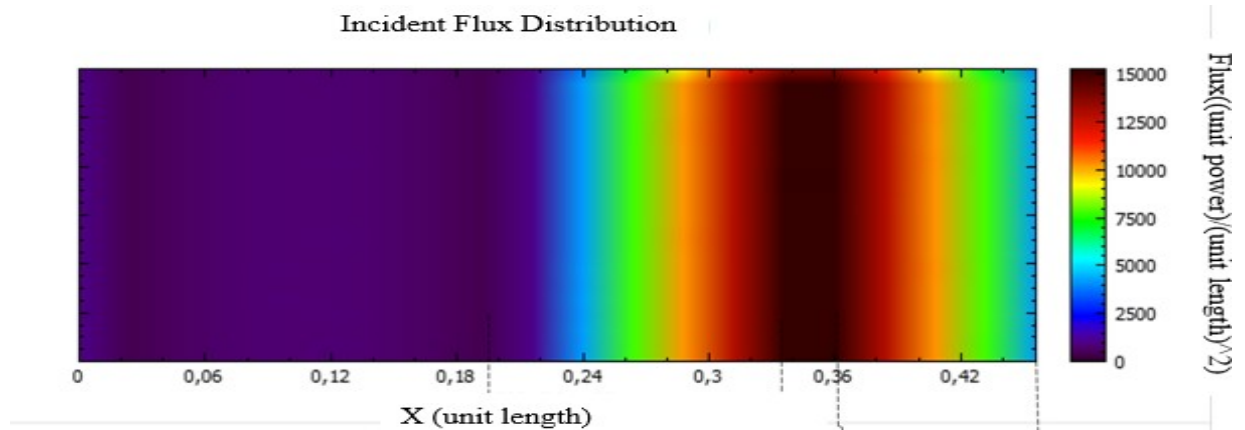


**Figure 4**: Distribution of the incident flux on the absorber tube surface obtained by the Monte Carlo rays tracing method with TONATIUH
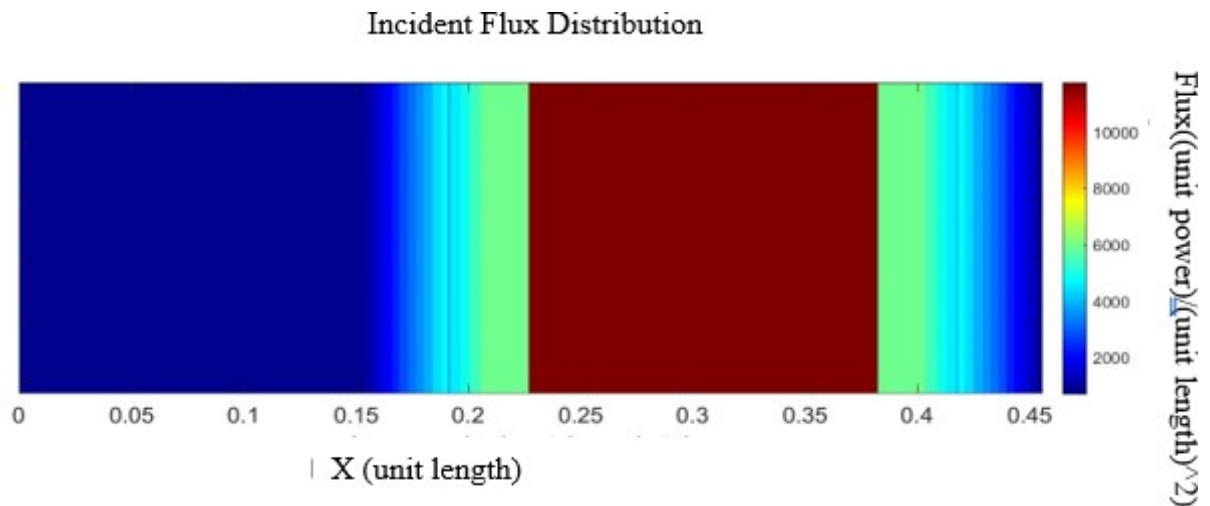
Incident Flux Distribution



**Figure 5**: Distribution of the incident flux on the surface of the absorber tube obtained by the analytical method withMATLAB

## SIMULATION OF THE LFP

## Methodology

In this part, the LFP is simulated for the geographical coordinates of Dakar with the Tonatiuh software. Actual measured data of the DNI was collected and only over the period from December to April. Therefore, the simulations are run only during this period. Four specific days are chosen in this period namely December 28th, February 1st, March 22nd and April 5th. The simulations are run using time steps of 15 minutes. To avoid losses by cosine effect, the receiver is moved longitudinally with respect to its axis of symmetry. The data determined for each simulation point are the power received by the absorber tube, the power incident on the field, the thermal power recovered by the thermal fluidand the optical efficiency.

## Results and Discussions

Figure 6 shows that the power received by the absorber tube follows globally the variations of the incident power on the field, with the day of February 1st, which gives the highest powers. Each day a peak of power received by the absorber tube is observed around 13 h. This phenomenon is very characteristic of LFPs, which always give a peak ofproduction in the middle of the day compared to a parabolic trough [8]. Indeed, this moment corresponds to the instantwhen the sun is the highest in the sky and the optical losses by shading and blocking are lower.
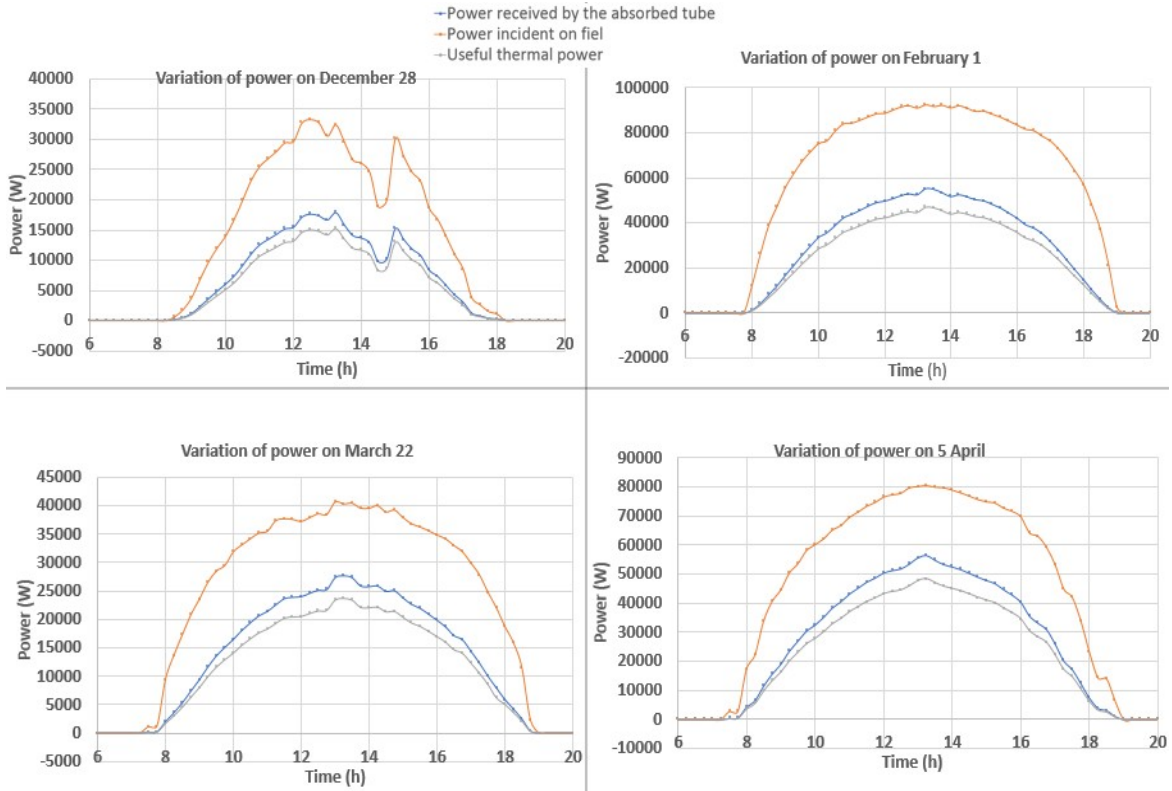
**Figure 6**: Powers obtained for simulation days

Figure 7 shows the variations of optical efficiency. This efficiency increases day by day over the period from December to April, with always the peak around 13 h. This phenomenon is also explained by the fact that during theperiod from December to April for the geographical coordinates of Dakar, the height of the sun increases day by day. The higher the sun is in the sky, the less optical losses will be important. This shows the dependence of optical performance of the LFP with the height of the sun.
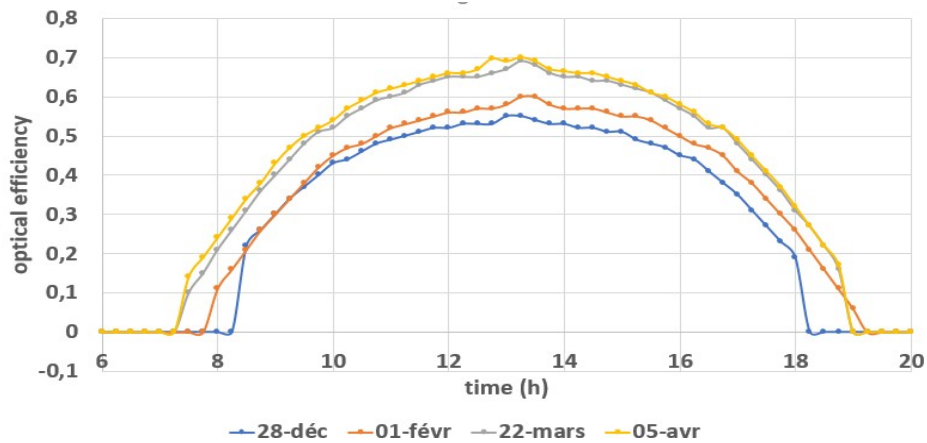


**Figure 7**: Variation of the optical efficiency of the field during simulation days

# CONCLUSION

In this work, an LFP was modeled and simulated for the city of Dakar Senegal with geographic coordinates 14.7° North and 17.4° West. The modeling was carried out using an analytical method. This method was compared to the ray tracing method, showing that it can be used for the calculation of the powers. The results of the simulations showed that the optical performance of the LFP is very dependent on the height of the sun. This means that a better field orientation, a more adequate tracking system, and optimized geometry could greatly improve the performance of the LFP. In our future works, the focus will be placed on the optimization and the realization of a prototype for the Sahelian rural areas.

# REFERENCES

1. A. Thiam, E. I. Cissé, B. A. Ndiogou, K. Faye and M. Faye, "Design and CFD modeling of a solar micro gas turbine for rural zones areas," International SolarPACES Symposium, 2018, AIP Conference Proceedings 2126, 140006 (2019).
2. F. Veynandt, "Cogénération héliothermodynamique avec concentrateur linéaire de Fresnel : Modélisation de l'ensemble du procédé," Ph.D. thesis, Toulouse University, 2011.
3. S. S. Mathur, T. C. Kandpal and B. S. Negit, "Optical design and concentration characteristics of Linear Fresnel Reflector Solar Concentrators-II. Mirror elements of equal width," Energy Conversion and Management 31 (1991), pp .221–232.
4. J. A. Duffie and W. A. Beckman, "Solar Engineering of Thermal Process," Second, John Wiley and Sons, NewYork, USA, 1991.
5. S. Bouhamadi, "Evaluation du potentiel de la technologie solaire thermodynamique à concentration en climat désertique et sahélien : Cas de la Mauritanie," Ph D thesis, Dakar Cheikh Anta Diop University, 2017.
6. G. Singh, "Technical note: Performance study of a linear Fresnel concentrating solar device," Renewable Energy18 (1999), pp .409-416.
7. G. Xiao, "Tilting mirror strips in a linear Fresnel reflector," 2012, hal-00675222
8. J. Dersch, G. Morin, M. Eck, A. Haberle "Comparison of Linear Fresnel and Parabolic Trough collector systems- System analysis to determine break even cost of Linear Fresnel Collectors," International SolarPACES Symposium, 2009.